Modelling Heat Transfer and Respiration of Occupants in Indoor Climate

By:

Rehan Yousaf

A doctoral thesis submitted in partial fulfilment of the requirements for the award of Doctor of Philosophy of Loughborough University

July 2016

To my wonderful family whose love
and patience with me during this "very
long" journey kept me motivated

We cannot solve our problems with the same thinking we used when we created them.

Albert Einstein

Abstract

Although the terms "Human Thermal Comfort" and "Indoor Air Quality (IAQ)" can be highly subjective, they still dictate the indoor climate design (HVAC design) of a building. In order to evaluate human thermal comfort and IAQ, one of three main tools are used, a) direct questioning the subjects about their thermal and air quality sensation (voting, sampling etc.), b) measuring the human thermal comfort by recording the physical parameters such as relative humidity, air and radiation temperature, air velocities and concentration gradients of pollutants or c) by using numerical simulations either including or excluding detailed thermo-physiological models. The application of the first two approaches can only take place in post commissioning and/or testing phases of the building. Use of numerical techniques can however be employed at any stage of the building design. With the rapid development in computational hard- and software technology, the costs involved in numerical studies has reduced compared to detailed tests. Employing numerical modelling to investigate human thermal comfort and IAQ however demand thorough verification and validation studies. Such studies are used to understand the limitations and application of numerical modelling of human thermal comfort and IAQ in indoor climates.

This PhD research is an endeavour to verify, validate and apply, numerical simulation for modelling heat transfer and respiration of occupants in indoor climates. Along with the investigations concerning convective and radiation heat transfer between the occupants and their surroundings, the work focuses on detailed respiration modelling of sedentary human occupants. The objectives of the work have been to: verify the convective and radiation numerical models; validate them for buoyancy-driven flows due to human occupants in indoor climates; and apply these validated models for investigating human thermal comfort and IAQ in a real classroom for which field study data was available. On the basis of the detailed verification, validation and application studies, the findings are summarized as a set of guidelines for simulating human thermal comfort and IAQ in indoor climates.

This PhD research involves the use of detailed human body geometries and postures. Modelling radiation and investigating the effect of geometrical posture has shown that the effective radiation area varies significantly with posture. The simulation results have

shown that by using an effective radiation area factor of 0.725, estimated previously (Fanger, 1972) for a standing person, can lead to an underestimation of effective radiation area by 13% for the postures considered.

Numerical modelling of convective heat transfer and respiration processes for sedentary manikins have shown that the SST turbulence model (Menter, 1994) with appropriate resolution of near wall region can simulate the local air velocity, temperature and heat transfer coefficients to a level of detail required for prediction of thermal comfort and IAQ. The present PhD work has shown that in a convection dominated environment, the detailed seated manikins give rise to an asymmetrical thermal plume as compared to the thermal plumes generated by simplified manikins or point sources.

Validated simulation results obtained during the present PhD work have shown that simplified manikins can be used without significant limitations while investigating IAQ of complete indoor spaces. The use of simplified manikins however does not seem appropriate when simulating detailed respiration effects in the immediate vicinity of seated humans because of the underestimation in the amount of re-inhaled CO2 and pollutants from the surroundings. Furthermore, the results have shown that due to the simplification in geometrical form of the nostrils, the CO2 concentration is much higher near the face region (direct jet along the nostrils) as compared to a detailed geometry (sideways jet).

Simulating the complete respiration cycle has shown that a pause between exhalation and inhalation has a significant effect on the amount of re-inhaled CO2. Previous results have shown the amount of re-inhaled CO2 to range between 10 - 19%. The present study has shown that by considering the pause, this amount of re-inhaled CO2 falls down to values lower than 1%. A comparison between the simplified and detailed geometry has shown that a simplified geometry can cause an underestimation in the amount of re-inhaled CO2 by more than 37% as compared to a detailed geometry.

The major contribution to knowledge delivered by this PhD work is the provision of a validated seated computational thermal manikin. This PhD work follows a structured verification and validation approach for conducting CFD simulations to predict human thermal comfort and indoor air quality. The work demonstrates the application of the validated model to a classroom case with multiple occupancy and compares the

measured results with the simulation results. The comparison of CFD results with measured data advocates the use of CFD and visualizes the importance of modelling thermal manikins in indoor HVAC design rather than designing the HVAC by considering empty spaces as the occupancy has a strong influence on the indoor air flow. This PhD work enables the indoor climate researchers and building designers to employ simplified thermal manikin to correctly predict the mean flow characteristics in indoor surroundings.

The present work clearly demonstrates the limitation of the PIV measurement technique, the importance of using detailed CFD manikin geometry when investigating the phenomena of respiration in detail and the effect of thermal plume around the seated manikin. This computational thermal manikin used in this work is valid for a seated adult female geometry.

Acknowledgements

There are so many people in my life without whom I would have never been able to finish writing this thesis. A number of times in the last 7 years, I thought about quitting the PhD and lost belief in myself. If I have to name one person who didn't lose belief in me, then it is my supervisor, Prof. Dr. Malcolm J. Cook. His sincere and devoted guidance helped me gather my energies and continue working on my PhD further. I deeply acknowledge his support and guidance. I admire his patience, positive attitude and readiness to help that never let me down and feel the disadvantages that an off-campus student with a full time job in the industry has to face.

I would like to thank Dr. Tong Yang who remained at my side with all her advice and supported me throughout her stay at Loughborough University. I am also indebted to Dr. Dusan Fiala and Prof. Andreas Wagner who during my stay at Karlsruhe University supported me with their valuable suggestions and guided me to establish a sound understanding of the subject of human thermal comfort.

I would like to thank all my colleagues at the company Pöyry Switzerland, especially Dr. Severin Wälchli who not only accepted the role of being my supervisor at the company but also aided me with his practical knowledge in the realm of CFD.

I would like to thank Dr. Julian Highfield and Aaron Turner from the high performance computing (HPC) centre of Loughborough university who paved my way to perform all my simulations at the HPC clusters. Without their timely help, it would be very hard if not impossible to achieve the simulation results in time.

Last but not least, I would like to thank my family who without doubt understood the importance of finishing off this PhD work, remained patient with me and kept on supporting me and ensured a completion of this PhD work.

Table of Contents

Nomenclature

ρ	Density [kg/m^3]
Γ	Diffusion coefficient [kg/m-s]
ϕ	General variable
β	Thermal expansion factor
β',C_μ, C_ε, C_1,C_2,C_3	Turbulence model constants
∇G_v	Divergence of spectral incident radition
δ_{ij}	Kronecker delta
[-]	Dimensionless quantitiy
Ø	the in-scattering phase function [Sr^{-1}]
A	Linear
C_p	Specific heat at constant pressure [J/kg-k]
D_{AB}	binary mass diffusion coefficient in [m^2/s]
F	View factor
g	Gravity
h_c	Convective heat transfer coefficient [W/m^{2}K]
h_m	Mass transfer coefficient [m/s]
J_p	Radiosity at a point p
k	Von Kàrmàn constant = 0.41

K_a	absorption coefficient [m^{-1}]
K_s	Scattering coefficient [m^{-1}]
I_b	Blackbody emission intensity [W/(m²Sr)]
I_v	spectral radiation intensity [W/(m²Sr)]
P	Pressure [Pa]
q''	Heat flux [W/m^2]
R	Universal gas contant 8.314 [J/mol-K]
S	Source or sink
s’	Path length [m]
T	Temperature [K]
V	Volume [m3]
y^+	Normalised distance to the wall
Ω	solid angle [Sr]
α	Thermal diffusivity of the fluid in [m^2/s]
λ	Thermal conductivity [W/m-K]
μ	Dynamics viscosity of fluid [kg/m-s]
μm	Micro meter
σ	Stefan-Boltzman
σ_p	Turbulent Schmidt number
τ	Shear stress [N/m^2]

υ	Kinematic viscosity of fluid [m^2/s]

Subscripts

A_{eff}	Effective area
A_p	Projected area
A_s	Surface area
f_{eff}	Effective radiatin area factor
f_p	Projected area factor
1-2	From surface 1 to surface 2
x,y,z	directions

Superscripts

ave	Average
c	Comfort
I,j,k	Unit vectors representing x,y and z directions
k	Turbulence kinetic energy
k-ε	Turbulent energy and dissipation turbulence model
k-ω	Turbulent energy and dissipation rate turbulence model
n	Neutral
r,s	Position Vector
RNG	Renormalization Group

ε	Turbulent dissipation

List of Abbreviations

ach^{-1}	air change per hour
ANSI	American National Standards Institute
ASHRAE	American Society for Heating Refrigeration and Air Conditioning
BSA	Body Surface Area
CFD	Computational Fluid Dynamics
CIBSE	Chartered Institution of Building Services Engineers
ET	Effective Temperature
HVAC	Heating Ventilation and Air Conditioning
IAQ	Indoor Air Quality
ISO	International Standards Organization
MRT	Mean Radiant Temperature
PIV	Particle Image Velocimetry
PMV	Predicted mean vote
PPD	Percentage people dissatisfied
PPM	Parts per million
RSM	Reynolds Stress equation Model
RTE	Radiation Transfer Equation
SBS	Sick Building Syndrome
SET	Standard Effective Temperature
SST	Shear Stress Transport

List of Figures

List of Tables

1 Introduction

Human-environment thermal interactions play an important role in numerous areas of human endeavour from the safety of fire-fighters, thermal comfort in various environments to energy efficient planning of heat and ventilation systems. The thermal interactions that occur between humans and their immediate environments are however very complex and thus difficult to predict.

1.1 Purpose of Study

Although the target conditions for an indoor environment may vary, the general guidelines orient themselves towards the human demands of thermal comfort, visual comfort and an acceptable air quality in the indoor climate. Research comprising both experiments and field studies have been carried out to identify the problems in different building systems that lead to high energy demand, poor indoor air quality, thermal and/or visual discomfort etc. It is shown in a number of studies that poor building design or systems therein not only lead to health problems in buildings, but can also lead to a decrease in work efficiency, especially in learning institution buildings (Griffiths & Eftekhari, 2008), (Mendell & Heath, 2005).

The subjective nature of thermal comfort and indoor air quality (IAQ) make it difficult to be expressed in terms of physical units which are valid for everyone. The best and still most widely used method of accessing thermal comfort and IAQ is the field study by using "questionnaires". These are sets of questions related to the perception of the indoor climate. The occupants of a particular indoor climate answer the questionnaire which is later statistically analysed to estimate the global perception of thermal comfort in that occupied space. Besides the individual and very much non tangible variables such as psychological and cultural influences, health condition etc. some common physical factors are prominent in every field of study.

A number of researchers have investigated these physical factors affecting human thermal comfort and indoor air quality using numerical modelling and/or experimental techniques. All these studies recognized the fact that in order to mathematically define the perception of thermal comfort and IAQ, the information about the immediate surroundings of the occupant is necessary. The more accurate this

information, the better is the mathematical representation of thermal comfort and IAQ.

1.2 Importance of the work

Although a lot of work has been done in developing numerical models, it was either done for thermal comfort or for IAQ. Validated numerical models that can consider thermal comfort together with human respiration processes to estimate the IAQ are not very common. Often in experimental work, intrusive measurements lead to inaccurate results and lack of exact boundary conditions thereby leading to validation errors when using this data for numerical modelling. Numerical modelling on the other hand is dependent on precision of the numerical methods, turbulence and heat transfer models, numerical mesh etc.

With the development in both software and hardware techniques, the need to work with full scale numerically validated models that can be used with confidence to predict both thermal comfort and IAQ at the same time is very strongly felt. The importance of the present work lies in the development of a well verified and validated model capable of capturing the global as well as local aspects of human thermal comfort and IAQ. The work provides a validated seated human model capable of breathing that can be directly used in any indoor surrounding to investigate the local human thermal comfort and IAQ conditions. The work provides a set of guidelines, following which indoor human thermal comfort and IAQ can be numerically investigated to achieve reliable results.

The aim of the present research was to develop a full scale validated Computational Fluid Dynamics (CFD) approach for modelling the physical parameters influencing IAQ and human thermal comfort.

The major limitation of the present work is that, although capable, the current model is not validated for transport of heavier particles and their deposition on surfaces (settling effects). The work is valid to consider air as multi-component mixture of gases and estimating the flow of particles that are considered as airborne. The size limitation of such airborne particles is in the range of 2.5 μm to a maximum of 5 μm (Hathway, et al., 2013), (Gao & Niu, 2006), (Roberts, et al., 2006).

A detailed analysis of settling and deposition of heavier particles requires the modelling, verification and validation of multi-phase flows, that is beyond the scope of the present PhD work.

1.3 Objectives

The aim of the research work was achieved through the following objectives:

1. Conduct a detailed literature review of the on-going and previous work regarding modelling of human thermal comfort, indoor air quality and the factors affecting them.
2. Conduct benchmark studies of the factors affecting human thermal comfort and indoor air quality.
3. Conduct a full scale experimental study to determine the temperature and flow field due to a sedentary breathing and non-breathing human thermal manikin.
4. Conduct CFD validation based on the full scale experiments.
5. Use the developed CFD techniques to model a real classroom case and compare the measured classroom data with the CFD results.
6. Summarize the conclusions as guidelines for CFD modelling of IAQ and thermal comfort in indoor climates.

1.4 Contributions to Knowledge

The main contribution to knowledge delivered by this PhD work is the provision of a validated seated computational thermal manikin. The systematically validated seated thermal manikin can be readily imported into any indoor surrounding to estimate the effect of human thermal comfort, the thermal plume analysis and to analyse the effect of respiration on the micro and macro surrounding of the occupants.

In order to use the seated computational thermal manikin, a set of generic guidelines are documented that cover the use of the validated computational manikin from mesh generation and application of the appropriate physical models to important aspects of post-processing of the quantities of interest.

Besides the provision of validated set of guidelines, the presented PhD work highlights the limitation of using simple point source thermal plume theory to complex

human geometry and quantifies the effect of human posture on the effective radiation and projection areas that are very important in thermal radiation study.

This PhD work also contributed to knowledge by highlighting the effect of simplified and detailed human geometry on the amount of dispersion of CO2 (and airborne contaminants) within the macro climate (surrounding room) as well as the transport and level of re-inhalation of CO2 within the micro-climate generated due to thermal buoyancy of the seated human itself.

The novelty of the present work lies in the fact that the same model can be employed for investigating the macro and micro climates surrounding the seated human occupants. The validated simulation models and techniques used for estimating human thermal comfort, indoor air quality, effects of respiration and thermal plume can be effectively used by human thermo-physiological models.

1.5 General Methodology and Thesis layout

The thesis is subdivided into 9 chapters. The introduction to the work in chapter 1 is followed by a detailed literature review in chapter 2 which serves as the basis for selecting the research methods presented in chapter 3. As the aim of the work is to develop a validated numerical model for indoor climates which can identify the major physical parameters influencing human thermal comfort, emphasis is placed on the explanation of the chosen numerical method namely “Computational Fluid Dynamics” (CFD) which is given in a dedicated chapter (chapter 4). Chapter 5 explains how the chosen CFD code is verified to solve the airflow and thermodynamics governing equations accurately. The model validation is presented in chapter 6 by first conducting full scale experiments employing different measuring techniques and later comparing the results with numerical CFD simulations. The verified and validated numerical model is then employed for modelling respiration in chapter 7.

Based on the outcome of the verification and validation studies, a multiple occupancy real world scenario of a classroom is simulated as an application example and the results of simulation and measured values are compared. This application work is documented in chapter 8 and the research work is concluded in chapter 9 by describing the applicability, short comings and advantages of different methods used

and in particular the importance of using them in a complementary and coherent fashion.

2 Literature Review

This chapter encompasses the literature that was reviewed to define the research methodology. The importance of human thermal comfort and the indoor air quality in buildings is the key feature which serves the basis for the presented work. An introduction to indoor air quality (IAQ) and human thermal comfort and their interdependency is discussed in sections 2.2 and 2.3. Sections 2.4 and 2.5 review primarily the state-of-the-art analytical, numerical and experimental methods, their theoretical backgrounds and the relevant published work. The conclusions drawn on the basis of this literature review are summarized in section 2.6.

The literature review presented in this chapter is aimed to identify the physical parameters influencing the indoor climate and human thermal comfort thereby forming the basis of the research methods presented in chapter 3.

2.1 Introduction

Humans spend most of their time in indoor climates e.g. house, office, schools etc. and therefore require fresh air to breathe, and balanced surroundings to feel comfortable. Fresh air needs to be supplied to these indoor climates in order to maintain acceptable conditions free of hazardous pollutants. The required IAQ can be achieved by ventilating the spaces either naturally or mechanically. Irrespective of the method of air supply, the goal of air supply remains the same i.e. "to decrease the concentration of hazardous pollutants in indoor air", the type and concentration level of each pollutant is either dictated by the indoor climate itself or the environmental surrounding and therefore demand different ventilation rates and/or air treatment.

The term "comfort" in the modern world has become very multidisciplinary. The term comfort now encompasses psychological, physiological and environmental factors to a greater extent. This makes the global assessment of comfort very difficult and puts a huge expectation on the part of building designers. In the present work, emphasis is laid on the thermal comfort in the indoor climates.

Both IAQ and thermal comfort are interdependent and have shown to have a great influence on occupants' health and efficiency. Provision of IAQ and thermal comfort

for the occupants demands control of several physical parameters such as air temperature, air speed, humidity and pollutants. In order to control these parameters, construction and technological measures need to be taken. Construction measures include better insulation of buildings, better quality of windows and better construction methods. Technological measures include better heating, ventilation and air conditioning (HVAC) methods. Both construction and technical measures to control the physical parameters influencing IAQ and thermal comfort demand energy, the conservation of which is considered as one of the world's biggest challenges.

The following sections deal with IAQ and thermal comfort and the parameters affecting them and provide an overview of the published work in terms of the experimental, analytical and numerical methods used to assess and evaluate the IAQ and human thermal comfort.

2.2 Indoor Air Quality (IAQ) and Respiration

The term "Indoor Air Quality" covers two major non-thermal aspects of indoor climates: a) Hygienic aspects and b) comfort aspects. As quality is a relative term and is perceived differently by different people, a general measurable quantity is often needed to setup guidelines and minimum requirements.

Depending upon the metabolic activities human respiration requires between 0.1 - 0.9 l/s of fresh air (Awbi, 2003). The human respiration cycle is composed of inhalation and exhalation processes. Air in its basic composition is a mixture of nitrogen (78%), oxygen (21%), carbon dioxide (0.03%), water vapour (variable) and some rare gases (< 0.01%) at the surrounding temperature (Burchill, 2011). The surrounding outdoor air may not be "ideal fresh" as it may contain pollutants emitted due to traffic, industrial wastes etc. The exhaled air does not constitute the same mixture components as in the inhaled air due to the take up of oxygen in our bodies for metabolic activities. As a result of these metabolic activities, carbon dioxide is produced as a by-product thereby decreasing the oxygen to 16% and increasing carbon dioxide to 5% in the expired air. This expired air is fully saturated. The temperature of this expired air ranges between about 34°C and 37°C (Burchill, 2011) (Höppe, 1981).

CO2 is very often considered as an indicator of indoor pollution. Pettenkofer (1858) conducted a number of experimental studies in different buildings and concluded that a CO2 concentration of 0.1 vol.% (1000 ppm) should not be exceeded in indoor climates. This CO2 concentration value of 1000 ppm is known as the "Pettenkofer number" (Recknagel & Sprenger, 2007). Other researchers such as Yaglou et. al. (1936) also constituted that human bio-effluents are the governing indoor pollutants until Fanger et. al. (1988) showed that the building fabric, furnishing and interior decoration elements can have a much higher influence on IAQ than the human bio-effluents alone.

Humans sense the indoor air quality mainly by their sense of smell. A previous study (Milton, et al., 1999) showed that the percentage of absence of working people in offices with low air change per hour (ach^{-1}) is 0.5% -1% higher than those working in offices with higher air change rate. Another study showed that improving the air quality not only leads to the avoidance of sick building syndrome (SBS) symptoms but also increase the working efficiency of the occupants (Wargocki, et al., 2000). The German institute for working safety (Institute für Arbeitssicherheit, 1995) published a report in 1995 stating that a building with SBS symptoms can result in a decrease in the working efficiency by 2% -8%.

The spread of airborne infections have been reported by a number of researchers (Dye, et al., 1999), (Corbett, et al., 2003) (Viboud, et al., 2004). In most of these findings, the main cause of the spread is the exhaled air of an infected human. Considering the complexity of the indoor environment and the human occupancy, it is very difficult, if not impossible, to experimentally investigate the effect of human respiration on the micro and macro surrounding. Different researchers have tried to quantify the effect of breathing in order to estimate the dispersion zone of the airborne infections (Laverge, et al., 2013) (Lavergea, et al., 2014).

The advancement in the use of CFD has led a number of researchers to systematically investigate the effect of different factors such as room air flow conditions, thermal plume, human activities (talking, walking, coughing etc.) on respiration (Lia, et al., 2013) (Spitzer, et al., 2010). In terms of respiration and IAQ, an important quantity defining the transport of CO2 and other airborne particles is the amount of re-inhaled exhaled air and the amount of exhaled air trapped within the

thermal plume around the occupant. The amount of this re-inhaled exhaled air is reported to be 10% by Gao & Niu (2006) and 5 % by Laverge, et al. (2013). A recent study by Jianjian, et al. (2016) stated this value to range between 0.06% and 0.15%.

Although CFD can be effectively used to investigate IAQ and effect of respiration on the spread of infectious diseases, the characterization of the boundary conditions, verification and validation of the physical models and the computational thermal manikin is inevitable. The characterization of boundary conditions range from arbitrary and assumed values (Gao & Niu, 2006) (Zhao, et al., 2005) (Zhu, et al., 2006) to detailed observation of one or the other characteristic such as nasal area, tidal volume, frequency, angle of expired air etc. (Melikov, 2004), (Melikov & Kaczmarczyk, 2007) and (Gupta, et al., 2010).

The work done by Jianjian, et al. (2016) considered only the nasal track of a 4 years old child and investigated different angles of the exhaling air out of the nose but could not account for the geometrical shape and the appropriate development of the thermal plume and its effect on the dispersion. Mahyuddin, et al.(2015) investigated experimentally the air flow conditions (air velocity and air temperatures) within an experimental chamber and modelled the same using CFD. The aim of his work was to supplement the experiments and analyse the effect of respiration on the surrounding in detail. Comparison of results between the experimental and simulated conditions were done for different turbulence models. The geometrical details of the occupant during experimental measurement were not the same as that in the CFD simulations. Moreover the CFD thermal manikin was simplified to avoid numerical complications thereby leading to discrepancy in comparison while estimating the spread of thermal plume, entrainment of exhaled air in the plume and the level of re-inhalation.

The respiration cycle is documented to be a sinusoidal process (Castro, 1998). Gupta, et al. (2010) conducted a series of experiments and devised sinusoidal correlation for modelling the respiration cycle together with other respiration relevant characteristics such as tidal volume, breathing frequency, angle of exhaled jet, temperature and velocity of the exhaled air etc. In some of the respiration and IAQ studies, the effect of the pause between inhalation and exhalation was not

appropriately considered thereby leading to a high level of re-inhalation of the exhaled air of about 10% (Gao & Niu, 2006).

During sedentary activity, the normal tidal volume or the air volume breathed in during a single breath is reported to be around 500 ml with a normal respiratory frequency of 12 breaths per minute with time of inhalation and exhalation ranging between 1.5 to 2.5 seconds and an automatic pause of 1-2 seconds (Guyton, 1984), (Castro, 1998), (Douglas & Haldane, 1909).

Although some pioneering work is done by Gupta, et al. (2010), further validation studies are required to investigate the effect of body posture, metabolic activity, and respiration flow characteristics in real world indoor climates with multiple occupancies. A detailed validated computation thermal manikin capable of breathing is still difficult to be used for multiple occupancy involving the multi-phase flows generated due to the presence of aerodynamically large size particles.

Fanger's studies showed that IAQ is directly affected by the pollutants from building fabrics. The major guidelines and regulations related to IAQ such as CIBSE Guide A (2006), ASHRAE 62 (ANSI/ASHRAE, 2003), CEN report (CR 1752 CEN, 1988) present pollutants as the only factor affecting the perception of IAQ. However studies such as that by Fang et. al. (2000) showed that the sensed IAQ is highly related to the temperature and humidity of the inhaled air. The results of Fang's work show that the occupants prefer rather dry and colder air in the respiration region. To the knowledge of the author, the effect of air velocity on the air quality is not yet reported.

For estimating and guaranteeing IAQ, most of the standards and regulations employ the mass balance calculation to calculate the ventilation rate required to achieve an acceptable IAQ. A number of further analytical models such as those proposed by Shair & Heitner (1974), Nazaroff & Cass (2002), and Switzer & Wayne (1992) have been developed based on the mass balance equation which describe the relationship between sources emitting pollutants into an enclosed well-mixed compartment, the physical parameters of the compartment, and the pollutant concentration as a function of time.

The work done by Pettenkofer (1858) indicated that the CO2 levels are much higher in the upper region of the rooms as compared to the lower regions. This observation

was in conjunction with the fact that the expired air with high CO2 flowed upwards due to the temperature gradients in the room. Homa et. al. (1988) in his experiments inferred the significance of the thermal plume generated by human occupants. He indicated the influence of the thermal plume on the room air flow and hence the IAQ.

Baughman et. al. (1994) gave the concept of mixing time i.e. the interval from the instantaneous release of a point source pollutant until the relative standard deviation of concentration diminishes to 10% or lower. In light of his experimental work, Mora and Gadgil (2002) showed that the pollutant mixing time due to the thermal plume generated by a standing body in a $31m^3$ room is about 45 min. Work done by Cook (1998) presented the thermal plume analysis to show the rate of entrainment of surrounding air into the thermal plume which has a direct influence on the HVAC system and the IAQ.

2.3 Human Thermal Comfort

According to ASHRAE standard 55 (ANSI/ASHRAE, 2004), "thermal comfort is that condition of mind that expresses satisfaction with the thermal environment". This definition is mainly a psychological definition of thermal comfort. A thermo-physiological definition of thermal comfort is given by Mayer (1993) as "the minimum rate of nervous signals from the thermal receptors in the skin and in the hypothalamus". The energetic definition of comfort can be deduced from the work done by Fanger (1972) by stating that " thermal comfort is said to be reached when heat flows to and from the human body are balanced and skin temperature and sweat rate are within a comfort range depending upon the metabolic activity" in other words thermal comfort can be defined as the absence of any thermal stresses.

Though thermal comfort as per definition is a very subjective term, efforts are being made by HVAC engineers, physiologists and researchers to predict the human thermoregulation and human thermal comfort in different environments to design a healthy, comfortable and energetically optimized surrounding. This effort led to a number of experimental studies and the use of the results of these studies to form a number of mathematical and statistical correlations. One comprehensive study was conducted by Rohles and Nevins (1971). They exposed human subjects to different temperature and humidity conditions and recorded their perception of comfort which

he later scaled to integer values ranging from 1 (representing cold) to 7 (representing hot).

Fanger's experimental work (Fanger, 1972) led to the derivation of a thermal comfort equation. His equation is based on thermal balance i.e. the heat is generated by the body due to metabolic activities and dissipated to the surroundings due to a) convection b) radiation c) water vapour diffusion through the skin d) evaporation of sweat and e) respiration. If the human body is in thermal balance i.e. the heat generated is equal to the heat dissipated, the ideal state of thermal comfort is said to be achieved. If the heat dissipated is less than that generated, the person feels warm and vice versa. Fanger used data of human subjects exposed to different thermal conditions within a climate chamber. Together with this data and the thermal comfort equation, Fanger formalized thermal sensation indices namely PMV (Predicted Mean Vote). PMV values range from -3 (cold) to +3 (hot) with 0 being the neutral state. From PMV the index PPD (Predicted Percentage of Dissatisfied People) is derived. Both PMV and PPD have been adopted as an ISO standard (ISO 7730) for analysing thermal sensation.

Pioneering work of devising thermal sensation indices was done by Houghoton and Yaglou (1923) co-relating air temperature and humidity and devising ET (Effective Temperature) indices. Due to its over-estimation of humidity effect in cold temperatures and underestimation in warm temperatures, this indices was replaced by ET* (Revised/new Effective Temperature) and SET* (Standard Effective Temperature) by Gagge and his co-workers (1971) (1986).

Gagge (1973), Azer and Hsu (1977) and Höppe (1993) predicted thermal sensation indices on the physiological functionality of their two node thermal comfort model in which they considered a human to consist of two thermal compartments i.e. the skin and the core. In all these thermo-physiological models, the surrounding environment was kept uniform and at standardized values.

Multi-nodal thermo-physiological models such as Stolwijk's model (Stolwijk, 1971), Wissler's model (Wissler, 1964), Tanabe's 65 Multi-Node model (Tanabe, et al., 2001) and Fiala's Multi-node model (Fiala & Lomas, 1999) remedied the short coming of two node models by subdividing the body into different parts each

perceiving the thermal sensation. The application of multi-nodal models has gained significant importance when dealing with human subjects exposed to non-uniform environments. The multi-nodal thermo-physiological model can provide information about local discomforts but still needs information about the local environment (air temperature, air speed, incident radiation conditions etc).

The major aim of keeping the indoor environment comfortable led to further field studies and experiments thereby deducing a number of empirical co-relations. One such co-relation is the "Thermal Neutrality" T_n referring to the air temperature at which, on average, the majority of people would feel neither hot nor cold. This temperature is affected by both the average annual climate and the seasonal fluctuations associated with it and is defined as follows;

$$T_n = 17.6 + 0.31 \times T_{ave} \qquad \text{(Eq. 2-1)}$$

where T_{ave} is the average outdoor dry bulb temperature [^oC].

In the recent past the concept of adaptive thermal comfort has gained popularity in building indoor environment research. The pioneering work has been done by Humphrey and his co-workers (Humphrey & Nicol, 1998). Adaptive modelling approach means that people respond to a change in thermal environment by adjusting their behaviour in order to counteract any thermal discomfort. Most of the work done on adaptive comfort is based on the survey of thermal comfort in indoor/outdoor conditions.

Based on extensive survey studies, Humphrey developed mathematical equations (Humphrey & Nicol, 1998) for calculating indoor thermal comfort temperature T_c [^oC] from outdoor monthly mean temperature as follows;

Free Running Building:

$$T_c = 11.9 + 0.534 \times T_{ave} \qquad \text{(Eq. 2-2)}$$

Heated or Cooled Building:

$$T_c = 23.9 + 0.295(T_{ave} - 22)\exp\left[-\left(T_{ave} - 22/33.941\right)\right]^2 \qquad \text{(Eq. 2-3)}$$

Unknown system (an average of all buildings):

$$T_c = 24.2 + 0.43(T_{ave} - 22)\exp\left(\left[-\left(T_{ave} - 22/28.284\right)\right]^2\right) \quad \text{(Eq. 2-4)}$$

where T_{ave} is the average outdoor dry bulb temperature [^{o}C].

2.4 Parameters Affecting IAQ and Human Thermal Comfort

IAQ is mainly dictated by the strength and concentration level of pollutants introduced in the indoor space along with their distribution, it implicitly considers the local air velocities, air temperatures, turbulence intensities, humidity levels and pressure conditions in the indoor environments. Similarly thermal comfort is dependent on basic physical parameters such as local turbulence intensities, air temperature, air humidity, air speed, radiation temperature, pressure conditions in the indoor climate along with personal parameters of clothing and metabolic activity level. The common factors influencing IAQ and human thermal factors make the two phenomena highly inter-dependable.

An important factor that affects the physical parameters is the human occupancy itself. The human occupant induces on one hand a thermal load and on the other hand it is a source for CO2 and bio-effluents as a result of metabolic activities. An increase in building performance standards in terms of air tightness, insulation and reduced heat gain from equipment, result in an increase in the significance of the human thermal load. The heat rising above an occupant generates a buoyant thermal plume. The strength of this buoyant plume is especially dominant in mixed and natural ventilation systems with low air flow movements. This buoyant plume is basically a convection dominated flow which not only has a direct influence on the IAQ but also has indirect influence on the energy consumption as mentioned by Ye, et al. (2006).

The importance of this thermally-induced flow due to human metabolic heat has led to many investigations on this subject. For example, Mora and Gadgil (2002) showed the impact of occupants and obstructions on pollutant mixing, and Clausen et al (1993) stated the relative importance of air pollution, human thermal load and noise on human thermal comfort. A number of studies have reported the buoyancy driven flow generated due to the metabolic heat release of the human body, for example,

Brohus (1997) and Murakami (2000). The measure of this buoyancy driven flow has mostly been in terms of the air velocity as it dictates the phenomenon of entrainment of surrounding air and contaminants e.g. the work done by Clark & Toy (1975) reported velocities exceeding 0.3 m/s above the head region. Borges, et al. (2002) and Sideroff & Dang (2005) in their validation experiments reported a maximum velocity of between 0.3 m/s and 0.4 m/s at 40 cm above the head. Özcan, et al. (2005) investigated flow surrounding the human head and reported a maximum vertical air velocity of 0.38 m/s. Recent experimental work from Spitzer et al. (2010) based on PIV measurements reported air velocities of about 0.3 m/s near the head region. This large range of reported air speeds indicate that the local flow around the human body is not only dependent on the individual's physical condition, it is very strongly coupled with the body posture, the thermal surrounding and the methodology used to measure the air speed.

With the development in numerical techniques and computational resources in the past decade, a number of researchers have modelled buoyancy induced flows using Computational Fluid Dynamics (CFD). In CFD, Computer Simulated Persons (CSPs) or Computer Thermal Manikins (CTMs) with varying degrees of complexity are modelled. Cropper, et al. (2008) and Yang, et al. (2007) simulated standing postures with buoyancy dominated flows. The maximum velocity reported in the thermal plume was 0.4 m/s.

Sørensen & Vøigt (2003) simulated seated subjects and reported maximum velocities of between 0.4 and 0.5 m/s. A number of other researchers carried out CFD simulations and reported maximum air flow velocities for seated CTMs between 0.17 m/s and 0.26 m/s (Murakami, et al., 2000), (Topp, 2002), (Hayashi, et al., 2002).

Based on previous simulation and experimental work, it is seen that the maximum air velocities generated due to thermal buoyancy effects above and around the human body vary between 0.17 m/s and 0.5 m/s. Experimental work to date has used different measuring techniques for studying human related air flows. These techniques range from simple hot wire anemometry and smoke tracing to highly sophisticated Particle Image Velocimetry (PIV) and Phase Doppler Anemometry (PDA). Homma and Yakiyama (1988) used infrared thermograms in their experiments for observing temperature distributions around subjects together with

smoke wire photography and hot wire anemometers to measure local velocities. Their results show that the velocities above the head range between a minimum of 0.05 m/s to a maximum of 0.3 m/s for standing subjects. They documented average buoyancy-driven volume flows above the seated human subjects ranging between 28 l/s and 60 l/s depending upon the subject´s posture and clothing.

The geometrical and aero-thermal boundary conditions in the CFD simulations as well as those in the measurements vary from one investigation to the other. In addition, the numerical algorithms, turbulence models and their implementation in CFD codes differ from one another thereby imparting a certain level of difference in the results. The difference in results and the level of inaccuracy may also vary from one measurement setup to the other. All of these factors are are assumed to have led to a variation in the reported flow conditions.

The mean air velocities and air temperatures in the room and near the human body may provide a global picture of IAQ and thermal comfort but will fail to address local discomfort problems such as draught. The local air velocities in the thermal plume, the temperature at the human body surface and that in the thermal plume together with the surrounding radiant and air temperature led the researchers to investigate an important derived parameter for assessing the thermal comfort i.e. "heat transfer coefficient". Depending upon the nature of heat transfer these coefficients can be classified as "convective" and "radiative". The importance of the heat transfer coefficients on human thermal comfort was clearly demonstrated by a number of studies such as one conducted by Mayer (1983) in Germany in air conditioned rooms and proving that mean values of velocity and temperature cannot give enough information to address the draught phenomena as a major cause of human thermal discomfort characterized by turbulence intensities. An increase in the local heat transfer coefficients leads to increases in cooling effect and vice versa. As the heat transfer coefficient is a derived quantity (dependent on other basic parameters), a number of studies were conducted for simple geometries such as cylinders, spheres and vertical plates for different flow regimes and analogy is made to the human body shape (Nishi & Gagge, 1972), (Rapp, 1976). Evaluating heat transfer coefficients for human shaped subjects are mainly conducted on heated thermal manikins. Using

real human subjects for conducting such studies would demand a very large sampling in order to cover the variance in the geometrical features.

de Dear et. al. (2001) conducted detailed studies on heated manikins in natural and forced convective environments and measured radiative and heat transfer coefficient for each body part. For the complete body he calculated a value of 4.5 W/m^2K for the radiative heat transfer coefficients (both sitting and standing postures) and convective heat transfer coefficient values of 3.4 W/m^2K and 3.3 W/m^2K (natural convection) for standing and sitting postures respectively. For forced convection he derived convective heat transfer coefficients for each body part as well as for the whole body (e.g. $h_c = 10.3v^{0.6}$) for whole body in sitting or standing posture where h_c is the convective heat transfer coefficient and v is the air flow speed). Rapp (1973) compared the mean convection coefficients of nude man sitting, reclining or standing in low velocity air environments, spheres and cylinders placed in low velocity environments and found that the 11 investigations find a mean experimental value of 3.8 W/m^2K for the nude man (with max. deviation of ± 1.7 W/m^2K and a probable error of 12%) and 4.1 W/m^2K (with max. deviation of ± 0.75 W/m^2K and probable error of 9%) for the corresponding sphere (with equal DuBois surface area as the man). A recent comparison study conducted by Yi et. al. (Yi, et al., 2007) showed that over the past 2 decades, a number of researchers have conducted experimental studies on convective heat transfer coefficient however due to variation in the experimental setup and conditions a wide range of h_c values are reported.

2.5 Summary

The literature study on the concepts of IAQ and human thermal comfort revealed the fact that a lot of work has been done on standardizing the indoor air quality and human thermal comfort. A number of environment indices predict the human thermal perception in conjunction with its thermo-physiological activities. The study visualized the importance of the fact that the prediction and modelling of IAQ and thermal comfort needs the information of the surrounding environment and is as good as the measurement and/or modelling of the surroundings.

The literature review focuses mainly on air velocity, air temperature, radiant temperature, the variations in local air velocities and temperatures, the heat transfer

coefficients and concentration distribution in indoor spaces due to the presence of human subjects.

Besides the above mentioned main factors affecting IAQ and thermal comfort, contextual factors such as cultural variations (e.g. local climate, adaption etc), psychological factors (e.g. experience, expectation, knowledge, attitude etc), demographic factors (e.g. age, gender etc) also play a role on the human thermal comfort. On the basis of very little literature and scientific proof available, the effect of these factors though not negligible, are not investigated as part of this literature review as they are difficult to investigate numerically.

The literature review concludes that numerical simulations of IAQ and human thermal comfort play an important role in today's design strategies. This increase in the use of such numerical simulations however demands an increase in the validation and verification of the numerical models by applying them over different scales (Laboratory scales and real life scenario scales) in a synergetic manner to give more confidence in design.

In order to validate, verify and compare the numerical simulation with real life scenarios, different physical parameters and their derivatives affecting the IAQ and human thermal comfort are chosen. These parameters involve the air velocities, air temperature, radiative and convective heat transfer coefficients and the concentration distribution of pollutants. This PhD work is intended to provide an insight into the detailed numerical modelling of the above mentioned factors.

3 Research Methods

Researchers studying problems associated with heat and mass transfer mechanisms in indoor climates develop and employ different methods to achieve their goals. These methods range from simple analytical analysis and measuring techniques using simple devices to detailed numerical analysis and use of highly sophisticated measuring devices. Research methods outlined in this chapter present a non-competitive and non-adversarial approach among the methods so as to visualize the importance of analytical, computational and experimental methods complementing to one another in a synergetic manner. Only such a complementary and synergetic approach following verification and validation procedures can lead to a sound basis of applying a numerical model for complex real world scenario , in contrast, the other methods are lack in application either due to their simplicity (analytical methods) or associated costs (experiments).

This chapter provides the methodology and an overview of the research methods applied during the course of this research. The choice of the different methods is based on the literature review in chapter 2 and the availability of tools and facilities at the Loughborough University.

As the research carried out in context of this PhD work underpins mainly “Computational Fluid Dynamics (CFD)”, and its valid application in real world scenarios, the basics and underlying theory of CFD are explained separately in detail in Chapter 4.

3.1 Introduction

The literature review in chapter 2 has shown that as far as the environmental interaction is concerned, IAQ and Indoor human thermal comfort are inter-related and depend on common physical parameters such as air velocity, air temperature, humidity level etc.

In the preliminary design stages, analogies are made to simple analytical solution of problems and empirical correlation are applied to the complex problems. Almost all the analytical approaches simplify the reality to a great extent. These models are sufficient to provide an approximation of the phenomena but are difficult to apply to a

real world building design scenario. Factors such as thermal gradients in the rooms, complex geometrical design, occupant position and posture etc demand detailed spatial and transient information of physical parameters to provide a correct estimation of IAQ and human thermal comfort. The spatial and temporal information of these physical parameters can either be achieved via direct measurements or by means of numerical simulations. Full scale direct measurements can only be carried out during commissioning and/or post-commissioning stage where as numerical simulations can give the detailed spatial and transient information prior to the realization of the indoor space. The application of numerical simulation however demand verification and validation of the methods involved and their limitations along with a need of high computational resources. In this PhD work the numerical simulations are compared with analytical methods and measurements in environmental chamber as well as in a real world surrounding.

3.2 Thesis Methodology

In the present research work emphasis is placed on the numerical simulations of heat and mass transfer phenomena and the factors affecting the human thermal comfort and IAQ in indoor climates. Analytical and/or experimental methods are used to verify and/or validate the numerical simulations, gain more confidence in their use and envisage their benefits and shortcomings while applying in real world scenarios.

The working methodology used in the presented work is outlined as follows;

a) Verification of the numerical CFD code for both convective and radiative heat transfer mechanisms by comparing the results of numerical simulations for simplified and complex human body geometries against available analytical/empirical solutions.

b) Validation of the numerical CFD code for both convective and radiative heat transfer mechanisms by comparing the results of numerical simulations for simplified and complex human body geometries against previously conducted simulation work.

c) Validation of numerical CFD code for convective heat transfer mechanisms by comparing the results of numerical simulations for detailed human body geometry against first hand experimental work. At this stage, entrainment effects predicted by the flow solver were estimated and an analogy was made to the thermal plume

theory of a point source. The entrainment coefficient was taken as comparison variable.

d) Adding breathing to the validated numerical model and investigate the local flow phenomena along with IAQ.

e) Application of validated numerical model to a classroom with multiple occupancy. The simulation are aimed to predict the values of the major factors affecting IAQ and human thermal comfort for a classroom with multiple occupancy. The simulation results are then compared with field study results of the same classroom.

f) The conclusion of the complete verification, validation and application study are summarized in form of guidelines.

3.3 Numerical Methods

Problems of major interest evolving in day to day life are often too complicated to be solved by analytical methods. For example time and economic constraints often do not allow to use measurement techniques for full scale investigations. In such cases, the use of more complex models becomes inevitable. These models require numerical algorithms and computations to solve them.

The most prominent work in the field of human thermal comfort is that conducted by Fanger (Fanger, 1972), which is incorporated in many national and international standards on occupant comfort in buildings e.g. ISO 7730 and ASHRAE Standard 55. Fanger's work is based on experimental investigations of human projected area (the radiation area projected on a plane perpendicular to parallel rays) of standing and sedentary human subjects using photographic techniques (Fanger, 1972) (Dunkle, 1963).

Based on the projected areas, Fanger devised effective radiation areas (area of the human body that takes part in radiation exchange with the surroundings) as well as view factors between the human body and its surroundings.

Once the human radiation data based on the above noted factors is acquired, one of the most influencing thermal comfort criteria i.e. the "Mean Radiant Temperature (MRT)", which is defined as "that uniform temperature of an imaginary black enclosure which results in same heat loss by radiation from the person, as the actual

enclosure" (Fanger, 1972) can be calculated. MRT is one of the most influencing criteria for estimation of human thermal comfort.

Following a numerical approach however eliminates any such dependency of order thereby leading to controllable and less error prone results.

For this study, the following method was chosen.

- Calculation of view factors using the net radiation exchange method for the human body as a whole and comparing it with the experimental results obtained by Fanger.
- Calculation of the effective radiation area factor, defined as "the ratio between the body areas that takes part in radiation to the total body surface area", and comparing it with the results obtained by Fanger.
- Calculation of the projected area factor defined as "the ratio between the projected area and the effective radiation area", and comparing it with the results obtained by Fanger.

In order to minimize the computational load, various simplifications were employed in the simulation methodology as given below.

- The medium (indoor air) was considered as non-participating medium for radiation heat transfer. This assumption is truly valid in indoor climates with very low optical thickness (Cannistraro, et al., 1992) of the medium.
- The human body was not subdivided into sectors but was considered as a whole.
- Flow and turbulence equations were not solved in parallel to radiation equations.
- All surfaces were assumed to be gray diffuse.
- Surfaces of non-interest were assumed to be black bodies (emission = absorption = 1).

Several studies have been carried out which show the flow and phenomena of heat and mass transfer around human geometries. These studies are performed both using experiments and CFD simulations (see chapter 2 for details). Different experimental methodologies, mesh generation tools and CFD codes were used in different studies. For the present PhD work, ANSYS CFX (Ansys, Inc., 2016) was chosen as the CFD code for investigating the heat and mass transfer phenomena associated with human thermal comfort. In addition to the heat and mass transfer

mechanisms, the investigation of pollutant dispersal in indoor climate is also a major aim of this PhD work. Pollutants were represented by means of additional scalars that mainly follow the convective flow paths. This assumption holds true for small particles with hydraulic diameter below 2.5 μm (Gao & Niu, 2006). Modelling heavier particles demand the flow particles to be simulated using Lagrangian and/or Eulerian multi-phase approach and is beyond the scope of the present work. The current work should enhance the use of CFD in indoor climate by validating the simulation work with laboratory controlled experiments as well as in real world application scenarios of a classroom with multiple occupancy.

Prior to the experimental validation planned to be carried out at Loughborough University UK, simulations were carried out to choose an appropriate turbulence model. The results achieved using the different turbulence models are compared with previous studies. A mesh independency study for each of the model is also performed in the course of this PhD work.

In the presented report, the benchmark case was taken from the work done by Sørensen and Voigt (Sørensen & Vøigt, 2003). The chosen benchmark compares its results with published work and measurements by particle image velocity (PIV). One of the major reason of considering the work from Sørensen and Voigt as benchmark was the use of detailed 3D CSP geometry which was an exact replica of the experimental thermal manikin.

3.4 Analytical Methods

Not all the problems and processes in physics have exact solutions. Most of the problems that provide an exact solution are ones involving simple physics phenomena. Analytical methods are methods that make analogy to simple exact solutions of problems and apply these analogies to complex problems. The application of analytical solutions gives rise to equations with or without empirical constants. For the current PhD work, analytical models are used in order to verify the numerical CFD code ANSYS CFX.

In order to verify the radiative heat transfer models in ANSYS CFX, the view factor of simple objects was analytically calculated and simulated. The view factors of these simple objects (parallel plate, cylinders & sphere) have an exact analytical solution.

In order to verify the convective heat and mass transfer models in ANSYS CFX, the convective heat transfer coefficients for a flat vertical plate (for which analytical/empirical solution exist) were calculated and simulated.

3.5 Experimental Methods

As the indoor environment should respect the IAQ and thermal comfort indices, information regarding the above mentioned physical parameters was necessary for healthy, comfortable and optimized designing of indoor spaces.

One way of getting information about these physical parameters in a built environment is direct measurement of these parameters individually by using sensing devices. These measurements are mostly done on site either at the commissioning stage or in operational stage to ensure that design criteria are achieved. Another aspect of conducting measurements using sensing devices is to validate a numerical and/or analytical model. The main physical parameters influencing directly the IAQ and human thermal environment are air temperature, radiant temperature, air velocity, humidity and pollutant concentration.

3.5.1 Measuring Air Temperature

Air temperature defined physically is the measure of how slowly or quickly the molecules of gases constituting the air move. In other words, air temperature is the measure of the kinetic energy of the air. A temperature sensing device is called thermometer. Depending upon the science of sensing temperature, different thermometers are available. For the experimental work conducted during the course of this PhD work, temperature sensing was done using thermocouples and infrared cameras. The specifications of the used devices are given below.

Thermocouples:

Thermocouples measure the temperature based on the Seebeck effect. The Seebeck effect is the phenomenon in which a potential difference is produced at the junction of

two metals/alloys when placed at different temperatures. This potential difference (voltage) is dependent on the type of the metals/alloys used. After careful calibration of the voltage-temperature dependence, the coupled metals can be used to measure temperatures for a wide range of applications. Thermocouples are mainly characterised by their sensitivity and the temperature working range.

For the current work Chromal-Alumel (K-Type) thermocouples were used. These thermocouples have a measuring range between -40°C to +750°C with a measurement sensitivity of about 50 µV/°C.

Data Loggers:

Pendant type HOBO onset temperature data loggers (type; 64K - UA-001-64) were used to record the air temperature data. These loggers have a measuring range between -20°C to +70°C with an accuracy of ± 0.53°C (for temperature range between 0°C to + 50°C). The response time of the above sensors in airflow of 2 m/s is 10 minutes, typical to 90% value.

These sensors are found to be appropriate in terms of their measuring range as well as response time as all the measurements planned during the course of this PhD work done in indoor climates and for longer durations (ranging from 1 to 3 hours) with constant aero- and thermodynamics conditions.

Infrared Camera:

For surface temperature measurement and thermography, FLIR B 335 Infrared camera was used. The measurement range of FLIR B 335 is between -20°C to +120°C with an accuracy of ± 2°C.

3.5.2 Measuring Air Velocity

The speed of air in a particular direction is termed as air velocity. There are different methods of measuring this parameter. For the experimental work two commonly used methods were employed and are briefly discussed below.

Velocity Probe:

Velocities at flow inlets were measured using a Testo 480 type velocity probe. The measurement accuracy for such a probe is ± 0.2 m/s.

Particle Image Velocimetry (PIV):

The detailed investigation of flow field in the experimental work was done by using the Particle Imaging technique namely Particle Image Velocimetry (PIV). PIV is a visualization technique that uses small particles in the fluid to trace and track the flow field. For this research, a planar PIV system is used. In a planar optical system, very small diameter particles of a non-reacting, light-scattering fluid are injected (seeded) into the space. These particles are illuminated by a pulsating sheet of light. A camera is placed at 90º to this sheet of light to capture the in-focus planar region of the light sheet in which the particles are illuminated. Images are taken in quick succession to capture the position of the light scattering particles. These images are then transferred to a computer for analysis to visualise the velocity field as defined by the movement of the particles.

In order to capture the flow field in the current research work, a LaVision (LaVision, 2011) PIV system was utilised, consisting of two 4MP (2048x2048 pixel) cameras, a dual cavity 200mJ/pulse Nd:YAG laser, a 6 nozzle Laskin type seeder and associated timing, processing and calibration equipment (for detailed technical specification of each component visit developer's homepage www.lavision.de).

3.5.3 Measuring Humidity Level

Under the laboratory conditions, the inlet humidity level was controlled. During the experiments, the indoor humidity levels were measured using HOBO U12 Type sensors with a measuring accuracy of ± 2,5%.

3.5.4 Measuring Indoor Air Quality

CO2 is very often used as a representative of IAQ and the measurement involves the use of CO2 analysers and recorders. There are several CO2 analysers available in the market. For the laboratory. and field study, Telaire 7001 CO2 sensor were used with a measurement accuracy of ± 50 ppm.

3.6 Summary

This chapter has presented an outline to the research methodology adopted for the present PhD work along with a brief overview of the numerical, analytical and measurement techniques used during the course of this PhD work. Most of the

research was conducted using CFD techniques which are explained in detail in chapter 4.

4 CFD Modelling

Physical phenomena involving flow, heat and mass transfer are well described by the laws of conservation of momentum, energy and mass. In order to resolve physical phenomena of flow, heat and mass transfer with respect to time and space, solution of partial differential Navier-Stokes equations are employed. Due to the non-linear nature of most of the flow governing equations, their solution for flows of practical importance are extremely tedious and non-trivial when not impossible. With the development of high speed computers, and evolution of numerical algorithms, the Navier-Stokes equations can be solved numerically for complex real world scenarios there by giving rise to the Computational Fluid Dynamics (CFD) Modelling. Many commercial and non-commercial institutions continuously develop codes pertained to CFD.

The present chapter provides a concise overview of important fluid mechanics and dynamics concepts forming the basis of modern CFD theory which underpins tasks in later chapters of verification, validation and application in real world scenarios. As the CFD Code chosen for this research work is ANSYS CFX, some code specific terminology is used in the upcoming section with references to the code manuals.

4.1 Governing Equations of Flow

CFD codes solve the partial differential equations defining the flows and the associated processes such as transfer of heat and mass etc. These partial differential equations evolve from the basic conservation laws of physics for a closed system i.e. a system which is defined by definite boundaries across which there exists no exchange of energy, mass and momentum. These laws are outlined below.

a) Law of total mass conservation: The total mass of a closed system is conserved i.e. the total mass in a closed system remains constant over time. The mass conservation law is also termed as continuity law.

b) Law of momentum conservation: This law is based on Newton's second law and states that the total momentum (linear or angular) in a closed system remains constant over time.

c) Law of total energy conservation: This law states that the total energy of a system is conserved i.e. the total energy in a closed system remains constant over time. In simple words energy can neither be created nor destroyed it may however change its forms.

Considering the fact that the total energy (E) of fluid is the sum of its internal thermal energy (i), kinetic energy (K.E) and potential energy (P.E), the first law of thermodynamics needs to be considered for modelling any heat flow phenomena. This law states that a change in the energy of a closed system is equal to the difference between the heat energy supplied to the system and the work done by the system on its surroundings.

In order to describe a flow on a macroscopic level (ignoring molecular motion etc), three scalar field properties i.e. pressure (p), density (ρ) and Temperature (T) as well as the three components (u, v, w) of the vector velocity have to be calculated as function of space (x, y, z) and time (t).

Considering that fluid flow is a function of these scalar variables, their dependence on the space and time can be defined using the partial differential equations. A mathematical description of the above mentioned laws in the form of equations are given in the next sub sections.

4.1.1 Continuity Equation

The mass conservation (continuity) equation for a compressible fluid (fluid density is varying) is expressed mathematically as:

$$\frac{\partial \rho}{\partial t} + \frac{\partial (\rho U)}{\partial x} + \frac{\partial (\rho V)}{\partial y} + \frac{\partial (\rho W)}{\partial z} = 0 \qquad \text{(Eq. 4-1)}$$

where

$U, V \text{ and } W$ are the component of velocities in the x, y and z directions respectively.

The equation 4.1 shows that fluid flow is a function of change in density and velocity components.

4.1.2 Momentum Equation

The momentum conservation equation is based on the Newton's second law which states that the rate of change of momentum of a fluid particle equals the sum of forces on the particle. It is also expressed as a product of body's mass (m) and acceleration(a).

In CFD, the quantities are often calculated in a given volume element i.e. "per unit volume" and mass per unit volume is density (ρ),so a partial differential representation of "F = ma" with the summation of all the forces per unit volume in x-direction is given by:

$$\frac{\partial}{\partial t}(\rho U)+\frac{\partial}{\partial x}(\rho UU)+\frac{\partial}{\partial y}(\rho UV)+\frac{\partial}{\partial z}(\rho UW) = \frac{-\partial P}{\partial x}+\frac{\partial}{\partial x}\left(\mu\frac{\partial U}{\partial x}\right)+\frac{\partial}{\partial y}\left(\mu\frac{\partial U}{\partial y}\right)+\frac{\partial}{\partial z}\left(\mu\frac{\partial U}{\partial z}\right)+\frac{1}{3}\frac{\partial}{\partial x} \times\left[\mu\left(\frac{\partial U}{\partial x}+\frac{\partial V}{\partial y}+\frac{\partial W}{\partial z}\right)\right]+\rho g_x \quad \text{(Eq. 4-2)}$$

for y-direction;

$$\frac{\partial}{\partial t}(\rho V)+\frac{\partial}{\partial x}(\rho UV)+\frac{\partial}{\partial y}(\rho VV)+\frac{\partial}{\partial z}(\rho VW) = \frac{-\partial P}{\partial x}+\frac{\partial}{\partial x}\left(\mu\frac{\partial V}{\partial x}\right)+\frac{\partial}{\partial y}\left(\mu\frac{\partial V}{\partial y}\right)+\frac{\partial}{\partial z}\left(\mu\frac{\partial V}{\partial z}\right)+\frac{1}{3}\frac{\partial}{\partial y} \times\left[\mu\left(\frac{\partial U}{\partial x}+\frac{\partial V}{\partial y}+\frac{\partial W}{\partial z}\right)\right]+\rho g_y \quad \text{(Eq. 4-3)}$$

similarly for z-direction;

$$\frac{\partial}{\partial t}(\rho W)+\frac{\partial}{\partial x}(\rho UW)+\frac{\partial}{\partial y}(\rho VW)+\frac{\partial}{\partial z}(\rho WW) = \frac{-\partial P}{\partial x}+\frac{\partial}{\partial x}\left(\mu\frac{\partial W}{\partial x}\right)+\frac{\partial}{\partial y}\left(\mu\frac{\partial W}{\partial y}\right)+\frac{\partial}{\partial z}\left(\mu\frac{\partial W}{\partial z}\right) +\frac{1}{3}\frac{\partial}{\partial z} \times\left[\mu\left(\frac{\partial U}{\partial x}+\frac{\partial V}{\partial y}+\frac{\partial W}{\partial z}\right)\right]+\rho g_z \quad \text{(Eq. 4-4)}$$

where

ρ is fluid's density (or mass per unit volume)

P is the normal pressure (negative sign indicates its compressive nature)

μ is the dynamic viscosity of fluid

g_x, g_y, g_z are body forces (e.g. gravity) acting on the unit volume in x, y and z directions.

In addition to body forces, there are surface forces which act on the fluid. These forces are viscous forces and pressure forces. Body forces on the other hand act on the complete volume of the body in space such as gravitational forces, electromagnetic forces etc.

The viscous forces acting on the fluid surface are related to the shear stress τ by the general correlation;

$$\tau = \mu \frac{\partial U}{\partial x} \qquad \text{(Eq. 4-5)}$$

The equations (Eq. 4-2) to (Eq. 4-4) originate from the Newton's second law and represent the effect of viscous and body forces on a fluid particle. These equations are named as Navier Stokes equation which form the basis of fluid flow.

4.1.3 Energy Equation

Heat is transferred in space and time by means of conduction, convection and radiation. In terms of fluid mechanics two modes i.e. conduction and convection are combined in general energy equation. The radiative mode of heat transfer is treated separately.

The conservation of thermal energy in terms of temperature $\tilde{T}$ can be represented in its most simplest form by the equation;

$$\frac{\partial}{\partial t}(\rho\tilde{T}) + \frac{\partial}{\partial x}(\rho U\tilde{T}) + \frac{\partial}{\partial y}(\rho V\tilde{T}) + \frac{\partial}{\partial z}(\rho W\tilde{T}) = \frac{\partial}{\partial x}\left(\Gamma\frac{\partial\tilde{T}}{\partial x}\right) + \frac{\partial}{\partial y}\left(\Gamma\frac{\partial\tilde{T}}{\partial y}\right) + \frac{\partial}{\partial z}\left(\Gamma\frac{\partial\tilde{T}}{\partial z}\right) + S_T \qquad \text{(Eq. 4-6)}$$

where

$\Gamma = \frac{\mu}{\sigma}$ is the diffusion coefficient

$\sigma = \frac{\mu C_p}{\lambda}$,where c_p is the specific heat of at constant pressure, λ is the thermal conductivity and μ is the dynamic viscosity of the fluid. This ratio is also termed as Prandtl-Schmidt number. The description of different dimensionless numbers representing the nature of flow, its behaviour and its physical meanings are given in chapter 5. The term S_T represents any heat source (or sink) acting on the body of the fluid element.

4.1.4 Concentration Equation

Similar to the energy equation, the transport of a material's concentration "c" can be written mathematically as follows;

$$\frac{\partial}{\partial t}(\rho c) + \frac{\partial}{\partial x}(\rho U c) + \frac{\partial}{\partial y}(\rho V c) + \frac{\partial}{\partial z}(\rho W c) = \frac{\partial}{\partial x}\left(\Gamma_c \frac{\partial c}{\partial x}\right) + \frac{\partial}{\partial y}\left(\Gamma_c \frac{\partial c}{\partial y}\right) + \frac{\partial}{\partial z}\left(\Gamma_c \frac{\partial c}{\partial z}\right) + S_c \quad \text{(Eq. 4-7)}$$

Where Γ_c is diffusion coefficient in terms of its concentration.

By generalizing the conservation equations, the following form of flow governing equation can be written as;

$$\frac{\partial(\rho \phi)}{\partial t} + \nabla(\rho \phi u_i) = \frac{-\partial p}{\partial x_i} + \nabla(\Gamma \mathrm{grad}\ \phi) + S_\phi \quad \text{(Eq. 4-8)}$$

The term $\frac{\partial(\rho \phi)}{\partial t}$ represents the unsteady effects of flow, $\nabla(\rho \phi u_i)$ represent the convective effects, $\frac{-\partial p}{\partial x_i}$ is the pressure gradient, $\nabla(\Gamma \mathrm{grad}\ \phi)$ explains the diffusive effects and S_ϕ represent the effects induced due to a source or sink acting on the fluid body.

It is important to see that there are 6 unknown quantities i.e. pressure, temperature, three velocity components and density but only 5 differential equations of conservations (mass, three momentum equations i.e. 1 for each direction and

energy). In order to solve the set of equations, the equation of state is employed. The equation of state in its most general form is given as the idea gas law combining the different thermodynamic variable together i.e.;

$$p \times V = n \times R \times T \quad \text{(Eq. 4-9)}$$

where

p is the pressure of a fluid [Pa]

V the volume of the fluid [m3]

n the number of moles of the fluid [mol]

R is the universal gas law constant (8.3144621 [J/mol·K]) and

T is the temperature of the gas [K].

With equal number of unknowns and equations, the Navier-Stokes system of partial differential equations can be mathematically closed to solve the flow field. It is however important to note that the conservation forms of governing equations described above are derived for laminar flows. In order to apply the above equation for turbulent flows, the turbulent induced terms need to be resolved. The upcoming section deals briefly about turbulence and the different turbulence models implemented in ANSYS CFX.

4.2 Turbulence Modelling

Turbulence is defined as an irregular and chaotic flow. This flow is unsteady (varies with time) in nature and is composed of several rotational flow structures of different length scales known as "eddies". The large scale eddies are inertia dominated with negligible viscous effects whereas for the small scale eddies the viscous effect become important.

Considering any property of a fluid undergoing a turbulent flow, that property of the fluid (e.g. pressure, velocity, concentration etc) can be decomposed into a mean and a fluctuating strongly time dependent component.

A simple representation of this decomposition can be shown mathematically as:

$$\phi = \bar{\phi} + \phi' \qquad \text{(Eq. 4-10)}$$

with

$$\phi' = \frac{1}{\Delta t}\int_{t}^{1+\Delta t} \phi \, d \qquad \text{(Eq. 4-11)}$$

where Δt is the time interval which is long compared to the time scale of the turbulent fluctuations but small enough to capture the unsteady mean flow.

Considering that the velocity U, V and W are decomposed into a mean velocity component "u, v, w" and a fluctuating velocity component "u', v' and w'", the equivalent mathematical representations would be;

U = u + u', V = v + v' and W = w + w'. For a considerably small time scale, u ≈U, v ≈ V and w ≈ W then the mass conservation equation could be written as;

$$\frac{\partial \rho}{\partial t} + \frac{\partial(\rho u)}{\partial x} + \frac{\partial(\rho v)}{\partial y} + \frac{\partial(\rho w)}{\partial z} = 0 \qquad \text{(Eq. 4-12)}$$

With P = p + p', the momentum equations will take the form;

For x-component,

$$\frac{\partial}{\partial t}(\rho u) + \frac{\partial}{\partial x}(\rho uu) + \frac{\partial}{\partial y}(\rho uv) + \frac{\partial}{\partial z}(\rho uw) = \frac{-\partial p}{\partial x} + \frac{\partial}{\partial x}\left(\mu \frac{\partial u}{\partial x}\right) + \frac{\partial}{\partial y}\left(\mu \frac{\partial u}{\partial y}\right) + \frac{\partial}{\partial z}\left(\mu \frac{\partial u}{\partial z}\right) + \frac{1}{3}\frac{\partial}{\partial x} \times \left[\mu\left(\frac{\partial u}{\partial x} + \frac{\partial v}{\partial y} + \frac{\partial w}{\partial z}\right)\right] + \frac{\partial}{\partial x}(-\rho\overline{u'u'}) + \frac{\partial}{\partial x}(-\rho\overline{u'v'}) + \frac{\partial}{\partial x}(-\rho\overline{u'w'}) + \rho g_x \qquad \text{(Eq. 4-13)}$$

for y-component,

$$\frac{\partial}{\partial t}(\rho v) + \frac{\partial}{\partial x}(\rho uv) + \frac{\partial}{\partial y}(\rho vv) + \frac{\partial}{\partial z}(\rho vw) = \frac{-\partial p}{\partial y} + \frac{\partial}{\partial x}\left(\mu \frac{\partial v}{\partial x}\right) + \frac{\partial}{\partial y}\left(\mu \frac{\partial v}{\partial y}\right) + \frac{\partial}{\partial z}\left(\mu \frac{\partial v}{\partial z}\right) + \frac{1}{3}\frac{\partial}{\partial y} \times \left[\mu\left(\frac{\partial u}{\partial x} + \frac{\partial v}{\partial y} + \frac{\partial w}{\partial z}\right)\right] + \frac{\partial}{\partial x}(-\rho\overline{u'v'}) + \frac{\partial}{\partial x}(-\rho\overline{v'v'}) + \frac{\partial}{\partial x}(-\rho\overline{v'w'}) + \rho g_y \qquad \text{(Eq. 4-14)}$$

and for z-component,

$$\frac{\partial}{\partial t}(\rho w)+\frac{\partial}{\partial x}(\rho uw)+\frac{\partial}{\partial y}(\rho vw)+\frac{\partial}{\partial z}(\rho ww)=\frac{-\partial p}{\partial z}+\frac{\partial}{\partial x}\left(\mu\frac{\partial w}{\partial x}\right)+$$
$$\frac{\partial}{\partial y}\left(\mu\frac{\partial w}{\partial y}\right)+\frac{\partial}{\partial z}\left(\mu\frac{\partial w}{\partial z}\right)+\frac{1}{3}\frac{\partial}{\partial z}\times\left[\mu\left(\frac{\partial u}{\partial x}+\frac{\partial v}{\partial y}+\frac{\partial w}{\partial z}\right)\right]+\frac{\partial}{\partial x}(-\rho\overline{u'w'})+ \quad \text{(Eq. 4-15)}$$
$$\frac{\partial}{\partial x}(-\rho\overline{v'w'})+\frac{\partial}{\partial x}(-\rho\overline{w'w'})+\rho g_z$$

Similarly the energy equation represented previously in terms of temperature with $\widetilde{T}=T+T'$ would become;

$$\frac{\partial}{\partial t}(\rho T)+\frac{\partial}{\partial x}\left(\rho u\widetilde{T}\right)+\frac{\partial}{\partial y}\left(\rho v\widetilde{T}\right)+\frac{\partial}{\partial z}\left(\rho w\widetilde{T}\right)=\frac{\partial}{\partial x}\left(\Gamma\frac{\partial T}{\partial x}\right)+\frac{\partial}{\partial y}\left(\Gamma\frac{\partial T}{\partial y}\right)+$$
$$\frac{\partial}{\partial z}\left(\Gamma\frac{\partial T}{\partial z}\right)+\frac{\partial}{\partial x}(-\rho\overline{u'T'})+\frac{\partial}{\partial y}(-\rho\overline{v'T'})+\frac{\partial}{\partial z}(-\rho\overline{w'T'})+S_T \quad \text{(Eq. 4-16)}$$

Substituting the mean and fluctuating terms in the concentration transport equation, the concentration equation can be re-written as follows;

$$\frac{\partial}{\partial t}(\rho c)+\frac{\partial}{\partial x}(\rho uc)+\frac{\partial}{\partial y}(\rho vc)+\frac{\partial}{\partial z}(\rho wc)=\frac{\partial}{\partial x}\left(\Gamma_c\frac{\partial c}{\partial x}\right)+\frac{\partial}{\partial y}\left(\Gamma_c\frac{\partial c}{\partial y}\right)+$$
$$\frac{\partial}{\partial z}\left(\Gamma_c\frac{\partial c}{\partial z}\right)+\frac{\partial}{\partial x}(-\rho\overline{u'c'})+\frac{\partial}{\partial y}(-\rho\overline{v'c'})+\frac{\partial}{\partial z}(-\rho\overline{w'c'})+S_c \quad \text{(Eq. 4-17)}$$

If the decomposition of fluid properties due to turbulence flow is substituted in the general transport equation, it gives rise to nine additional unknown terms of the form $\bar{\rho}\overline{u_i'u_j'}$, known as Reynolds stresses in the time averaged Navier Stokes equations thereby receiving the name Reynolds Averaged Navier Stokes or RANS equations. For a detailed derivation of these equations, a number of text books are referred (Versteeg & Malalasekera, 2007) (Shaw, 1992). In order to solve the turbulent flow fields, these unknown Reynolds stresses must be related to known quantities to form a closed system of equations. This method of estimating the Reynolds stresses using different set of equations and approximations is called "Turbulence Modelling".

One can avoid the turbulence modelling either partially or fully. An example of partial modelling of turbulence is Large Eddy Simulations (LES) where only the largest eddies are resolved for spatial and temporal scales and the smaller are modelled using averaging processes. A Direct Numerical Simulation (DNS) on the other hand, resolves the flow without any averaging and without the use of a turbulence model.

The level of complete resolution and the calculation grid required depends on the physical process under investigation. According to Kolmogorov length scaling method, a full resolution of spatial and temporal scales for smallest eddies for a F1 car at 140 mph need at least $5.5e^{13}$ cells per cubic meter for a complete resolution of flow (CD-adapco, 2016). Considering the practical flows involving large domains and simulation time, both partial and complete resolution of Navier Stokes equations is still not realizable due to computational and financial constraints.

In the present work, focus is made on RANS based turbulence modelling. RANS based turbulence modelling can be subdivided into two major classes i.e. eddy viscosity models and "Reynolds Stress Models (RSM)". Eddy viscosity turbulence models underpin the turbulence viscosity theory proposed by Boussinesq (1903). He defined the Reynolds stresses as a function of turbulent viscosity and mean strain rate tensor (isotropic). A generalized representation of the Boussinesq analogy can be mathematically described as follows;

$$\bar{\rho}\overline{u_i' u_j'} = \mu_t \left(\frac{\partial \mathrm{U}_i}{\partial \mathrm{x}_j} + \frac{\partial \mathrm{U}_j}{\partial \mathrm{x}_i} \right) - \frac{2}{3}\rho k \delta_{ij} \qquad \text{(Eq. 4-18)}$$

where

μ_t is the turbulent viscosity

i and j are suffix notation with i or j = 1 representing x-direction, i or j = 2 the y-direction and i or j = 3 the z-direction

ρ is the fluid density

$k = \frac{1}{2}(\overline{u'^2} + \overline{v'^2} + \overline{w'^2})$ is the turbulence kinetic energy and

δ_{ij} is Kronecker delta which corresponds to 1 if i = j and equals to zero if i ≠ j

Examples of eddy viscosity models are zero equation length scale models, single equation Spalart-Allmaras models, two equation k-ε and k-ω and Shear Stress Transport (SST) turbulence model.

The Reynolds Stress turbulence (RSM) models, also called second-moment closure models do not use the eddy viscosity hypothesis, nor they consider the strain to be isotropic in nature. RSM models can account for directional effects of strain

(anisotropic) hence requiring the solution of 6 additional equations. RSM models are not employed during the present PhD work and therefore only the k-ε, RNG k- ε , k-ω and Shear Stress Transport (SST) turbulence models, investigated during the PhD work are discussed in the later sections.

4.2.1 k- ε Turbulence Model

As discussed previously, eddy viscosity based turbulence models model the Reynolds shear stresses using equation (Eq. 4-18). In k-ε type of turbulence models, the turbulent viscosity term μ_t is considered to follow the following co-relation;

$$\mu_t = C_\mu \rho \frac{k^2}{\varepsilon} \qquad \text{(Eq. 4-19)}$$

Where C_μ is a function of turbulence kinetic energy and near wall flow velocity. In reference to ANSYS CFX, the values of *k* i.e. turbulent kinetic energy and ε being its dissipation rate, are found by solving additional transport equation equations as follows:

For *k:*

$$\frac{\partial}{\partial t}(\rho k) + \frac{\partial}{\partial x_j}(\rho U_j k) = \frac{\partial}{\partial x_j}\left[\left(\mu + \frac{\mu_t}{\sigma_k}\right)\frac{\partial k}{\partial x_j}\right] + P_k - \rho\varepsilon + P_{kb} \qquad \text{(Eq. 4-20)}$$

For ε:

$$\frac{\partial}{\partial t}(\rho\varepsilon) + \frac{\partial}{\partial x_j}(\rho U_j \varepsilon) = \frac{\partial}{\partial x_j}\left[\left(\mu + \frac{\mu_t}{\sigma_\varepsilon}\right)\frac{\partial \varepsilon}{\partial x_j}\right] + \frac{\varepsilon}{k}(C_{\varepsilon 1} P_k - C_{\varepsilon 2}\rho\varepsilon + C_{\varepsilon 1} P_{\varepsilon b}) \qquad \text{(Eq. 4-21)}$$

The solution of transport equations for k and ε give rise to additional closure coefficients which were found empirically. A list of these coefficients for standard k-ε model are given Table 4-1.

Table 4-1: Empirical coefficient used for k-ε turbulence model

C_μ	$C_{\varepsilon 1}$	$C_{\varepsilon 2}$	σ_k	σ_ε	Pr_t
0.09	1.44	1.92	1	1.3	0.9

If the coefficients C_μ, $C_{\varepsilon 1}$ and $C_{\varepsilon 2}$ are taken as function of local Reynold's number instead of global Reynold's number, the model can be adapted to represent the so called "Low Reynold k-ε turbulence" model. This adaption however would demand a very fine near wall resolution along with introduction of non-linear damping functions.

In equations (Eq. 4-20 and (Eq. 4-21, P_k represents the generation of turbulence due to viscous forces, P_{kb} and $P_{\varepsilon b}$ represent the generation and dissipation of turbulence due to buoyancy effects.

Mathematically,

$$P_k = \mu_T \left(\frac{\partial U_i}{\partial X_j} + \frac{\partial U_j}{\partial X_i} \right) \frac{\partial U_i}{\partial X_j} - \frac{2}{3} \frac{\partial U_k}{\partial X_k} \left(3\mu_T \frac{\partial U_k}{\partial X_k} + Pk \right) \qquad \text{(Eq. 4-22)}$$

Depending upon the nature of the problem, the buoyancy can be modelled either by using Boussinesq approximation (Xiaoxiong, 1995) or by solving the buoyancy terms completely. In Boussinesq buoyancy model, the density is not coupled to pressure variations. The temperature effect of density is accounted by means of the thermal expansion factor "β".

For the case of full buoyancy model, the term P_{kb} needs the solution of density variation and is mathematically defined as;

$$P_{kb} = -\frac{\mu_t}{\rho \sigma_\rho} g_i \frac{\partial \rho}{\partial x_i} \qquad \text{(Eq. 4-23)}$$

Where σ_ρ is the Turbulent Schmidt number.

When Boussinesq model is employed, the term P_{kb} involves the solution of temperature field only and is coupled to the turbulence production using the thermal expansion coefficient. Mathematically P_{kb} used for Boussinesq model is defined as follows:

$$P_{kb} = \frac{\mu_t}{\rho \sigma_\rho} \rho \beta g_i \frac{\partial T}{\partial x_i} \qquad \text{(Eq. 4-24)}$$

with σ_ρ being the Turbulent Schmidt number set to 0.9 per default in ANSYS CFX and holds good for most subsonic applications.

The dissipation term $P_{\varepsilon b}$ for isotropic dissipation is defined as;

$$P_{\varepsilon b} = C3.\max(0, P_{kb}) \quad \text{(Eq. 4-25)}$$

and

$$P_{\varepsilon b} = C3.\max(0, P_{kb}).\sin\emptyset \quad \text{(Eq. 4-26)}$$

for anisotropic dissipation.

where C3 = 1 and Φ being the angle between the velocity and gravity vectors.

4.2.2 RNG K- ε Turbulence Model

Using the mathematical renormalization group theory, the k-ε turbulence model was modified to replace the empirical constants with mathematically derived constants The RNG-k-ε model is another eddy viscosity model similar to k-ε model. The turbulent viscosity is modelled using the following equation.

$$\mu_t = C_{\mu RNG}\,\rho\,\frac{k^2}{\varepsilon} \quad \text{(Eq. 4-27)}$$

The transport equation for turbulence kinetic energy k remains the same as in standard k-ε model i.e.

$$\frac{\partial}{\partial t}(\rho k) + \frac{\partial}{\partial x_j}(\rho U_j k) = \frac{\partial}{\partial x_j}\left[\left(\mu + \frac{\mu_t}{\sigma_k}\right)\frac{\partial k}{\partial x_j}\right] + P_k - \rho\varepsilon + P_{kb} \quad \text{(Eq. 4-28)}$$

for ε, the equation is modified and is represented mathematically as follows;

$$\frac{\partial}{\partial t}(\rho\varepsilon) + \frac{\partial}{\partial x_j}(\rho U_j \varepsilon) = \frac{\partial}{\partial x_j}\left[\left(\mu + \frac{\mu_t}{\sigma_{\varepsilon RNG}}\right)\frac{\partial \varepsilon}{\partial x_j}\right] + \frac{\varepsilon}{k}(C_{\varepsilon 1 RNG}P_k - C_{\varepsilon 2 RNG}\rho\varepsilon + C_{\varepsilon 1 RNG}P_{\varepsilon b}) \quad \text{(Eq. 4-29)}$$

where

$$C_{\varepsilon 1 RNG} = 1.42 - f_n \quad \text{(Eq. 4-30)}$$

$$f_n = \frac{\eta\left(1-\frac{\eta}{4.38}\right)}{(1+\beta_{RNG}\eta^3)} \quad \text{(Eq. 4-31)}$$

$$\eta = \sqrt{\frac{\mathrm{P}_k}{\rho C_{\mu RNG}\varepsilon}} \qquad \text{(Eq. 4-32)}$$

The constants used in RNG-k-ε model are listed in Table 4-2.

Table 4-2: Empirical coefficient used for RNG k-ε turbulence model

$C_{\mu RNG}$	$C_{\varepsilon 1 RNG}$	$C_{\varepsilon 2 RNG}$	σ_k	σ_ε	β_0
0.085	1.42-f_n	1.68	1.0	0.7179	0.015

Comparing the standard and RNG k-ε model, it is seen that the major affect lies in improving the modelling of dissipation terms.

4.2.3 K-ω Turbulence Model

k-ω belongs to the eddy viscosity turbulence model group. The turbulent viscosity is related to the turbulent kinetic energy k and turbulent frequency ω using the co-relation;

$$\mu_t = \rho \frac{k}{\omega} \qquad \text{(Eq. 4-33)}$$

Instead of using the equation of turbulent dissipation rate ε, an equation for turbulent frequency ω for large scales is used. The ω-equation has significant advantages near the surface. The model differs from the low Reynold's turbulence model in that, that it avoids the use of the non-linear damping terms which are numerically tedious and demand higher resolution of calculation grid near the solid surfaces.

The basic k-ω model was proposed by Wilcox (1986) (1998) solves transport equation for k as follows;

$$\frac{\partial}{\partial \mathrm{t}}(\rho k) + \frac{\partial}{\partial \mathrm{x_j}}(\rho \mathrm{U_j} k) = \frac{\partial}{\partial \mathrm{x_j}}\left[\left(\mu + \frac{\mu_\mathrm{t}}{\sigma_\mathrm{k}}\right)\frac{\partial k}{\partial \mathrm{x_j}}\right] + \mathrm{P}_k - \beta' \rho k \omega + \mathrm{P}_{kb} \qquad \text{(Eq. 4-34)}$$

transport equation for ω is defined as;

$$\frac{\partial}{\partial t}(\rho\omega) + \frac{\partial}{\partial x_j}(\rho U_j \omega) = \frac{\partial}{\partial x_j}\left[\left(\mu + \frac{\mu_t}{\sigma_\omega}\right)\frac{\partial \varepsilon}{\partial x_j}\right] + \alpha\frac{\omega}{k}P_k - \beta\rho\omega^2 + P_{\omega b} \quad \text{(Eq. 4-35)}$$

In contrary to the standard k-ε turbulence model, the empirical coefficients employed in the standard k-ω model are derived with the assumption that the velocity near the wall surface is resolved adequately thereby demanding a fine spatial resolution. The coefficients used in standard k-ω model are given in Table 4-3.

Table 4-3: Empirical coefficient used for k-ω turbulence model

β'	β	α	σ_k	σ_ω
0.09	0.075	5/9	2	2

The production term P_{kb} remains the same as in standard k-ε and RNG k-ε models. The buoyancy term $P_{\omega b}$, in ω equation for isotropic dissipation rate is defined as;

$$P_{\omega b} = \frac{\omega}{k}((\alpha + 1).C3\max(P_{kb}, 0) - P_{kb}) \quad \text{(Eq. 4-36)}$$

In case of directional dissipation being taken into account, the formula takes into account the angle ø between the velocity and gravity vectors i.e.

$$P_{\omega b} = \frac{\omega}{k}((\alpha + 1).C3\max(P_{kb}, 0).\sin\text{ø} - P_{kb}) \quad \text{(Eq. 4-37)}$$

As the k-ω turbulence model includes coefficients validated for the bounded and near wall regions, its application in fully developed free turbulent zone is not considered reliable (Versteeg & Malalasekera, 2007).

4.2.4 SST Turbulence Model

Considering the facts that the k-ω model predicts well the near wall region and k-ε the free stream region, the SST turbulence model was developed by F.Menter (Menter, 1994). The model combines the advantages of k-ε and k-ω to achieve an optimal model formulation applicable to a majority of flow problems. The heart of the SST turbulence model is a blending factor F1. The value is set to one near the solid surface thereby activating the k-ω model near to wall surfaces and switched to zero

for the rest of the calculation domain thereby making use of k-ε turbulence model in region away from wall. Further improvements are done in the model such as the treating of C_μ in equation (Eq. 4-19) as a variable instead of a constant. The specific mathematical details of the different implementations in SST model can be found in literature (Menter, 1994).

4.3 Turbulence Modelling and Near Wall Treatment

As the fluid flow approaches a solid surface, viscous forces due to wall shear increase whereas the inertial forces due to momentum decrease. With a decrease in flow velocity, the Reynold's number decreases and the flow becomes almost laminar in nature as the viscous forces overwhelm the inertial forces. Very near to the wall, the flow stops and the velocity at the wall approaches zero. At this point, the fluid shear stress is almost equal to the wall shear stress. A simple graphical description of different flow zones generated for a flow past a flat plate is shown in Figure 4-1.

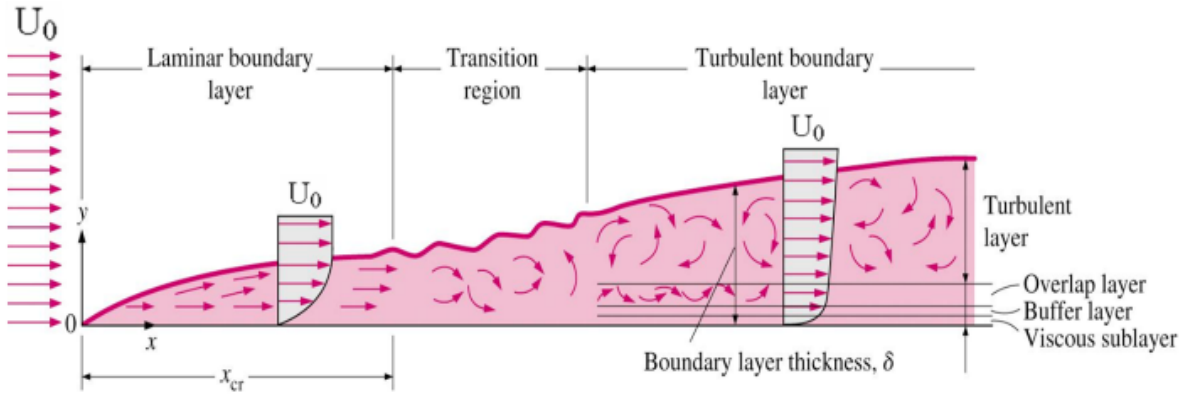

Figure 4-1: Diagrammatic representation of turbulent boundary layer along a flat plate (Incropera, 2006)

In the viscous sub-layer zone, the flow velocity varies almost linearly with the distance from the wall. In this zone, there are practically no turbulent fluctuations and only the viscous stress dominates. The buffer zone on the other hand represents a zone with turbulent eddies which are rapidly damped thereby causing sudden dissipation of turbulent shear stresses. The overlap zone, also called log-law zone or inner zone can be defined as a region in which the length scale of turbulent eddies are almost proportional to the distance from the wall surface. In this zone the ratio of viscous and turbulent shear stresses are almost equal. The outer zone is dominated

by constant turbulent eddies with size proportional to the boundary layer thickness δ as shown in Figure 4-1.

The above discussion emphasizes that the level of turbulence near to a solid surface is directly related to distance from the surface and the flow velocity. In CFD analysis, the distance from a solid surface and the relevant velocity are often represented in dimensionless term "y^+" and "u^+" respectively.

Mathematically;

$$y^+ = \frac{\Delta y . u_\tau}{\nu} \qquad \text{(Eq. 4-38)}$$

and

$$u^+ = \frac{U_0}{u_\tau} \qquad \text{(Eq. 4-39)}$$

where Δy is the distance from wall and

$$u_\tau = \sqrt{\frac{\tau_w}{\rho}} \qquad \text{(Eq. 4-40)}$$

is the friction velocity. The kinematic viscosity is represented by υ and the tangential velocity parallel to the wall surface is given the symbol U_0.

Based on experimental analysis, a plot of these two dimensionless quantities is similar to one shown in Figure 4-2.

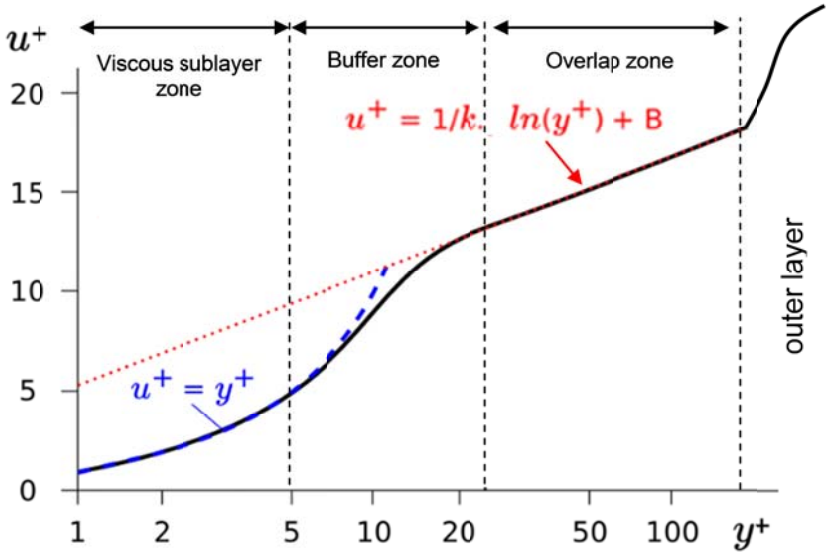

Figure 4-2: Diagrammatic representation of u+ as a function of y+ (Chmielewski & Gieras, 2013)

Experimental work for a number of applications (Salim & Cheah, 2009), (Versteeg & Malalasekera, 2007) show that the viscous sub-layer exist for y+ values below 5. For y+ values between 30 and 300 the variation in velocity follows the log law i.e.

$$u^+ = \frac{1}{\mathrm{k}}\ln(y+) + B \qquad \text{(Eq. 4-41)}$$

where k is the von Kàrmàn constant and B is the equation constant depending upon the roughness level of the wall.

In the buffer zone with y+ values between 5 and 30, neither the linear nor the log law is seen to exist. The point of intersection between the overlap/log zone and viscous/linear zone is at a y+ value of approximately 11 (located in the buffer zone).

For the outer zone, the law of wake holds good. The law of wake for a maximum velocity $U_{max} = U_0$ and local velocity u at a distance y from the wall and friction velocity u_t is mathematically defined using the following correlation;

$$\frac{U_{max} - u}{u_t} = \frac{1}{\mathrm{k}} ln \frac{y}{\delta} \qquad \text{(Eq. 4-42)}$$

where k = 0.41 is the Von-Kàrmàn constant

For confined flows with surface/wall boundary conditions, the ideal way would be to make the grid so fine that all the effects of viscosity dominant region and sharp gradients of energy and flow can be resolved for the complete turbulent boundary layer. This however is practically impossible for real world problems. The issue is mostly overcome by either crossing the near wall region using analytical/empirical co-relations called "wall functions" or by using the "low Reynolds number turbulence models". The low Reynolds number turbulence models employ damping functions (functions to represent the damping of turbulence across the buffer and viscous sub-layer) to extend the application of turbulence model to near wall region demanding finer solution meshes. Some CFD codes employ a mix of the two techniques.

ANSYS CFX use wall function methods for the high Reynolds number turbulence models. These wall functions are however modified from the standard wall functions due to their strong sensitivity to the mesh e.g. for a mesh (fine mesh) that captures a velocity approaching to zero near the solid surface. In order to overcome this issue, the wall frictional velocity u_τ is replaced with u* and consequently y+ is replaced with y*. Mathematically:

$$u^* = \sqrt[4]{C_\mu}.\sqrt{k} \qquad \text{(Eq. 4-43)}$$

and

$$y^* = \frac{\Delta y.u^*}{\nu} \qquad \text{(Eq. 4-44)}$$

In order to avoid the sensitivity to mesh in the standard wall functions, ANSYS CFX uses the so called "scalable wall function" by limiting the y^* to the point of intersection of linear and log law region i.e. 11.06.

Mathematically;

$$\tilde{y}^* = \max(y^*, 11.06) \qquad \text{(Eq. 4-45)}$$

For scalable wall function the dissipation is calculated using the equation below;

$$\varepsilon = \frac{\rho u^*}{\tilde{y}^* \mu}.\frac{{C_\mu}^{3/4}}{k}\ k^{3/2} \qquad \text{(Eq. 4-46)}$$

For simulations involving very low free stream turbulences, the value of u^* is further modified using a limiter (CFX, 2010), limiting factor of 0.01 as follows:

$$u^* = \max\left(\sqrt[4]{C_\mu}.\sqrt{k}, 0.01.\frac{u}{\tilde{y}^*}\right) \quad \text{(Eq. 4-47)}$$

Similar to the calculation of flow, heat transfer is modelled for scalable wall functions by employing non-dimensional temperature flow profile using the following equation;

$$T^+ = 2.12.ln(y^*) + \beta \quad \text{(Eq. 4-48)}$$

It is important to note that even though the scalable functions can resolve the issue of local mesh refinement near the solid surface, it still can lead to numerical issues and incorrect estimations of flow and heat transfer in case of low Reynolds number flow due to the following assumptions;

a) The total shear stress across the near wall cells remain constant.

b) The turbulent kinetic energy remains constant over the inner layer and drops quadratic to zero within the viscous sub-layer.

c) The dissipation rate is inversely proportional to the wall distance over the inner region and remains constant across the viscous sub-layer.

Instead of using the scalable wall function for low Reynolds number turbulence models and k-ω based models, an automatic wall function is used by ANSYS CFX. This automatic wall function is basically a switch between the "low Reynolds number refined treatment" near the solid surface and "wall functions" away from the wall.

Based on the experimental and analytical results, an algebraic equation exist for the turbulent frequency ω for both log-law as well as viscous sub-layer region as shown below.

For log law zone

$$\omega_l = \left(\frac{u^{*2}}{\alpha k \nu y^+}\right) \quad \text{(Eq. 4-49)}$$

and for sub-layer zone

$$\omega_s = \left(\frac{6\nu}{\beta(\Delta y)^2}\right) \quad \text{(Eq. 4-50)}$$

The blending between the turbulence frequency in the log and viscous sub-layer near the wall is achieved using the following equation;

$$\omega_w = \omega_s \sqrt{1 + \left(\frac{\omega_l}{\omega_s}\right)^2} \quad \text{(Eq. 4-51)}$$

In order to calculate the heat transfer, the automatic wall function calculates the temperature profile using the dimensionless temperature T^+ using the following equation:

$$T^+ = Pr.y^*.e^{-\Gamma 1} + [2.12.ln(y^*) + \beta]e^{(-\frac{1}{\Gamma})} \quad \text{(Eq. 4-52)}$$

where

$$\beta = (3.85Pr^{\frac{1}{3}} - 1.3)^2 + [2.12.ln(Pr) \quad \text{(Eq. 4-53)}$$

$$\Gamma 1 = (\frac{0.01(Pr.y^*)^4}{1 + 5.Pr^3 y^*}^2 \quad \text{(Eq. 4-54)}$$

Pr is the Prandtl number (see chapter 5 for definition)

4.4 Discretization

In order to solve the flow governing equations (continuous in nature) numerically on a digital computer, they have to be replaced into digital format by means of a process called discretization. An ideal discretization would mean a zero deviation between the continuous governing equations and the discretized equations. Mathematically this is only possible if the solution points or the number of grid points are increased to infinity. This however is not achievable and therefore the process of discretization leads to a certain level of numerical errors. The errors can be reduced by increasing

the order of the discretization scheme e.g. a 2nd (or higher) order discretization contains less errors as compared to a 1st order discretization.

For the current PhD work a finite volume discretization methodology is used. The order of discretization employed is the so called "high resolution discretization". This terminology is specific to ANSYS CFX code and represents a gradual local shift from the 2^{nd} order discretization order to the first order. This shift however is internally controlled and occurs only in case of unrealistically high variable gradients forcing the solution to divergence. Based on the above mentioned schemes, a simulation run was said to be converged when the root mean squared residuals (RMS) of the governing flow equations fall below 4^{th} order of their initial magnitude. As a number of simulation runs were planned to run in a queue to investigate effect of different variables (multiple simulation runs), a simulation run was set to stop automatically with the residual level falling below 1e-5. Depending upon the simulation, different stopping criteria e.g. variance and/or average of a physical quantity at a location of interest etc. can be setup for controlling the run.

ANSYS CFX uses the finite volume discretization scheme. A detailed explanation of discretization is not presented here as it is beyond the scope of this PhD work but can be found in different numerical analysis text books e.g. (Versteeg & Malalasekera, 2007), (Wilcox, 1998). For all the simulation work conducted during this work, higher order finite volume discretization was used. The solution of the discretized equations were obtained using a coupled solver which in contrary to the segregated solver solves the velocity and pressure variables simultaneously thereby requiring less iterations to achieve the numerical solution and is comparatively less prone to numerical discretization errors.

4.5 Geometry and Mesh Generation

The physical geometry that needs to be subjected to numerical CFD analysis can be created using a number of available CAD (Computer Aided Design) tools. The geometry to be investigated is discretized into smaller mesh components using a mesh generation tool. These small meshed regions serve as calculation blocks for the solution of governing flow, heat and mass transfer equations. Not every geometrical detail is important for a CFD analysis. A number of functions and tools

are made available in the mesh generation tool to extract and refine the underlying CAD geometry.

For the present work, the main CAD tool used was Rhinoceros (Rhinoceros, 2010). Rhinoceros has the ability to export the geometry in a number of formats. For the current PhD work, either parasolid (.x_t) or stereolythic format (.stl) were exported to the mesh generator ANSYS ICEM CFD (Ansys, Inc., 2016) for further pre-processing of geometry and mesh generation. ANSYS ICEM CFD is a very thorough mesh generator that offers a number of mesh shapes such as hexahedral, tetrahedral or a mix of the two with or without the presence of inflation cell - prism layer cells. Inflation cells are hexahedral cell that grow normal to a surface and are necessary to capture the strong gradients near to a wall surface.

4.6 Boundary Condition Modelling

The boundary of the meshed domain that needs to be investigated using numerical CFD methods can either be a solid or a fluid. Appropriate physical conditions are applied on the boundaries to give a unique numerical solution. Different types of boundary conditions are used for numerical analysis. A brief description of the different boundary types are given below.

4.6.1 Wall

A solid wall boundary condition specifies that the fluid cannot flow across the boundary surface. For mass and momentum equations, a no-slip condition is applied which means that the flow comes to rest at the wall. A free-slip condition on the other hand allows the flow to move free at the wall (no wall shear). For the energy transport equation, one can specify either the wall temperature or the wall heat flux. Similar to the application of heat flux, a species source flux (e.g. a pollutant), can be applied to the wall surface. A special case of wall is a "symmetry wall". At a symmetry wall boundary condition, the component of velocity normal to the boundary is set to zero. Similarly the gradients normal to the surface of all other variables are specified as zero.

4.6.2 Inlet

An inlet boundary condition specifies the fluid flow across the boundary surface into the calculation domain. An inlet boundary condition allows the application of flow mainly in form of velocity, mass flow rate or pressure. Other transport relevant variables such as turbulence variables, temperature, and strength of sources/species can be applied depending upon the problem under investigation.

4.6.3 Outlet

An outlet boundary condition specifies the fluid flow across the boundary surface out of the calculation domain. If the exiting flow conditions for mass are known, the velocity or mass flow rate can be specified if the exiting flow are unknown, different type of known pressure conditions such as static pressure, total pressure etc can be applied.

4.7 Convergence Control and Criteria

A CFD simulation progresses iteratively to a distinct mathematical solution in space and time. The reason for this iterative approach is the conversion (discretization) of the flow governing equations which are non-linear in nature into a computer solvable algebraic counterpart. The conversion of non-linear partial differential equations to algebraic forms lead to the so-called discretization errors. The flow governing equations are solved for every mesh cell present in the calculation domain. The amount by which the discretized equation remain unsatisfied due to truncation/conversion errors in each iterative loop is called a "residual". For an ideal well posed numerical problem, the residuals shall decrease until the digital accuracy of the computer is achieved. This process of guiding the numerical problem to find a unique mathematical solution is called convergence. In order to achieve convergence, different numerical schemes are implemented in the CFD codes. These schemes are equipped with different numerical parameters and variables that can be adjusted to control the convergence.

It is however important to note that a mathematically converged solution does not necessarily replicate the physical phenomena under investigation. Guiding the solution to convergence therefore not only requires the monitoring of the residual but

also the setting of control points to check different physical variables, their validity and plausibility along with their development during the course of the simulation.

Depending upon the process under investigation, different judgment criteria can be set to see if the numerical problem is marching towards a unique solution. The major criteria should be a global balance of mass, momentum, energy and the involved scalar quantities. Normalized residuals (normalized to the largest value for a well initialized problem) should be considered while judging the convergence. For most of the subsonic flows involving a single phase, the code developers recommend that the normalized residuals should fall at least 2-3 order of magnitudes before a solution is considered to be converged (CFX, 2010). If the solution is not well initialized i.e. the initial guess in the case of a steady state simulation is far from a unique solution, the normalized residuals should fall by higher orders of magnitudes. On the other hand if the simulation is very well initialized, the relative error from one iteration to the next will be very small hence a large drop in normalized magnitude of the residual cannot be expected. In the case of transient simulations, the normalized residuals should fall by 4-5 orders of magnitude within a time step before the time step should be declared as converged. It is however important to note that in transient analysis, the end solution is strongly dependent on the initial conditions hence the falling of residuals alone does not indicate the true representation of the physical phenomena under investigation.

The drop in normalized residuals by 2-3 orders of magnitude for steady state and 4-5 orders of magnitude for transient simulation are only guidance values. Engineering judgment of the phenomena under investigation and monitoring the behaviour of the variables of major importance should be considered as a decisive criteria when defining the simulation to be converged.

4.8 Time Stepping

The flow resolved in a transient simulation is strongly dependent on the physical time step. For steady state simulations in which the simulations do not progress in real physical time, ANSYS CFX uses an under-relaxation technique called the "false time stepping". This false time step is mainly a time representative of average flow conditions in the numerical domain under investigation and is used mainly to achieve

a mathematically converged solution. The final steady state solution however should be independent of this time step. If this is not the case and different results are seen at different iteration level, the processes investigated are said to inhibit transient behaviour and should be run in transient model. In certain cases the mesh refinement can resolve the issue and hence should be checked prior to switching to a transient run. Simulation specific false time steps used in the course of this PhD work are mentioned in the relevant sections.

4.9 Summary

This chapter is aimed to provide an overview of the theoretical aspects of CFD, the governing flow equations, turbulence models, issues related to near wall modelling, discretization of the computational domain and definition of boundary types. Once all the modelling approaches mentioned in this chapter are employed and a comparison of different possible turbulence and radiation models being made (see chapter 5), an outline of the modelling approach is formulated and presented as a conclusion at the end of chapter 5. This devised modelling approach is then followed for further validation and application phases of this PhD work.

5 Model Verification

Verification is the process of ensuring that the numerical code correctly represents the physical phenomena under investigation by solving the underlying mathematical equation and laws of physics equations correctly. In the current research work, ANSYS CFX Code is verified against models for which an analytical solution exists and also against some previously published work.

Even though Navier in 1822 and Stokes in 1845 established the differential equations of flows, it is the invention of CFD that has led the way to the detailed investigation of complex flow phenomena. Being a constantly developing computational technique, CFD is prone to a number of problems e.g. verification and validation, multiple-solutions, conflicts between accuracy and computing power, boundary condition treatments and turbulence modelling issues.

The equations governing energy and fluid flow along with the key concepts of turbulence and its modelling are explained previously in chapter 4. The current chapter focuses on the verification and validation of CFD simulations for indoor building climates and aims to provide guidelines for correctly predicting the radiative and convective flows for modelling heat and mass transfer phenomena associated with human occupancy. As many processes in the indoor climate are associated with mass transfer phenomena such as human respiration, variation in pollution concentration etc., mass transfer modelling cannot be avoided. As no direct analytical/empirical solution of mass transfer is known to the author at this point of writing, the "Heat and Mass Transfer Analogy" is referred (Incropera, 2006). This analogy being based on the conservation equation, implies that a set of simulations/experiments for mass and heat transfer for a particular geometrical configuration are interchangeable. Considering this fact leads this research work to focus primarily on the verification and validation of heat transfer coefficients and once verified and validated to apply the model to investigate different scenarios.

This chapter is subdivided into 2 sections. The first section deals with the verification of radiative heat transfer models and the second section focuses on verifying the convective heat transfer models.

5.1 Radiative Heat Transfer Modelling

Unlike conduction and convection where the energy transfer is dependent on the temperature gradients and material properties in the vicinity, radiation energy transfer takes place between separated bodies with or without the medium interference. If a generalized case of radiating medium along with radiating surfaces is considered, integration needs to be done to obtain the heat balances and to satisfy the energy equation. As radiation involves different energy spectrum, an additional integration needs to account for the spectral variation of variables such as wavelength or frequency i.e. heat flows are integrated over all wave lengths. As just the boundary conditions are specified, the actual spectral heat flows are unknown, thereby requiring an iterative approach.

To take into account all the various effects, a solution of an integral-differential equation known as the “Radiation Transfer Equation (RTE)” (Siegel & Howell, 1992) is required.

$$\frac{dl_{v(r,s)}}{ds} = -(K_{av} + K_{sv})l_{v(r,s)} + K_{av}l_{b(v,T)} + \frac{K_{sv}}{4\pi}\int_{4\pi} dl_{v(r,s')}\emptyset(s.s')d\Omega' \qquad \text{(Eq. 5-1)}$$

where

r is the position vector

s is the direction vector

s‘ is the path length [m]

K_a is the absorption coefficient [m^{-1}]

K_s is the Scattering coefficient [m^{-1}]

l_b is the Blackbody emission intensity [W/(m²Sr)]

l_v is the spectral radiation intensity depending on position and direction [W/(m²Sr)]

T is the local absolute temperature[K]

Ω is the solid angle[Sr]

∅ is the in-scattering phase function [Sr^{-1}]

The solution of RTE is iterative and is highly dependent on the three spatial co-ordinates, 2 local directions and the frequency of the wavelength(s) involved. A simplified graphical description of the terms used in equation 1 is shown in Figure 5.1.

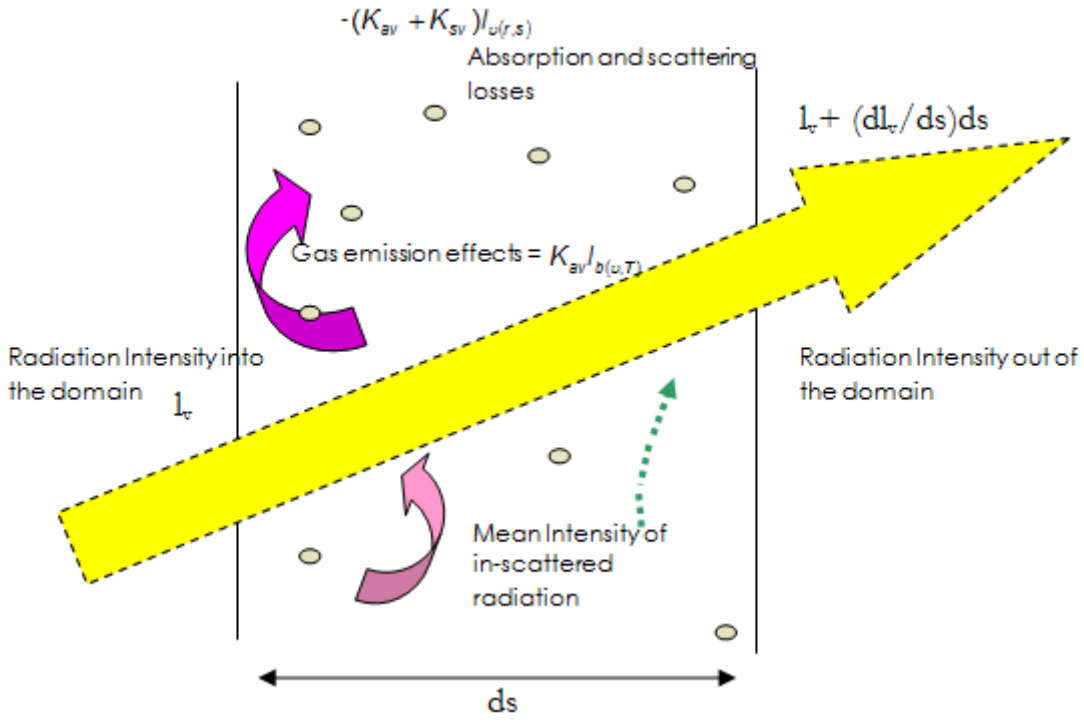

Figure 5-1: Description of radiation modelling phenomena

For a numerical solution of Eq. 5.1, an adequate calculation grid is required. In case radiation alone needs to be resolved without any medium`s participation, only surface meshes/grids need to be defined and the extra solutions of equations like scattering due to local emission and absorption are ignored, thereby making the solution simpler e.g. considering two finite surface areas A_1 and A_2 having certain set of material properties and inclined to each other, the radiative heat exchange between them can be calculated using Stefan-Boltzman law:

$$Q_{12} = \varepsilon_1 \varepsilon_2 \sigma A_1 \varphi_{12} \left(T_1^4 - T_2^4\right) \qquad \text{(Eq. 5-2)}$$

where

Q_{12} is the total heat exchange between the surfaces 1 and 2

ε_1 and ε_2 are the emissivitivities of the two surfaces

A_1 and A_2 are the surface areas of the two surfaces

φ_{12} is the view factor between surface 1 and 2.

T_1 and T_2 are the absolute temperatures of surfaces 1 and 2 respectively.

Still in a simplified form, the dependence on spatial coordinates, local direction coordinates, path lengths and frequency, the solution of RTE can be very time consuming.

This problem is overcome by the use of different algebraic and/or numerical methods to approximate the radiation heat transfer with acceptable accuracy for different situations. Applying a certain method to solve RTE by approximating the spectral and directional dependencies in simplified and time efficient manner is known as “Radiation Modelling”.

ANSYS CFX is a general purpose CFD code giving the additional flexibility to solve radiation transport phenomenon. It is capable of solving the radiation transport equation decoupled from flow and energy equations. This however should only be used when it is assured that the phenomena like energy scattering and absorption by a medium are negligible and can be ignored.

A number of directional and spectral models are implemented in ANSYS CFX these are briefly described in the upcoming sections.

5.1.1 Rosseland or Diffusion Approximation Model

If a medium is optically very dense, the radiation can travel only a short distance before it is completely absorbed or scattered. For such a situation, the RTE can be transformed to a diffusion heat transfer equation much similar to that of heat conduction. This diffusion approach can however be applied to optical thickness values > 5 (Siegel & Howell, 1992). It is important to note that an optical thickness (optical depth) is a dimensionless quantity. The optical thickness can be defined as “the natural logarithm of the ratio of the incident to transmitted radiant power through a material” (McNaught & Wilkinson, 1997) (Kitchin, 1987).

The Rosseland model is a very simplified representation of the radiative heat transfer and delivers the heat flux equation as:

$$q_r = -\frac{4}{3a_R} \times \nabla(\sigma T^4) \qquad \text{(Eq. 5-3)}$$

Where

a_R is defined as Rosseland mean absorption coefficient.

This model however is not valid in the near wall regions due to the evaluation of an emissive power jump (for details see dedicated literature on radiation modelling (Siegel & Howell, 1992)). For this reason a slip wall treatment is implemented in ANSYS CFX for the heat flux at the wall.

$$q_{r,w} = -\sigma\left(\frac{T_w^4 - T_g^4}{\psi}\right) \qquad \text{(Eq. 5-4)}$$

where

σ is Stefan-Boltzman Constant

T_w is the temperature of the boundary wall

T_g is the temperature of the gas adjacent to the wall

And

ψ is the slip coefficient.

5.1.2 Spherical Harmonics, Differential Approximation or P1 Model

This model is also a simplification of the RTE which assumes that the radiation intensity is isotropic at a given location in space e.g. this assumption can be used for fuel flame studies but in the regions away from the vicinity of the flame (Siegel & Howell, 1992). This model is also valid for optical thickness greater than 1 and needs appropriate wall treatment (CFX, 2010). The differential heat transfer equation is multiplied by powers of cosines generating a set of moment equations. To find a closure, the intensity is approximated by a series expansion in terms of spherical harmonics denoted by P. As the series is truncated after the first term the method takes the name P1.

After a considerable amount of mathematical work (see (Siegel & Howell, 1992) for detailed derivations) an equation for radiative heat flux to be used in energy equation is derived. i.e.

$$q_{rv} = -\left(\frac{1}{3(K_{av} - K_{sv}) - AK_{sv}} \nabla G_v \right) \qquad \text{(Eq. 5-5)}$$

where

K_{av} is the absorption coefficient at a certain frequency

K_{sv} is the scattering coefficient at a certain frequency

A is the linear anisotropy coefficient

And ∇G_v is the divergence of spectral incident radiation (in three dimension).

5.1.3 Discrete Transfer Model

In Discrete Transfer Model, the original RTE is solved by discretization along rays. The path along the ray is discretized by using the sections defined by breaking up of the path at element boundaries. To understand the phenomena, consider Figure 5-2.

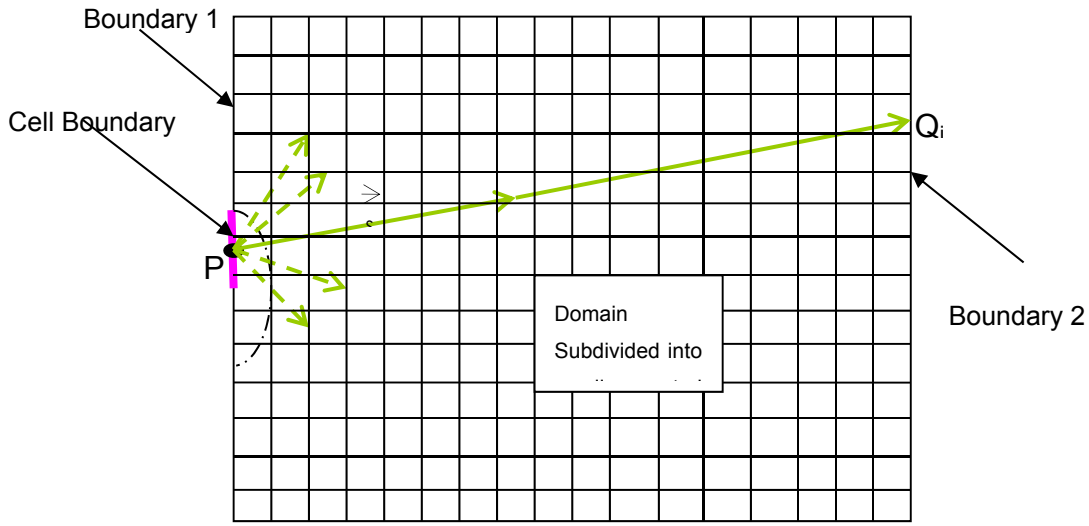

Figure 5-2: Description of DTRM without internal blocking

Assuming P as the centre point of a boundary cell, a hemisphere is centred at it and subdivided into a prescribed number of solid angles. Each solid angle defines a direction along which the RTE is to be solved. The path of each of these rays is

followed till it hits another boundary. Let Q_i be the point of impingement as shown above. This point although is not centre of the cell, it is assumed that the radiation intensity at this point and at the centre point is equal. Now "start back" from point Q_i takes place, i.e. the path of the beam is followed backwards to its origin i.e. point P and the RTE is solved to give the form:

$$I_v(r,s) = I_{vo}\exp^{(-(K_{av}+K_{sv})s)} + I_{bv}\left(1-\exp^{(-K_a s)}\right) + K_{sv}\,\bar{I}_v \qquad \text{(Eq. 5-6)}$$

where

I_{vo} is the radiation intensity leaving the boundary and

I_v is the mean radiation intensity.

The incident radiation heat fluxes at any point are calculated by summing up the effects of all the radiation beams arriving at that point (e.g. P in the following equation) and is mathematically given by:

$$G_p = \sum_i I_{PQ_i}\left(s_{PQ_i} \bullet n\right)\nabla\Omega_{PQ_i} \qquad \text{(Eq. 5-7)}$$

where

I_{PQi} is the radiation intensity from P to Q_i

s_{PQi} is the unit vector parallel to the direction of the ray

n is the unit vector normal to the wall at point P and

P_{Qi} is the followed direction.

As the solution of RTE needs the knowledge of boundary conditions, a temperature and wall characteristics based boundary condition is written internally as follows:

$$J_p = \varepsilon_w \sigma T_w^4 + (1-\varepsilon_w)G_p \qquad \text{(Eq. 5-8)}$$

Where J_p is the radiosity at point p, e_w is the emissivity of the wall, T_w is the wall temperature, σ is the Stefan-Boltzmann constant and G_p is the irradiation at point P.

The equation needs to be solved iteratively unless the emissivity of wall is defined as 1.

5.1.4 Monte Carlo Method

Monte Carlo is basically a statistical approach applied successfully at first by Siegel and Howel (1992) for solving radiation heat transfer. In this method, it is assumed that the intensity of radiation is proportional to the differential angular flux of photon released from a sampled source, thereby thinking of radiation field as a photon gas.

The path of this photon released from a surface is tracked and all the physical interactions like reflection, absorption etc are noted and written in the form of a so called “history”. A number of histories for a photon are generated and recorded until its weight falls below a certain value calling this point “die out” point. By appropriate formulation of this history, all the required physical information can be gathered e.g. counting the number of photons (energy bundles) and multiplying it with the emissivity, one gets the information about the total and the absorbed radiative flux.

Using Monte Carlo method avoids the need of spectral discretization as the differential quantities are not of interest while calculating the radiative heat transfer phenomena.

As discussed earlier, the heat absorption and reflection depend on the properties of materials. Some materials absorb the radiation of particular wavelength in a spectrum more than the other present in the same spectrum.

There are three ways in which ANSYS CFX deal with the spectral behaviour and are briefly explained in the next paragraphs.

Gray Band Modelling

Activating the gray model for spectral calculations leads to an assumption that the wavelength dependency in the RTE is dropped out of calculation. This method leads to considerable less CPU time. The assumption is valid as far as the radiation effect of gases in medium does not need to be modelled.

Important examples of use of non gray models are reheat furnaces and atmospheric layers where the wavelength dependency is not negligible and so gray model cannot be used.

Multi-band Modelling

The spectrum generated is based on discrete spectral bands. Result of each spectral band is calculated separately and is summed to get the total flux quantities. For the activation of this model in ANSYS CFX at least two bands must be defined .The CFD solver checks the two and their union to assure that the complete spectral band is solved.

Multi-Gray Modelling

This model considers a number of gases as gray but with a certain user supplied weightage. A correlation must be applied between the weightage and the absorption coefficient of each gas present in the domain.

5.2 Verification using Simple Geometrical Configurations

In order to verify the radiation models implemented in the CFD tool ANSYS CFX, a comparison has to be made between simulation results and analytical/experimental results. Due to the geometrical complexity of objects, exact analytical solutions for the parameters governing radiative heat transfer (e.g. view factor) exist only for simplified geometries. Co-relations are derived for complex geometries mainly based on experimental measurements thereby inducing certain level of inaccuracy. For the present work, the verification of radiation model in ANSYS CFX is conducted primarily for view factors using simple geometrical configurations for which exact analytical solutions exist. This work is followed by comparing simulation results of view factors, effective radiation area factor and projected area factors with those obtained during an experimental study for a human body.

Calculation of view factors is set as a common criteria for comparison. Analytical solutions for calculating view factors of a number of simple configurations and geometrical arrangements are available in the literature (Siegel & Howell, 1992) (Mobiok & Weber, 2000). However ANSYS CFX does not automatically give view factors as output. For these and other reasons of simplicity, finite and diffuse gray areas were modelled for the calculations. “Net radiation method for enclosures” is used (Siegel & Howell, 1992) to obtain the view factors where view factor (VF) $F_{1\text{-}2}$

Per definition, is “the ratio of energy arriving at an area A_1 divided by the energy leaving an area A_2”.

As a closed calculation domain needs to be modelled and meshed in CFD, all the boundaries except one radiating boundary were considered as black body. This is achieved in CFD by setting surface temperatures to absolute zero i.e. setting it to 0 Kelvin or -273.15°C.

In order to avoid an iterative solution (see previous sections) and make the problem simpler and easily controllable, the wall emissivities were set to 1. As fluid flow is of no interest, the fluid flow solver was switched off. Only the radiation solver was switched on using the expert control parameters in ANSYS CFX.

As seen in the discussion about the available radiation models and their limits, only two models i.e. DTRM and Monte Carlo are considered appropriate for modelling radiation in indoor climates. These two models are compared for their robustness and accuracy for calculating view factors of a simple enclosure (analogue to parallel and perpendicular plates). A comparison of the two models in terms of the percentile error is shown in Figure 5-3.

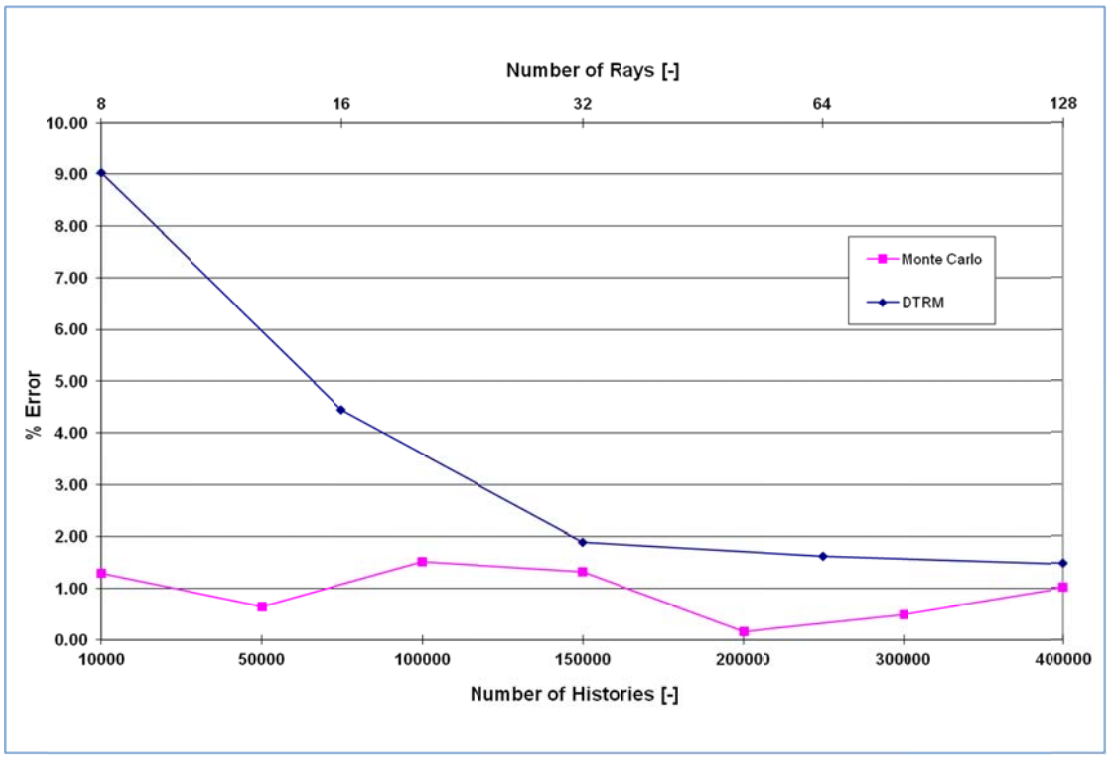

Figure 5-3: Comparison of accuracy between two thermal radiation models implemented in ANSYS CFX (Version 10.0)

A comparison of simulation results shows that with 8 rays used for directional tracking in the DTRM, the percentage error is much higher than with Monte Carlo radiation model with 10000 histories. The percentage error in the solution for Monte Carlo radiation model remains almost constant with the increase in number of recorded histories. The percentage error is decreased from 9% to less than 2% when the number of tracking rays in DTRM were increased from 8 to 128 (results comparable to Monte Carlo model). On average, for simple geometrical configurations, Monte Carlo simulations took almost 10% less time to achieve the same accuracy level as DTRM. The enclosure was later equipped with a complex human body shape and the results of radiation simulations were compared. The results showed that for complex geometrical configurations of a human body in enclosed space, the time required for the Monte Carlo simulation to reach the same level of accuracy became 12% more than DTRM. All simulations were carried out on an Intel Dual Core computer with 3 GHz processor and 2 GB RAM.

It was recognized that the benefit of using Monte Carlo method lies in the fact that ANSYS CFX cannot simulate directional radiation and semi-transparent objects using DTRM simulation method. In light of the above facts, the results for simple geometries in the upcoming sections are based on Monte Carlo simulations. For the complex human body, DTRM method was employed.

5.2.1 Parallel plates

A simple algebraic analytical solution exists for two parallel plates facing each other. In terms of indoor climate this geometrical case is analogous to the walls of a room facing each other. Mesh used for parallel as well as for perpendicular plate simulation study is shown in Figure 5-4 and Figure 5-5.

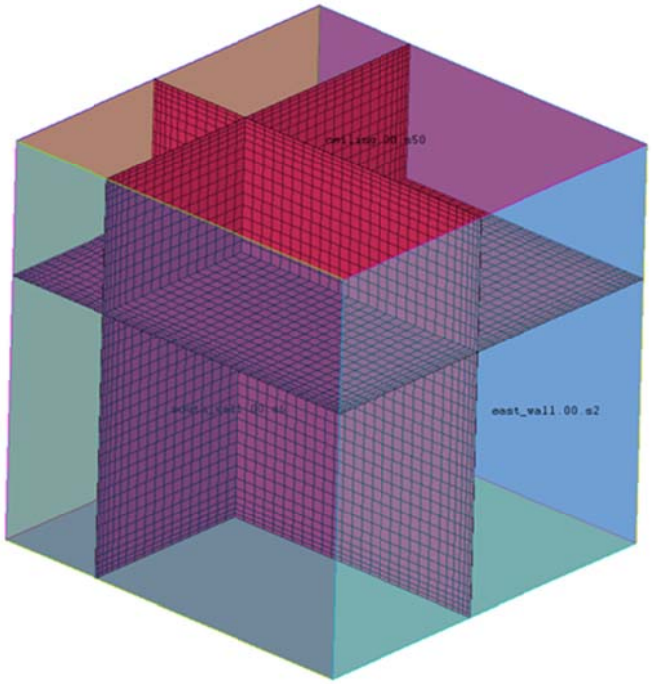

Figure 5-4: Modelled and meshed geometry of enclosure using block structure methodology.

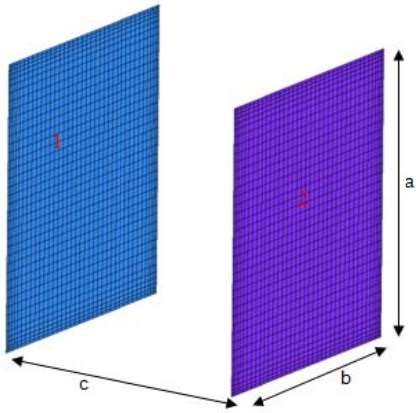

Figure 5-5: Two parallel opposing walls of a room with dimensions of a [m] * b [m] and held at a distance of c [m].

The analytical solution for such a situation presented by Siegel and Howell (1992) is given by following equation;

$$F_{1-2} = \frac{2}{\pi XY}\left\{\ln\sqrt{\frac{(1+X^2)(1+Y^2)}{1+X^2+Y^2}} + X\sqrt{1+Y^2}\tan^{-1}\left(\frac{X}{\sqrt{1+Y^2}}\right)\right\} + \frac{2}{\pi XY}\left\{Y\sqrt{1+X^2}\tan^{-1}\left(\frac{Y}{1+X^2}\right) - X\tan^{-1}X - Y\tan^{-1}Y\right\} \quad \text{(Eq. 5-9)}$$

where

F_{1-2} is the view factor between the plates 1 and 2,

X = a/c, and

Y = b/c.

The comparison of simulated view factors with the ones obtained using the analytical solution is shown in Figure 5-6.

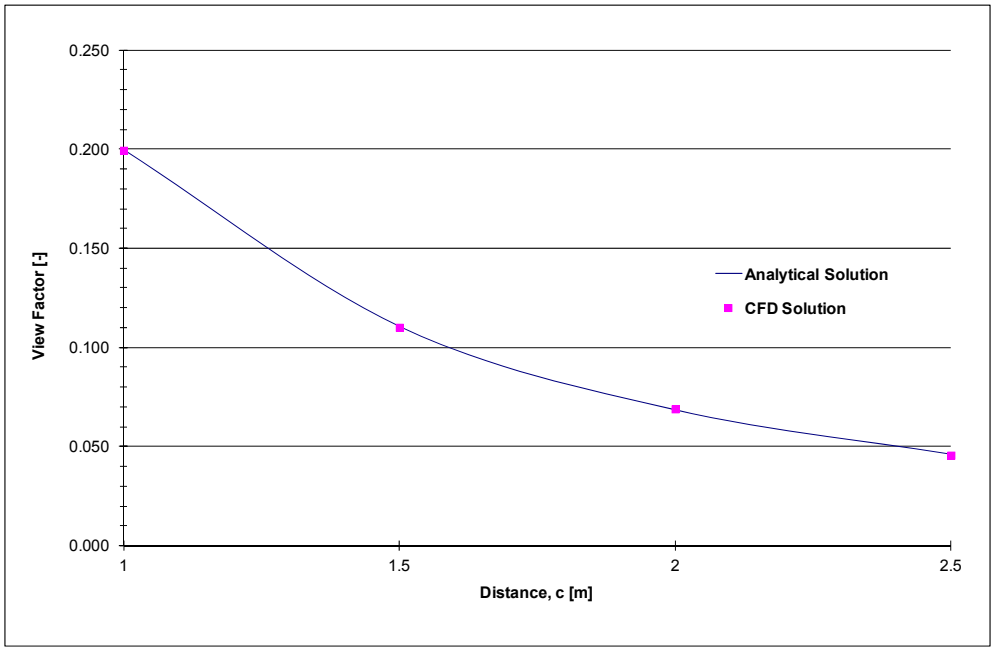

Figure 5-6: Comparison of view factor calculated by analytical solution and CFD simulation for parallel plates.

The results illustrate the fact that as the two plates are held close to each other, they have less opportunity to ‘see’ the remaining surfaces of the domain, and hence radiate mainly to each other. When the distance between the two is increased they have a higher possibility to ‘see’ the surroundings thereby leading to a lower view factor value to the opposing parallel plate.

The CFD simulation results agree very well with the results obtained by the solution of analytical equation. This close agreement verifies the use of the radiation model implemented in ANSYS CFX and helped gain confidence in its use for a geometrical configuration of parallel plates.

5.2.2 Perpendicular plates

Perpendicular plates represents the condition occurring at the junction between floor/ceiling and its adjacent wall in a room. This configuration is of considerable importance when studying the radiant floor or ceiling heating/cooling systems.

The analytical solution for such a situation presented by Siegel and Howell (1992) is given by following equation;

$$F_{1-2} = \frac{1}{\pi b}\left\{\begin{array}{l}\left(b\tan^{-1}\frac{1}{b} + c\tan^{-1}\frac{1}{c} - \sqrt{c^2+b^2}\tan^{-1}\sqrt{\frac{1}{c^2+b^2}}\right) + \\ \frac{1}{4}\ln\left[\left(\frac{(1+b^2)(1+c^2)}{1+b^2+c^2}\right)\left[\frac{b^2(1+b^2+c^2)}{(1+b^2)(b^2+c^2)}\right]^{b^2}\left[\frac{c^2(1+b^2+c^2)}{(1+c^2)(b^2+c^2)}\right]^{c^2}\right]\end{array}\right\} \quad \text{(Eq. 5-10)}$$

where

F_{1-2} is the view factor between plate 1 and 2 and

a, b and c are the room dimensions as shown in Figure 5-7.

The meshed perpendicular plates are shown in Figure 5-7. The comparison of simulated view factors with the ones obtained using the analytical solution is shown in Figure 5-8.

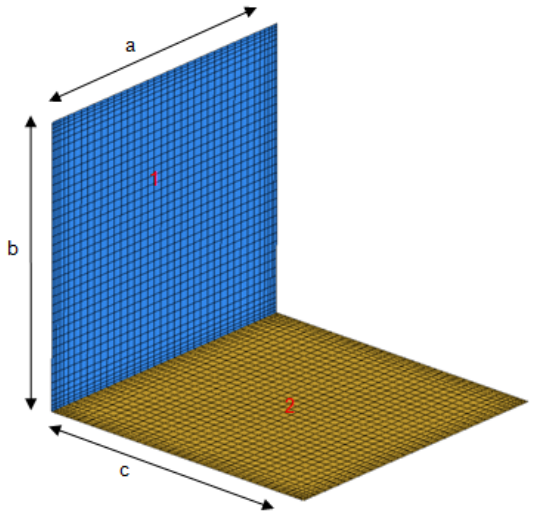

Figure 5-7: Perpendicular walls of a room with dimensions of a [m] * b [m] and c [m].

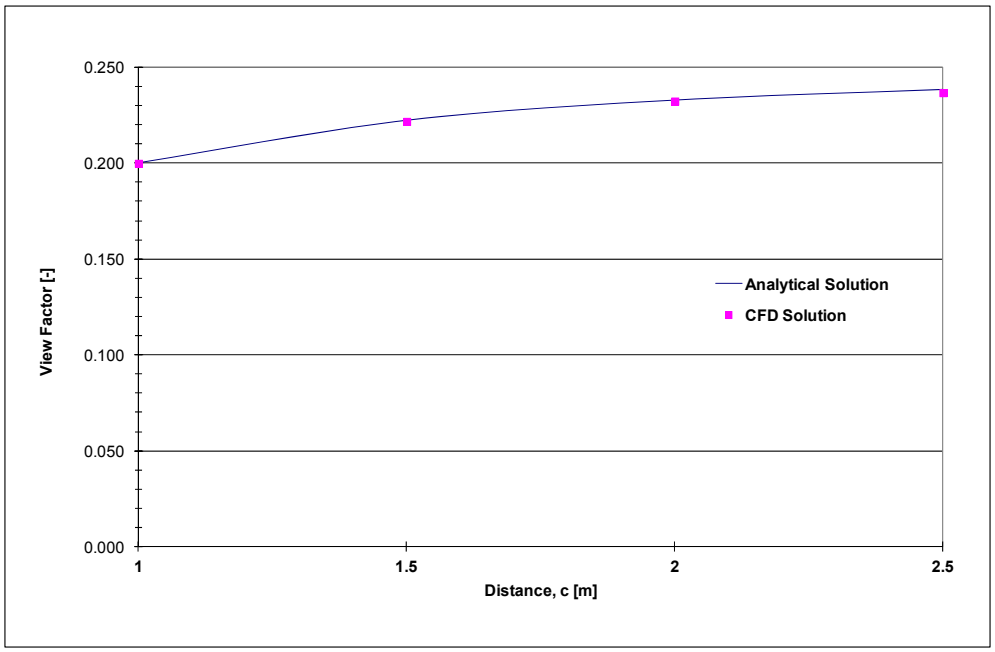

Figure 5-8: Comparison of view factor calculated by analytical solution and CFD simulation for perpendicular plates.

The results show that due to an increase in the length of the floor, the wall would see more of the floor thereby giving a higher view factor value. An increase in the view factor would in turn lead to higher radiant heat transfer to the floor area. The results correspond well with the analytical solution.

5.2.3 Cylinder facing a plate

Human thermal comfort simulation studies often model the human body as a cylinder (Bjørn, 2001). This geometrical configuration therefore uses a cylinder to represent the human body in an enclosed surrounding. A mesh representing the geometrical configuration of a cylinder facing a wall is shown in Figure 5-9.

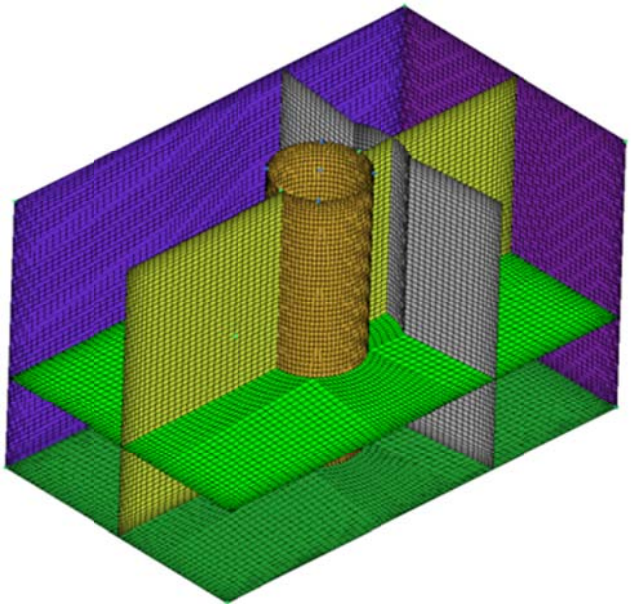

Figure 5-9: Meshed domain showing a cylinder placed in a room.

The analytical solution as presented by Kubaha (Kubaha, 2005) is given below;

$$\varphi_{PC} = \frac{2}{B}\int_{0}^{B/2} f(g)\,dg \qquad \text{(Eq. 5-11)}$$

where

φ_{pc} represents the view factor between the plate and cylinder and

f(g) is given by the co-relation:

$$f(g) = \frac{A}{A^2+g^2} - \frac{A}{\pi\left(A^2+g^2\right)}\left\{\cos^{-1}\left(\frac{Y}{X}\right) - \frac{1}{2C}\left[\begin{array}{l}\sqrt{X^2+4C^2}\cos^{-1}\left(\dfrac{Y}{X\sqrt{A^2+g^2}}\right)\\ +\, y\sin^{-1}\left(\dfrac{1}{\sqrt{A^2+g^2}}\right) - \dfrac{\pi X}{2}\end{array}\right]\right\} \qquad \text{(Eq. 5-12)}$$

where

A = c/r, B = b/r, C = a/r

X = A²+C²+g²-1 and Y = C²-A²-g²+1

The meshed assembly of the vertical plate and a cylinder is shown in Figure 5-10. The comparison of simulated view factors with the ones obtained using Analytical solution is shown in Figure 5-11.

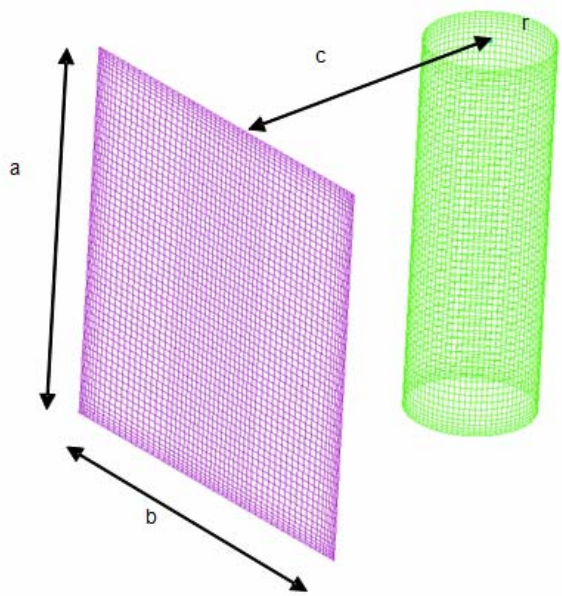

Figure 5-10: A cylinder of radius r [m] and height a [m] is facing a wall of equal height a [m] and width b [m]

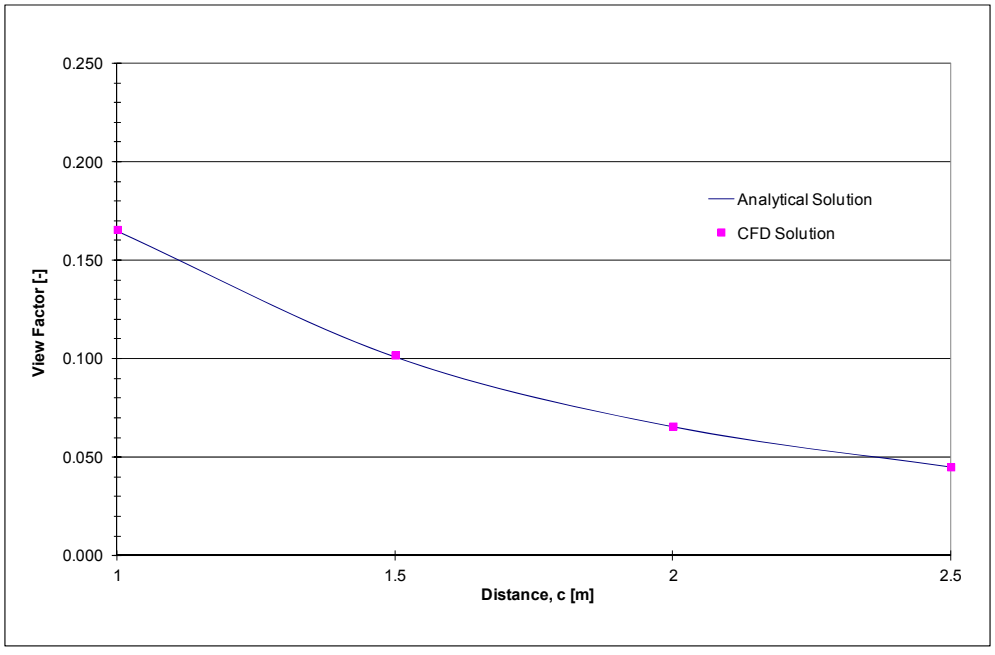

Figure 5-11: Comparison of view factors calculated by analytical solution and CFD for a cylinder facing a wall.

The results show that moving away from the wall the cylinder gets the opportunity to 'see' not only the facing wall but also the surrounding walls (left and right). As a result the view factor for the opposite wall decrease and view factors for the side walls increase. This phenomena would lead to a lower radiation to the opposite parallel wall.

The CFD simulation results agree very well with the results obtained by the solution of analytical equation. This close agreement verifies the use of the radiation model implemented in ANSYS CFX and helped gain confidence in its use for a geometrical configuration of cylinder within rectangular surrounding, a case very often used in indoor climate to estimate the radiative heat loss by a human body to the surroundings.

5.3 Verification using Complex Human Geometry

In order to simulate the human radiative heat transfer phenomena for verification purposes, a bench mark had to be established.

The most prominent work in the field of human thermal comfort is that conducted by Fanger, which is incorporated in many national and international standards on occupant comfort in buildings e.g. ISO 7730 and ASHRAE Standard 55. Fanger applied Stefan Blotzman law to represent the total human thermal radiation exchange as follows:

$$Q = A_{eff} \times \varepsilon \times \sigma\left(T_s{}^4 - T_{MRT}{}^4\right) \qquad \text{(Eq. 5-13)}$$

where

Q is the heat exchanged [W]

A_{eff} is the effective radiation area [m^2]

ε is the emissivity of the human surface [-]

σ is Stefan-Boltzman constant 5.67e−8 [W/m^2K^4]

T_s is the surface temperature of human body (clothed/naked) [K] and

T_{MRT} is the “Mean Radiant Temperature” [K] which in turn is a function of surface radiosities and surface view factors of the surfaces in consideration.

Fanger’s work is based on experimental investigations of the human projected area (the area projected on a plane perpendicular to parallel rays) of standing and sedentary human subjects using photographic techniques.

Based on the projected areas, Fanger devised effective radiation areas (area of the human body that takes part in radiation exchange with the surroundings) as well as view factors between the human body and its surroundings.

The experimental methodology followed by Fanger based the calculation of radiation data on “projected areas of human bodies”. This method leads to inaccuracies caused by errors in calculation of the projected areas of human bodies for the dependent variables i.e. view factors and effective radiation areas.

Following a numerical approach however eliminates any such dependency of order thereby leading to controllable and less error prone results.

For the present research work, the following approach was chosen.

1. Calculation of view factors using the net radiation exchange method for the human body as a whole and comparing it with the experimental results obtained by Fanger.
2. Calculation of the effective radiation area factor, defined as “the ratio between the body areas that takes part in radiation to the total body surface area”, and comparing it with the results obtained by Fanger.
3. Calculation of the projected area factor defined as “the ratio between the projected area and the effective radiation area”, and comparing it with the results obtained by Fanger.

In order to minimize the computational load, various simplifications were employed in the simulation methodology as follows.

- The medium (air) was considered as non-participating medium for radiation heat transfer. This assumption is truly valid in indoor climates with very low optical thickness of the medium.
- The human body was not subdivided into regions as is the case when investigating detailed local thermal comfort, rather it was considered as a whole.
- Flow and turbulence equations were not solved in parallel to radiation equations.
- All surfaces were assumed to be gray diffuse.
- Surfaces of non-interest were assumed to be black bodies (emission = absorption = 1). The surface temperatures were set to 0 Kelvin in order to minimize the interference effects.

As mentioned previously the verification of human radiative heat transfer simulation is carried out for the factors that affect the radiative heat transfer, the next sub-sections explain these factors and present the results of the verification process.

5.3.1 View Factors

View factor is the fraction of radiation emitted by a surface and intercepted by another surface. Fanger calculated and plotted the view factors between a person and the surroundings (vertical and horizontal rectangular surfaces) on the basis of mean projected area factor values for standing and sedentary poses for different orientations. He calculated the view factors and plotted them against the ratio of the height of the sub sectioned wall and the distance from the person's centre to the wall.

The human body geometry was modelled in detail using the software Poser 6.0 (Poser V6, 2013) and meshed by using ANSYS ICEM CFD. An example of the geometry and mesh generated for the geometry is shown in Figure 5-12 (a) and (b) respectively.

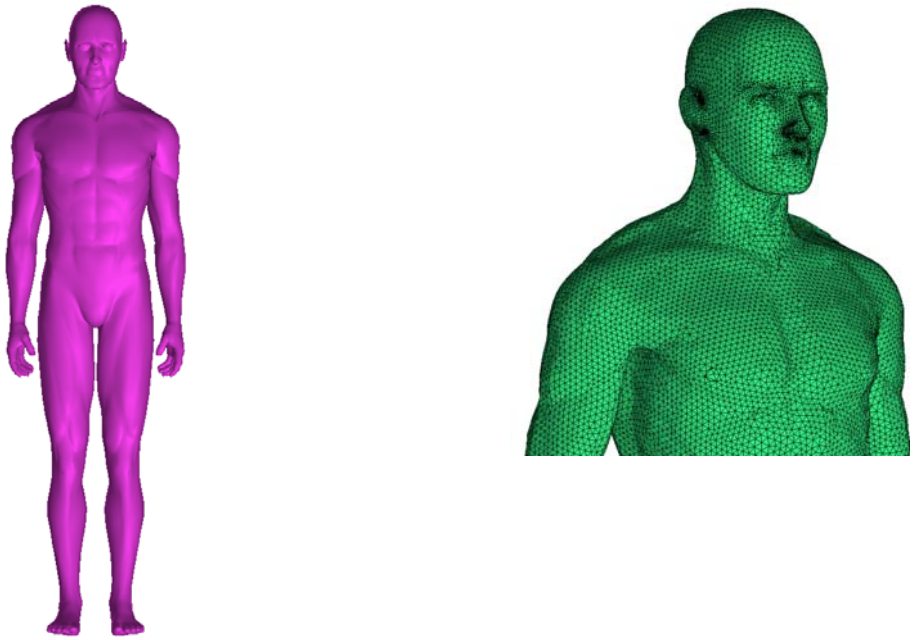

(a) (b)

Figure 5-12: (a) Geometry created using modelling software Poser, (b) meshed geometry using ANSYS ICEM CFD.

The height and weight of the detailed human male model is taken to be 1.785 m and 82.4 kg respectively representing the average height and weight of a German man (Institut für Rationelle Psychologie, 2007). Using the Du Bois formula (DuBois & Du Bois, 1989), the body surface area is calculated to be 2.01 m^2 The formula for body surface area according to Du Bois is given as follows:

$$BSA = 0.007184 \times W^{0.425} \times H^{0.725} \quad \text{(Eq. 5-14)}$$

Where

BSA is the body surface area in m^2

W is the weight of the human subject in kg and

H is the height of the human subject in cm

The modelled human body geometry of surface area of 2.01 m^2 is enclosed by a rectangular space as shown in Figure 5-13. The body is located such that its centre is at 3 m distance from the front wall considering the lower part of the body to be located 1 m below the wall's lower edge. The length and height of the walls were then varied to get the dimensionless ratios a/c and b/c as shown in Figure 5-14.

The above mentioned positioning of the human body and geometrical configuration of the surrounding was necessary on one hand to be comparable to the experimental setup of Fanger and on the other hand to have a flexible simulation setup enabling multiple simulations without having to perform tedious geometrical and mesh changes for each run.

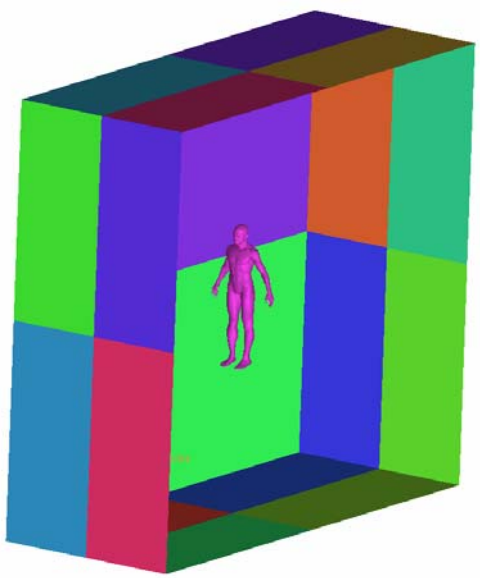

Figure 5-13: Human body in an enclosed surrounding.

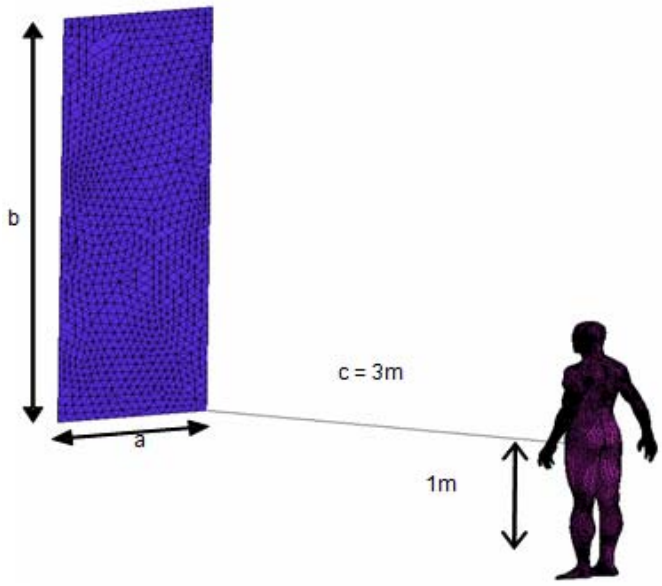

Figure 5-14: Geometrical setup for view factor calculations.

The simulations were conducted for different a/c and b/c ratios and were compared with the results provided by the experimental work of Fanger. The comparison between the simulated and experimental results are shown in Figure 5-15. The simulation results showed similar trends in view factors as a function of b/c ration for both the simulations as well as the experimental work by Fanger. Even though a very good agreement with the experimental work of Fanger is seen for lower a/c ratio, the

results of CFD simulations for higher a/c ratios are found to be on the lower side compared to the experimental results. This trend indicates that the view factors estimated by Fanger over-predict the heat transfer to the opposite walls when their width to distance ratio a/c increases. This deviation is more pronounced for a/c ratio of 5.

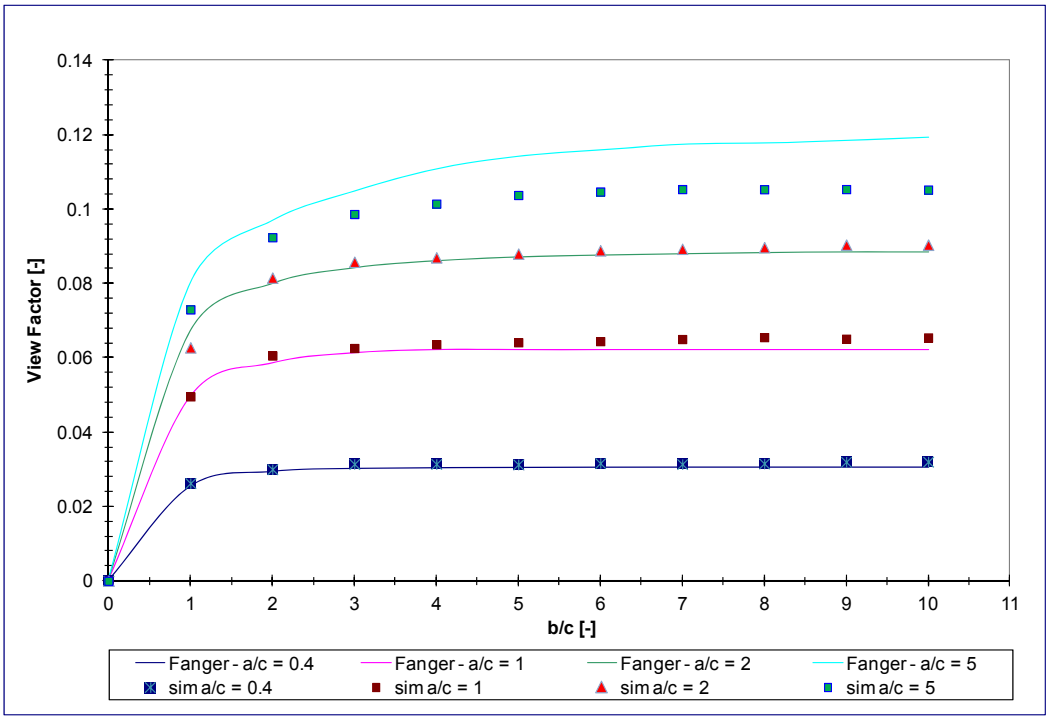

Figure 5-15: Comparison of View Factors calculated by Fanger and CFD Simulation.

This difference is thought to be attributed to the limitation in the way the view factors are experimentally calculated by Fanger during the experiments. The larger the room dimensions, the larger the experimental error using the photometry method (Fanger, 1972) becomes. Present work highlights this discrepancy. Estimating the view factors for human thermal comfort calculation using Fanger's experiments for very large indoor spaces would mean an over-estimation of the radiation heat transfer to the opposite walls.

It is important to mention here that altering the a/c and b/c ratios led to changes in domain size. In order to retain a good quality mesh, cells had to be increased with an increase in domain size. This resulted in number of mesh cells varying from a minimum of 500,000 (for the smallest a/c and b/c ratios) to a maximum of approx. 6 million (for the largest a/c and b/c ratios).

5.3.2 Effective Radiation Area Factor

Effective radiation area is defined as the area of the body that effectively takes part in radiation heat exchange. The effective area factor is a ratio between this effective area and the total body surface area.

Mathematically,

$$f_{eff} = \frac{A_{eff}}{A_s} \qquad \text{(Eq. 5-15)}$$

where A_{eff} is a function of location and posture (also pertaining to the view factor) and A_s is the total surface area of the human body (including clothing)

To investigate the dependency of posture on effective radiation area factor, three different standing postures were modelled as shown in Figure 5-16.

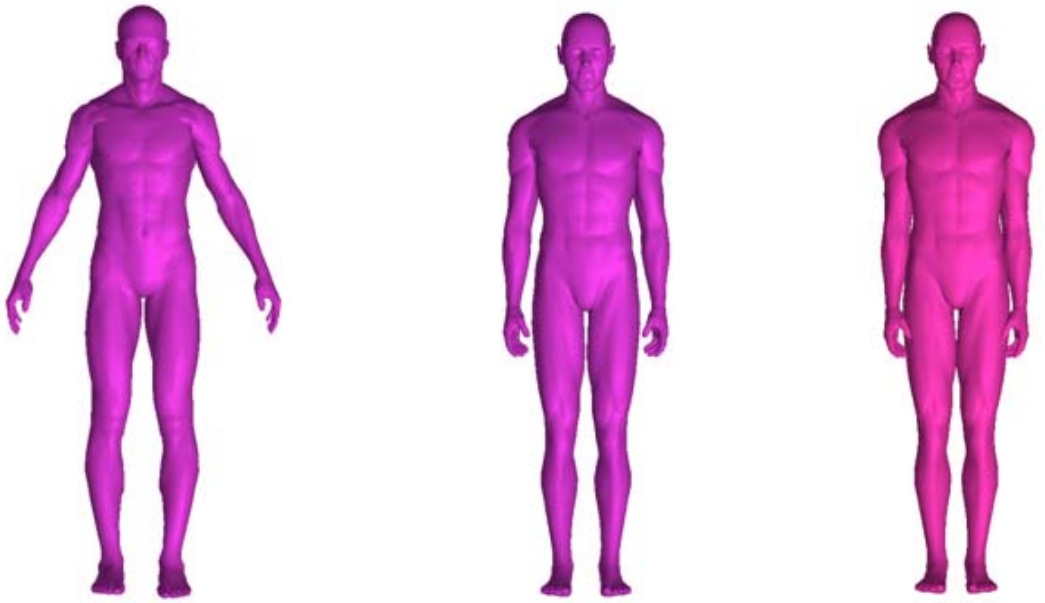

P1 P2 P3

Figure 5-16: Different postures used in CFD simulations for investigated the effective radiation area factor

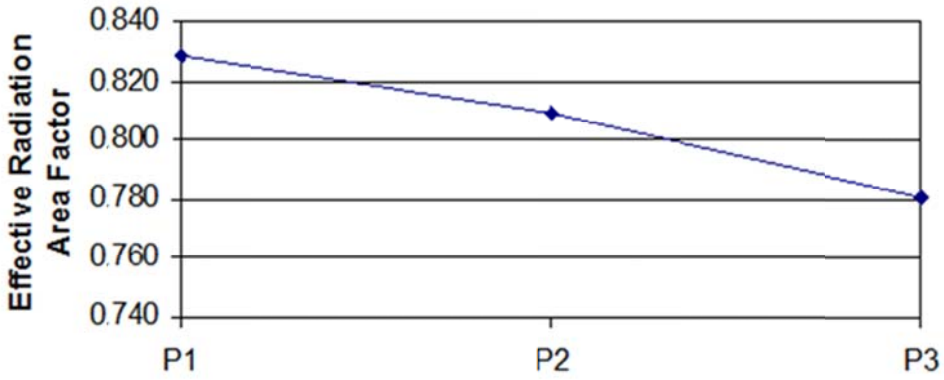

Figure 5-17: Simulation results of the variation in effective radiation area factor for various postures.

Fanger calculated an effective radiation area factor of 0.725 ± 0.013 for a standing person ignoring the effects of sex, surface area, clothing, postures and the convexities of the human body shape. In contrast to Fanger, the results of this numerical simulation study (see Figure 5-17) indicate that even a small change in posture can significantly influence the effective radiation area factor, namely from about 13% for posture P1 to about 7% for posture 3 (compared to Fanger's A_{eff} = 0.725).

5.3.3 Projected Area Factor

Projected area is a term used mainly in case of directional rays. It is defined as the area projected on a plane perpendicular to the rays.

Fanger calculated the projected area for human bodies experimentally thereby deducing a dimensionless factor called "projected area factor" defined mathematically by;

$$f_p = \frac{A_p}{A_{eff}} \qquad \text{(Eq. 5-16)}$$

Depending upon the position of the human body in space, the direction of rays is defined by an azimuth angle α and an altitude angle β as shown in Figure 5-18.

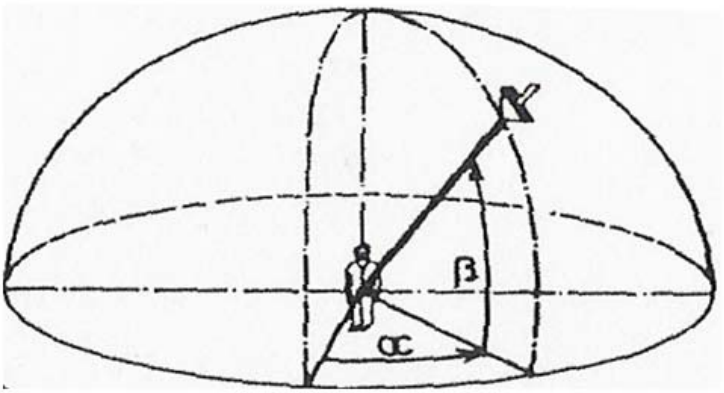

Figure 5-18: Explanation of azimuth (α) and altitude (β) angles (Fanger, 1972).

CFD simulation results of projected area factor simulations are shown qualitatively for the human body facing direct radiation (Figure 5-19). The shadow is seen to be projected on a plane perpendicular to the direction of solar radiation (see Figure 5-19 and Figure 5-20).

Due to the differences in the effective radiation area factors of the human body between the models used in this study and subjects in the Fanger experiments (stiff postures), it is not appropriate to make a direct comparison of simulated and experimentally measured projected area factors.

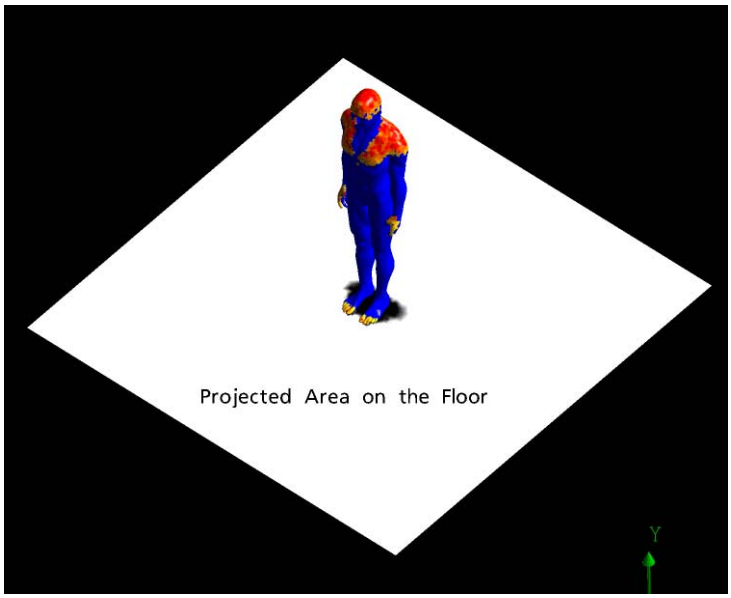

Figure 5-19: Qualitative result of simulation showing the projected radiation area on the floor.

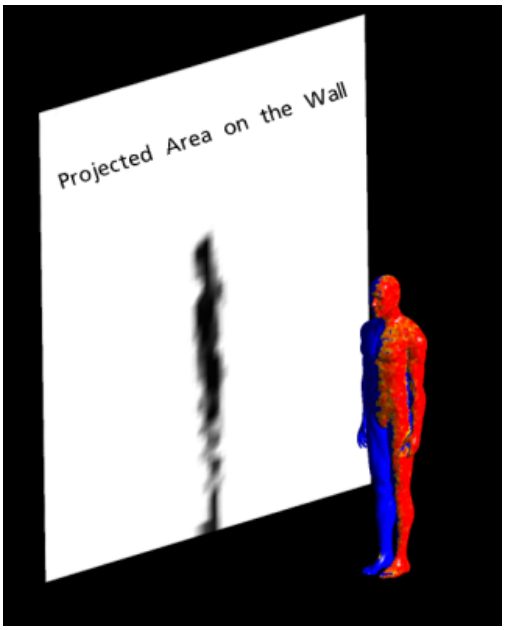

Figure 5-20: Qualitative result of simulation showing the projected radiation area on the wall.

In order to enable a comparison, the predicted projected area factors were normalised by dividing the predicted values by factor 0.725 which was the effective area factor of Fanger's subjects.

The comparison is presented for β = 90° and β = 0° in for different azimuth angles is shown in Figure 5-21.

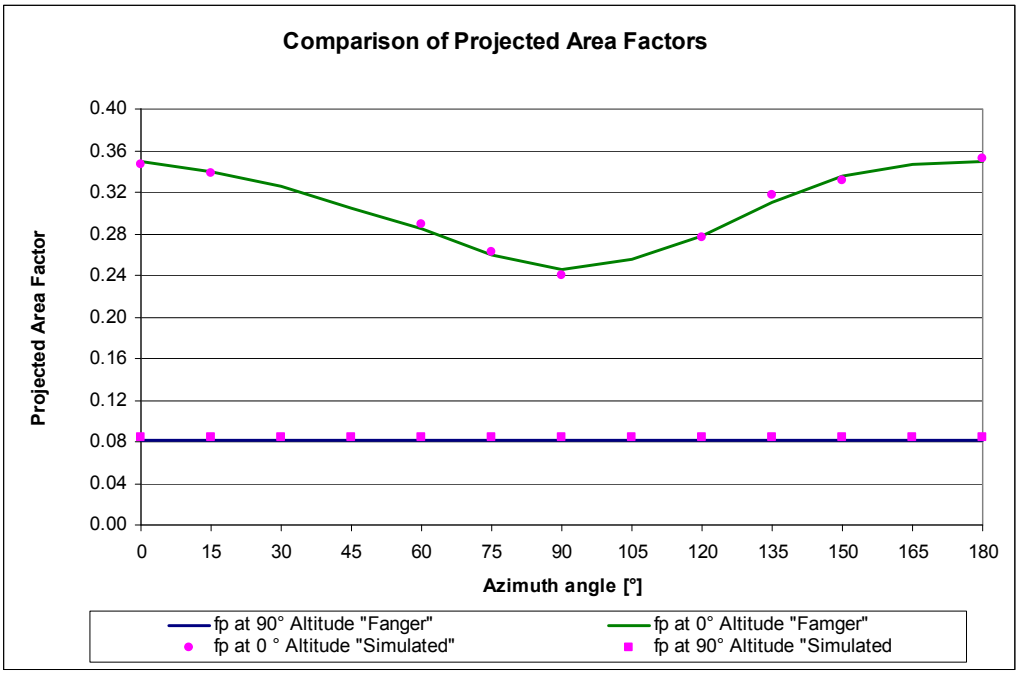

Figure 5-21: Comparison between projected area factors as obtained by Fanger and as computed by detailed CFD simulations for altitude angles of 0° and 90°.

For the case of short wave radiation (directional radiation flux), the normalized projected area factors obtained using numerical simulations showed close agreement with data obtained experimentally by Fanger. The verification of radiation models in ANSYS CFX show that a directional radiation flux modelling e.g. in the case of direct light sources, is only possible by using the Monte Carlo radiation model. For indoor conditions with no direct fluxes present, the use of DTRM gives sufficient accuracy for practical purposes.

5.4 Convective Heat and Mass Transfer Modelling

Convection phenomena in indoor climates can be natural, forced or mix of both. With forced convection, the flow conditions are mostly dominated by high Reynolds number and can be easily addressed using CFD simulations with little emphasize on mesh generation and independency studies. In forced convective flows, the energy and momentum equation are coupled in such a way that the momentum affects the energy equation (advection term in energy equation, see chapter 4 for explanation of different terms). The mixed or natural convection processes on the other hand demand great care as the flow is mainly driven by buoyancy. In buoyant flows, the density gradient affects the momentum equations and vice versa thereby leading to a two-way coupling. Solving ideal gas law equations to explore the convective heat transfer phenomena would mean that the density variation is solved as a function of temperature and pressure. This approach is numerically expensive and can be replaced efficiently using the Boussinesq approximation. Using the Boussinesq approximation for modelling buoyancy is a good compromise between representation of the physics and numerical stability. The Boussinesq approximation avoids the coupling between local temperature, pressure and density, instead it applies a local gravitational body force on the fluid, which is mainly a function of the fluid's thermal expansion and the local temperature difference with reference to a datum. It is important to note that this approximation holds good for normal indoor climates as temperature differences are low. The Boussinesq approximation should not be used in environments involving high temperature gradients. The upper limit of this temperature gradient is recommended to be 30 K (Etheridge & Sandberg, 1996).

When the fluid flows over a surface held at a different temperature than that of the fluid itself, it accepts or rejects heat to/from the fluid due to the thermal gradient. This results in the transfer of heat by convection. Considering the heat and mass transfer analogy (Incropera, 2006), the same statement is true for a surface presenting a concentration gradient with the surrounding fluid leading to transfer of mass by convection (e.g. water vapour transferring to air in case of respiration, sweating etc.).

The verification studies for fluid flow modelling in this chapter focus on comparison of natural convective heat transfer coefficients using simulations with those obtained using experimental work for simple geometries (vertical plate and cylinder). This verification study extends to complex human body geometry and highlights the temperature and flow fields predicted by different turbulence models implemented in ANSYS CFX. The results are then compared with previous numerical and experimental work.

Prior to the modelling of convective heat transfer, it is important to get an understanding of different physical properties that affect the convective heat transfer. Different dimensionless numbers describe the effects of the physical properties of fluids and are commonly used in heat transfer analysis. From a building designer's point of view, it is very important to have a rough estimate of these numbers for a given flow phenomena under investigation. The most important of these dimensionless numbers in terms of natural and forced convection are described below.

Reynolds number (Re): Describes the ratio of inertial forces to viscous forces.

Mathematically,

$$\mathrm{Re} = \frac{\rho \times \upsilon \times L}{\mu} \qquad \text{(Eq. 5-17)}$$

where

ρ is the fluid density in [kg/m^3]

υ is the kinematic viscosity of the fluid in [m^2/s]

L is the characteristic length in [m] and

μ is the dynamic viscosity in [kg/m-s].

Prandtl number (Pr): Describes the ratio of momentum diffusivity to thermal diffusivity.

Mathematically,

$$\mathrm{Pr} = \frac{C_p \times \mu}{k} \qquad \text{(Eq. 5-18)}$$

where

C_p is the specific heat of the fluid at constant pressure

μ is the dynamic viscosity of the fluid in [kg/m-s] and

k is the thermal conductivity of the fluid in [W/m-K].

Nusselt number (Nu): Describes the ratio of the convective and conductive heat transfer rates.

Mathematically,

$$\mathrm{Nu} = \frac{h_c \times L}{k} \qquad \text{(Eq. 5-19)}$$

where

h_c is the convective heat transfer coefficient in [W/m^{2}K]

L is the characteristic length in [m] and

k is the thermal conductivity of the fluid in [W/m-K].

Grashoff number (Gr): Describes the ratio of buoyancy to viscous forces.

Mathematically,

$$\mathrm{Gr} = \frac{g \times \beta \times (T_s - T_f) \times L^3}{\upsilon^3} \qquad \text{(Eq. 5-20)}$$

where

g is the acceleration due to gravity i.e. 9.81 [m/s^2]

β is the thermal expansion coefficient in [1/K]

T_s and T_f are the surface and film temperature respectively in [K]

L is the characteristic length in [m], and

υ is the kinematic viscosity of the fluid in [m^2/s].

Rayleigh number (Ra): Describes the combined effect of buoyancy, viscous and diffusive forces.

Mathematically,

$$\mathrm{Ra} = \mathrm{Gr} \times \mathrm{Pr} \qquad \text{(Eq. 5-21)}$$

where

G_r is the Grashoff`s number and

P_r is the Prandtl number

Richardson number (Ri): Describes the strength of natural to forced convection.

Mathematically,

$$\mathrm{Ri} = \frac{Gr}{Re^2} \qquad \text{(Eq. 5-22)}$$

where

Gr is the Grashoff`s number and

Re is the Reynold`s number

It has been experimentally noticed that for Ri < 0.1 the natural convection effects are negligible and for Ri > 10 the forced convection effects are negligible. In between 0.1 to 10 both natural and forced convection effects are non-negligible.

Schmidt number (Sc): Describes the ratio between momentum and mass diffusivities.

Mathematically,

$$\mathrm{Sc} = \frac{\upsilon}{\mathrm{D_{AB}}} \qquad \text{(Eq. 5-23)}$$

where

υ is the kinematic viscosity of the fluid in [m^2/s] and

D_{AB} is the binary mass diffusion coefficient in [m^2/s] (mixture property)

Lewis number (Le): Describes the ratio between thermal and mass diffusivities.

Mathematically,

$$\mathrm{Le} = \frac{\alpha}{D_{AB}} \qquad \text{(Eq. 5-24)}$$

where

α is the thermal diffusivity of the fluid in [m^2/s] and

D_{AB} is the binary mass diffusion coefficient in [m^2/s] (mixture property)

Sherwood number (Sh): Describes the concentration gradient at the surface.

Mathematically,

$$\mathrm{Sh} = \frac{h_m \times L}{D_{AB}} \qquad \text{(Eq. 5-25)}$$

where

h_m is the mass transfer coefficient in [m/s]

L is the characteristic length and

D_{AB} is the binary mass diffusion coefficient in [m^2/s] (mixture property)

From equation Eq. 5-19, the convective heat transfer coefficient can be calculated as:

$$h_c = \frac{\mathrm{Nu} \times k}{L} \qquad \text{(Eq. 5-26)}$$

where

h_c is the heat transfer coefficient in [W/m^2K]

Nu is the Nusselt`s number [-]

k is the thermal conductivity of the fluid in [W/m-K] and

L is the characteristic length in [m]

According to Newton’s law of cooling, the convective heat flux is proportional to the difference between the surface and fluid temperature.

Mathematically,

$$q'' = h_c(T_s - T_\infty) \quad \text{(Eq. 5-27)}$$

Where

q'' is the convective heat flux [W/m^2]

T_s is the surface temperature in [K]

T_∞ is the fluid temperature in [K] and

h_c is the convective heat transfer coefficient in [W/m^{2}K]

The convective heat transfer coefficient is defined as the constant of proportionality in the Newton's law of cooling (Incropera, 2006). The heat transfer coefficient appearing as a constant of proportionality in the Newton's law of cooling is a quantitative characteristic of convective heat transfer between a fluid flowing over a solid surface.

A similar quantitative characteristic, h_m can be found using the mass and heat transfer analogy by employing the dimensionless Sherwood (Sh) , Lewis (Le), Prandtl (Pr) and Schmidt numbers (Sc) .The correlation describing the mass transfer coefficient in dependence to the heat transfer coefficient is given by the following equation;

$$\frac{h_c}{h_m} = kD_{AB} \times {L_e}^{1-n} \quad \text{(Eq. 5-28)}$$

where

h_c is the convective heat transfer coefficient in [W/m^{2}K]

h_m is the mass transfer coefficient in [m/s]

L_e is the characteristic length in [m]

D_{AB} is the binary mass diffusion coefficient in [m^2/s] (mixture property)

k is the thermal conductivity of the fluid in [W/m-K] and

n is constant with a value of 1/3 in most applications (Incropera, 2006)

5.5 Verification using Simple Geometrical Configuration

For analytical calculation of heat transfer coefficients, equation 5-25 is used. A number of different correlations for estimating Nusselt number exist for fluid flow passing over simple geometries such as flat plate, cylinders, spheres etc. (see Incropera, 2006 for a list of different correlations). These correlations are mainly based on experimental investigations. For the present verification study, vertical flat plate and horizontal cylinder configurations are used.

All the simulations were carried out on a Intel Xenon Cluster using a double precision ANSYS CFX solver. Each of the simulation was run on 1 computational node of the cluster with 20 cores equipped with 2.4 GHz processors a RAM of 2 GB per core. The simulations were set to stop when the residual for all the flow equations fall below 1e-4.

5.5.1 Natural Convection over a Vertical Flat Plate

The heat transfer coefficients on a vertical plate of width (w) and height (h) at an isothermal temperature placed in quiescent air (at a temperature different from that of the plate) can be calculated by using empirical correlation proposed by Churchill and Chu (1975).

$$\mathrm{Nu} = \left\{ 0.825 + \frac{(0.387 \times \mathrm{Ra}^{1/6})}{\left[1 + \left(\frac{0.492}{\mathrm{Pr}}\right)^{9/16}\right]^{8/27}} \right\}^2 \qquad \text{(Eq. 5-29)}$$

For a vertical plate immersed in air at 20°C (ambient conditions), heat transfer coefficient were analytically calculated for the temperature difference "ΔT" existing between the surrounding air and the plate which was kept at temperatures of 50°C, 40°C and 30°C. The Nusselt number and the relevant Grashof, Rayleigh and Prandtl numbers were calculated based on the equations mentioned above are shown in

Table 5-1.

Table 5-1: Input values for calculating analytically the heat transfer coefficient from a vertical flat plate

Plate Temperature [°C]	ΔT [K]	Pr [-]	Ra [-]	Gr [-]
50	30	0.716	3.05e9	4.25e9
40	20	0.716	2.03e9	2.84e9
30	10	0.716	1.02e9	1.42e9

An example of the model geometry with a coarse mesh near to the vertical plate with different mesh refinement at the plate surface (with and without prism layers) are shown in Figure 5-22 (a) - (d). Due to the fact that the convective flow simulations involving complex human geometries cannot be meshed using the block structuring methodology in ANSYS ICEM CFD within a realistic amount of time for practical applications, the tetrahedral meshing technique with/without prism layers is used for simple cases in order to remain consequent.

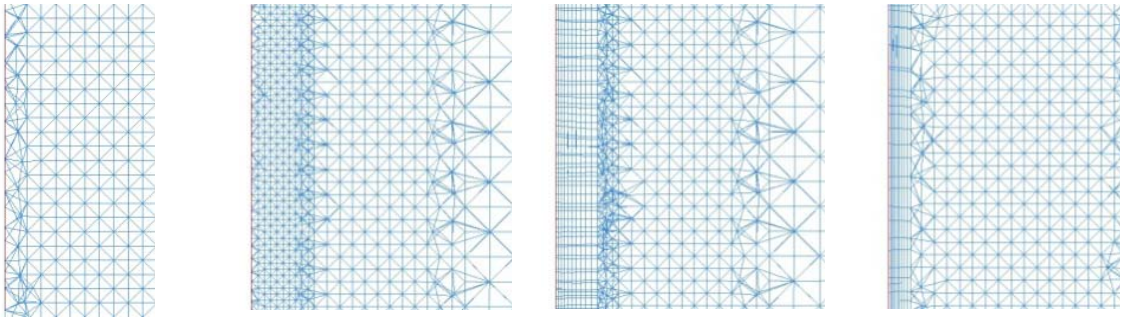

(a) without refinement and prism layers

(b) with refinement, without prism layers

(c) with refinement and prism layers

(d) without refinement, with prism layers

Figure 5-22: Different meshes generated using ANSYS ICEM CFD for the vertical flat plate configuration

The vertical flat plate configuration was employed to conduct a mesh independency test and investigate the effect of mesh and y+ on the heat transfer coefficients. (See details about meshing, y+ etc in chapter 4). The coarse mesh had no prism layers nor any local refinement at the plate. The results of the mesh independency study along with the required clock run time is given in Table 5-2.

Table 5-2: Results of mesh independency study using vertical flat plate

Mesh Type	Local refinement	Prism layers [-]	y+ value [-]	Heat Transfer Coefficient [W/m^{2}K]		Number of cells [M]	Run Time [s]
				Simulation	Analytical		
Coarse	no	0	22.8	1.58	4.54	0.17	285
Coarse	yes	0	14.8	3.1		0.35	434
Coarse	yes	10	13	3.58		0.39	226
Coarse	no	10	13	2.78		0.24	151
medium	no	0	19.4	1.72		0.38	433
medium	yes	0	11.88	3.2		1.39	864
medium	yes	15	2.8	4.6		1.47	630
medium	no	15	2.8	3.6		1.28	327
fine	no	0	17.6	2.4		1.23	818
fine	yes	0	11.09	3.8		4.41	1650
fine	yes	20	1.9	4.97		4.63	1626
fine	no	20	1.9	3.7		1.73	725

While conducting the study, the mesh quality (see chapter 4) was adjusted such that no mesh cell quality was below 0.2. For mesh independency test, simulations were carried out using ANSYS CFX v 14.5 and only SST turbulence model was considered. Once the mesh parameters were chosen, RNG k-ε and SST turbulence models were employed to conduct the verification study (see chapter 4 for an overview of different turbulence models).

Buoyancy was modelled using the Boussinesq approximation. It is important to note that this approximation holds good for normal indoor climates as temperature

differences are small. Boussinesq approximation should not be used in environments involving high temperature gradients (e.g. fire scenarios, outdoor conditions with direct solar radiation etc.). The upper limit of this temperature gradient is recommended to be 30 K by Etheridge & Sandberg (1996) whereas Kato and his co-workers (Kato, et al., 1993) reported, the temperature gradient to be acceptable up to a temperature differences of 43 K.

The results of the mesh dependency study showed that with an increase in mesh size and a decrease in y+ value, there is a general tendency of improvement in the simulation results. It is however important to note that even though the y+ value remain constant, there is a large relative change in heat transfer coefficient values showing the impact and importance of local mesh refinement.

For further verification studies, a medium mesh having the following parameters was chosen:

Number of prism layers = 15

First prism cell height = 0.001 m

Hotplate surface cell size = 0.0025 m

The model boundaries are shown in Figure 5-23. The hot plate was modelled as a solid wall with a constant temperature whereas the walls on the top and bottom of the plate (in plane of the plate) are given symmetry boundary conditions (see chapter 4 for details). The remaining boundaries are modelled as opening boundaries at 20°C ambient temperature and 0 Pa relative pressure.

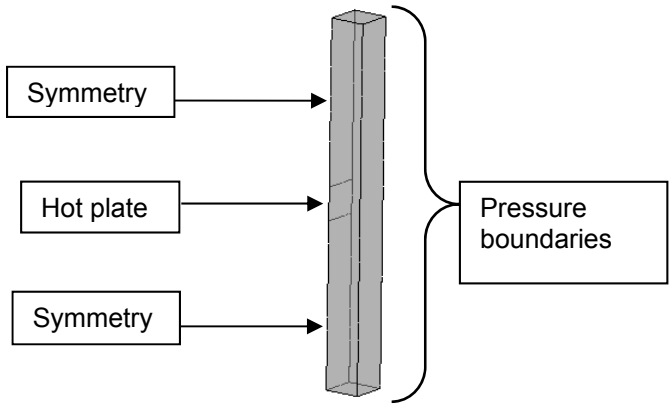

Figure 5-23: ANSYS CFX model employed for verification study of natural convective flow over a flat vertical plate

The results of the comparison between simulated and analytical solutions of heat transfer coefficient on a flat vertical plate for natural convective flow is shown in Figure 5-24. The abscisa represents the temperature difference between the plate and surrounding and the ordinate shows the heat transfer coefficient calculated at the plate.

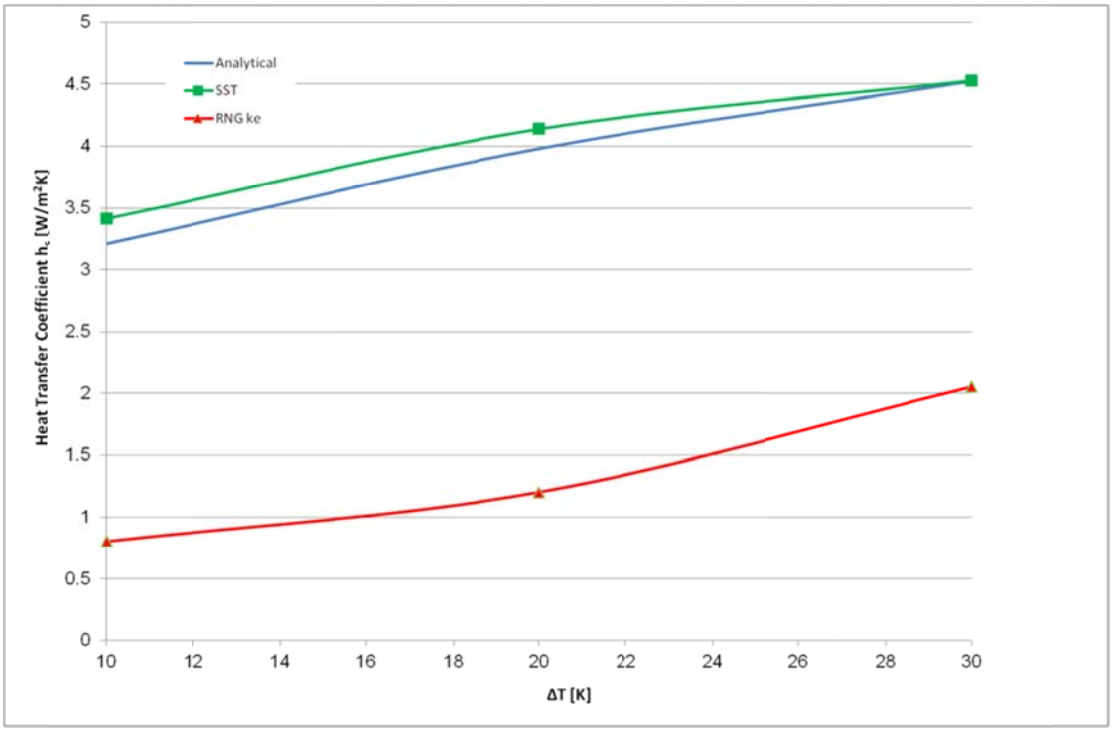

Figure 5-24: Results of verification study for natural convective flow over a flat vertical plate.

The results show that for a pure natural convective flow case, the SST turbulence model predicts the heat transfer much better than the RNG k-ε turbulence model. With higher thermal forces (temperature gradients between the surface and surrounding air temperature), the SST turbulence model predicts results closer to the analytical/empirical solution and starts to deviate from the analytical solution as the magnitude of the thermal forces decrease. For the vertical flat plate natural convection flow, the SST turbulence model over-predicted the heat transfer coefficient when compared to the referenced values.

5.5.2 Natural Convection over a Cylinder

The average heat transfer coefficients over the circumference of a horizontal cylinder of a constant diameter "D" and length "L" can be empirically calculated using the co-relation proposed by Churchill and Chu (1975);

$$\mathrm{Nu} = \left\{ 0.60 + \frac{(0.387 \times \mathrm{Ra}^{1/6})}{\left[1 + \left(\frac{0.559}{\mathrm{Pr}}\right)^{9/16}\right]^{8/27}} \right\}^2 \qquad \text{(Eq. 5-30)}$$

For a horizontally immersed cylinder in air at 20°C (ambient conditions), heat transfer coefficient were analytically calculated for the temperature difference "ΔT" existing between the surrounding air and the cylinder which was kept at temperatures of 50°C, 40°C and 30°C. The Nusselt number and the relevant Grashof, Rayleigh and Prandtl numbers were calculated based on the equations shown previously. The calculated values are given in Table 5-3.

Table 5-3: Input values for calculating analytically the heat transfer coefficient for horizontal cylinder

Cylinder Temperature [°C]	ΔT [K]	Pr [-]	Ra [-]	Gr [-]
50	30	0.716	3.81e8	5.32e8
40	20	0.716	2.54e8	3.54e8
30	10	0.716	1.27e8	1.77e8

The 3-D CFD model used for the verification study is shown in Figure 5-25 whereas the mesh details near to the modelled cylinder are shown in Figure 5-26. (a)-(d).

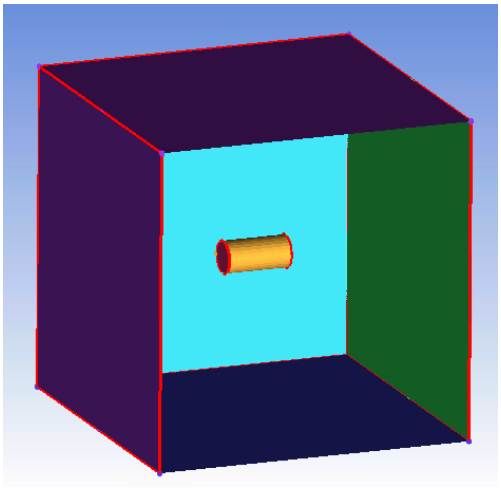

Figure 5-25: 3-D geometrical model used for verification of natural convective flow over a cylinder

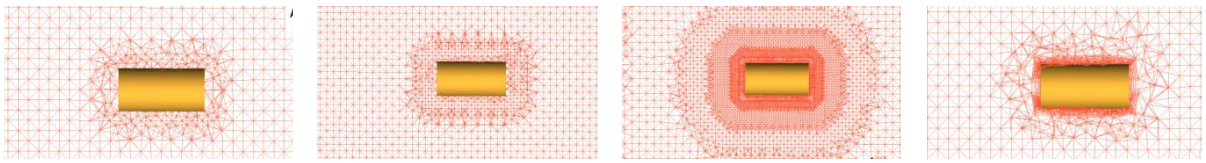

(a)	(b)	(c)	(d)
without refinement and prism layers	with refinement, without prism layers	with refinement and prism layers	without refinement, with prism layers

Figure 5-26: 3-D geometrical model used for verification of natural convective flow over a cylinder

Similar to the mesh independency study of vertical plate, the model was run for different meshes until a mesh independency was observed. The surface heat transfer coefficient was set as the variable for results comparison. The results of the mesh independency study is shown in Table 5-4.

All the meshes were checked for the mesh quality as it has a very strong impact on the eminence of the results. As a guideline, a minimum mesh quality of 0.2 is recommended for convection flow studies in the areas where mass transfer effects are of prime importance.

Table 5-4: Results of mesh independency study using horizontal cylinder

Mesh Type	Local refinement	Prism layers [-]	y+ value [-]	Heat Transfer Coefficient [W/m^{2}K]		Number of cells [M]	Run Time [s]
				Simulation	Analytical		
Coarse	no	0	27	1.4	4.47	0.182	310
Coarse	yes	0	15	3.01		0.6	450
Coarse	yes	10	12	3.4		0.72	380
Coarse	no	10	12	2.8		0.58	340
medium	no	0	18	1.8		0.4	504
medium	yes	0	11	3.2		1.5	931
medium	yes	15	2.5	4.51		1.8	870
medium	no	15	2.5	4.1		1.4	820
fine	no	0	14	2.52		1.32	893
fine	yes	0	10	4.01		4.1	1800
fine	yes	20	1.8	4.97		4.63	1710
fine	no	20	1.9	3.7		1.73	980

The mesh sensitivity test shows a trend similar to that seen in the vertical plate study thereby confirming the importance of local refinement. It is also noted that to reach the same convergence level, the run time decreased with a mesh having prism layers. This is due to the fact that tetrahedral type mesh cells due to their shape, require more numerical load to minimize the discretization errors specially in regions of high gradients compared to regular (or near to regular) shaped prism layer elements (hexahedral).

Considering the results of the mesh independency study, further verification studies for convective flow over a cylinder, using a medium mesh with the following parameters was used:

Number of prism layers = 15

First prism cell height = 0.001 m

Hotplate surface cell size = 0.0025 m

All the boundaries were modelled as opening boundary conditions with 0 pressure. The thermal buoyancy was modelled using Boussinesq approximation. The computational resources as well as the convergence criteria was kept the same as that in vertical plate verification study.

The results of the comparison between simulated and analytical solutions of heat transfer coefficient over the surface of a cylinder is shown in Figure 5-27. The abscisa represent the temperature difference between the plate and surrounding and ordinate shows the area averaged heat transfer coefficient calculated on the cylinder surface.

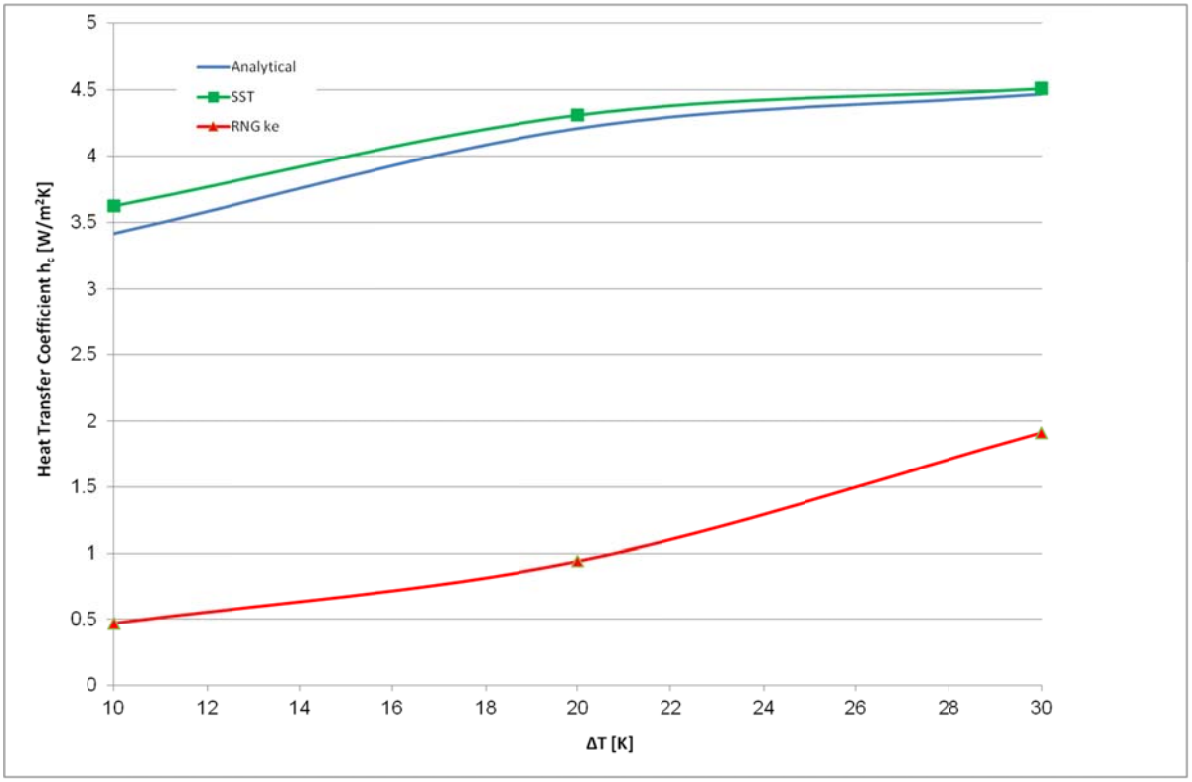

Figure 5-27: Results of verification study for natural convection flow over a cylinder

Similar to the case of convective flow over a vertical plate, the SST turbulence model predicts results closer to the analytical/empirical solution with high driving forces (thermal forces) being present in the considered system. The SST model shows again the tendency to slightly over-predict the heat transfer coefficients for the natural convective flow over a cylinder in comparison to the referenced values.

5.6 Verification using Complex Human Geometry

In the present research work, the benchmark case for verifying the heat transfer modelling capability of ANSYS CFX for complex geometries is taken from the work done by Sørensen and Voigt (2003). The chosen benchmark compares its results with published work and measurements by particle image velocity (PIV). One of the major reasons for considering the work from Sørensen and Voigt as benchmark was the use of detailed 3D CSP geometry which was an exact replica of the experimental thermal manikin.

5.6.1 Model and mesh generation

The CSP model is a female manikin originally manufactured by PT.Teknik, Denmark (P T Teknik, 2016). The geometrical model for CFD calculations is used in a number of previous studies used for investigation of indoor human thermal comfort, air pollution and respiration.

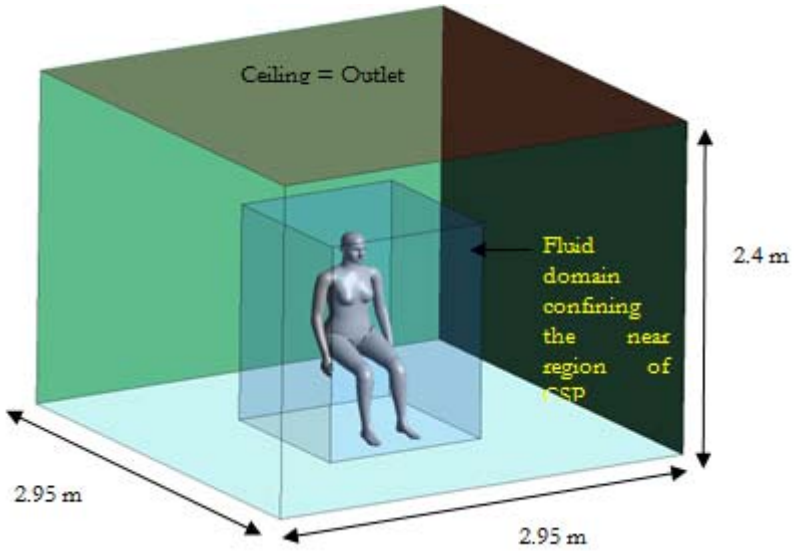

Figure 5-28: Geometrical model used for verification of natural convective flow over a complex human body shape.

The geometrical setup consists of the CSP placed in the centre of a rectangular shaped room 2.95 [m] *2.95 [m] * 2.4 [m] (L*B*H) as shown in Figure 5-28. The complete floor is considered as an air inlet and the complete ceiling as air outlet thereby simulating an upward flow.

A hypothetical inner fluid domain is modelled which should serve two major purposes i.e. a) provide a better mesh control by refining the region of interest and b) provide a confined space to evaluate thermal comfort which can be very useful when investigating multiple instance cases.

Different meshes were generated using very coarse to very fine cells. The meshes were all generated using ANSYS ICEM CFD tool. In the work done by Sørensen and Voigt (2003), the meshes and the simulation were carried out using a different CFD code namely STAR CCM+ (CD-adapco, 2002).

Due to different meshing approaches in different mesh generation software, a complete similarity in mesh quality cannot be guaranteed. It should however be noticed that a final converged simulation result should be independent of the type and method of mesh generation to a major extent.

The ruling criteria for the definition of mesh type was the number of boundary layers, the distance of first grid point from the surface of CSP and the number of surface cells on CSP. A combination of these criteria give an increase or decrease in the total number of volume cells thereby defining the mesh as fine or coarse.

Considering the complexity of the geometry all the meshes were generated using tetrahedral shaped cells with hexahedral prism layers to explore the boundary layers. The following sub-sections provide a brief overview of the different meshes used in this study.

5.6.1.1 Coarse Grid

In the first instance a mesh without any boundary layers is generated. The CSP surface was meshed with a total of approx. 25000 cells and complete volume with about 460000 cells. A cross section of the meshed domain and the manikin surface is shown in Figure 5-29(a) and (b).

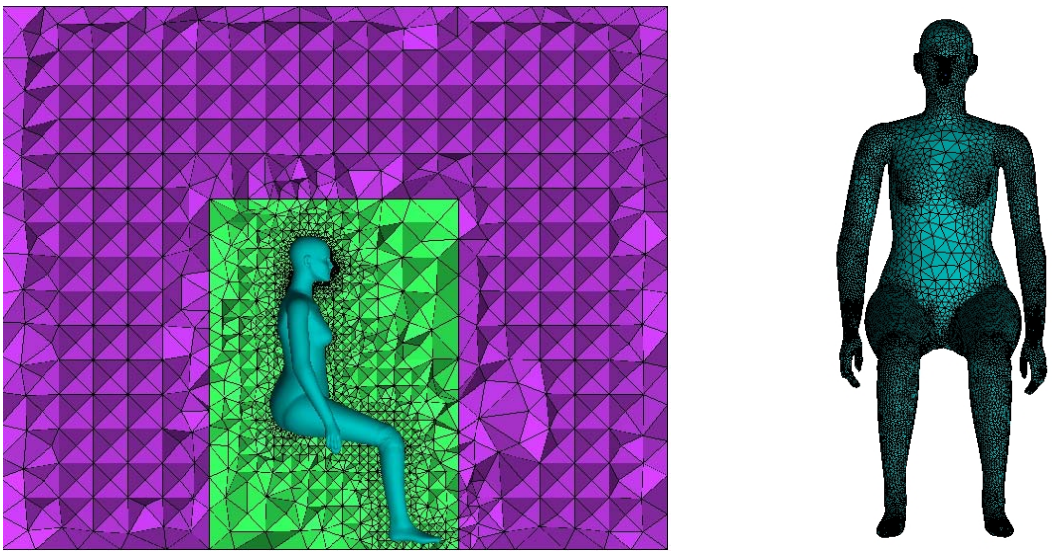

(a) (b)

Figure 5-29: Coarse mesh used for verification of natural convective flow over a complex human body shape.

5.6.1.2 Medium Grid

After obtaining the first results with coarse mesh, a medium quality grid with 11 prism layers was generated as shown in Figure 5-30 (a) and (b). The first prism height was at 2 mm with a growth ratio of 1.3. The complete CSP surface was meshed with about 37000 cells and the complete volume with about 1.7 Million cells

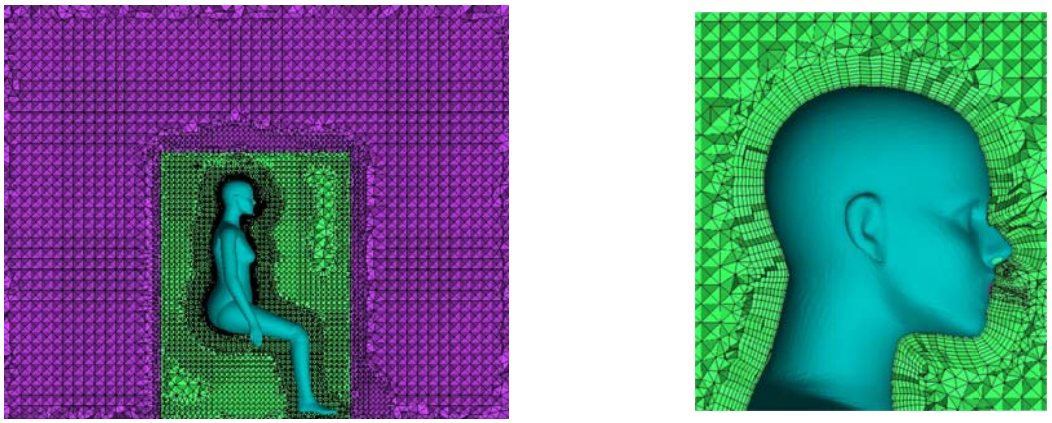

(a) Cross section through the calculation domain (b) Mesh resolution near manikin head

Figure 5-30: Medium quality mesh used for verification of natural convective flow over a complex human body shape.

5.6.1.3 Fine Grid

In the next stage of mesh generation, the grid was made finer near the CSP, especially with the background thought of resolving the surface heat transfer phenomena in detail. A very fine mesh not only helps to see the mesh independency but also aids to exploring the capabilities of CFX in terms of wall functions as it is often seen that poor heat transfer mechanisms are not only due to turbulence models themselves but due to the implemented wall functions. ANSYS CFX uses implemented scalable wall functions for most of the turbulence models and a trademark "automatic wall functions" (See chapter 4 for details) for SST model thereby claiming to have resolved the problem of mesh dependencies and using arbitrarily fine grids in the near wall region. Currently generated fine mesh for the verification study consists of about 87000 surface cells for the CSP body and 20 prism layers around the CSP with the first prism layer laying at 0.5 mm thereby giving a total of about 4.5 Million volume cells as shown in Figure 5-31.

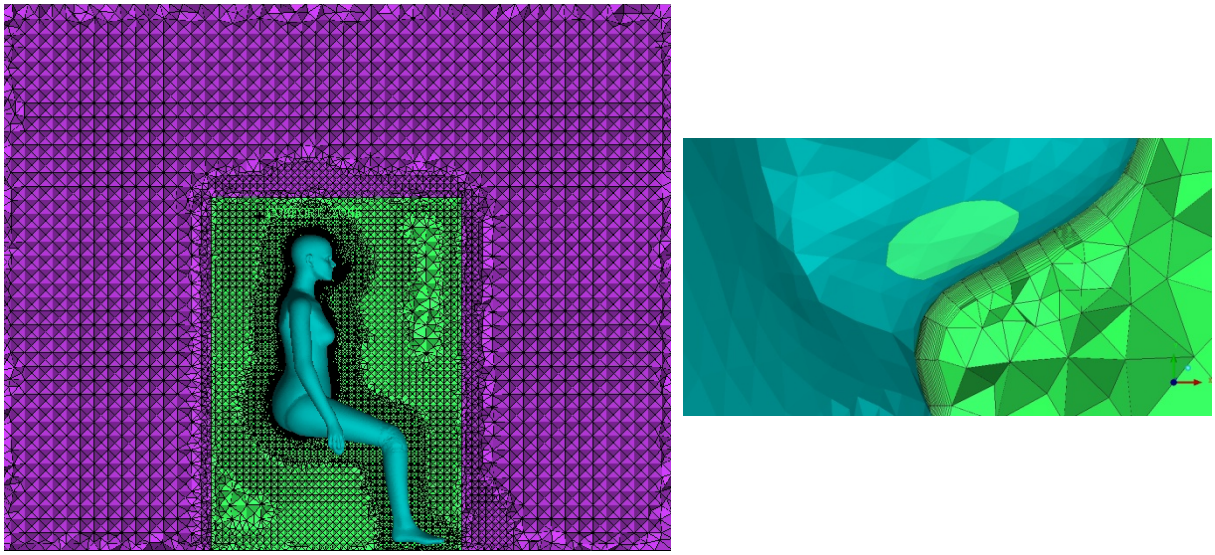

(a) Cross section through the calculation domain

(b) Mesh resolution near manikin`s nose

Figure 5-31: Fine quality mesh used for verification of natural convective flow over a complex human body shape.

5.6.2 Simulation Methodology

In order to avoid geometrical and boundary condition dependent variations in the results, the CSP model and the surroundings were kept similar to those used

Sørensen and Voigt. The numerical influences such as the implementation of the near wall treatment (different in different CFD codes), the solver type (implicit, explicit etc.) and numerical schemes together with the implementation of a turbulence model can play a vital role in the prediction of flow, heat and mass transfer phenomena As the code considered in the current PhD work is ANSYS CFX, four turbulence models namely a) zero eddy viscosity transport Model b) k-ε model c) RNG k-ε model and d) SST model with different grid resolutions were studied to see their impact on simulation results.

5.6.3 Boundary Conditions and Solution Parameters

Steady state simulations using Boussinesq approach were carried out. The discrete transfer surface to surface model was used to model the radiative heat transfer. Solving steady state in ANSYS CFX requires the use of false time stepping (see chapter 4). For the current study, a different type of false time stepping was investigated. As a result of this study, "local time step factor with time step factor of 7 for momentum equation and 10 for energy equation was found to be appropriate for reaching a Root Mean Square (RMS) residual convergence level of 1e-4 with a double precision solver. Once converged, the simulations were run forward to a residual convergence level of 1e-5 with a physical time step of 0.2 s to rectify the probability of the solution being dependent on time stepping. The simulations were further run using "auto time step" (an averaged time step calculated internally by the solver) as recommended by the software developer. A fluctuation in residuals was observed without major influence on the general flow characteristics. These fluctuations are due to the fact that the auto time step calculated by the solver was lower than the physical time step of 0.2 s thereby resolving the small turbulent variations, not possible to be resolved with the used grid resolution

In addition to the RMS convergence, monitor points were set at a) surface of CSP for heat transfer coefficients b) temperature 15 cm away from the nose tip c) velocity 70 cm above the head and 15 cm away from the nose tip. The simulation was assumed to be converged when all the RMS residuals fall below 1e-5 and the fluctuation in the variable quantities at chosen monitor points remain below 0.1%.

To make sure about the quality of numerical calculations, a higher order discretization scheme (See chapter 4 for discretization details) is used. As a convergence check on all the transport equations, a global imbalance condition was imposed. This convergence check confirms that there is no imbalance in the solved equations for momentum, mass and energy. As a criteria, a global imbalance of 1% was used which is based on the recommendation provided by ANSYS CFX. Typical convergence plots are presented

The CSP was given a constant surface temperature of 31°C with a radiative emissivity of 0.95. Besides the fact that the benchmark case used the surface temperature, literature shows human skin temperature to range between 30 and 33°C (Benedict, et al., 1919). The emissivity of 0.95 is justified in the light of the literature published by de Dear and his co-workers (de Dear, et al., 2001). The surrounding walls were given a constant temperature of 19°C with a radiative emissivity of 0.97. The floor was defined as inlet with constant inlet velocity of 0.02 m/s with an inlet temperature of 19°C. All these boundary conditions correspond to the ones defined in the considered benchmark case.

The flow field surrounding the seated CSP and the heat transfer coefficients (convective and radiative) were used for comparison and validation purposes.

5.6.4 Results

All the results predicted in pursuit of validation of ANSYS CFX CFD code are presented as post-processed contour plots for the a) flow field near to the CSP b) temperature field near to the CSP and c) convective heat transfer coefficient on the front and back of the CSP body.

It is seen that not all the grids and not all the turbulence models give the same results. The results vary by more than 300% from the chosen experimental/benchmark work depending upon the model and grid type used. In the upcoming sections only the results obtained using medium grid SST model are presented as they best suited the chosen experimental and benchmark study. The rest of the results (other turbulent models and meshes) are given as a comparison study in appendix A as post-processed contours of flow field, temperature and convective heat transfer coefficients on the CSP body.

5.6.4.1 Flow Field

The post processed results of the chosen benchmark case are shown as contour plots of velocity in Figure 5-32. All contour planes are located in XY (left side of Figure 5-32 a and b) at the centre of the CSP i.e. at Z = 0 m and YZ (right side of Figure 5-32 a and b) at X = -0.12 m .

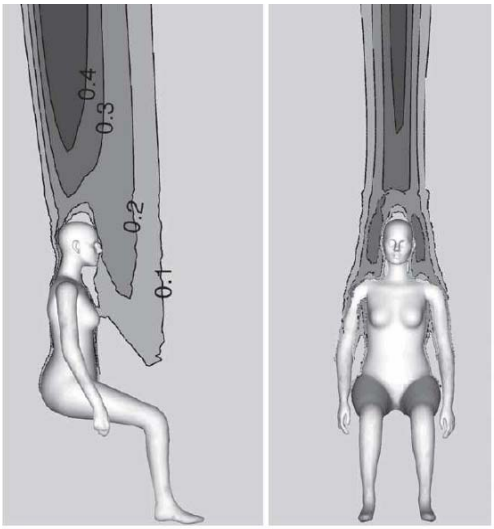

(a) Results from the work done by Sørensen and Voigt

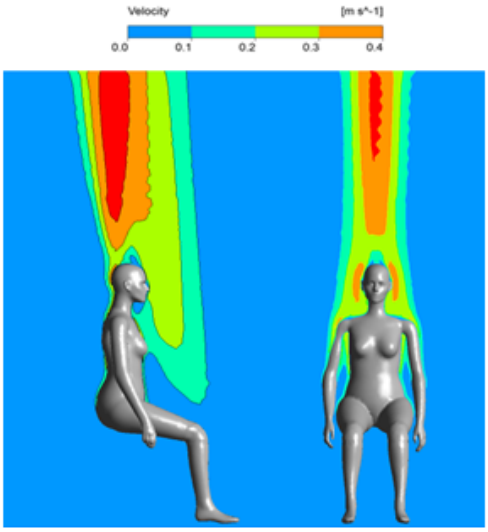

(b) Results of the present PhD work

Figure 5-32: Contour plots of velocity

5.6.4.2 Temperature Field

The results of the temperature fields from the chosen benchmark study are shown as contour plots of temperature. All contour planes are located in XY (left side of Figure 5-33 a and b) at the centre of the CSP i.e. at Z = 0 m and YZ (right side of Figure 5-33 a and b) at X = -0.12 m .

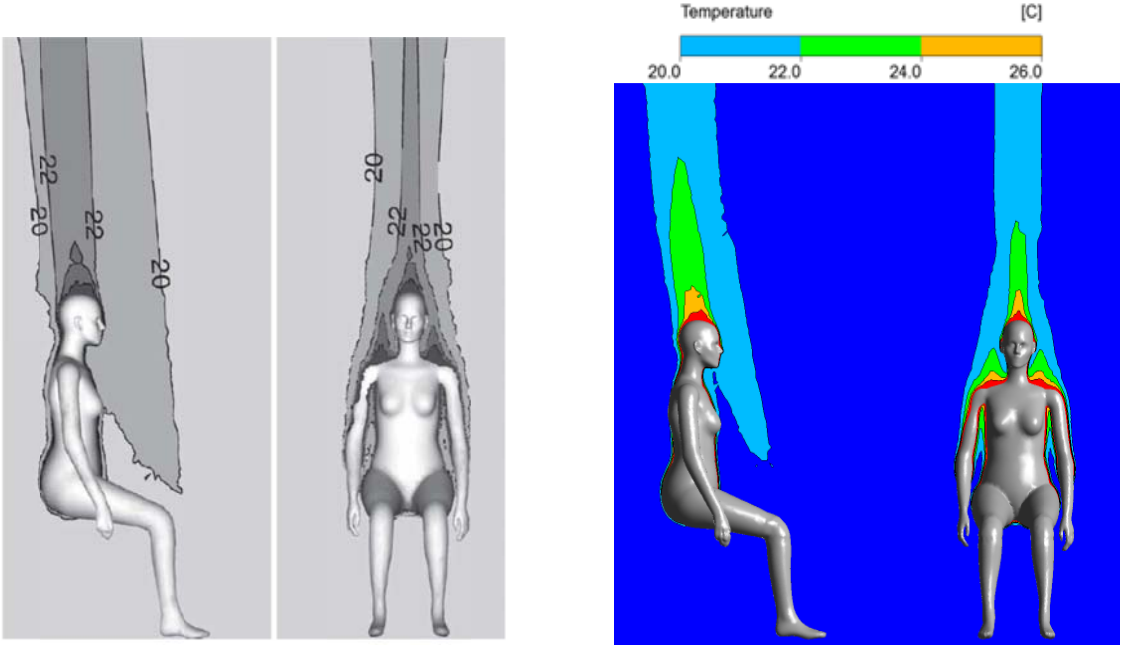

(a) Results from the work done by Sørensen and Voigt

(b) Results of the present PhD work

Figure 5-33: Contour plots of temperature

5.6.4.3 Convective Heat Transfer Coefficient

The convective heat transfer coefficients at the front and back of the seated CSP as predicted in the study carried out by Sørensen and Voigt is presented in The corresponding heat transfer coefficients results from the current PhD work are shown in Figure 5-34.

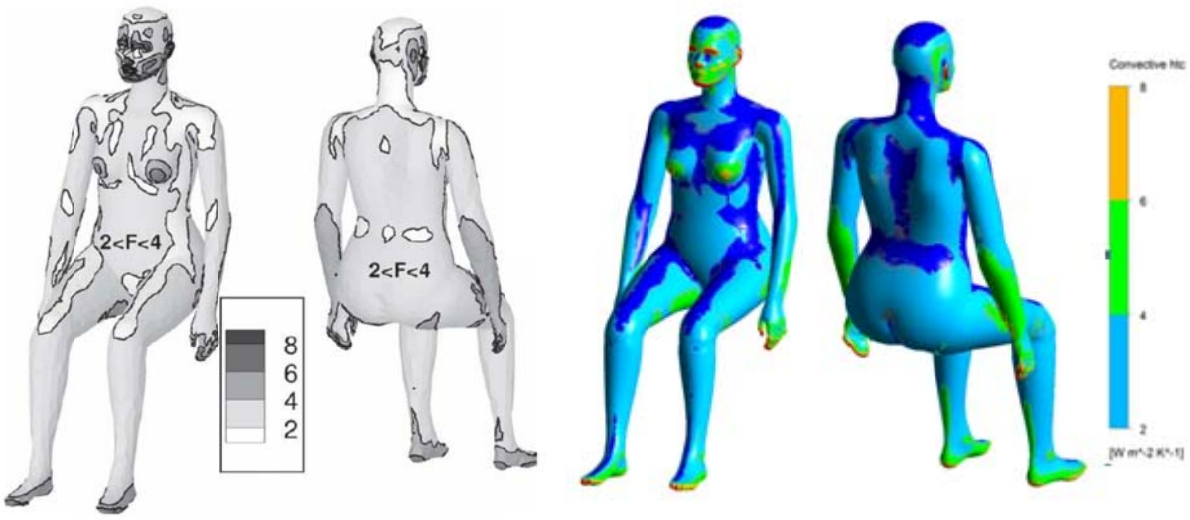

(a) Results from the work done by Sørensen and Voigt

(b) Results of the present PhD work

Figure 5-34: Contour plots of heat transfer coefficients

The comparison between the flow and temperature fields as predicted in the benchmark study and the current study shows good agreement with each other. The work done in the benchmark study reported a deviation of 2% between the measured and simulated values of convective heat transfer coefficients for the whole body i.e. 3.2 W/m^{2}K (measured) to 3.13 W/m^{2}K (simulated). Present PhD results correspond very well to the simulated benchmark case simulated using the SST turbulence model with medium and fine grids. The variable for comparing the results of the benchmark case and the present simulation is chosen to be the convective and radiative heat transfer coefficients. The results obtained during the course of this PhD work give a convective heat transfer coefficient value of 3.12 W/m^{2}K for medium grid and 3.4 W/m^{2}K for fine grid and a radiative heat transfer value of 4.68 W/m^{2}K for medium and 4.67 W/m^{2}K for fine grid. The differences in the field away from the CSP can be attributed to the grid type, numerical algorithms applied in the two different codes (STAR CCM+ code used in benchmark case and ANSYS CFX code used in the current study) and turbulence model used (low Reynolds turbulence model used in benchmark case and SST turbulence model used in current study).

The result of the complete study is summarized in Table 5-5. The results also show the minimum and maximum y+ values at the CSP surface along with the convective and radiative heat transfer coefficient averaged over the complete CSP surface. For all the turbulence models except SST, the actual y+ values are limited to 11.068 due to the scalable wall functions implemented in ANSYS CFX in order to keep the model within its application range (See chapter 4 for details of y+ and turbulence models). The temperature difference for evaluation of heat transfer coefficients is the difference between the CSP surface (31°C) and walls (19°C) i.e. 12 [K].

Table 5-5: Results of mesh independency and natural convection flow verification study using CSP

Grid	Variables	Turbulence models			
		Eddy viscosity	k-ε	RNG-k-ε	SST
Coarse	Convective HTC [W/m²K]	0.81	0.70	0.40	3.01
	Radiative HTC [W/m²K]	4.65	4.65	4.65	4.65
	y+ min	11.068	11.068	11.068	0.52
	y+ max	10.6	11.068	11.068	17.2
Medium	Convective HTC [W/m²K]	0.77	1.10	0.85	3.12
	Radiative HTC [W/m²K]	4.68	4.68	4.68	4.68
	y+ min	11.068	11.068	11.068	0.156
	y+ max	11.068	11.068	11.068	5.4
Fine	Convective HTC [W/m²K]	0.78	1.15	0.85	3.4
	Radiative HTC [W/m²K]	4.67	4.67	4.67	4.67
	y+ min	11.068	11.068	11.068	0.048
	y+ max	11.068	11.068	11.068	4.92

Based on the summarized results in Table 5-5, it is seen that radiation models implemented in ANSYS CFX give satisfactory results with DTRM model. The results show an area average radiative heat transfer coefficient of about 4.7 [W/m²K] which is very close to the experimental value of 4.5 [W/m²K] (de Dear, et al., 2001).

It is interesting to note that the radiative heat transfer coefficient (h_r) remained constant irrespective of the volume grid resolution. One explanation to this constant h_r is the fact that no radiation absorption in the medium is taken into account (i.e. a surface to surface modelling approach). In such a case the only thing that matters to the accuracy of the result is the level of grid resolution at the surfaces and the number of tracing rays. For the current model the standard 16 rays were used per surface for ray tracing and it is seen that even the coarse mesh turned out to be sufficient for predicting and validating the radiative heat transfer coefficient against published work. As noted in the heat transfer study with simple geometrical objects SST model however starts to over predict the heat transfer with a very fine grid when compared to the reference values.

5.7 Summary

In the first part of this chapter the performance of numerical techniques implemented in the software ANSYS CFX to simulate radiative heat transfer for simple and complex (human body) geometries were analysed.

The verification studies carried out for simple geometrical assemblies showed a very good agreement with the corresponding analytical solutions. The maximum relative error encountered was typically less than 2% in most cases. In the case of detailed human body geometries, the predicted view factors varied slightly from those obtained experimentally by Fanger. A careful analysis of the results indicated that the discrepancies were associated with differences in the body posture and with some 3D characteristics such as surfaces convexities and concavities which were ignored in Fanger study.

Literature sources, (Kubaha, 2005), (Raber & Hutchinson, 1944), (Dunkle, 1963) indicate values for effective radiation area factor for standing subjects between 0.75 up to 0.85. The values for effective radiation area factors calculated by Fanger are much lower due to consideration of a rather stiff posture. The present work indicates higher effective radiation area factors.

For the case of short wave radiation (directional radiation flux), the normalized projected area factors obtained using numerical simulations showed close agreement with data obtained experimentally by Fanger.

The aim of verifying and validating the parameters affecting the radiative heat transfer is achieved in this part of the research work thereby providing confidence to use these settings for the purpose of investigating the indoor climates with human occupancy.

The second part of this chapter deals with combined convective and radiative heat transfer. The convective heat transfer models in ANSYS CFX were verified for simple geometrical shapes as well as for detailed human geometry (mesh independency and comparison of different turbulence models). The results for radiative heat transfer for detailed human geometry (seated) show an area average heat transfer coefficient of about 4.7 [W/m²K] which correlates well to the experimental value of 4.5 [W/m²K] (see literature review for different experimental values).

It is interesting to note that the radiative heat transfer coefficient (h_r) remained constant irrespective of the volume grid resolution. One explanation to this constant h_r is the fact that no radiation absorption in the medium is taken into account (i.e. a surface to surface modelling approach). In such a case the only thing that matters to the accuracy of result is the level of grid resolution at the surfaces and the number of tracing rays. For the current model the standard 16 rays were used per surface for ray tracing and it is seen that even the coarse mesh turned out to be sufficient for predicting and validating the radiative heat transfer coefficient against published work.

Considering the medium grid resolution and SST turbulence model, it is seen that the area averaged convective heat transfer coefficient, h_c for the CSP body is 3.12 [W/m²K] which corresponds well to the convective h_c of 3.13 [W/m²K] in the chosen benchmark case (Sørensen & Vøigt, 2003) and 3.3 [W/m²K] in the work published by de Dear et. al (2001). This however is considerably lower than the widely excepted convective heat transfer coefficient of 4.43 [W/m²K] for a 12 [K] temperature difference (based on the correlation $h_c = 2.38 \times (t_s - t_w)^{0.25}$ [W/m²K] proposed by Fanger (1972)). This however can also be contributed to the geometrical setups, inaccuracies in boundary conditions and posture of manikin used during the experimental work.

The comparison between the flow and temperature fields as predicted in the benchmark study and the current study shows considerable resemblance. The differences in the field away from the CSP can be due to the grid type, numerical algorithms applied in the two different codes (STAR CD code used in benchmark case and ANSYS CFX code used in the current study) and turbulence model used (low Reynolds turbulence model used in benchmark case and SST turbulence model used in current study).

The automatic wall function implemented with the SST turbulence model shows much independency to the grid near the wall. The SST model however starts to over predict the heat transfer with a very fine grid when compared to the reference values.

The CFD basic principles in chapter 4 and the verification study in chapter 5 led to the appropriate selection of different physical models for CFD simulation of indoor climates. To conclude the summary of chapter 5, the methodology for the selection of a particular physical model is outlined in the form of a generalized flow chart as shown in Figure 5-35.

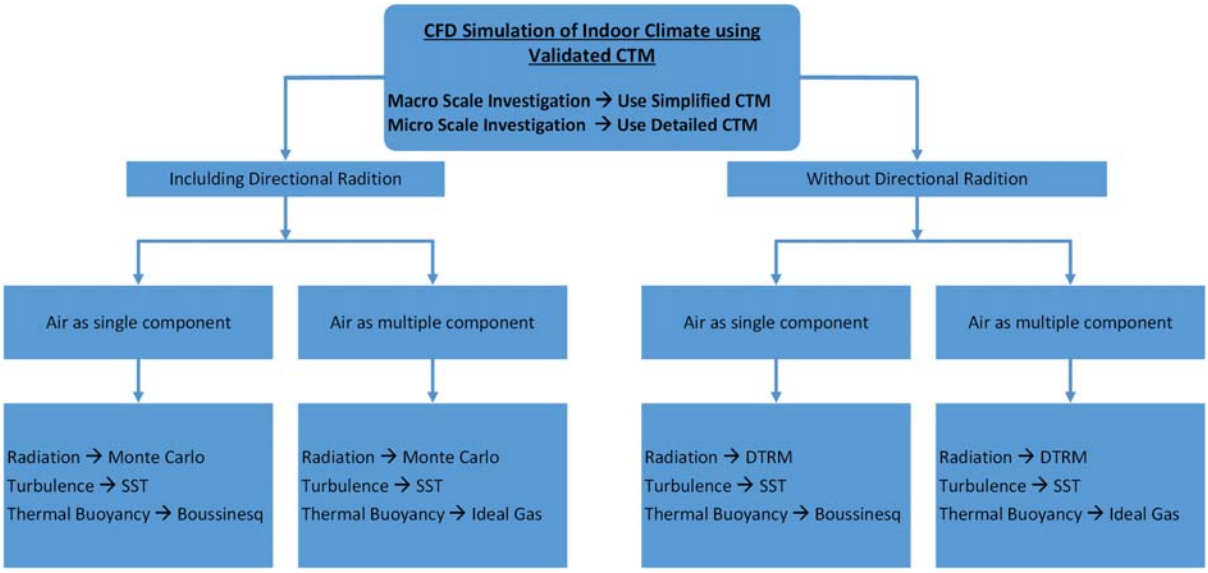

Figure 5-35: Flow chart showing the selection of appropriate physical models while simulating indoor climate using CFD.

6 Experimental Validation

Validation of a simulation is defined as the procedure of testing the extent to which that simulation can represent the underlying reality. In the current research work, experiments are conducted to measure the temperature and flow field around a sitting thermal manikin. The data achieved was compared to the CFD simulations conducted using ANSYS CFX so as to validate the use of the thermal manikin model for investigating aero- and thermodynamics related phenomena in indoor climates.

The work presented in this chapter makes use of analytical, measurement and numerical techniques to analyse the flow around the seated female thermal manikin as well as in the complete room. This chapter presents the results obtained using different measurement and simulation techniques for a test room with particular attention to the flow in the vicinity of the seated manikin.

6.1 Experimental Setup

The experiments were conducted in the environmental chamber at Loughborough university. The experimental chamber has the dimensions of 5.43×3.09×2.4 m in length, width and height respectively.

Three thermocouples were attached to the internal surface of each side wall to measure wall surface temperatures. In addition to the thermocouples, four hobo data loggers (HT1, HT2, HT3 and HT4) were suspended to measure air temperature at defined points. A thermocouple (TC1) was suspended above Victoria in order to capture the plume temperature. TC1 had to be moved towards the rear wall to avoid the line of the laser sheet (in order to avoid any reflection problems). The dimensions of the room along with the position of the different geometrical object and sources are shown in Figure 6-1.

The origin of measurement in the y direction is considered to be the wall with the air inlet duct whereas that in the x direction is the wall adjacent to the table 2, as shown in Figure 6-1.

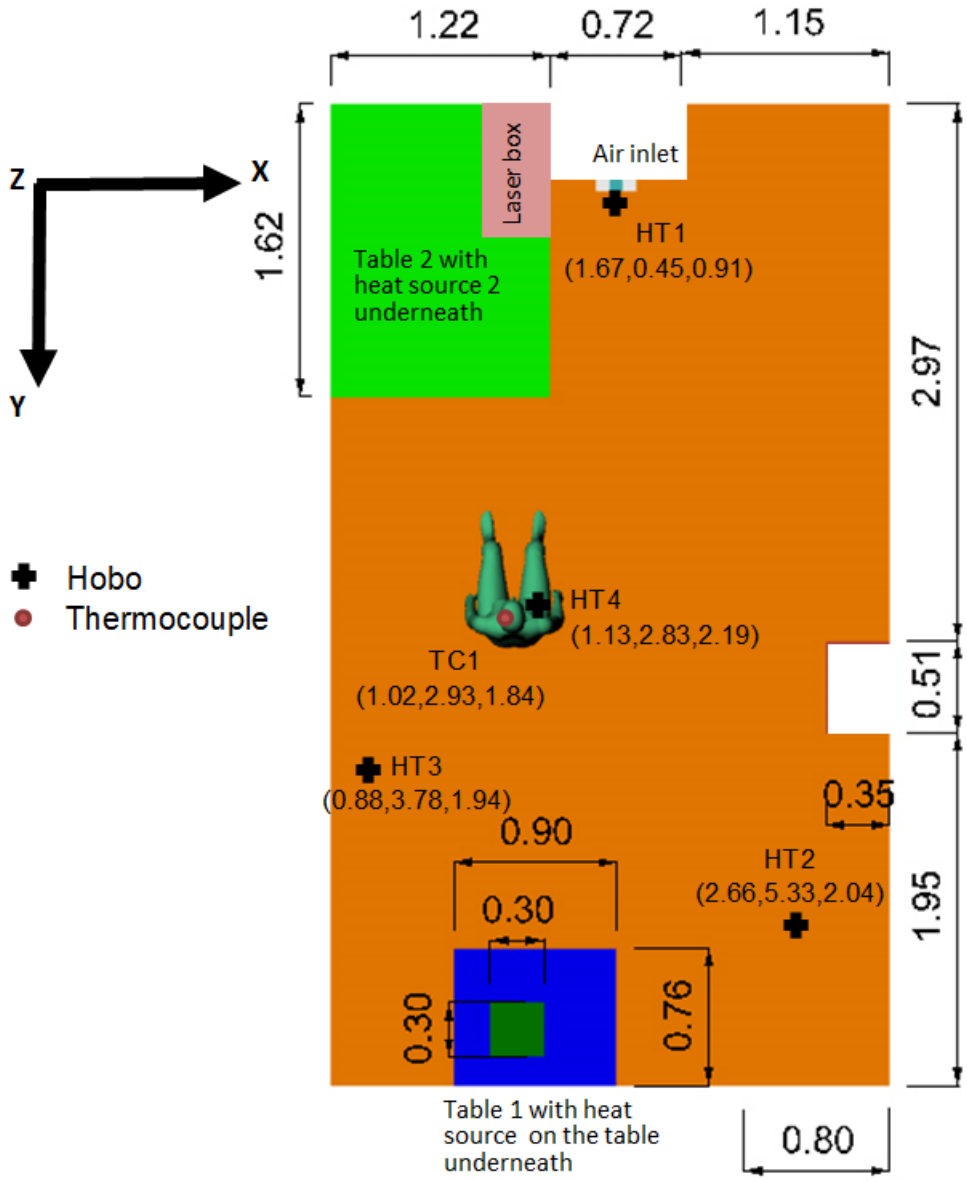

Figure 6-1: Dimensions (in units of metres [m]) of experimental chamber at Loughborough University

In order to capture the flow field, a LaVision GmbH (LaVision, 2011) PIV system was utilised, consisting of two 4MP (2048x2048 pixel) cameras, a dual cavity 200mJ/pulse Nd:YAG laser, a 6 nozzle Laskin type seeder and associated timing, processing and calibration equipment. The location of the equipment is shown in Figure 6-2 with the laser mounted in front of the manikin and the cameras mounted perpendicularly to the sheet ~1.5 m to the manikin's left-hand side. Due to issues with reflections at the laser sheet/manikin head intersection, the sheet was positioned ~1x10^{-3} m behind the centreline, shielding the reflections from the camera by using the natural curvature of the manikin's head.

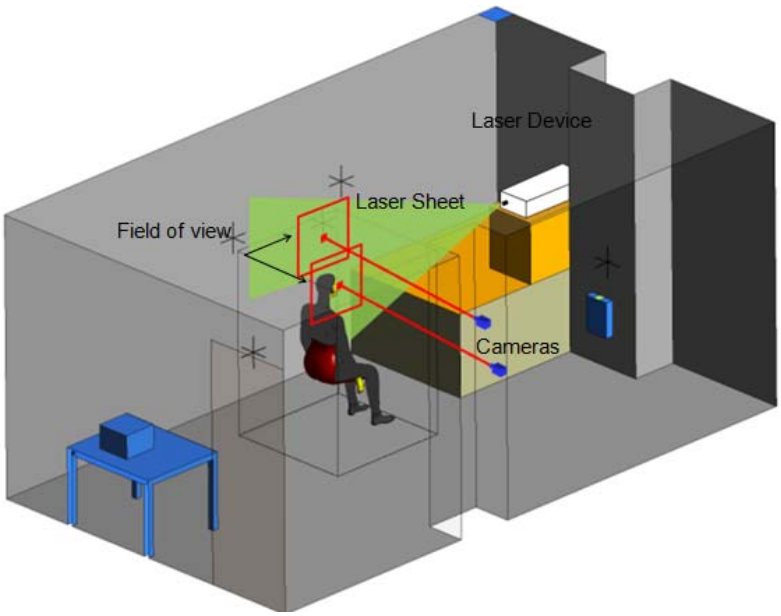

Figure 6-2: Visualization of test chamber with setup of PIV

To minimize reflections, the body of the thermal manikin was covered with black skin-tight clothing and the wall behind the manikin was covered with a black fabric. An image of the seated CSP and a raw image showing the combined fields of view (FoVs) from both cameras are presented in Figure 6-3 a and b.

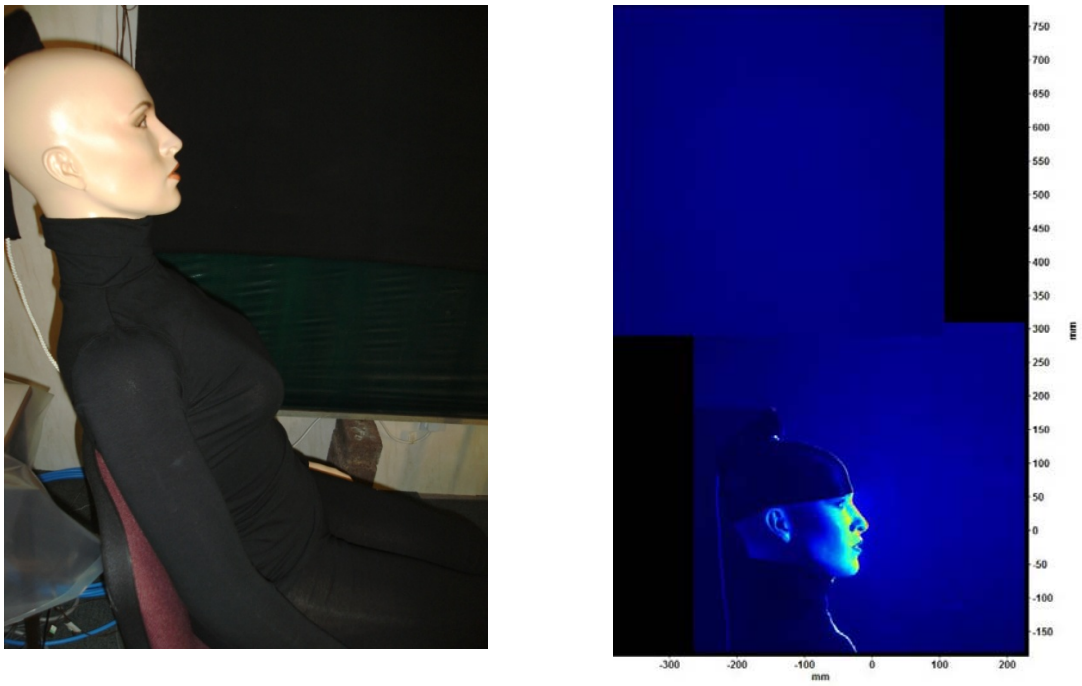

(a) Seated manikin "Victoria" (b) Raw PIV image of FoVs

Figure 6-3: Raw PIV camera images showing the two FoVs, one above the other.

Each camera`s FoV, approximately 0.5 x 0.5 m is combined to cover a 1.0 x 0.5 m area. The lower camera was positioned in such a way that the manikin's head was located toward the rear of the FoV, reducing the area of the frame in the laser shadow. The upper camera was located rearward of this, centred about the manikin's head in an attempt to centre the thermal plume in the frame. During the calibration procedure, a calibration plate (Figure 6-4a) was positioned in such a way as to be visible in both frames with a row of markers present in the frame overlap; thereby ensuring the frames' relative locations and rotation could be accurately determined. Seeding was performed using a 6 nozzle Laskin type seeder placed in the centre of the experimental chamber (Figure 6-4b).

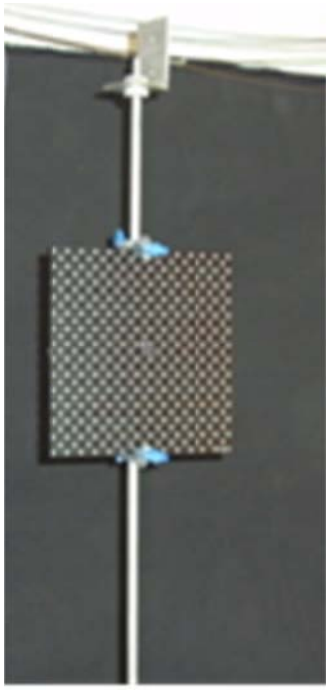

(a) *calibration plate with black covered background*

(b) *Seeder device*

Figure 6-4: Photograph of the setup used in the experiments.

This device produced seeding particles with a diameter of ~$1x10^{-6}$ m, using olive oil as the seeding medium. This was selected for its high refractive index, making particles highly visible when captured in the laser sheet, being close to neutrally buoyant, sinking at ~$1x10^{-10}$ m/s assuming Stokes flow, and having extremely fast

response time, of the order $1x10^{-9}$ s enabling the resolution of highly turbulent flow structures.

6.2 CFD Simulation

6.2.1 3-D Model and Mesh Generation

The CSP model, known as 'Victoria' is a female manikin manufactured by PT.Teknik, Denmark (P T Teknik, 2016). The geometrical model for CFD calculations has been used in a number of previous studies for investigation of indoor human thermal comfort, air pollution and respiration (Melikov & Zou, 1999), (Tanabe, et al., 1994), (Melikov, et al., 2002). The 3-D scanned data of the thermal manikin was taken from the work published by Nielsen et al. (2003).

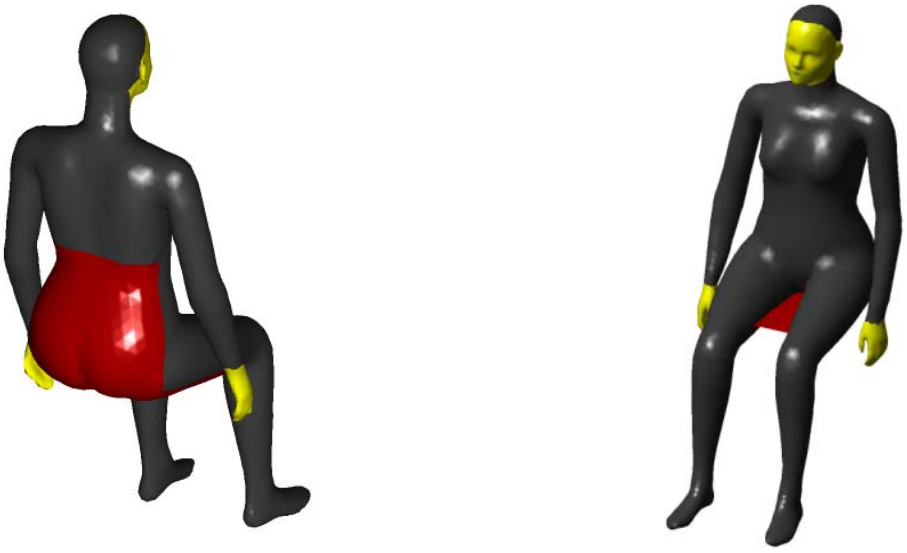

Figure 6-5: Seated model of thermal manikin "Victoria" with modelled simplification of chair (shown in red)

The model geometry was refined using the 3-D NURBS modelling software Rhinoceros (2010). A chair was modelled as a 2-D adiabatic object perfectly in contact with Victoria´s surface to take into account the blockage in airflow (Figure 6-5). No thermal conduction effects within the chair were modelled.

Using the dimensions of the experimental chamber, a 3-D room geometry was prepared in Rhinoceros. Both geometries i.e. the geometry of the thermal manikin and that of the test chamber, were merged into a single model. The region around the seated manikin was further enclosed in a virtual box measuring 1.1 m × 1.1 m ×

1.6 m. This virtual box denotes an inner fluid domain and serves two important purposes: a) to provide a better mesh control by refining the region of interest, and b) to provide a confined space to evaluate thermal comfort which can be useful when investigating multiple instances of the manikin geometry.

As the geometrical model was divided into two regions, the meshing was carried out using ANSYS ICEM CFD for the two zones, namely "virtual comfort domain" comprising the seated manikin and "Lab domain" comprising everything else. In the convective flow verification study in chapter 5, a similar meshing methodology was employed. The advantage of following this meshing methodology lies in the efficiency in mesh generation and mesh consistency in regions of interest. Parametric studies can be carried out by merging the virtual comfort zone into almost any surrounding.

As the CSP geometry is the same as in the chapter 5, the results of the mesh independency study were used as meshing guidelines giving approximately 3M volume cells as an optimum mesh size for the comfort domain with nine prism layers on the surface of the thermal manikin. An effort to further increase the number of prism layers resulted in the decrease in quality of the mesh and was therefore not pursued. The surroundings were modelled with a total of approximately 1.7 M volume cells. The mesh of the complete model and close up of the meshed thermal manikin is shown in Figure 6-6and Figure 6-7 respectively.

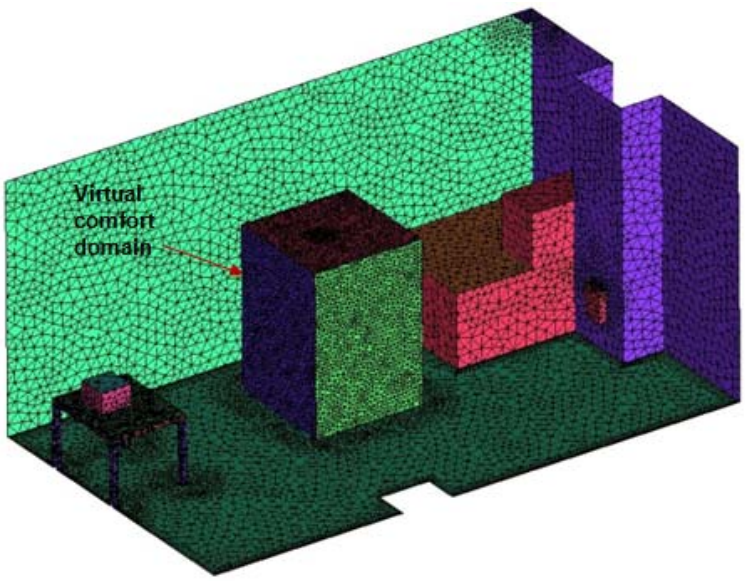

Figure 6-6: Meshed model of the test chamber along with the virtual comfort domain

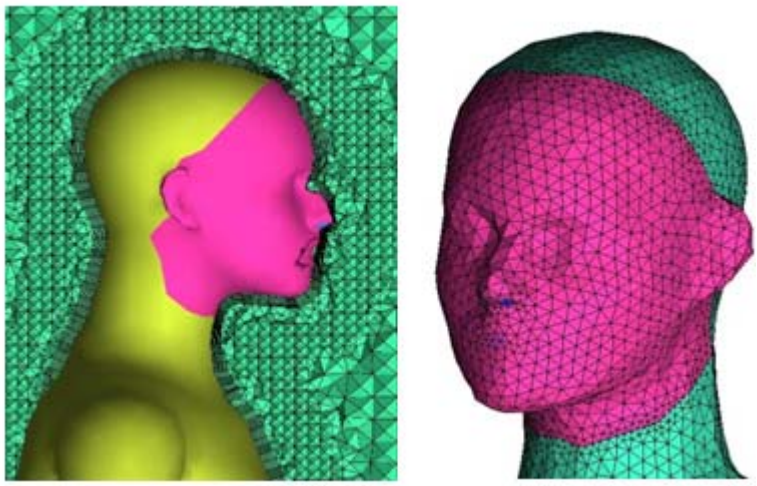

Figure 6-7: Surface mesh at CSP surface and on a cut plane in the calculation domain

6.2.2 Simulation Parameters

Steady state simulations were carried out using the Boussinesq approximation for thermal buoyancy. The discrete transfer surface to surface model was employed to model the radiative heat transfer (Siegel & Howell, 1992). Solving steady state in ANSYS CFX requires the use of false time stepping to control convergence. Setting an appropriate false time step aids the buoyancy dominant flows (Cook, 1998). For the current study the flow field is solved using a "local time stepping" methodology which uses different pseudo time steps in different regions of the flow. In order to get a faster convergence, the local time steps were multiplied by a "time step factor" of 5 for momentum and energy. Once the required level of convergence was achieved, the simulation was continued further using the false physical time scaling method implemented in ANSYS CFX. The value of this physical time step was set to be 0.2 seconds. The simulation was also verified to run with the default time stepping methodology of ANSYS CFX (automatic time step).

As the SST turbulence model predicted results closer to the analytical results for natural convection flows (see chapter 5), the validation simulations were carried out using the SST turbulence model (Menter, 1994). The results obtained were compared against the temperature and flow field measurements (PIV). Both simulations used a "high resolution" discretization scheme for advection terms and first order upwind for turbulence quantities as recommended by the software developers (CFX, 2010). A "High Resolution" discretization scheme was employed

due to its use of local blending factor between 1st and 2nd order thereby providing an excellent compromise between accuracy and robustness. In order to increase the accuracy of the results, the double precision capability of the unstructured Multi-grid ANSYS CFX solver was used.

In order to account for the viscous forces and the rapid change in variable gradients, the near wall region was resolved using an "automatic wall function" which switches between normal wall functions and low Reynolds number wall formulation thereby allowing the use of the k-ω model near the wall (where flow dominated by low Reynolds numbers occurs) and k-ε away from the immediate vicinity of wall (see chapter 4 for an overview on near wall modelling and turbulence models).

Root Mean Square (RMS) residuals below $1e^{-5}$ for mass, momentum and energy were set as the convergence criteria. Buoyancy driven flows are often dominated by turbulent structures at different scales and are often difficult to capture using RANS (Reynolds Averaged Navier Stokes) type turbulence models. Such flows often show oscillatory behaviour in the residuals and require additional numerical measures and monitors to achieve convergence. For this reason, along with the RMS residual check, the flow state in the region of interest was additionally monitored by using three monitor points set above the manikin´s head in the thermal plume for recording variations in velocity and temperature. A steady converged state was interpreted when no noticeable fluctuation at these monitor points was seen. An additional imbalance convergence check was applied on all the transport equations. This convergence check ensures that even if flow is locally stable and has reached the defined RMS values, there is no imbalance in the equations for momentum, mass and energy. The value of this imbalance convergence check was set to be 1%.

6.2.3 Boundary Conditions

Based on the measurements taken in the experimental chamber located at the “Civil and Building Engineering School” of Loughborough University (LU), the thermal manikin was given a constant surface temperature of 32.8°C on the clothed region and 34°C on the naked skin parts (face, neck and hands). The inlet was a 7 cm × 7 cm opening with an inlet air temperature of 19°C and an average flow velocity of 1 m/s. The outlet was modelled as a pressure opening with a relative pressure of 0 Pa.

The surfaces ‘floor’, ‘table 1’, ‘table 2’ and ‘laser box’ as shown in Figure 6-1 are modelled as adiabatic surfaces. For the rest of the surroundings, the boundary conditions are given in the Table 6-1 below.

Table 6-1: Boundary conditions for different surfaces and sources.

Boundary	**Temperature [°C]**
Right Wall	20.9
Left Wall	21.3
Back Wall	22.0
Front Wall	22.0
Ceiling	23.0
Door	23.2
Source 1	25.0
Source 2	25.0

Note that the surfaces are named as per the orientation with respect to the thermal manikin, e.g. a wall located to the left hand side of Victoria is named as "Left Wall". All the walls are considered as smooth walls. The wall temperatures are the average temperatures measured using thermocouples attached at various points on the internal wall surface. In addition to the thermocouples, thermal images using a thermal imaging camera were taken at the beginning and end of each experiment.

It is important to note that the wall temperatures were measured using the K-type thermocouples, the measurement tolerance of K-type thermocouples for typical indoor temperatures is around ± 1.5 K. The surface temperatures of the heat sources in the test chamber were calculated by thermal imaging each of the source surface at multiple points using a FLIR B 335 thermal camera and then taking an area average value of all the surfaces. As per manufacturer inputs, the temperatures tolerance for typical indoor climates is around ± 2 K.

6.2.4 Computational Details

All the calculations were carried out on an intel-Xenon 64 cluster using 24 No. 2.66 GHz processors. The required wall clock time for the calculated cases with 2000 iterations per case was approximately 5 hours.

6.3 Results

In order to declare the CFD results as converged, the convergence criteria mentioned in the previous section were checked. Instead of decreasing, the RMS residual values tended to remain static at around $1e^{-2}$. In an attempt to improve this, the following three approaches were used: a) mesh improvement b) identifying regions of high residuals for momentum, mass and energy, and c) running the same case for 1 minute in transient mode. Close examination of the mesh revealed that there are some cells with high skewness ratio. Improving this skewness ratio by local mesh refinement had little effect on reducing the residuals. High residuals were still found to be near the chair region where there is a region of recirculation and high shear. The points of maximum residuals are shown by red cross points in Figure 6-8.

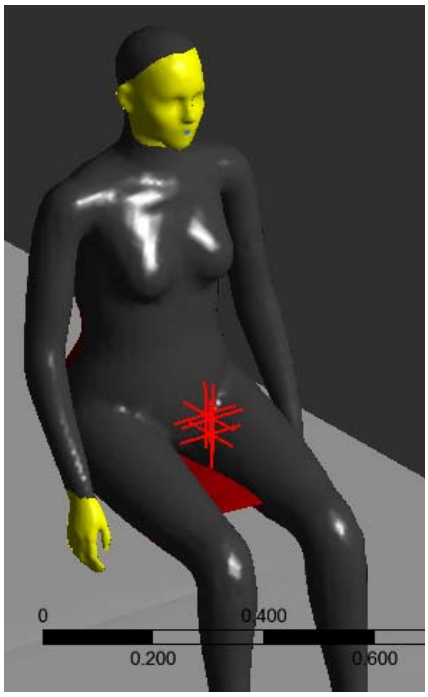

Figure 6-8: Points of maximum residuals located near to the chair region shown as red cross points.

In order to confirm this local peak in residuals due to transient wakes, a transient run of one minute (time step 0.1 second), with initial boundary condition taken from the steady state case was conducted. The RMS residuals fell far below $1e^{-6}$ within the first few seconds of the run confirming the presence of local transient behaviour. In order to overcome the problem, numerical improvements such as gradient relaxation factor, blend relaxation factors and variable false time stepping schemes were applied, thereby reducing the RMS residuals to $3e^{-4}$ and improving the flow stability.

The PIV process captures transient images at a frequency of approximately 3 Hz. A typical instantaneous image taken by the PIV measuring technique is shown in Figure 6-9 (a).

The instantaneous velocity images showed a wide range of maximum and minimum values of velocities for the measured period of time. This range is not only due to the transient behaviour of the flow in the thermal plume but also to the errors caused due to the statistical nature of image correlation used in PIV methodology to determine local flow velocities. The errors induced in PIV measurements are due to the finite number of tracer particles, the sampled volume size and due to the image resolution itself. For the presented work, the error elimination is based on the methodology of comparing the vectors with the neighbours to determine if they are statistical and physically consistent. Details of the employed error elimination methodology are given in detail by Westerweel (1997). Other error elimination methodologies can be found in literature (Hart, 1998). In order to understand the mean effect of the flow, an average representation of the flow is necessary. The averaging of the transient flow data is carried out by taking an ensemble average of the transient data and projected onto the evaluation plane.

The average velocities projected onto the evaluation plane passing through the thermal manikin using PIV show a developed thermal plume with a maximum averaged velocity of 0.24 m/s Figure 6-9 (b). The velocity scale is set from 0 m/s to 0.24 m/s and the white zone in the centre denotes values exceeding 0.24 m/s. The reference scale of 0.24 m/s is based on the maximum averaged velocity obtained after the ensemble averaging of the transient data.

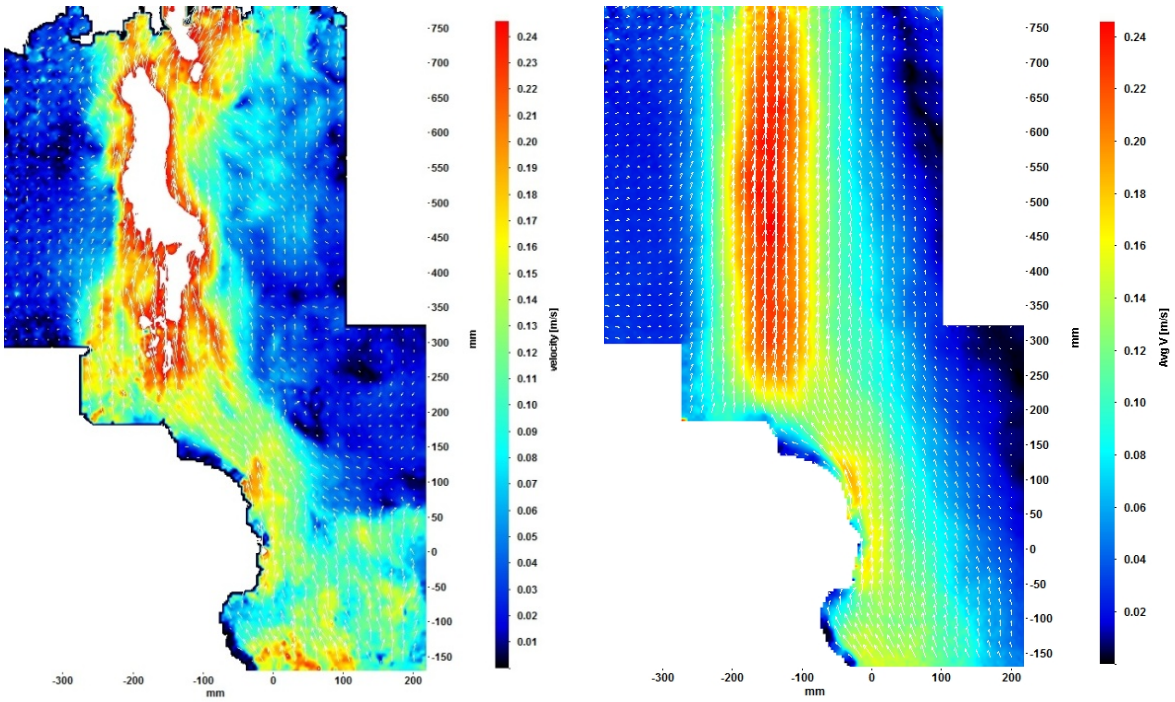

(a) Instantaneous velocity contours obtained using PIV tests in the chamber.

(b)Average velocity contours (over 10 minutes) obtained using PIV in the chamber.

Figure 6-9: Results of PIV measurements for velocity field

The CFD simulations presented in this chapter were run in a steady state. The average velocity contours at a plane located at the same co-ordinates as in the experimental work are shown in Figure 6-10(a) and (b).

Plotting the average velocity results on the plane as shown in Figure 6-10 (a) and (b) show that the SST turbulence model predicts higher velocities in the thermal plume when compared with the measured values. A quantitative analysis on a vertical line is carried out for both the PIV measurement and the CFD simulation. The vertical line is shown in black for the PIV measurement and in purple for the CFD simulation. The comparison of the results is presented in Figure 6-10 (c). Although the vertical velocity profiles follow a similar pattern, the magnitude of velocity differs from one another by 0.09 m/s at the same location (at reference height of 0.3 m).

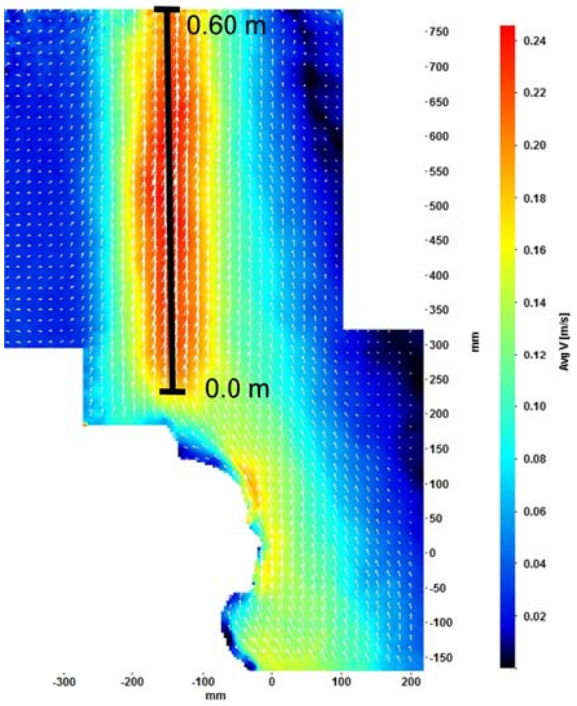

(a) Average velocity contours using PIV measurements

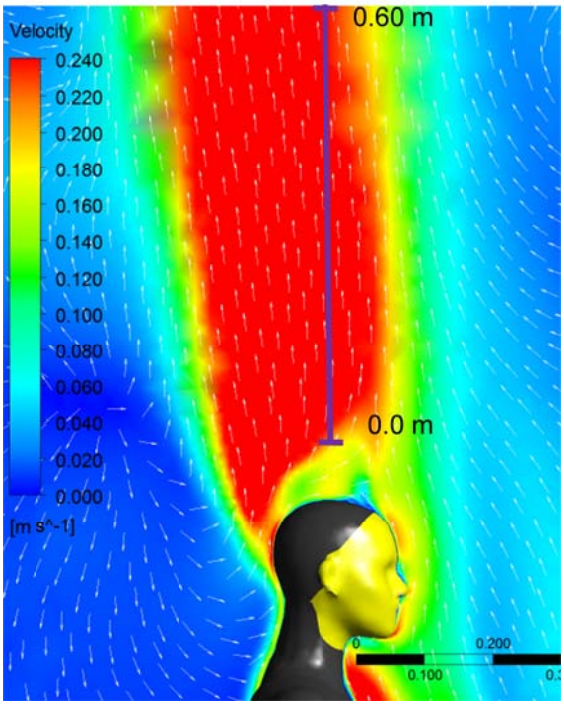

(b) Average velocity contours using SST turbulence model

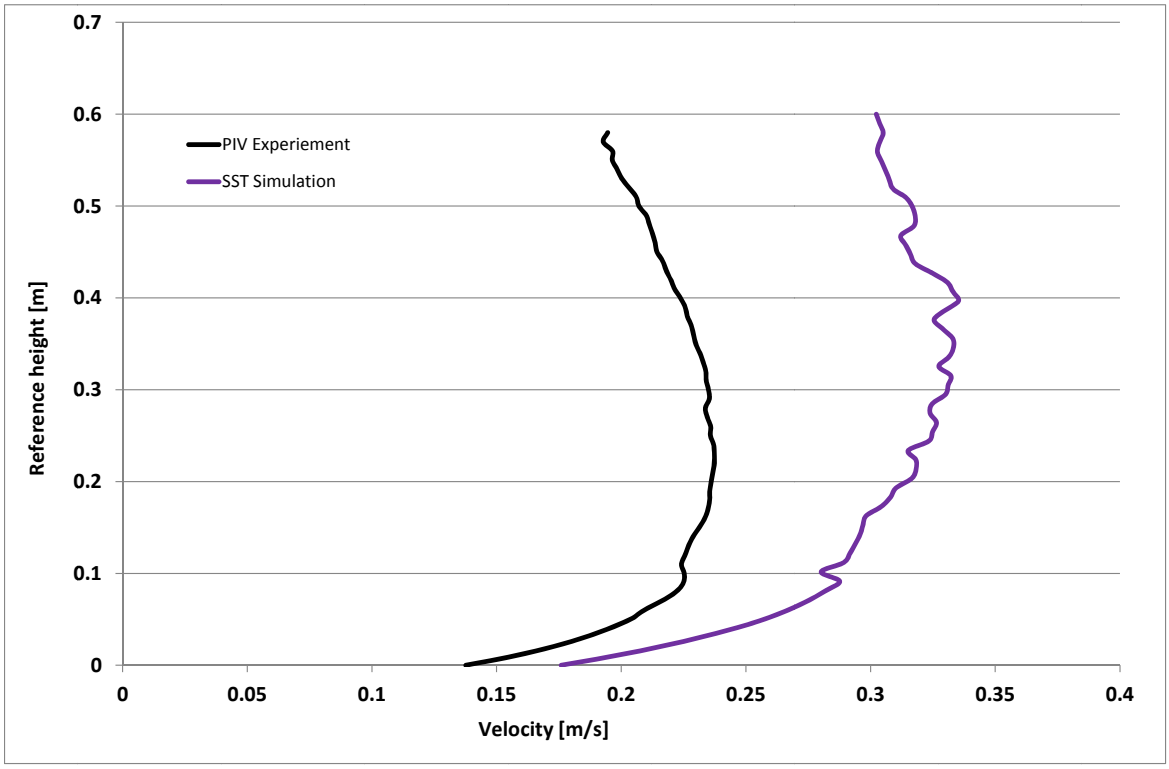

(c) Comparison of average velocities using PIV measurements and CFD simulations

Figure 6-10: Results of PIV measurements and CFD simulations.

Comparing the temperature values measured at different points in the measurement chamber and those predicted by the SST turbulence model show a difference of about 8% near the inlet (HT1) showing that the turbulence model under-predicts the temperature near to the inlet when compared to the measurements. For the rest of the sensor points, especially near to the CSP surface, the SST model over-predicts the temperature field by about 2.5%. (Figure 6-11). The error bars of ± 1°C in Figure 6-11 relate to the steady state CFD modelling.

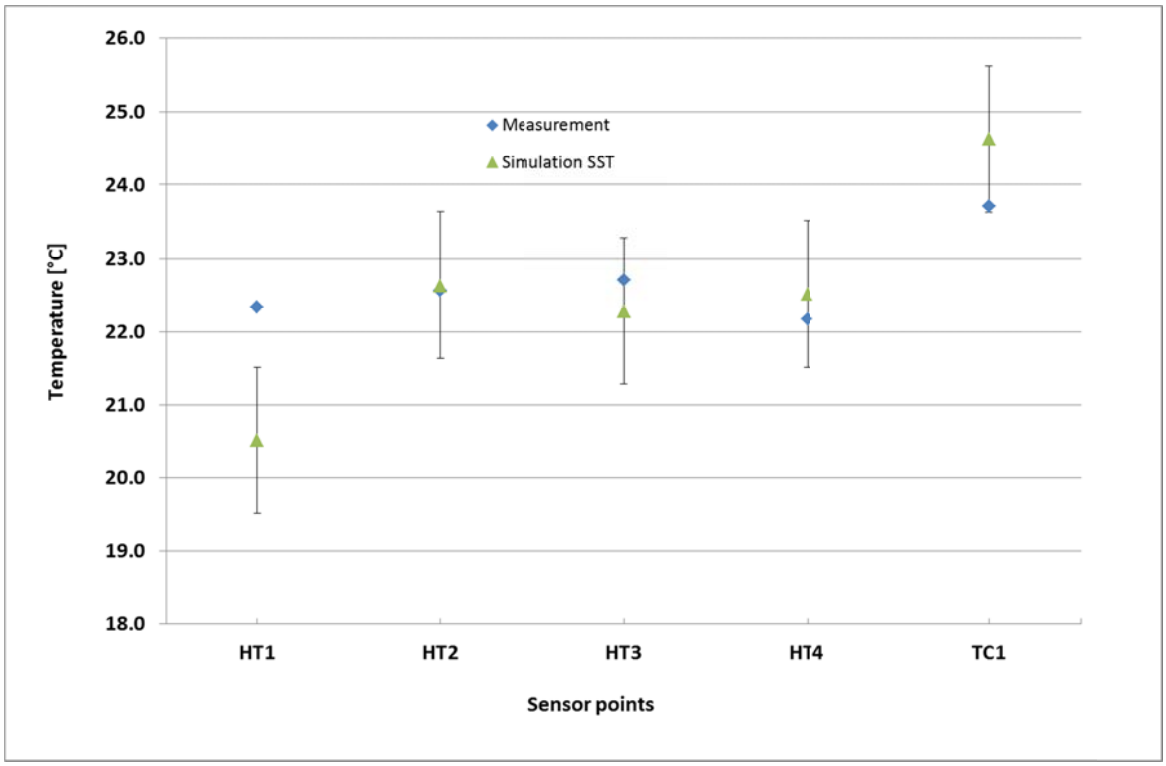

Figure 6-11: Comparison of measured and simulated temperature at installed sensor points.

The instantaneous velocities, once averaged using LaVision DaVis PIV processing software (LaVision, 2011), show a stable and well developed thermal plume which compares well with the steady state CFD simulation results (see Figure 6-10).

Simulation results based on the SST turbulence model show a wider thermal plume with higher velocities as compared to measurements. The maximum instantaneous velocity for the measured period of time showed a value of 0.41 m/s whereas the average velocity (ensemble averaging) in the thermal plume obtained using PIV was 0.24 m/s. The maximum average velocity in the thermal plume using CFD simulations was found to be 0.38 m/s. For the conducted CFD simulations, the

maximum y+ values on the surface of the manikin for simulation using the SST turbulence model was found to be 3.6.

In addition to the PIV measurements conducted at the environmental chamber of Loughborough university, simulation results for the velocity field is compared with the work done by Homma and Yakiyama (1988) as shown in Figure 6-12.

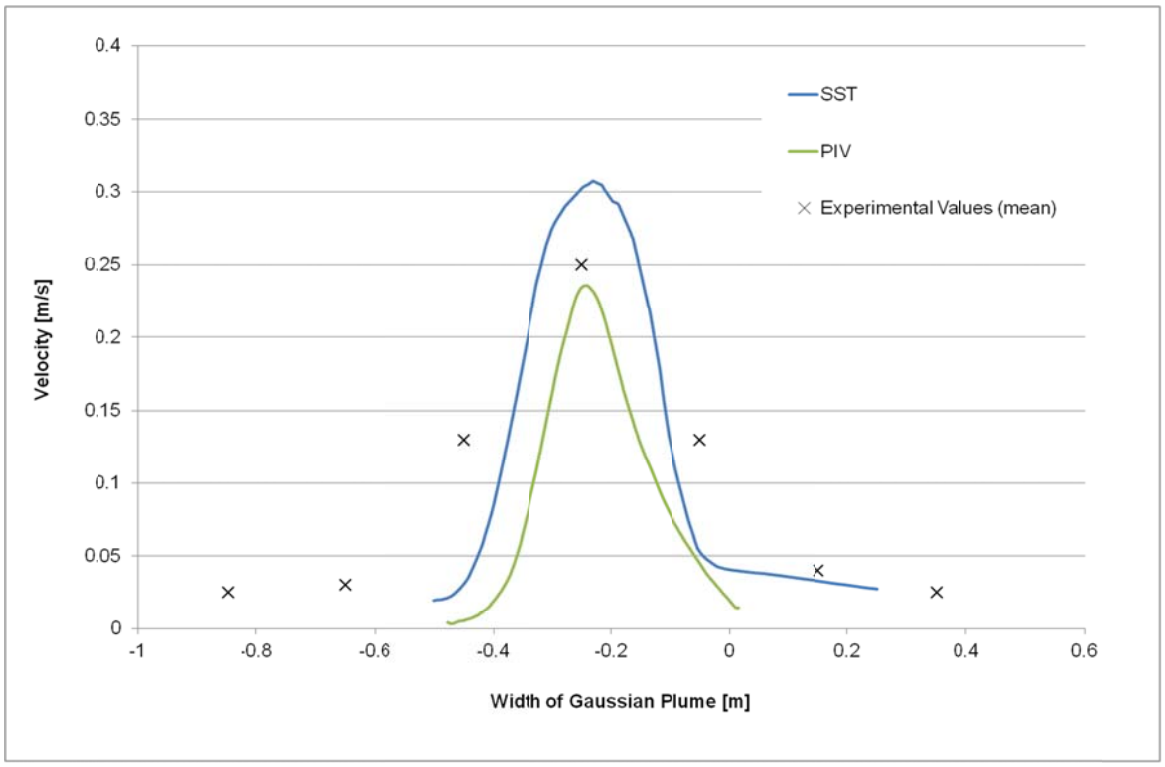

Figure 6-12: Comparison of measured and simulated velocities in the thermal plume

In the experimental work conducted by Homma and Yakiyama (1988), the volume flow rate was determined by defining a rectangular flow region installed with hot wire anemometers. Using traverse velocity measurements along the edges of this flow region equipped with hot wire anemometers forming a closed rectangle (see (Homma & Yakiyama, 1988) for their detailed experimental setup). The values were then averaged and integrated over the area to give the volume flow. They reported an average value of 41 l/s (min 28 l/s and max 60 l/s) for subjects with undershirt clothing and an average value of 40 l/s (min 29 l/s and max 53 l/s) for subjects with undershirts and long-sleeve clothing. It is not possible to gather the volume flow information from the PIV measurements. CFD results were analysed for the flow rate at the position analogous to the measuring positions described in experimental work

from Homma and Yakiyama Results obtained using the simulations gave a volume flow of 58 l/s above the seated manikin.

The thermal plume characteristics do not show an ideal plume development as given in the theory for thermal plumes generated by a point source. This fact of non-ideal and asymmetrical plume behaviour and variation in the strength of the thermal plume is discussed in previous literature e.g. Kofoed and Nielsen (1990), Zukowska et al (2007) (2012). The literature indicates that a quantitative analysis for a complex 3D plume generated by a seated human object/manikin means extending the plume theory possibly beyond its limits. In this research work, the application of plume theory is limited to the calculation of the dimensionless plume entrainment coefficients rather than calculating the volume flow based on these entrainment coefficients.

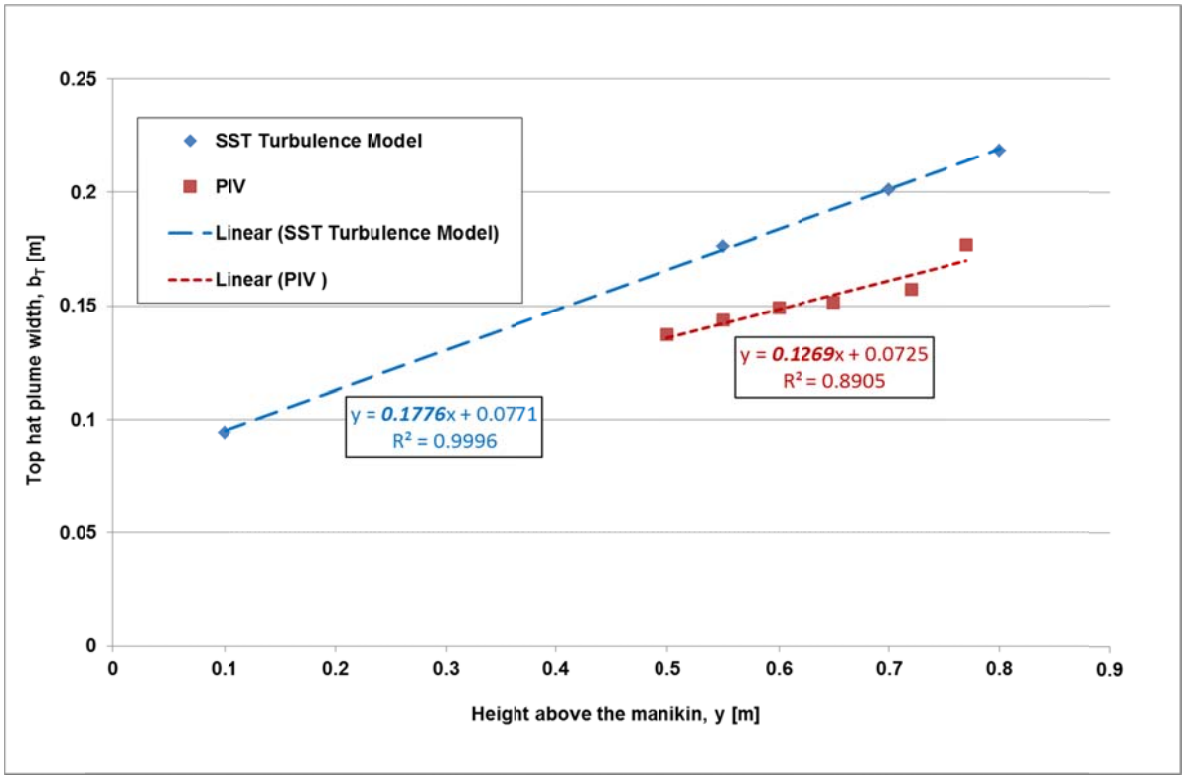

Figure 6-13: Comparison of measured and simulated velocities in the thermal plume

The bold italic numbers in the graph in Figure 6-13 show the gradient of the lines representing the entrainment coefficient. The entrainment coefficient governs the rate at which air is entrained into the thermal plume due to buoyant force.

The results in Figure 6-13 are plotted for the rear of the seated manikin where the thermal plume is considered to be well developed and representative of the assumption used in the derivation of the thermal plume theory. The results predict entrainment coefficients of 0.13 and 0.18 for PIV and SST turbulence model respectively.

6.4 Summary

This work has demonstrated how PIV can be used to investigate the low velocity air flows around human bodies and has been compared with analytical and CFD models. Simulation results based on the SST turbulence model show a wider thermal plume with higher velocities compared to the PIV measurements. Similar behaviour was also observed by Cook (1998) when using the standard k-ε model where a wider plume was thought to be caused by over-prediction of entrainment into the plume. As the SST model blends a k-ω model in the near wall region with a k-ε model in the outer region, it is likely that the SST model exhibits similar characteristics in terms of plume entrainment.

The velocity profiles obtained using PIV and SST turbulence models were analysed using thermal plume theory. The results show that PIV gives an entrainment coefficient of 0.13 corresponding well with the work done by Morton (1956). The values predicted by SST turbulence model however seems to have over predicted the entrainment coefficient when compared with the published work.

On the basis of the validation study presented here, it can be concluded that the SST model predicts well the flow fields associated with the thermally induced flows generated due to human metabolic heat. In order to exploit the full potential of the SST model reported by the code developer (CFX, 2010), (Menter, 1994) for buoyancy driven flows, more work is needed to investigate the meshing and numerical modelling requirements for this particular model.

The experimental data presented here has also shown the PIV technique to be useful for the validation of CFD simulations as a result of its planar nature and the comparable density of velocity data measured across a plane to that extractable from CFD simulations, allowing the easy and direct comparison of results over large areas. This data density also significantly reduces the experimental time than would be

required to acquire the same quantity of flow data using a traditional traversed point wise technique. The technique does however have its limitations, mainly in that, as discussed, plume volume flow rates cannot be calculated from the 2D planar data included in this study. Although this could be resolved by the use of a stereoscopic technique to acquire three component velocity data across a number of planes which would enable the volume flow rates within a region to be calculated. Field of views are also typically smaller than would be ideal for this type of study, mainly due to the restrictive laser power requirements of extremely large “Field of Views” (FoVs). This therefore makes the PIV technique more suited to detailed investigations of the flow fields over smaller areas, the validation of these areas with CFD simulations then providing confidence in the accuracy of CFD simulations over the wider domain.

The presented validation work shows the limitations of the PIV technique and the application of SST turbulence model when predicting the buoyancy driven flows in the immediate vicinity of a seated thermal manikin. The results obtained from the validation study serve as guidelines for further investigating the effect of respiration on the thermal plume and vice versa.

7 Modelling Respiration

Respiration is the process of breathing in the surrounding air via our nose and mouth and then breathing it out to the surrounding via the same route. Respiration process is used by the body to carry out the metabolic cycle for living. The air we breathe in is about 21% of Oxygen (O2), 78% of Nitrogen (N2), 0.03% of Carbon dioxide (CO2) and a variable amount of water vapour. The air is transported to the lungs and then further used by the body for the metabolic processes. As a result of these metabolic processes consisting of a number of chemical reactions in the body, CO2 is produced as a by-product. The resulting CO2 which is about 4-5% (by volume), along with 17-18% O_2 and about 78% of N_2 is exhaled. Considering the presence of several organic and inorganic pollutants/contaminants in air, the quality of inhaled air can vary strongly from one environment to another. An environment charged with high quantities of contaminants in the inhaled air can cause health issues for the occupants of that environment.

Measurements with real subjects in a built surrounding involving investigation of IAQ is always coupled with uncertainties and inhomogeneities that can easily lead of misinterpretation of results (Olmedo, et al., 2012) (Bjørn & Nielsen, 1988). These variables causing inhomogeneous test conditions include the presence or absence of occupants, occupants' position, posture, air flow conditions within the investigated zone etc. The effect of some of these variables cannot be ignored as they directly influence the analysis and evaluation of results as reported by different researchers (Karthikeyan & Samuel, 2008) (Steiger, et al., 2008). In order to keep the test conditions as homogeneous as possible, use of breathing thermal manikins (BTMs) has become popular (Melikov, 2004) (Melikov, et al., 2000). Using BTMs can restrict the above mentioned difficult to capture inhomogeneities and variations associated with tests on real occupants. The literature review has shown that alongside the use of BTMs, advancement in the computational hard- and software has led to significant interest in the use of computational methods to quantify the various phenomena associated with respiration process. Human thermo-physiological models rely on the inputs from either measurement or computational simulations (Huizenga & Hui, 2001), (Fiala, 1998), (Tanabe, et al., 2002), (Zhang, 2003). With the increase in

architectural complexity of buildings, innovations in HVAC and consciousness about energy saving, the importance of the indoor air climate has become a preliminary focus. In the author's view, a computational modelling approach using BTM that is validated using in-lab tests and measurements is the best methodology to reach an optimized building design.

Evaluating the effects of the surrounding air quality on respiration and vice versa has been a key focus in indoor climate and air quality studies in the last 20 years. It is reported that increase in CO2 level in the surroundings cause the occupants of that surrounding to breathe at higher rates (Hedger, 2011). In addition, poor indoor air quality (often represented by high CO2 concentration) is reported to affect the health and well-being of human beings (Meckler, 1996). Some of the previous experimental, analytical and numerical work concerning IAQ which highlights the importance of respiration is presented in chapter 2. This chapter focuses on the methodology followed to simulate the human respiration in an indoor climate. The results obtained showed the effect of inhalation and exhalation on the immediate vicinity of the body as well as its effect on the indoor surrounding. Present work compares a simplified and a detailed geometrical human body shape for the differences in the generated flow field and transport of contaminants. It is important to note that the detailed geometrical body shape used is that of the thermal manikin "Victoria" which was thoroughly validated for both convection and radiation phenomena in indoor climates (see chapters 2, 5 and 6).

7.1 Human Respiration Modelling

In order to computationally model a thermal manikin for breathing in detail, the following aspects need to be correctly addressed.

a. Buoyancy: modelling of thermal buoyancy so as to predict the thermal plume behaviour.
b. Geometry: predicting the effects of geometrical shapes and posture of the breathing model on the thermal plume and the surroundings.
c. Boundary conditions: proper implementation of the boundary conditions that are directly related to respiration modelling such as breathing rate, temperature of the exhaled air etc.

During the course of this PhD work, a detailed computational thermal manikin "Victoria" is validated to predict the extent of the thermal plume due to a seated female (see chapters 5 and 6). The validation was conducted against experiments using a thermal manikin (Victoria) used primarily for the thermo-physiological investigations in a climatic chamber at the Civil and Building Engineering School of Loughborough University. The model used for the experiments was equipped with a breathing unit. Similar to the validation process employed in chapter 6 for a sedentary non-breathing manikin, a series of breathing experiments were conducted in the climatic chamber. The flow field was visualized using the PIV technique (Figure 7-1).

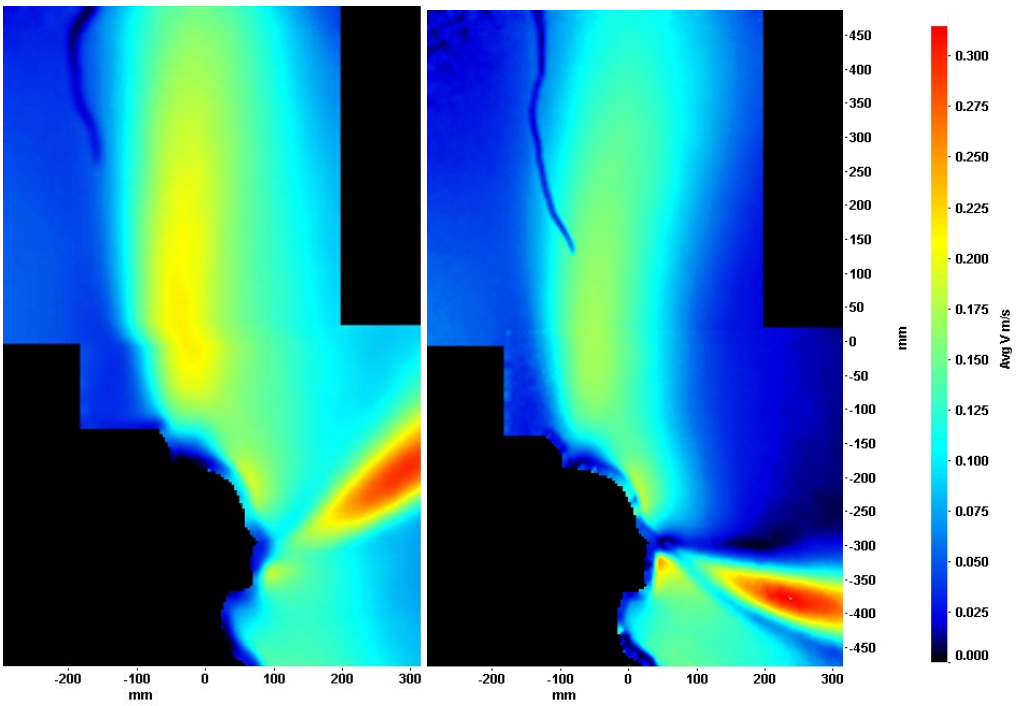

Figure 7-1: Test results of PIV for breathing manikin in LU chamber.

Analysis of PIV results of Victoria highlighted some significant discrepancies when compared with the previous published studies (see literature review). As a result of these discrepancies, the experimental model could not be used to validated the breathing process by means of a computational model. These discrepancies are mentioned below.

a. The pulmonary rate and hence the exhaled volume flow was not calibrated so it was not possible to source reliable inlet/outlet boundary condition data.

b. The temperature of the exhaled air coming out of the nostrils could not be controlled due to a missing air coil heating unit, thereby not enabling any thermal buoyancy effects due to exhaled air to be simulated.
c. CO2 could not be mixed with the air coming out of the nostrils thereby not enabling CO2 mixing or settling to be investigated.
d. The air tubes inside the nostrils were displaced from their originally documented position, thereby not allowing accurate geometrical data to be set regarding the angle of issuing air jet.
e. In the absence of a mixture analysing unit, it was not possible to quantify the amount of inhaled source particles.

As it was not possible to fix the above properties within the given time frame of the experimental tests, the experimental breathing tests were not pursued further for respiration validation.

7.2 Simulation Methodology

In order to investigate the effects of contaminant transport owing to the natural convection due to the presence of a human manikin, a simple empty room was first modelled with constant wall temperatures, the upper boundary is modelled as a free opening and the lower boundary is modelled as a very low velocity inlet with a contaminant source. The contamination is modelled as a passive scalar (particles following streamlines with no mass). This room was later equipped with a simplified breathing manikin as well as a detailed seated breathing manikin to investigate the effects of geometry and breathing on the thermal plume, dispersion of contamination and CO2 transport in the simulated space. In order to make a quantitative comparison, the surface area of the simple geometrical manikin was kept similar to that of Victoria.

The computational models were simulated in steady state for both exhaling and inhaling processes as well as in transient state for one complete breathing cycle. The exhaled air is modelled as fully saturated air (100% relative humidity) containing 4.5% (volume) of CO2 (Valerie & Sanders, 2010). The results are presented for temperature, relative humidity, contamination and velocity fields. The quantitative graphs for the above named variables are plotted as line averaged values. The lines

are located at positions shown in Figure 7-2. The colour of each of the line correspond to the distance from the centre line i.e. green line = 0 cm from the vertical centre line, purple line = 7.5 cm from the vertical centre line, blue line = 15 cm from the vertical centre line. Similarly the red line is located at -7.5 cm from the vertical centre line and light blue line at -15 cm from the vertical centre line. This colour coding is employed for the quantitative analysis presented later in this chapter.

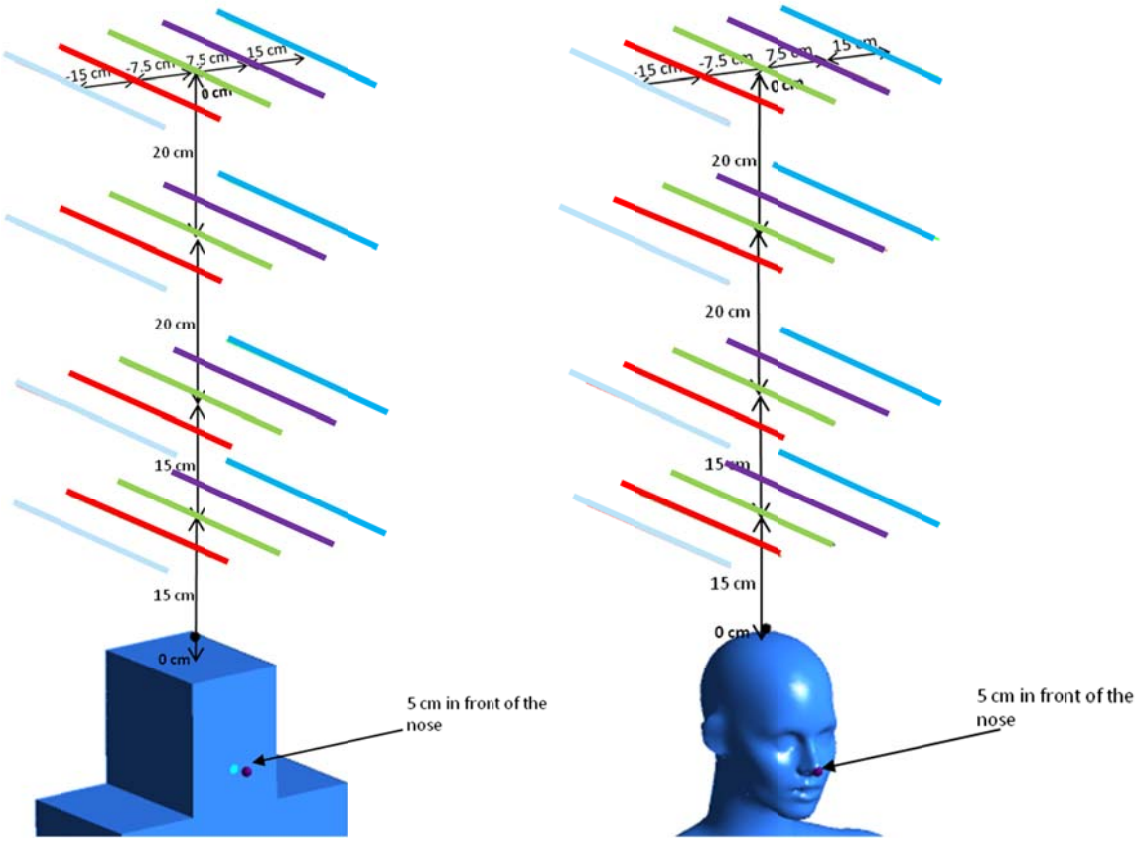

Figure 7-2: Evaluation points and lines

The length of each of the lines is set to 0.5 m. This length is based on the validation study presented in chapter 6 which showed that the thermal plume effects can be sufficiently evaluated by considering the length of 0.5 m. In addition to the lines, one point is located just above the top of the head in the wake zone and another 5 cm in front of the nose. As these two points are located in regions dominated by turbulence effects, they can be used as monitor points to estimate the turbulence level and to judge the numerical convergence.

The values of the passive scalar (representing contamination) are made non-dimensional in order to minimize the numerically induced effects due to small number

round-offs, internal discretization and interpolation of results from mesh centre points to mesh edges and vice-versa. The dimensionless concentration level *C_dim* is defined as;

$$C\_dim = \frac{c}{c_{max}} \qquad \text{(Eq. 7-1)}$$

where c is the concentration at a point in space and c_{max} is the maximum concentration at the floor level.

7.3 Geometrical Models and meshing

As the aim of the work is to develop a validated computational model of a sedentary manikin that can be employed for various investigations concerning indoor air quality, thermo-physiological studies and indoor climate designs, the model should be such that it can be fully integrated in different geometrical surroundings. For the current investigations, a surrounding box of size 1.2 m x 2.44 m x 2.46 m (W x L x H) is modelled.

The simplified and the detailed manikins were modelled separately in the surrounding box. The geometries were prepared using the CAD tool Rhino (Rhinoceros, 2010) as shown in Figure 7-3.

(a) (b)

Figure 7-3: Geometrical position of seated simple manikin (a) and seated detailed manikin (b)

The simplified and the detailed manikins were modelled separately in the surrounding box. The geometries were prepared using the CAD tool Rhino and meshed using the software ANSYS ICEM CFD. The mesh sizes were 700 k cells, 1.4 M cells and 2.4 M

cells for the empty room, room with simplified geometry and room with detailed geometry respectively. The geometrical models of the two geometries and a mesh plane passing through the centre of the computational domain are shown in Figure 7-4.

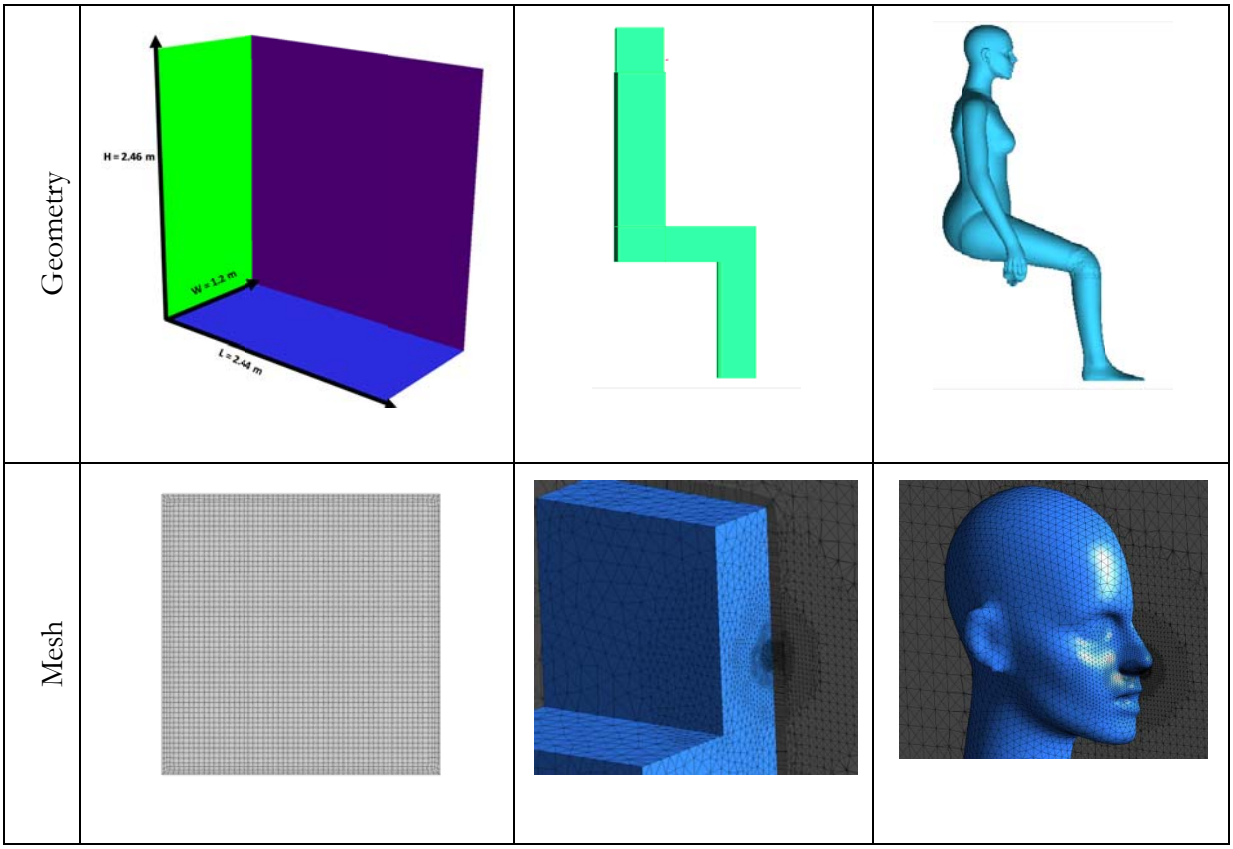

(a) Simple room (b) Simple manikin (b) Detailed manikin

Figure 7-4: Geometry and corresponding meshing at a plane along the centre of room

It is important to note that for both the simple and detailed manikin models, local mesh refinement and prism layers are generated. The mesh parameters were kept similar to those used for the validation studies in chapters 5 and 6.

7.4 Assumptions and Boundary Conditions

The major assumption made for this study was the restriction in the extent of the domain and type of domain boundaries. The side walls were modelled as symmetry walls (see chapter 4 for brief description) not exchanging any heat transfer or flow across the surface where as the top is modelled as an opening (with zero relative pressure) which allows a flow reversal/re-circulation depending upon the flow

solution. In case an inflow occurs, the temperature of inflow was taken as the average temperature of the outgoing air. The lower boundary was modelled as an inlet with a very low inlet velocity of 0.001 m/s with a relative humidity of 50% at an air temperature of 22°C. Relative humidity in case of inflow is modelled to follow the same principle i.e. average of outgoing relative humidity. The contamination source was released at floor level with a concentration of 0.001 kg/m^3. No contamination is modelled to enter the domain in the event of an inflow at the upper boundary (opening boundary).

The human body is given a constant surface temperature (mean surface temperature) of 31°C (Sørensen & Vøigt, 2003) (Benedict, et al., 1919). The nostrils are modelled as inlets (providing mass flow into the calculation domain) for exhaling simulations and outlets (extracting the mass out of the calculation domain) for inhaling simulations. The nostrils correspond to an area of 52 mm^2 (Melikov, 2004). This value corresponds well with the detailed study on the characterization of breathing parameters by Gupta, et al. (2010). The breathing flow rate is kept to a total of 6 litres per minute representing a sedentary person for both the inhaling and exhaling simulations. The value of 6 L/min is calculated according to the formula;

$$\dot{V} = V_T \times f_{resp} \qquad \text{(Eq. 7-2)}$$

where $\dot{V}$ is the breathing flow rate, V_T the tidal volume and f_{resp}, the respiration frequency.

For sedentary persons, the tidal volume is considered to be 500 mL (Guyton, 1984), (Castro, 1998) with a breathing frequency between 10 - 20 breaths per min (Asmussen & Nielsen, 1989). For the present work, the breathing frequency is kept to 12 breaths per min.

Two types of simulations are used for respiration studies, steady and transient. For steady state simulations, the constant (standard) false time stepping with coupled solver is used. For transient simulations, real time steps that vary with the user-set convergence criteria are used. One complete breathing cycle consists of an exhaling cycle of 2.5 seconds followed by a pause of 1 second and then an inhalation cycle lasting 2.5 second (Straub, 1998), (Castro, 1998). A set of transient simulations

(consisting of a complete breathing cycle) are conducted for the simple as well as the detailed manikin geometry. The boundary conditions described above are graphically shown in Figure 7-5.

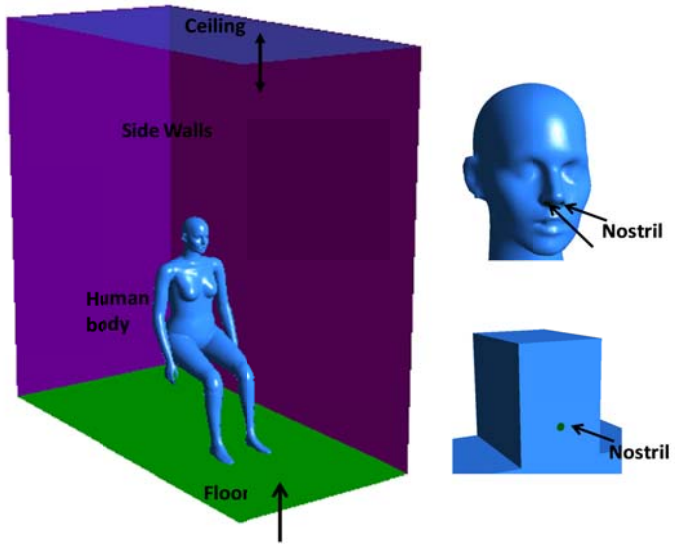

Figure 7-5: Graphical representation of the different boundary conditions

The nostrils for the detailed manikin are geometrically modelled to have a 3-D inclination consisting of two angles namely α and β of 30° and 45° respectively (Melikov, 2004). For the simplified model, a flat nostril area of 104 mm^2 (Melikov, 2004) with single inclination β was used (see Figure 7-6).

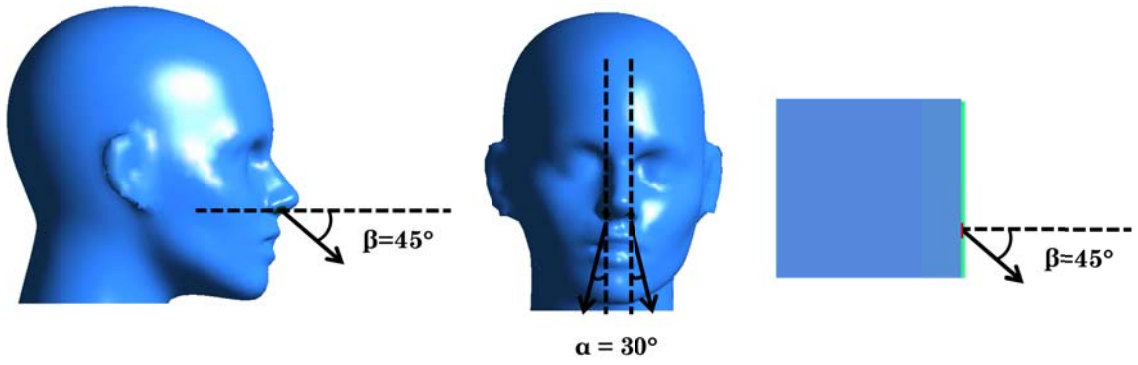

Figure 7-6: Nostril details of the modelled geometry

In case of exhaling, a volumetric CO2 concentration of 4.5% and water vapour mass fraction corresponding to a relative humidity of 100% was set at the nostrils. The exhaled air temperature was set to 35°C (Harger, et al., 1950) (Schonecht & Stock, 1995). The nostrils were modelled to have a turbulence intensity of 5% considering

the fact that the internal shape of the respiratory track would not allow a fully developed turbulent velocity profile. The top and bottom boundaries are given a zero gradient turbulence, i.e. considering the turbulence to be fully developed for the inflow condition.

7.5 Results

The results are presented graphically as contours of velocity, temperature, CO2, contamination (passive scalar), streamlines of velocity as well as iso-surfaces of contamination and CO2. Quantitative analysis of these variables are plotted at the locations stated in section 7.2.1.

7.5.1 Empty Room

The empty room with symmetry wall boundary conditions, lower boundary as inlet with a velocity of 0.01 m/s and contamination source of 0.001 kg/m^3 at air temperature of 22°C was simulated in a steady state. In the absence of asymmetric forces, the flow regime developed to a homogeneous flow, with pollutant concentration and temperature as shown at a central plane in Figure 7-7.

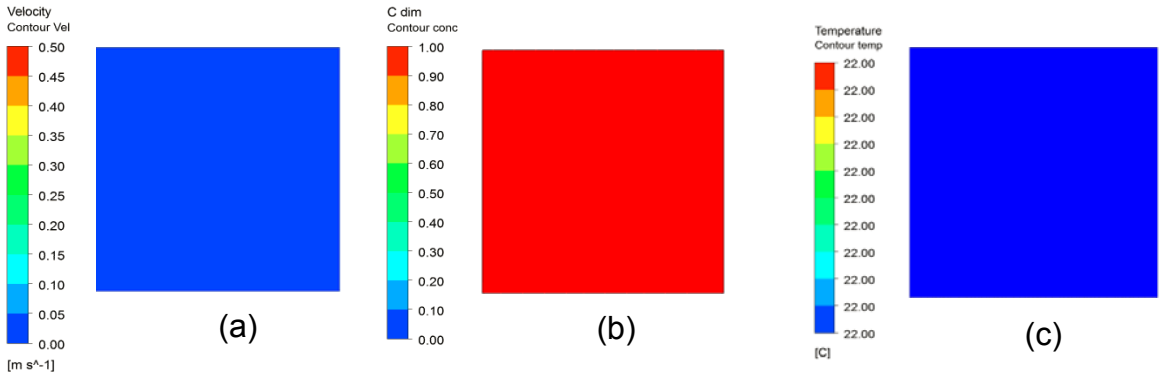

Figure 7-7: Results for empty room showing velocity contour (a), concentration contour (b) and temperature contour (c)

7.5.2 Modelling Exhalation

In order to see the effect of an exhaling sedentary person on an indoor environment, a simple rectangular shaped manikin as well as a detailed manikin, was simulated in the room with conditions mentioned in section 7.3.1. The nostrils were modelled as velocity inlets with sources of CO2 and humidity. The flow fields for temperature, velocity, relative humidity, room pollutant and exhaled CO2 by the two different

geometrical manikins are shown in the following figures for qualitative comparison. Qualitative comparisons are shown by means of graphs for different variable values at a height of 50 cm above the seating geometries. Evaluation of the above named variables conducted at different heights are given in Appendix B.

The effects on temperature and velocity variation of the complex and simplified manikin are shown in Figure 7-8.

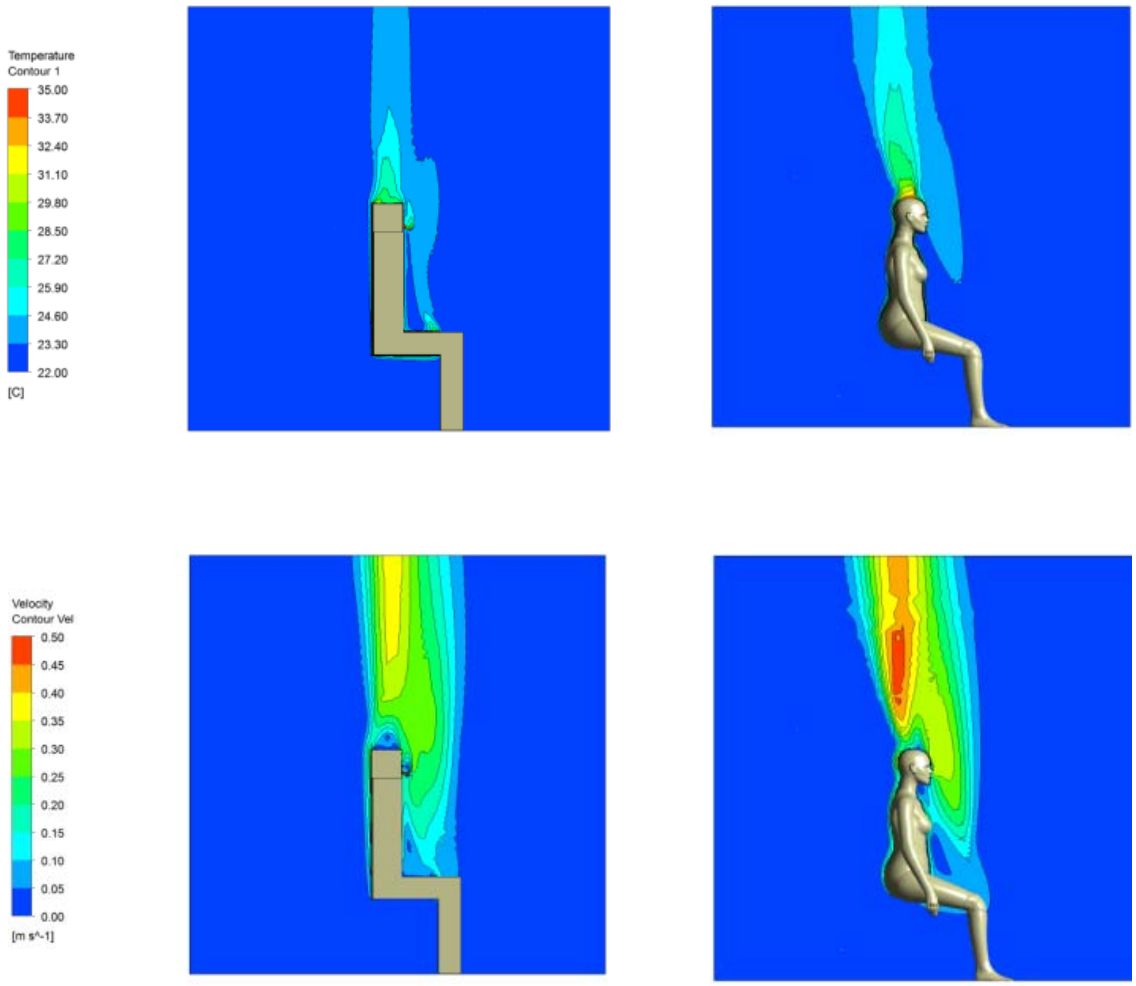

(a) Simple manikin (b) Detailed manikin

Figure 7-8: Temperature and velocity contours on a central plane in room occupied by (a) simple exhaling manikin and (b) detailed exhaling manikin

The simplified manikin shows a rather symmetrical thermal plume as compared to the detailed manikin. On the plane shown, the flow velocity in the thermal plume of the

detailed manikin has a maximum value of around 0.5 m/s whereas that for a simplified manikin reaches a maximum velocity of around 0.4 m/s. Considering the fact that both the geometries have the same surface area and same surface temperature, the change in the velocity distribution and the form of the thermal plume is attributed to the variation in the geometrical shapes.

A comparison of pollutant distribution due to thermal buoyancy of the sedentary geometries can be seen in Figure 7-9.

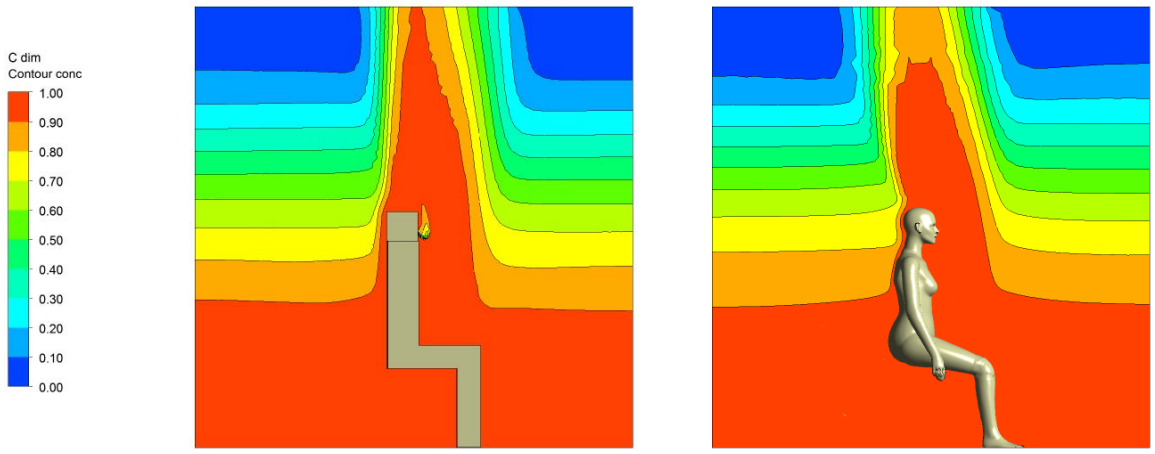

(a) Simple manikin (b) Detailed manikin

Figure 7-9: Variation in concentration level at a central plane in the room occupied by (a) simple exhaling manikin and (b) detailed exhaling manikin

The sharp decrease in concentration gradient exists in the vicinity of the opening boundary condition at the top marked by recirculation zones as shown in Figure 7-10. The flow pattern of re-circulating air as well as the concentration distribution will differ for the case that the geometry is placed underneath a solid wall.

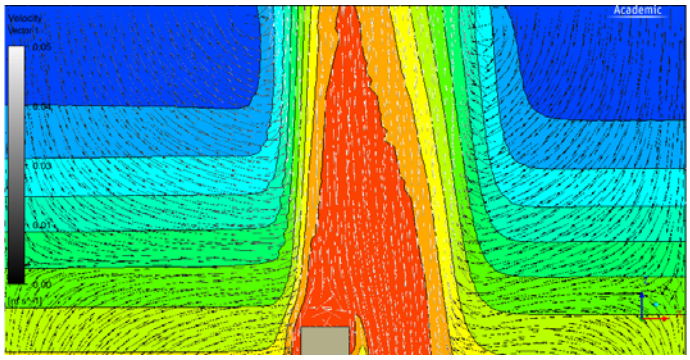

Figure 7-10: Concentration levels superimposed by velocity vectors showing flow entrainment into the thermal plume

Evaluating the CO2 distribution for the two geometrical manikins, it can be seen that the amount of exhaled CO2 in case of a simplified manikin gets entrained immediately in front of the nose whereas in case of the detailed manikin the entrainment follows a side-ways pattern due to the shape of the nose as shown in Figure 7-11.

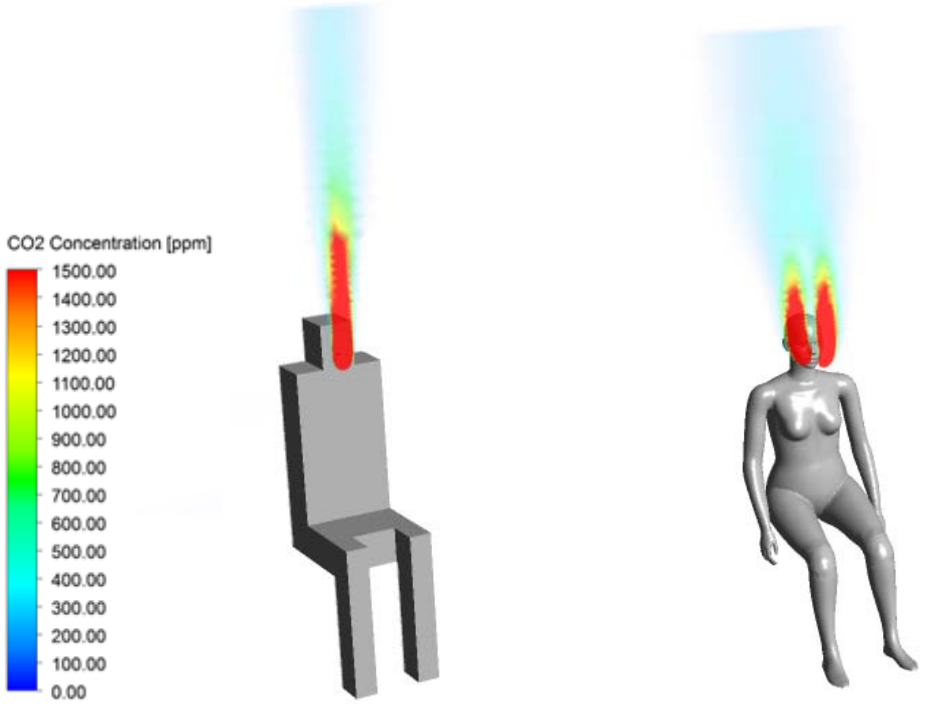

(a) Simple manikin (b) Detailed manikin

Figure 7-11: CO2 concentration represented as iso-volume in room occupied by (a) simple manikin and (b) detailed manikin

The generation of the 3D plume clearly shows that in the case of a detailed manikin, the CO2 distribution propagates not only along the vertical axis but is diverted sidewise following the warmer expired air hence a strong dependence on the nostril shape. This indicates that for a detailed manikin, the plume as well as the CO2 propagation is wider in the immediate vicinity of the sedentary person as compared to the simplified manikin. The plume distribution also shows that in the nose-tip region, the CO2 concentration level is very low. This fact is elaborated in Figure 7-12 showing CO2 distribution on a central plane passing along the nose for the two exhaling manikins.

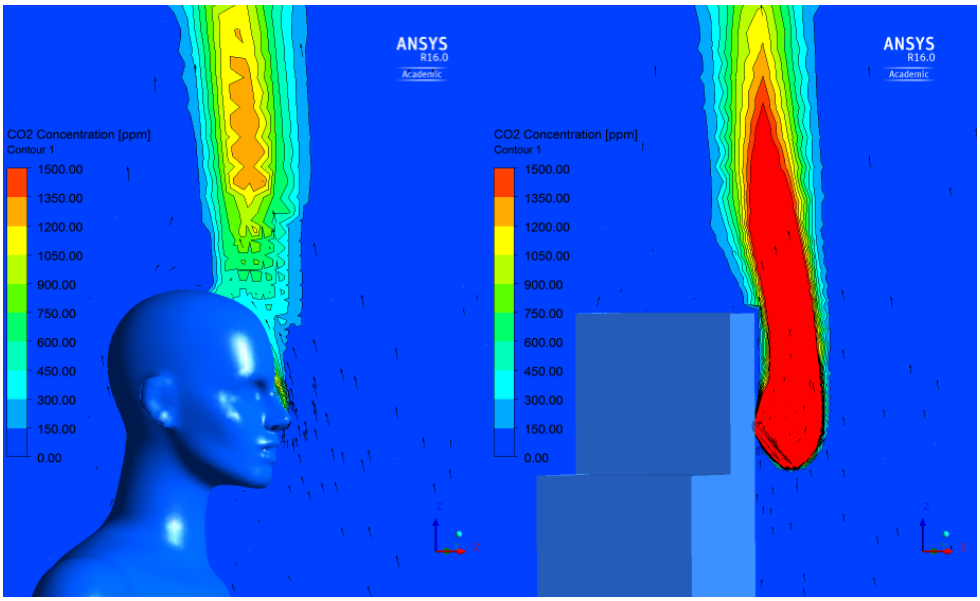

Figure 7-12: Close up view of a central plane showing contours of exhaled CO2

The results show that high CO2 concentration is present along the central axis of the simplified manikin in contrast to a detailed manikin. This characteristics shows that the dispersion of CO2 (and other pollutants) in the exhaled air is underestimated by using a simplified geometry.

The quantitative analysis for temperature, velocity, pollutant concentration, CO2 distribution and relative humidity for the exhaling manikins is shown at a location of 50 cm above the head in Figure 7-13 to Figure 7-22.

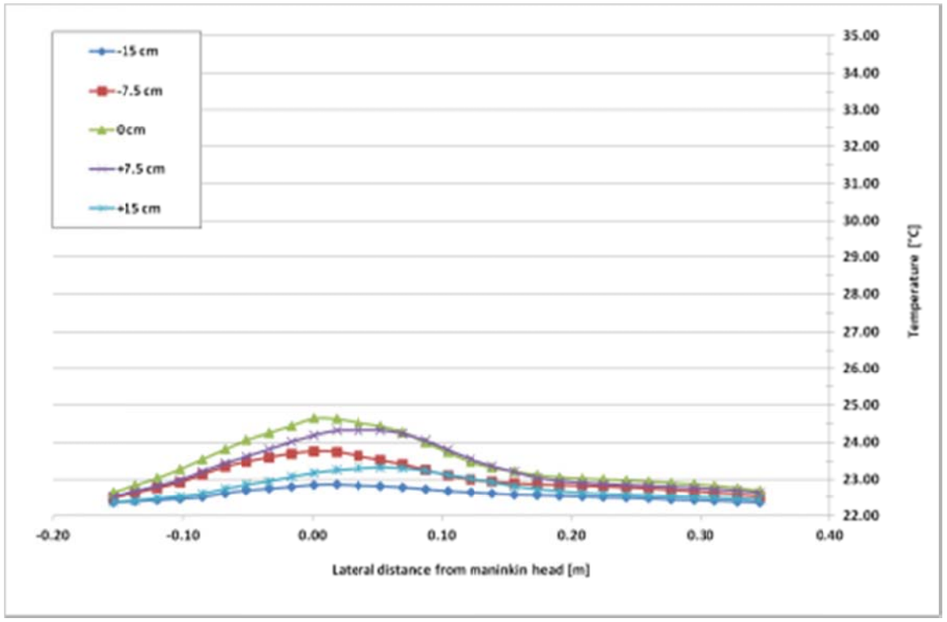

Figure 7-13: Temperature variation at 50 cm above simple manikin

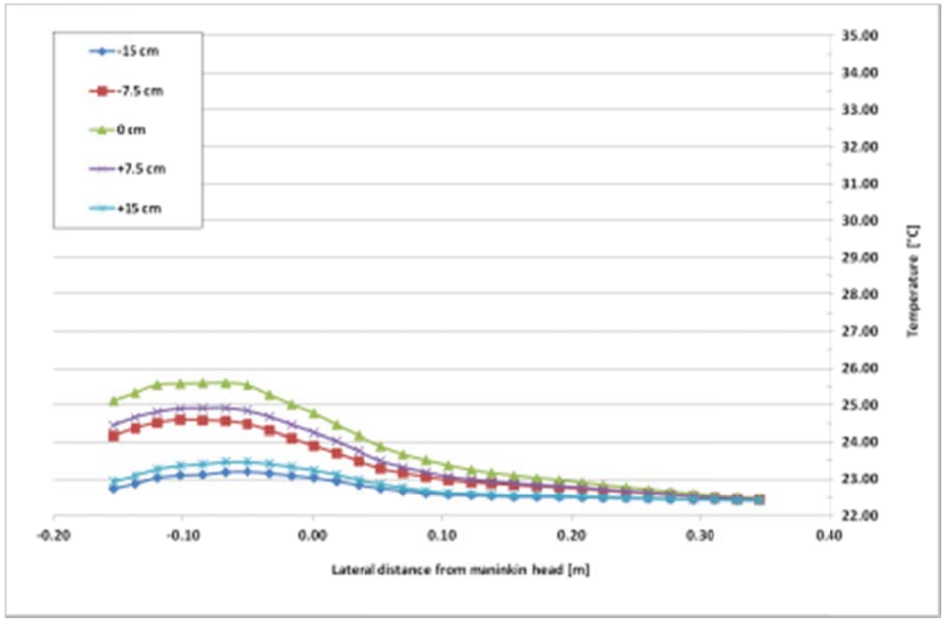

Figure 7-14: Temperature variation at 50 cm above detailed manikin

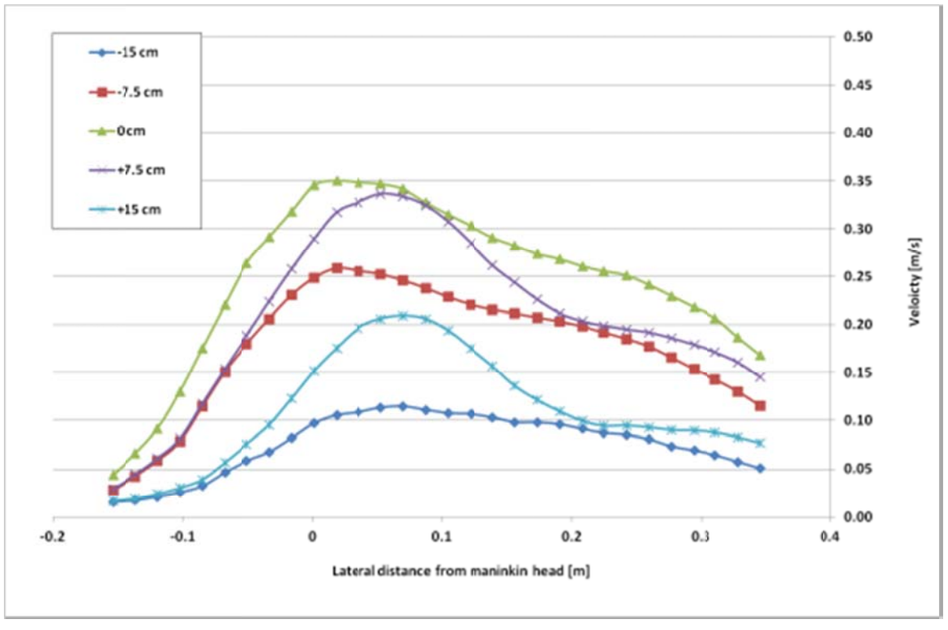

Figure 7-15: Velocity variation at 50 cm above simple manikin

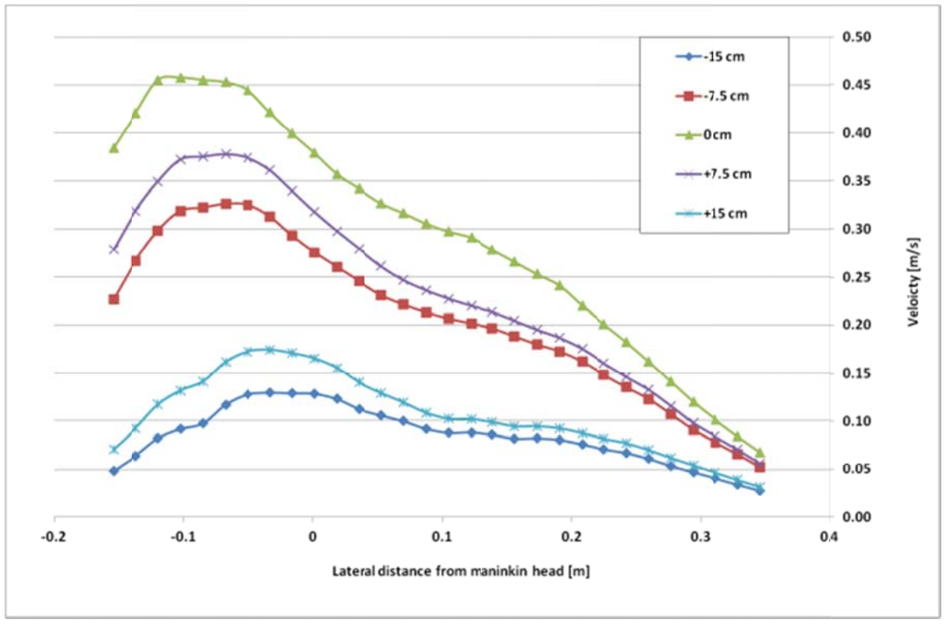

Figure 7-16: Velocity variation at 50 cm above detailed manikin

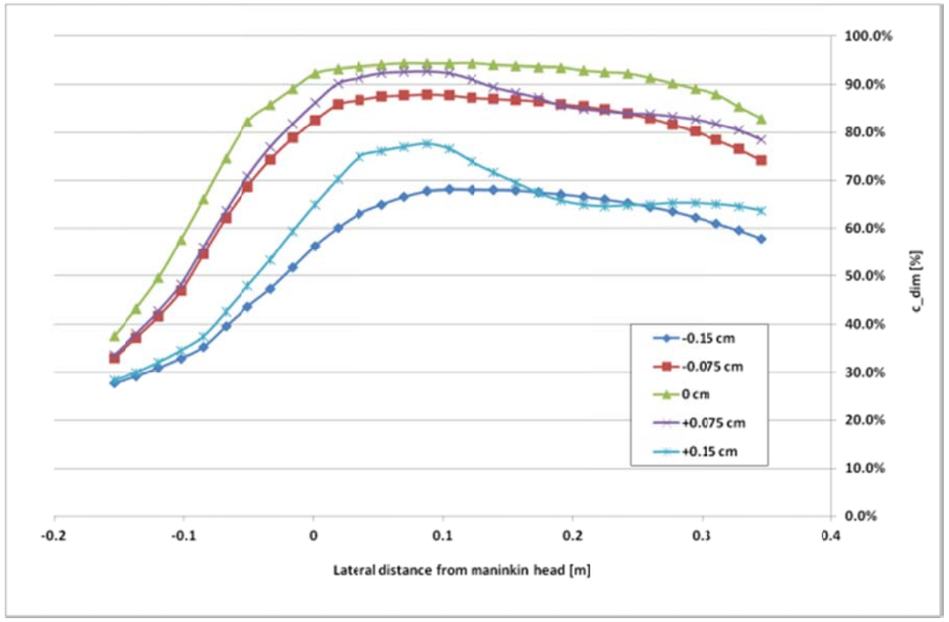

Figure 7-17: Pollutant variation at 50 cm above simple manikin

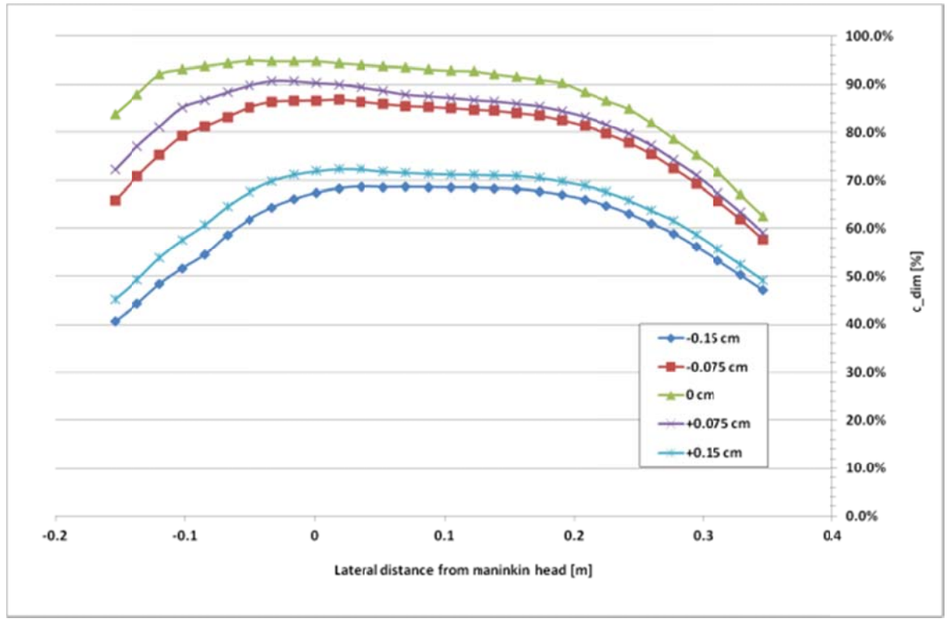

Figure 7-18: Pollutant variation at 50 cm above detailed manikin

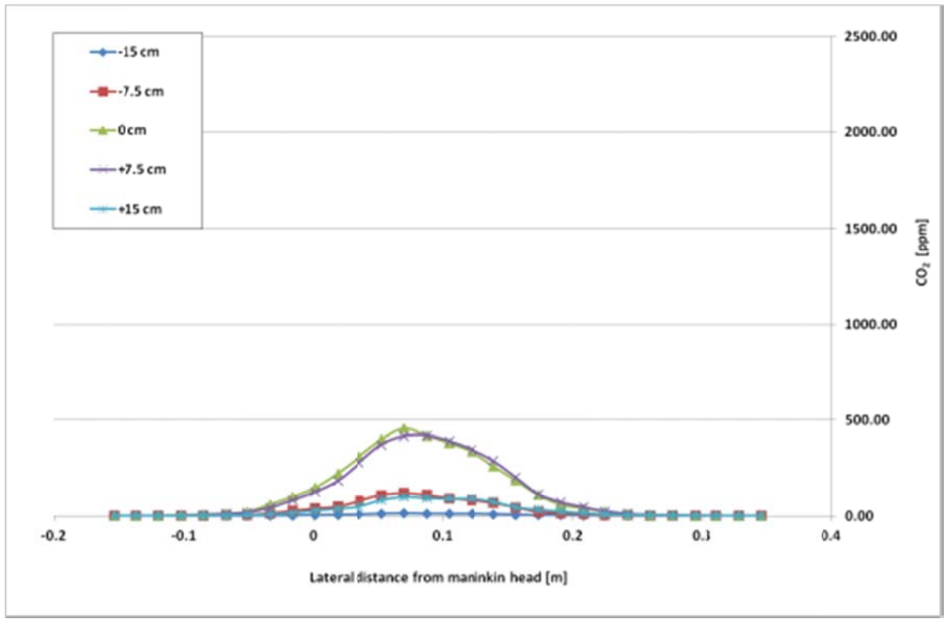

Figure 7-19: CO2 variation at 50 cm above simple manikin

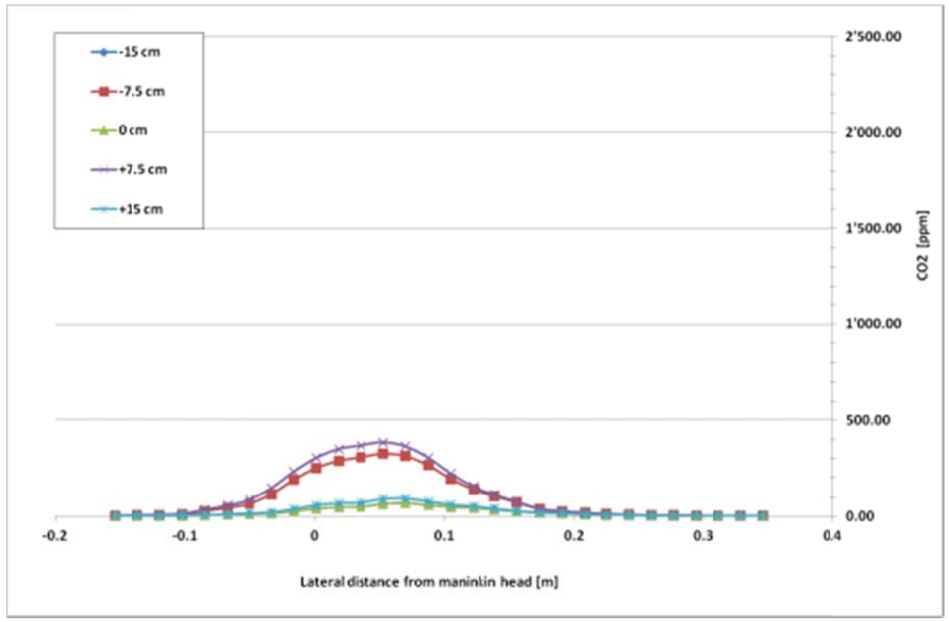

Figure 7-20: CO2 variation at 50 cm above detailed manikin

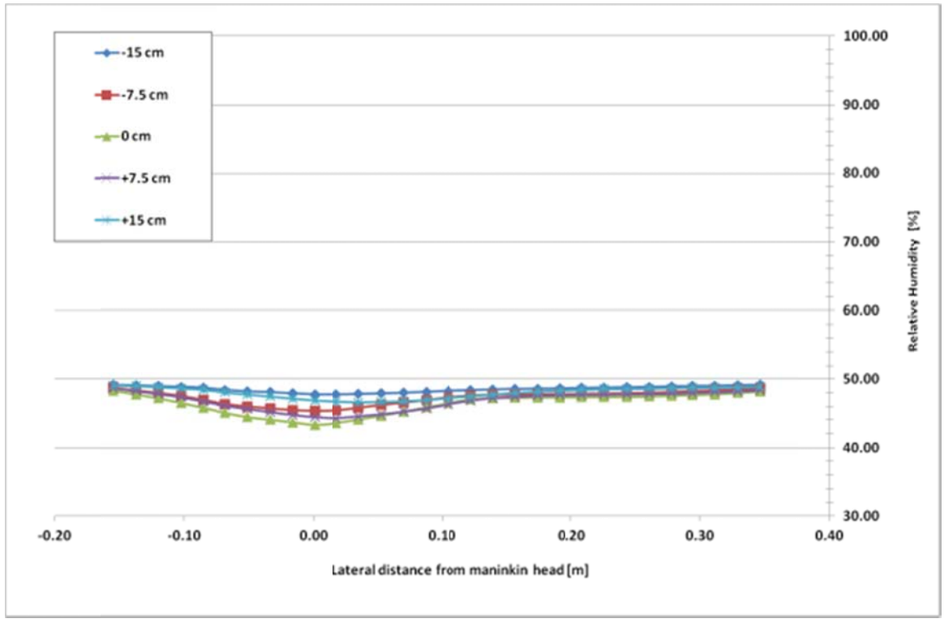

Figure 7-21: Relative humidity variation at 50 cm above simple manikin

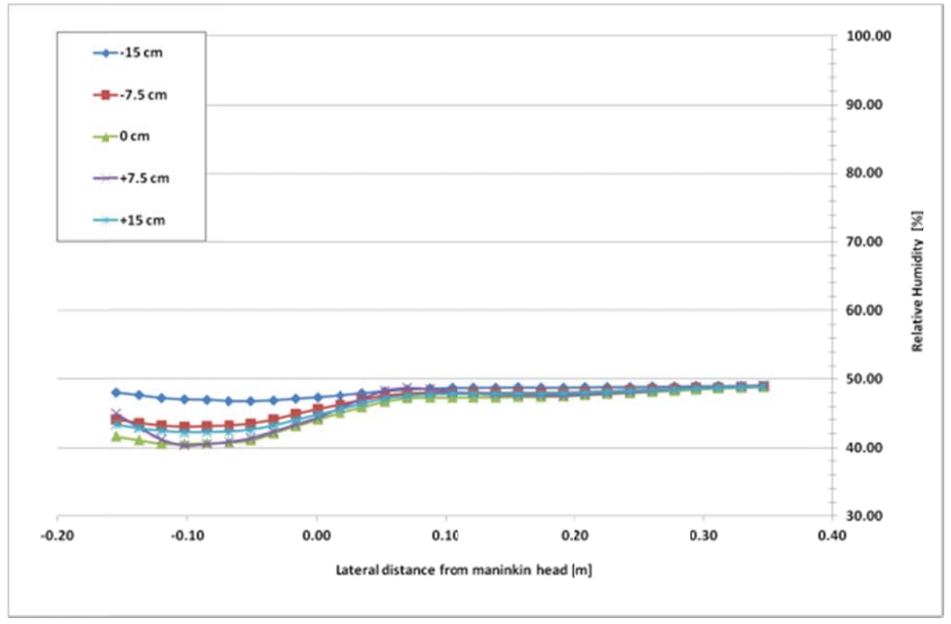

Figure 7-22: Relative humidity variation at 50 cm above detailed manikin

In the above graphs, a temperature increase towards the rear of the detailed manikin is seen which causes a drift in flow towards the rear of the manikin geometry. This drift is very similar to the results of the PIV and validation simulations (see chapter 6). The general form of the thermal plume remains very much similar to a non-breathing manikin illustrating the observation that for normal breathing (6 L/min as is the case in the current study), the thermal plume retains its shape and the exhaling process does not penetrate through the thermal plume region.

It can be seen that buoyancy forces lead to an increase in the local entrainment of air and hence the passive scalars. For the present work, the passive scalars are massless particles which follow the flow field and provide visualisation of the phenomena such as separation and entrainment. The extent of this entrainment in indoor climates depends on the particle size and their settling velocity and remains a subject of further research. In the case of the simple manikin, a sudden decrease in the concentration level is observed for the position +15 cm. This decrease is due to the fact that the majority of the evaluation points on the line lie in a region slightly outside the intensive thermal plume where the gradients fall rapidly.

Although the contours of CO2 concentration on a central plane in the close proximity of the nose show a completely different distribution pattern, this variation has very little influence at a distance away from the thermal manikin as can be seen in the quantitative analysis of CO2 at a distance 50 cm above the top of the manikins. A further analysis of relative humidity for the same location as above shows the effect of thermal buoyancy on the flow distribution and the corresponding change in the local relative humidity of the room air.

Considering the results of the above simulations, it can be seen that for a sedentary person breathing at low pulmonary rate of around 6 L/min, the thermal plume is not disturbed by the exhale-inhale mechanism. An increased breathing rate of about 8.5 L/min was employed by Gao et al (2006) and reported that the expired air does not penetrate through the thermal plume of a sedentary person. An additional simulation was performed during the present work with breathing rate of 10 L/min for the simplified sedentary manikin. A comparison between the results (6 L/min and 10 L/min) is shown in Figure 7-23.

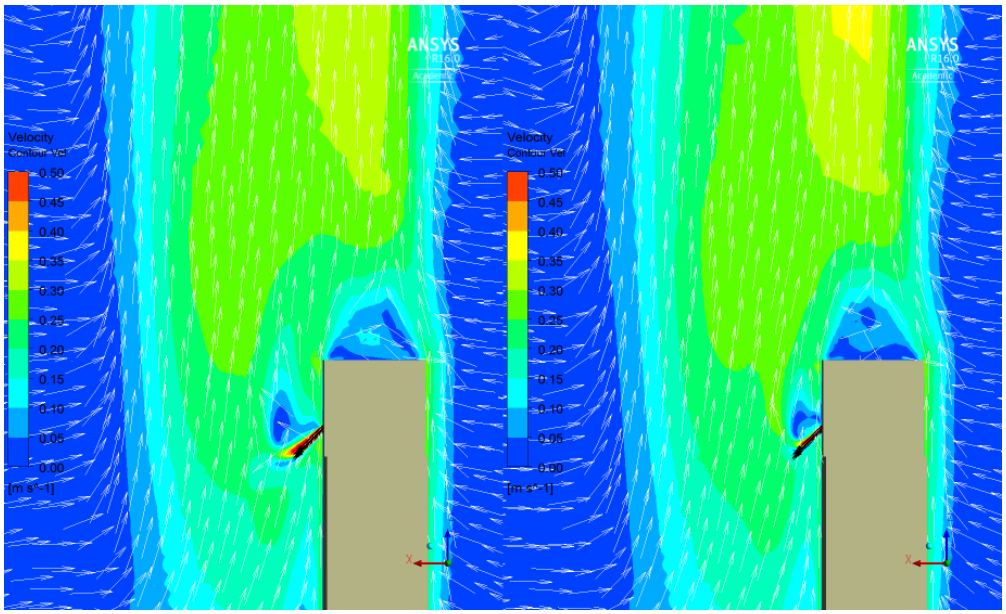

Figure 7-23: Comparison of exhaling simplified manikin with 10 L/min (left) and 6 L/min (right)

Figure 7-23 clearly indicates that even at high breathing rate of 10 L/min there is no disruption of the thermal plume by the expired air. 10 L/min is considered a high value for a sedentary person with light activity corresponding to a respiration rate of 20 breaths per minute (Asmussen & Nielsen, 1989). Other sources report this respiration rate to be in range of 12 - 18 breaths per minute (Barrett, et al., 2012) corresponding to breathing rates between 6 - 9 L/min.

Local variations in the thermal plume are however observed in the vicinity of the nose/head region. High activity rates or processes such as sneezing and coughing can lead to high flow velocities through the nostrils or mouth. For such processes the thermal plume is reported to be disrupted by Gao and his co-workers (2006) (2008).

7.5.3 Modelling Inhalation

In order to simulate inhalation, the nostrils of the sedentary geometries were modelled as velocity outlets. The amount of inhaled contaminants (passive scalar) depends upon the local flow fields. Qualitative analysis of different variables is shown on a central plane (see Figure 7-24) whereas quantitative values of these variables are for a height of 50 cm above the head of sedentary manikins. For the inhalation condition, no CO2 is present in the steady state inhale simulation. The general form of the thermal plume remains similar illustrating the fact that for normal breathing of 6

L/min (as is the case in the current study), the thermal plume retains its shape and the inhaling process does have an effect on the thermal plume region.

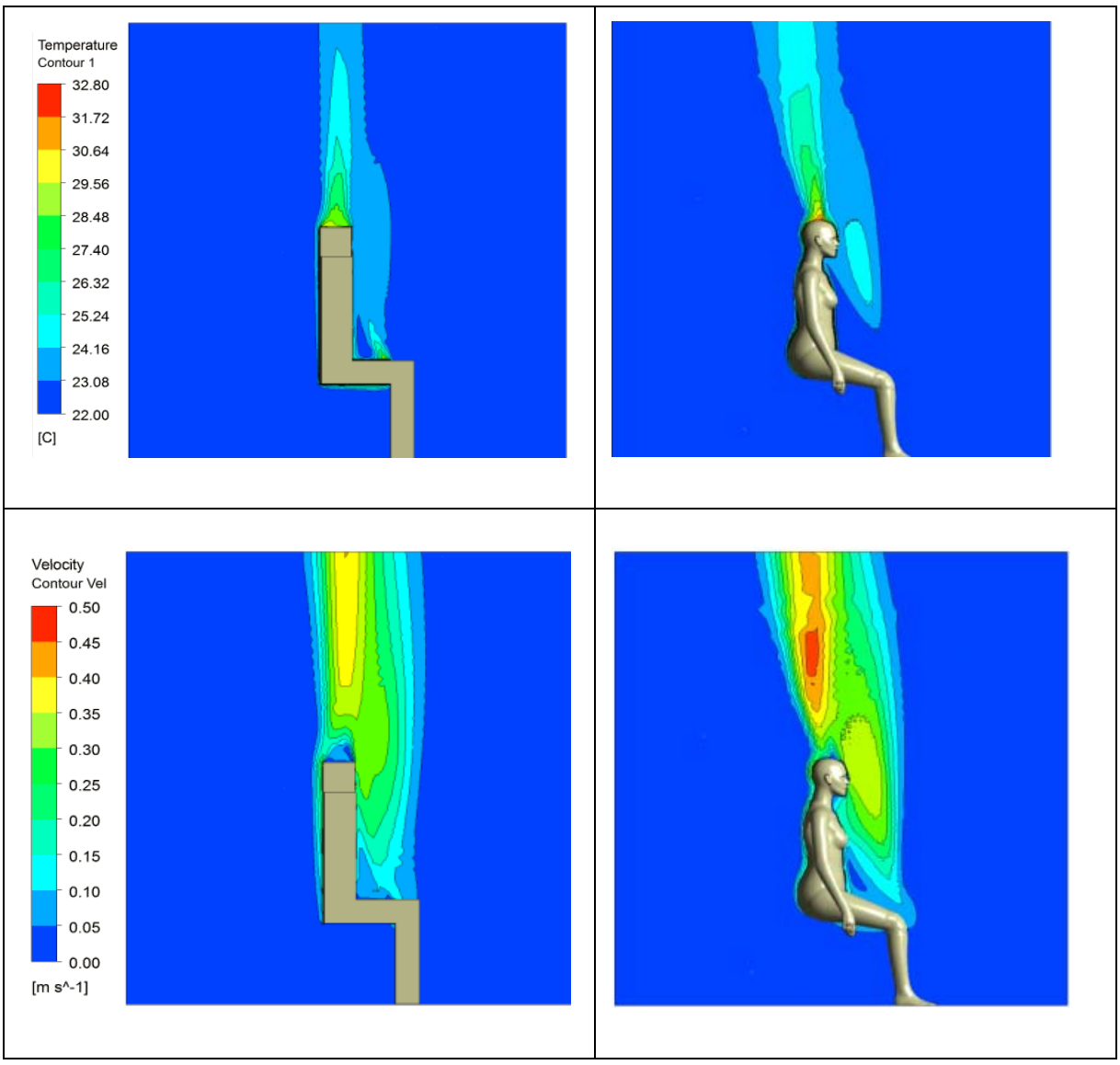

(a) Simple manikin (b) Detailed manikin

Figure 7-24: Temperature and velocity contours on a central plane in room occupied by (a) simple inhaling manikin and (b) detailed inhaling manikin

The flow and velocity fields near the nostril region differ from the exhaling simulation results. The velocity magnitude below the nostril region is higher as the inhalation process supports the natural buoyancy flow. Above the nostril region there is a retarding effect due to potential flow lines of the nostrils acting against the natural thermal buoyancy as shown in the close up view in Figure 7-25.

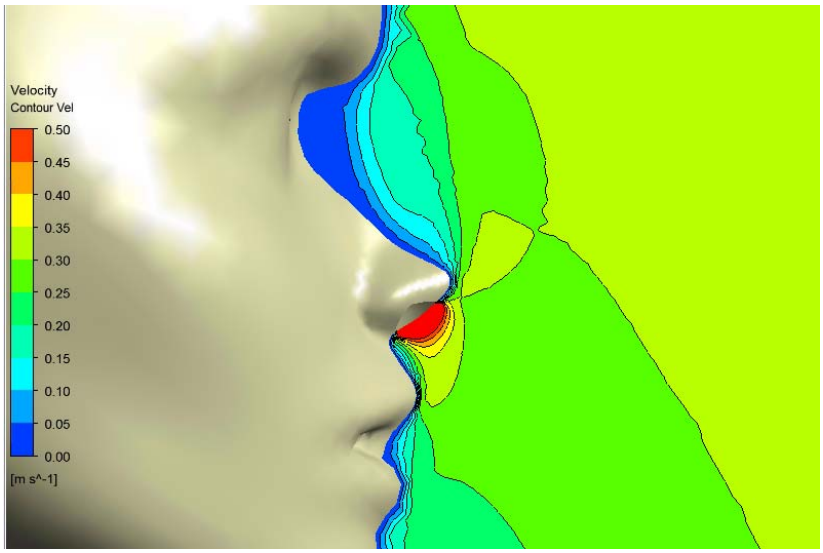

Figure 7-25: Close up view of the nostril region showing contours of velocity

The distribution of contaminants over the central plane is shown in Figure 7-26. A detailed evaluation at nostril boundaries show an increase of about 1.8% in the inhaled concentration for the detailed manikin when compared with the simplified manikin.

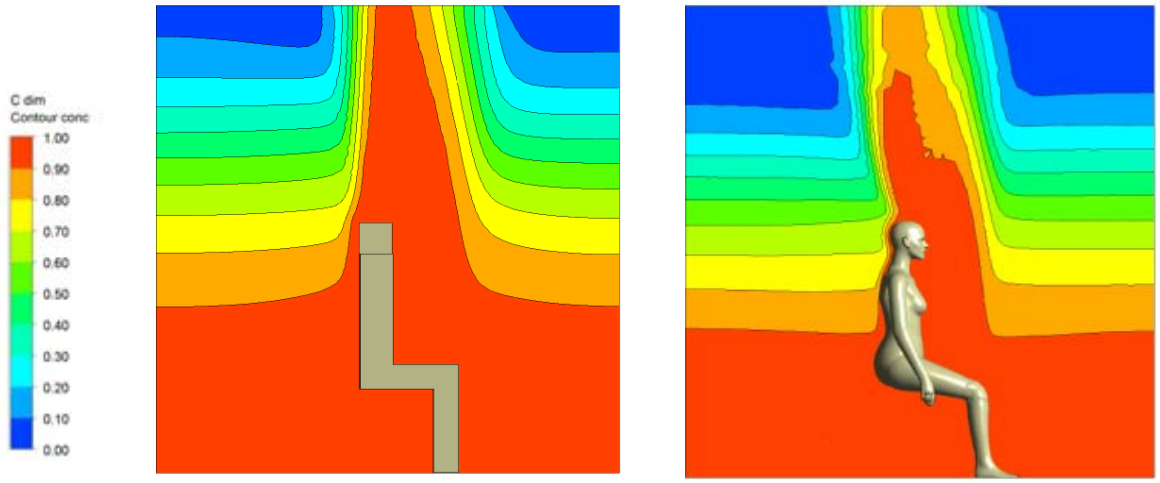

(a) Simple manikin (b) Detailed manikin

Figure 7-26: Variation in concentration level at a central plane in the room occupied by (a) simple exhaling manikin and (b) detailed exhaling manikin

This fact is attributed to the geometrical level of detail of the nose shape. A close up view of the two manikin further supports this (Figure 7-27).

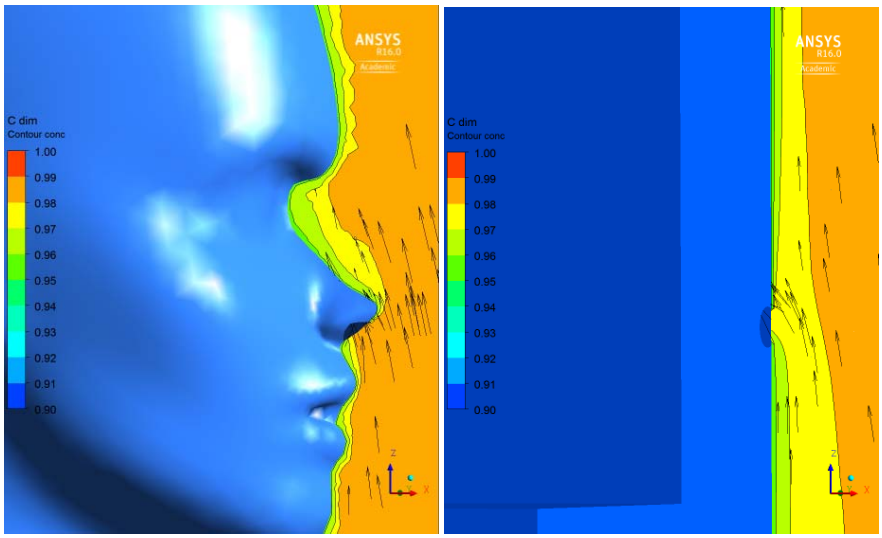

Figure 7-27: Close up view of a central plane showing contours of pollutant concentration over-layed with velocity vectors.

The results show how the detailed nose shape presents an additional blockage to flow which leads to a local accumulation of any pollutant flowing upwards due to thermal buoyancy. This accumulation is not present in simple geometry case.

The quantitative analysis for temperature, velocity, pollutant concentration and relative humidity for the inhaling manikins is shown at a location of 50 cm above the head in Figure 7-28 to Figure 7-35.

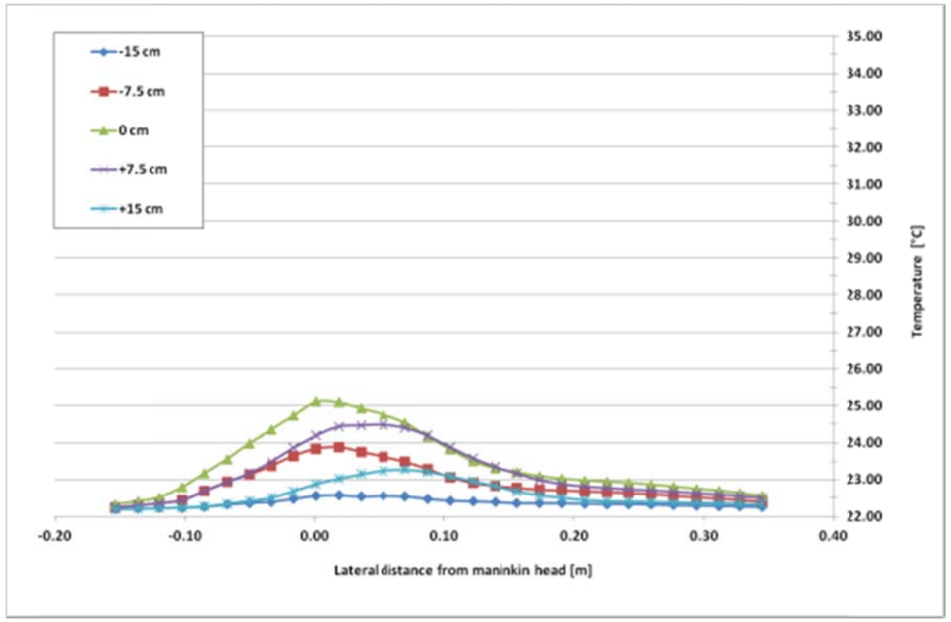

Figure 7-28: Temperature variation at 50 cm above simple manikin

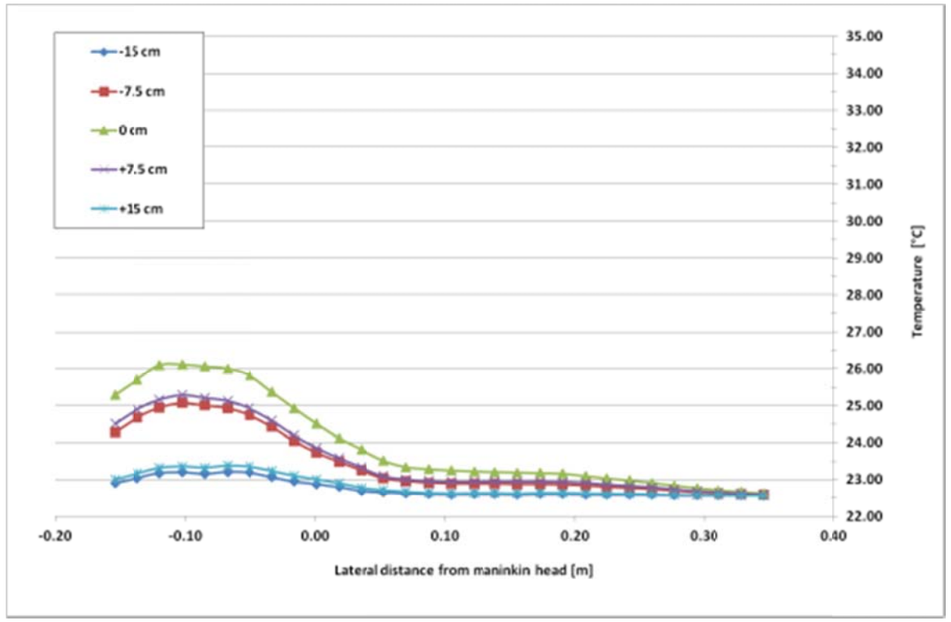

Figure 7-29: Temperature variation at 50 cm above detailed manikin

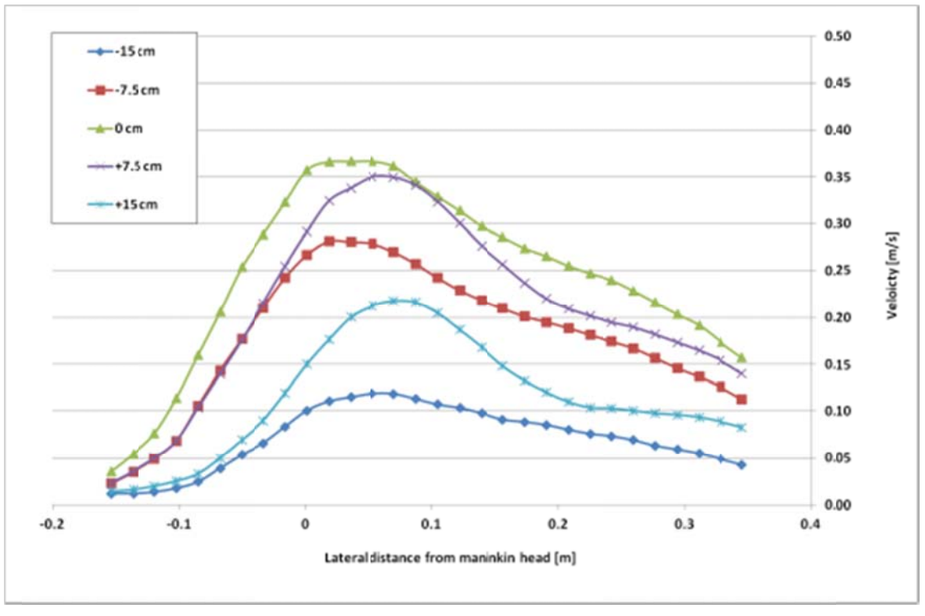

Figure 7-30: Velocity variation at 50 cm above simple manikin

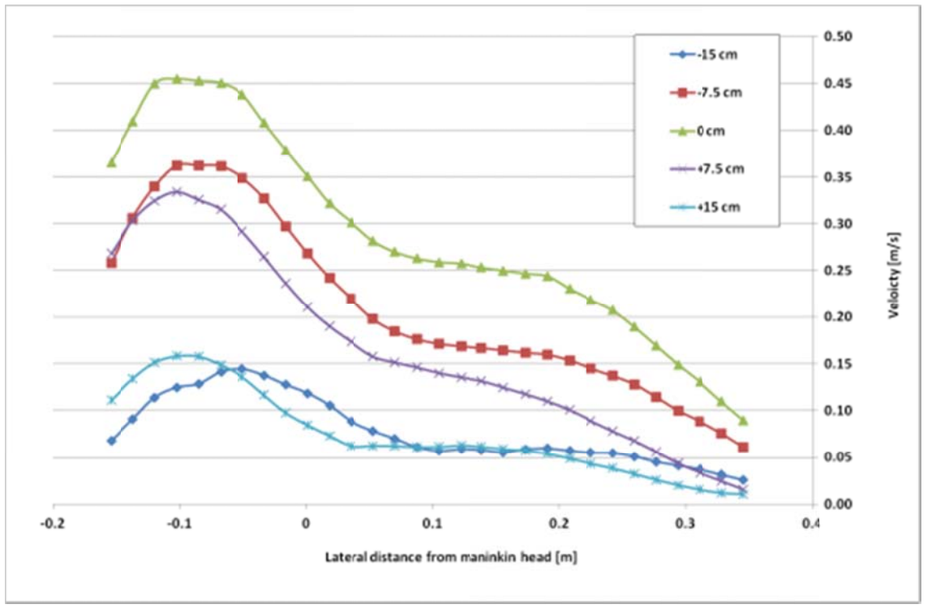

Figure 7-31: Velocity variation at 50 cm above detailed manikin

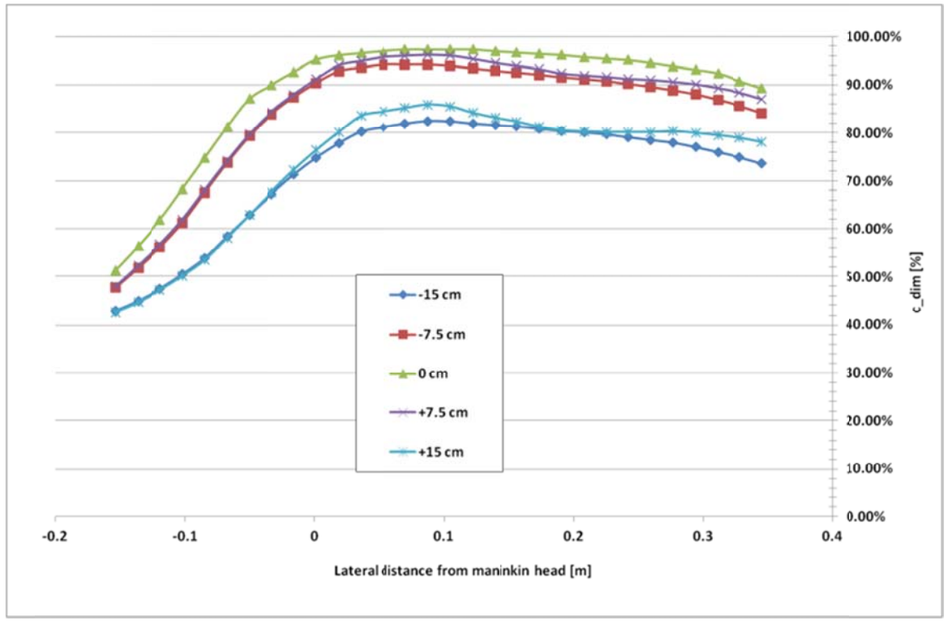

Figure 7-32: Pollutant variation at 50 cm above simple manikin

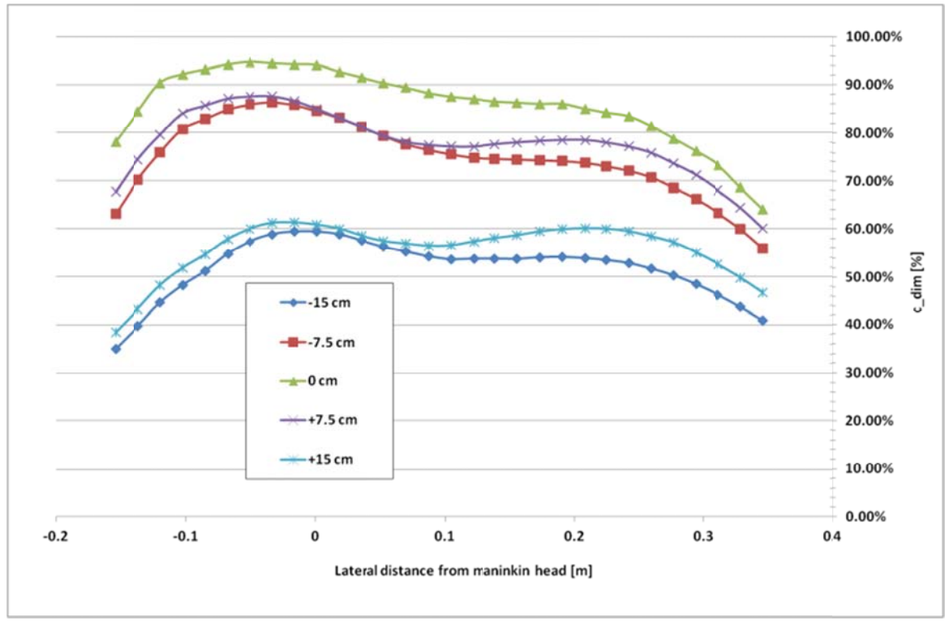

Figure 7-33: Pollutant variation at 50 cm above detailed manikin

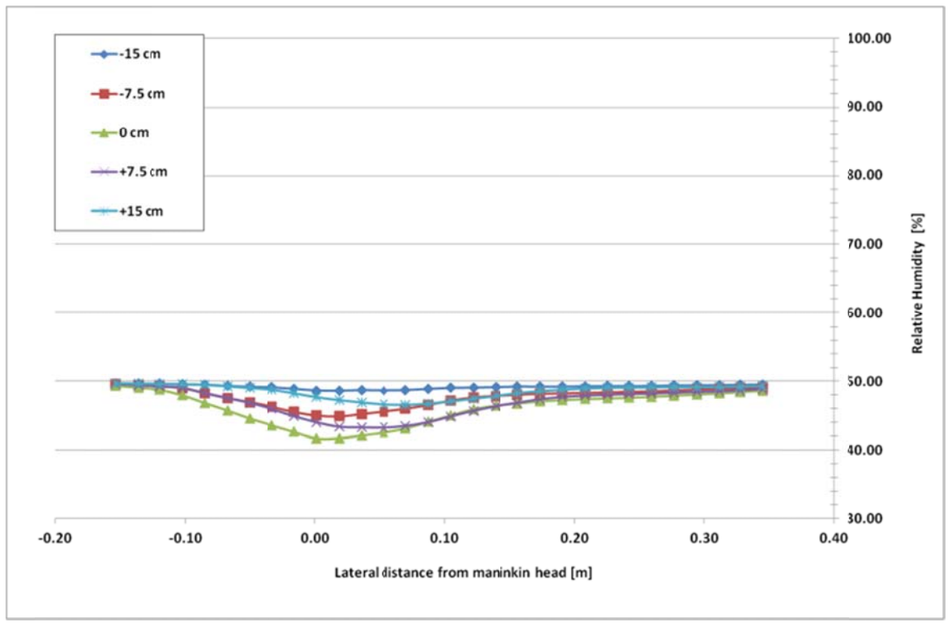

Figure 7-34: Relative humidity variation at 50 cm above simple manikin

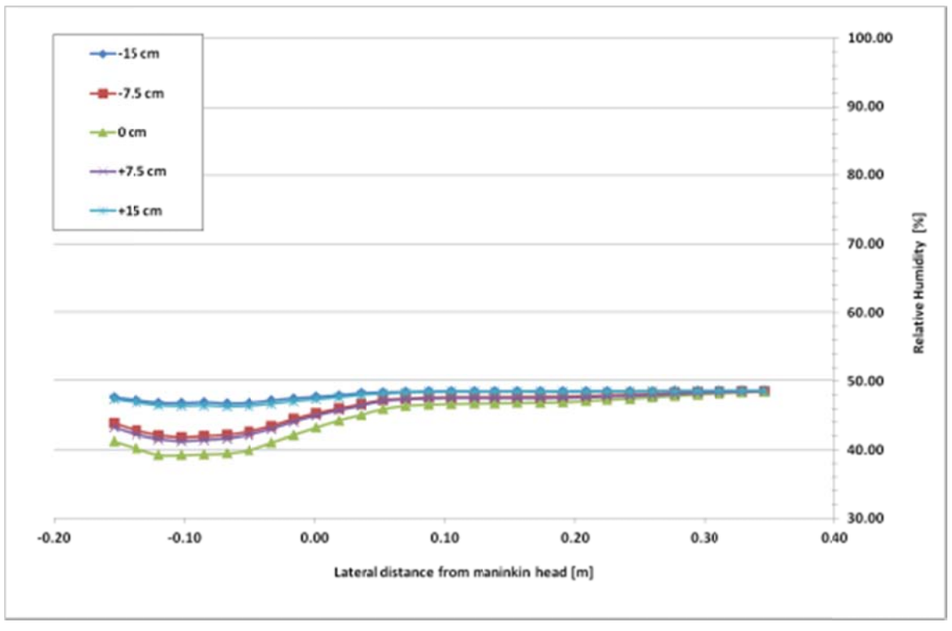

Figure 7-35: Relative humidity variation at 50 cm above detailed manikin

The results at 50 cm above the head show slight variations in the flow and distribution of pollutant. The relative humidity level at 50 cm above the inhaling manikin is slightly lower than that for exhaling manikins due to the fact that no additional source of moisture is present for the inhalation case. The amount of inhaled moisture and contaminants depend upon the local flow conditions of temperature and velocity.

7.5.4 Modelling the Respiration Cycle

In order to model the effect of the complete breathing cycle, a transient simulation was used. Instead of modelling the sinusoidal respiration cycle considered by Gupta, et al. (2010), the respiration cycle was approximated to a step function. The volume flow rates for exhalation, pause and inhalation are plotted against time in Figure 7-36.

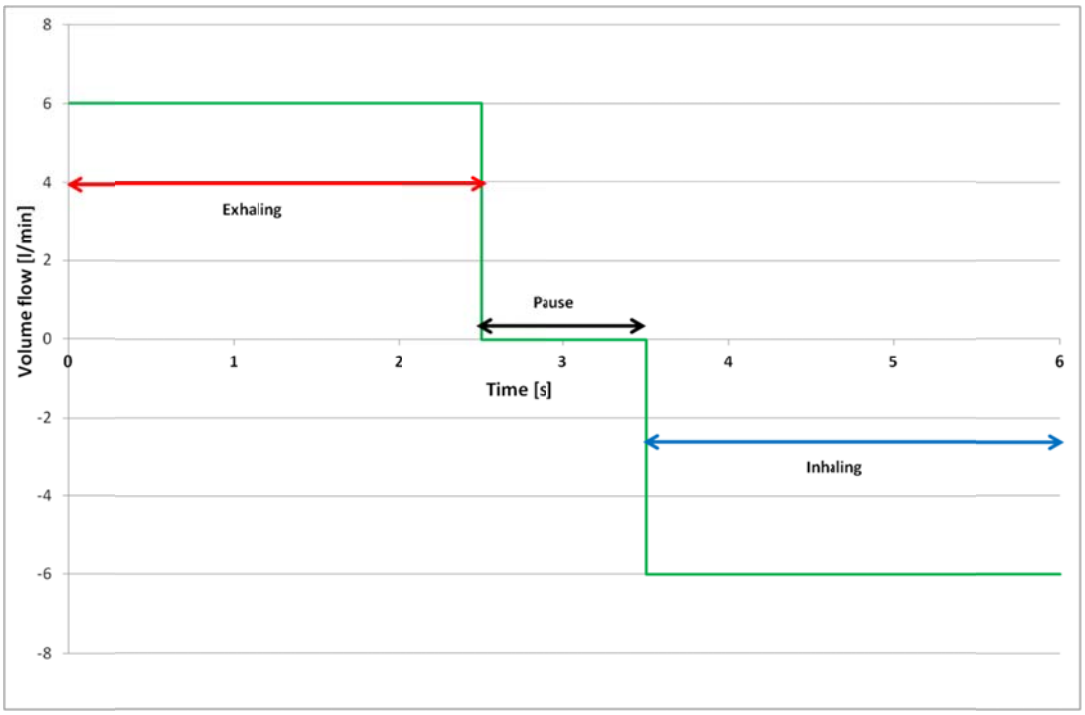

Figure 7-36: Graphical representation of respiration cycle

The volume flow rate for inhalation, exhalation as well as the time period of 2.5 seconds for inhalation/exhalation and pause of 1 second are based on the published data (Castro, 1998), (Douglas & Haldane, 1909), (Guyton, 1984), (Straub, 1998) and corresponds well with the recent work published by Gupta, et al. (2010).

The steady state simulation conducted for the exhalation process was used as initial boundary conditions for the transient state simulation. The effect of nose geometry can

be seen by considering a plane passing through the centre line (passing through the nose tip) of the two manikins as shown in Figure 7-37. The results show that a central plume region exists for the simplified manikin within which the exhaled CO2 is immediately entrained and transported upwards into the thermal plume, whereas for the case of the detailed manikin, the nostril geometry plays a vital role in displacing the exhausted CO2 away from the centre line. As a result, the CO2 concentration plot has two distinct (and wider) regions in comparison to the simplified manikin as shown in Figure 7-38.

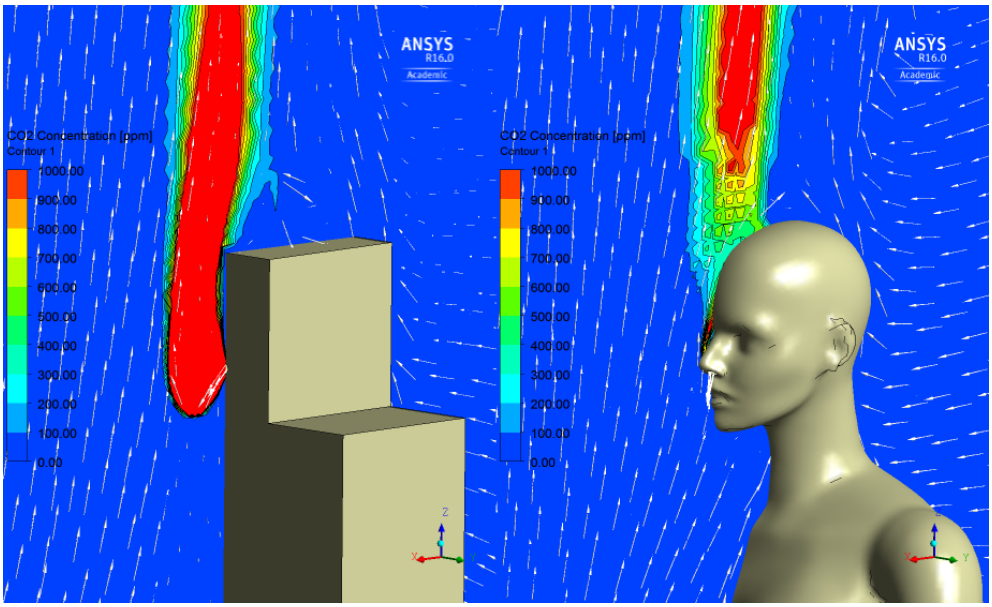

Figure 7-37: Flow field vectors with CO2 concentration plotted on a centre line plane (passing through the nose tip)

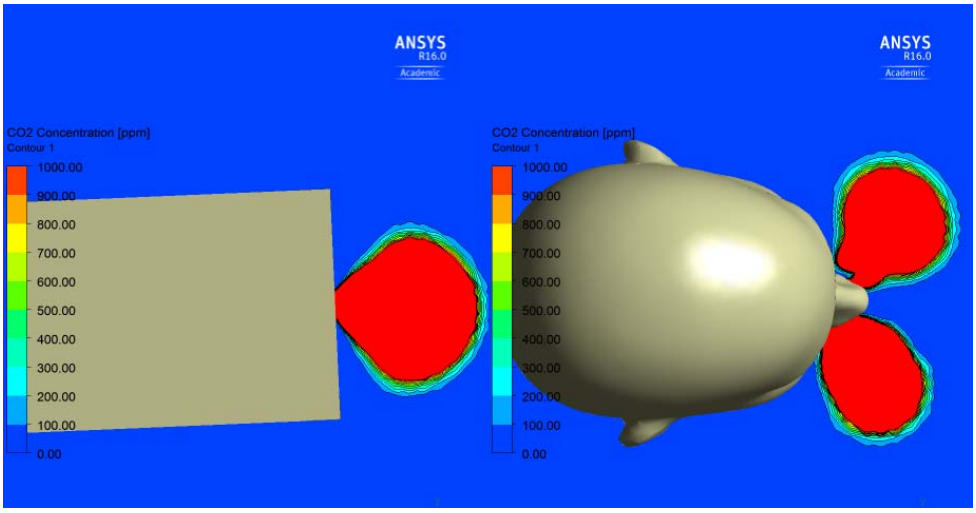

Figure 7-38: Plan view of a horizontal plane showing contours of CO2 concentration

In order to evaluate the distribution of the exhaled CO2, concentration levels are plotted at a) 5 cm in front of the nose at same height as the nose tip and b) 5 cm in front of the nose at 1 m above the nose tip. The results are shown in Figure 7-39.

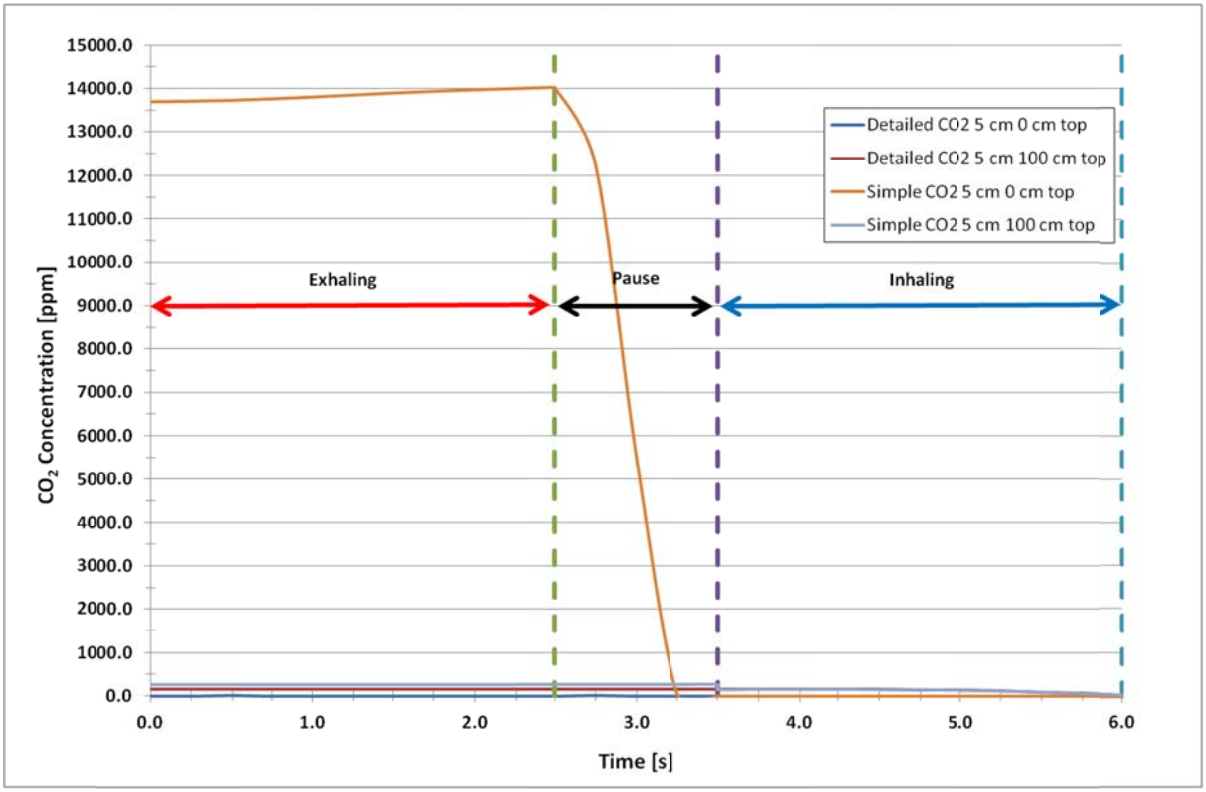

Figure 7-39: Concentration level of CO2 plotted as function of time

It can be seen clearly that in the case of exhalation using the simplified manikin, the CO2 concentration at a point located 5 cm away from the nose tip is significantly higher when compared to a detailed manikin. This concentration falls rapidly during the pause phase and tends to fall down to the background concentration (considered as zero for the present simulations) for the inhalation phase. The concentration levels of CO2 remain almost the same at a distance farther away from the nose region. This result strengthens the fact that propagation of CO2 (or similar gases/particles with very low settling velocity) for normal breathing persons in the room can be effectively modelled using simplified exhaling manikins. However, for person to person contamination studies, the use of simplified manikins is unsuitable because it may lead to an overestimation of the CO2 levels in the immediate vicinity of the manikin.

Another important fact that can be seen from the above figure is the effect of the pause while breathing. Simulations without considering a pause will result in higher local

concentration of the exhaled contaminant at the start of the inhalation process. The effect is significantly over-estimated if using a simplified manikin. Modelling a pause between exhalation and inhalation leads to dispersion of exhaled contaminants.

Resolving the respiration process using a transient approach enables visualization of the presence of any residual contaminants resulting due to the exhalation process. These residual contaminants cannot be visualized using a steady state simulation of the inhalation. Figure 7-40 shows the concentration level of CO2 on a central plane passing through the openings of the nostrils of the two geometries during the inhalation phase.

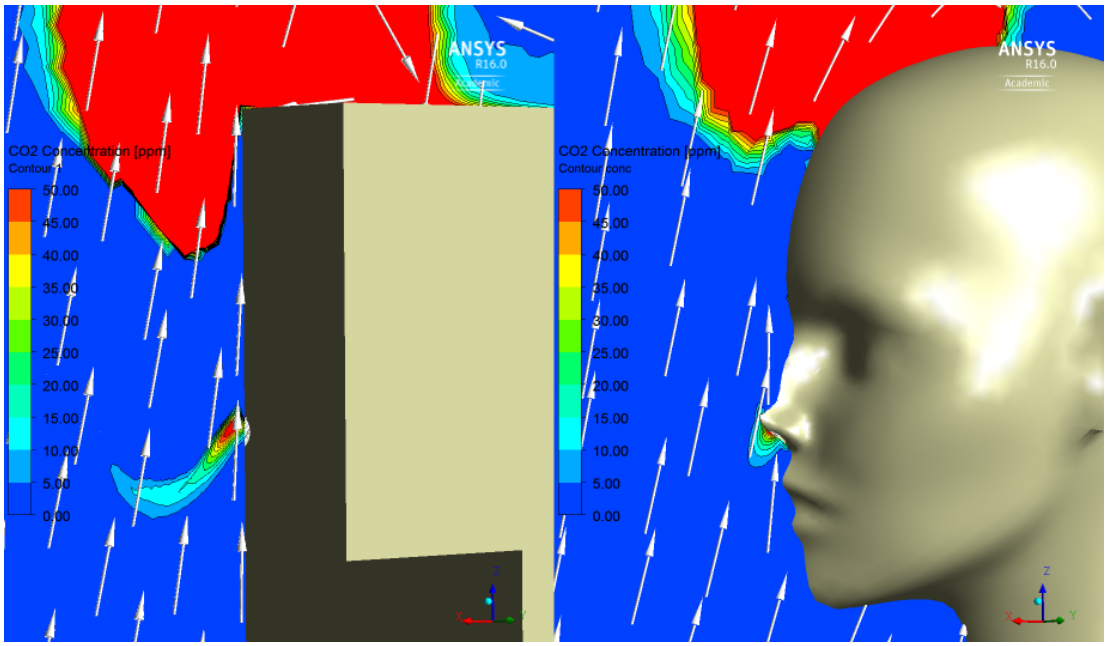

Figure 7-40: CO2 concentration shown on a vertical plane through the nostrils for inhalation process at time t = 3.75 s

The evaluation of results show that the amount of re-inhaled CO2 at about 0.25 s after the inhalation phase has completed is almost 37% higher for the detailed manikin as compared to the simplified geometry. This re-inhalation value will hold true for all exhaled gases/particles with settling velocities similar to CO2.

In terms of absolute values, the local re-inhaled CO2 concentration remains below 1% for both the simple and detailed geometries. At the end of the inhalation phase (time = 6 s), this local concentration of the residual exhaled CO2 falls to zero near the nose region as shown in Figure 7-41.

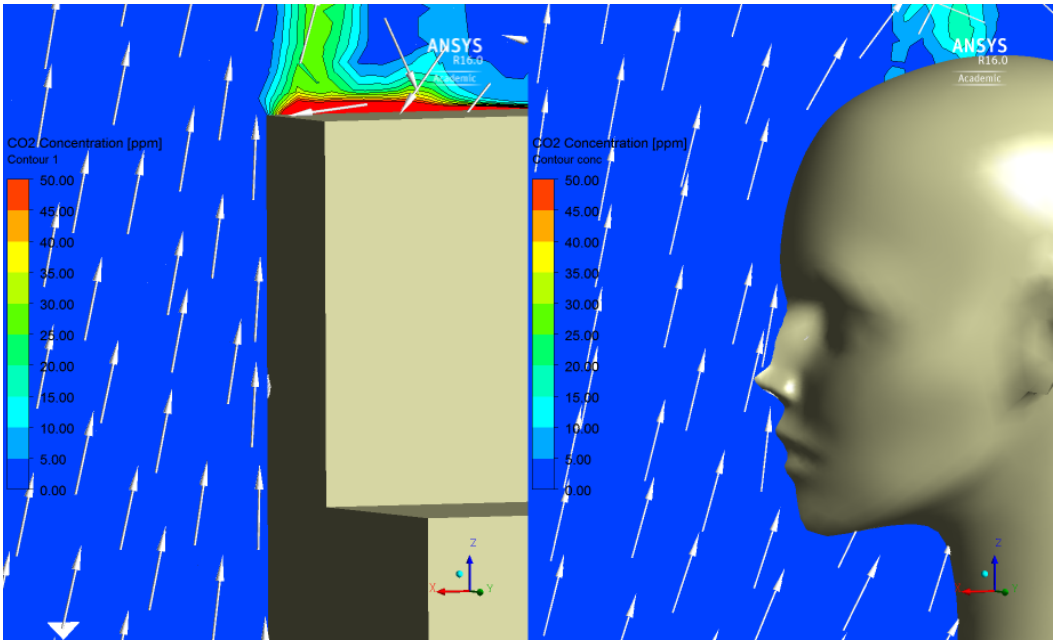

Figure 7-41: CO2 concentration level shown on a vertical plane through the nostrils for inhalation process at time t = 6 s

In the case of room contaminants emitted at the floor, concentration levels are evaluated at a) 5 cm in front of the nose at same height as nose tip and b) 5 cm in front of the nose at 1 m above the nose tip Figure 7-42. It can be seen that a simple manikin generates a higher concentrated jet along the nose centre line which dilutes the contaminant concentration to about 20% lower than for a detailed manikin at the same location. During inhalation, the concentration level at 5 cm in front of the nose level remains the same for both geometries whereas there exists a difference of about 2% at a height of 1 m above the nose tip level indicating the presence of a higher turbulence and inducement of flow in case of a detailed seated manikin.

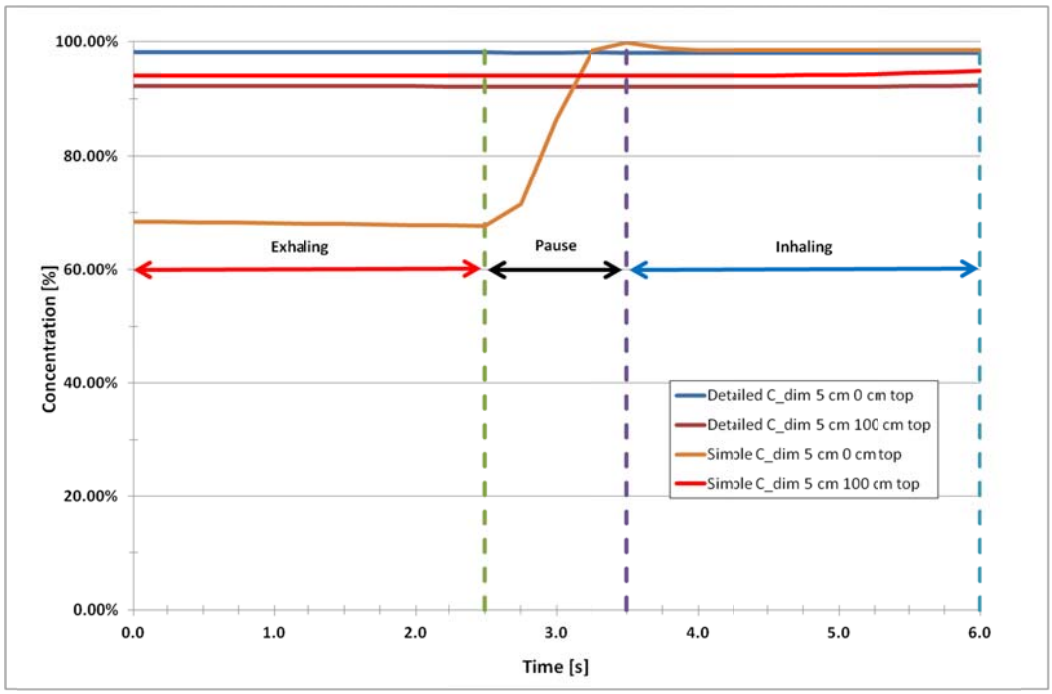

Figure 7-42: Contamination level plotted as function of time

Evaluating at the nostrils, the concentration level of the contaminant released at floor level remain 2% higher for the detailed manikin. This indicates the fact that any contaminants emitted at floor level are likely to be underestimated in their inhaled concentration in the immediate vicinity of the nose region when simulating using the simple manikin. The contaminant contours emitted at floor level are plotted for the transiently inhaling manikin at the end of the inhalation phase in Figure 7-43.

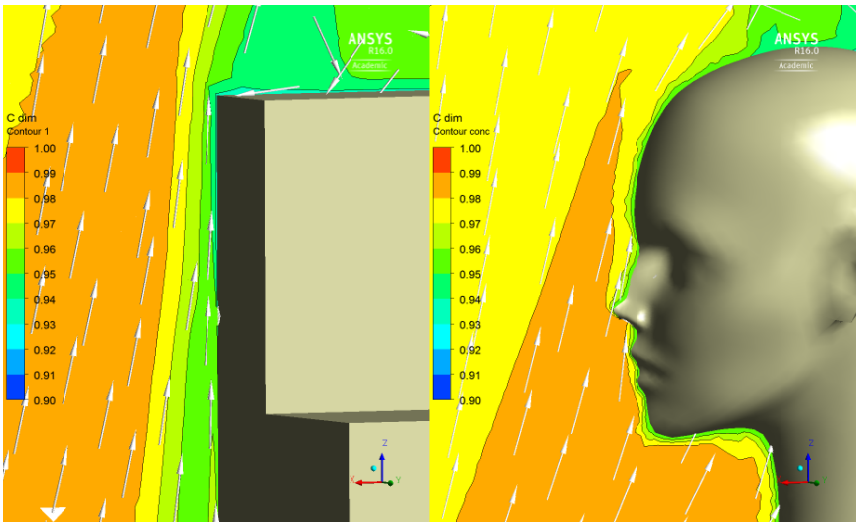

Figure 7-43: Vertical section through the nostril comparing contours of CO2 concentration for simple and detailed manikins

7.6 Numerical Issues with Modelling of Pollutants

During the numerical modelling of pollutants (low quantity scalar variables), it was noted that although for certain simulations the mathematical solution of the physical transport phenomena was correct, the results were not. The cause of this deviation between the mathematical and physical solution lie in the way the physics was defined and solved in the CFD code. A typical convergence plot for the steady state simulation setup for an empty enclosure is shown in Figure 7-44.

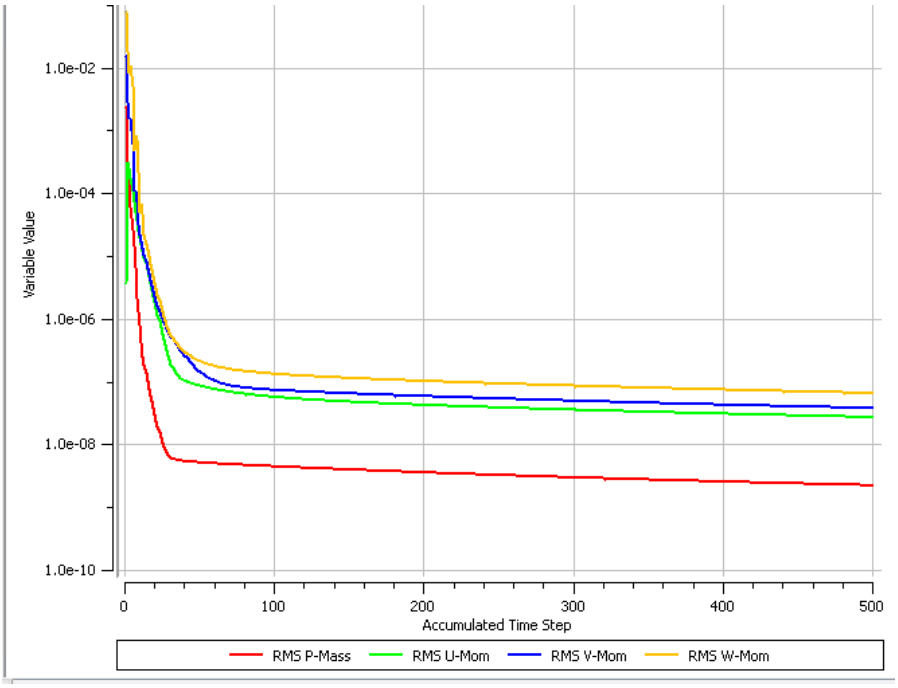

Figure 7-44: Residual plot with standard input parameters

The flow in the enclosure is buoyancy driven with a scalar source representing pollutant being applied at the floor level. The simulation was forced to run for 500 iterations (taking about 3 hours on an 8 core windows computer with 2.4 GHz processors). On the basis of a generally defined criteria, the simulation should have stopped far earlier. The results of the simulations showed mass imbalance at the boundaries to a level below 0.1%. The numerical simulation results did not present physically correct results for the passive scalar distribution although the numerically converged solution showed very low discretization errors (10^{-6} order of magnitude).

A detailed analysis of the problem showed that the error was due to an inaccurate representation of the conceived initial condition model for scalar variables. The initial

solution provided at the start of a solver run set the value of the scalar variables to zero for the whole computational domain (zero concentration at the beginning of the simulation run). The flow velocities and temperature were set to the mean values expected in the domain. The simulation was set to progress in time using a false time step of 0.1 s per iteration. With very low inlet flow velocities (0.001 m/s) and inappropriate initial conditions for scalar variable, the transport of the scalar was limited to just 5 cm above the floor. As the scalar variables that are massless particles do not contribute to mass imbalance, the mass-imbalance criteria was fulfilled declaring the simulation to be converged.

This led to the understanding that without employing an additional convergence level for scalar variables, a solution cannot be declared as converged. The problem is exacerbated by the fact that the initial concentration of the scalar variable was very low in the simulations. In cases with very low scalar variable values, the precision level of the calculation needs to be adjusted from "single precision" to "double precision" (to make use of 64 bit instead of 32 bit memory of a computational platform).

In light of the conclusions mentioned above, the same simulation run was restarted using initial boundary condition for the concentration level to be 1 (distributed uniformly throughout in room at the beginning of simulation). In addition to the initial conditions, a convergence criteria of 1e-5 on the flow residual of scalars was defined (not activated/defined per default). Considering the fact that low variable concentration and flow velocities are involved in the simulations, double precision solver was activated. The physical time step and the boundary conditions were kept the same. The convergence history plot for modified conditions is shown in Figure 7-45.

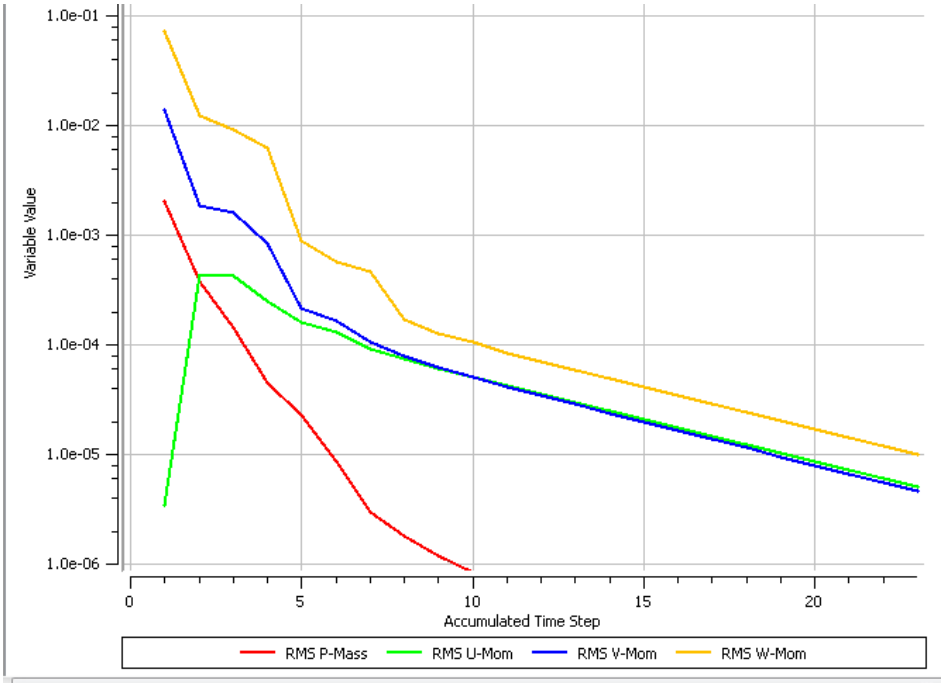

Figure 7-45: Residual plot with improved initial conditions and additional scalar convergence criteria

The simulations converged in less than 30 iterations consuming less than half an hour of simulation time on the same computational platform as before.

7.7 Summary

The present study shows that the major portion of exhaled CO2 gets entrapped in the thermal plume. Even for breathing rates of 10 L/min did not cause a disruption of the thermal plume (exhalation via nose). The expected settling effect of CO2 due to the fact that CO2 is heavier than air is overcome by the strength of the buoyant force generated due to the seated human body. The effect of the buoyancy generates a thermal plume which in-turn gives rise to a contaminant gradient. This thermal plume is symmetrical in nature for a simplified geometry whereas it tends to lean towards the rear for the detailed manikin. Evaluating this contaminant gradient for the two sedentary geometries showed that the entrainment level of the surrounding contaminants varies considerably in the immediate surrounding above the head region.

From the present work, it is very clear that modelling a pause in the respiration cycle is very important. The concentration of re-inhaled CO2/contaminants resulting due to exhalation is directly related to the pause time between exhalation and inhalation phenomena. Gao et. al. (2006) reported a re-inhalation value of almost 10% in the

absence of a pause. The current study with a pause of 1 s between exhalation and inhalation process documented values of re-inhaled CO2 to be below 1% for both the simplified and detailed manikins, thereby representing the fact that simulating a respiration cycle without a pause would lead to an over-estimation of the re-inhaled CO2 (and exhaled contaminants) which in practice will be imparted to the surroundings.

When using steady state simulations, the CO2 distribution in the room away from the thermal plume is not dependent on the level of detail of the thermal manikin. Although there is a dominant variance in the form of the thermal plume, the maximum velocity in the plume remains in the range of 0.35 - 0.5 m/s as in the previously reported studies (Clark & Toy, 1975), (Sørensen & Vøigt, 2003).

A major outcome of this chapter is that the seated models can be directly implemented to a complex indoor surrounding with single or multiple occupancy. Applying the presented breathing model for investigating thermal comfort and IAQ in a real indoor scenario requires changing the surrounding boundaries (box surrounding) to appropriate flow interfaces. An application of the simple and detailed manikins in a multiple occupancy classroom is presented in chapter 8.

8 Application of Breathing Thermal Manikin

8.1 Introduction

A number of studies have investigated the occupancy of humans in indoor climates. Most of these studies addressed separately the issues related to IAQ, energy demand, ventilation system efficiency, contamination distribution etc. In most of the previous work, the simulations were conducted without a validated computational model. Studies involving the use of a validated computational model for a real life scenario with multiple occupancy in indoor climates are limited. Most of the work with multiple occupancy differs from the measurements. In most of the cases the simulations are adjusted to give the measured values. The differences between the measurements and simulations are mainly attributed to improper or partial implementation of either the surrounding conditions or the physical processes (very often radiation and/or breathing) (Olmedo, et al., 2012). Computational limitations, such as turbulence models, numerical grid generation as well as hardware and the computational cost pose another barrier to applying a computational model for a real world scenario that can be validated by means of measurements (Bjørn & Nielsen, 1988).

Previous chapters of this PhD thesis evaluated the different environmental factors affecting the indoor climate due to presence of a human body. The human occupancy was represented by means of a computational thermal manikin in a simple box type surrounding. The systematic validation of different heat and mass transfer related phenomena in the indoor climate led to the development of a validated seated thermal manikin in an enclosure which can be directly embedded into a surrounding. Simplified and detailed manikins were further compared to investigate the effects of breathing (exhaling and inhaling) for both steady and transient cases. It was found that in regimes further away from the breathing zones, the IAQ is less affected by the shape of the breathing thermal manikin and that the exhaled air potentially remains entrained within the thermal plume (for normal breathing rates) due to the heat generated by a body. The present chapter focuses on the application of the validated model in a real indoor climate for the estimation of IAQ.

8.2 Experimental Work

The field data considered in this chapter is taken from an IAQ experimental study conducted as part of an MSc thesis work at Loughborough University (Hedger, 2011). The measurements conducted during the MSc thesis were performed in different classrooms of a school located in central London in the UK. Measurements of temperature, humidity and carbon dioxide level were conducted for different classrooms of the school for a complete month. No measurements were taken for the velocity conditions in the room. The data regarding the occupancy level in the classrooms was taken from the student presence record. For the current application study, the measured data of one of the classrooms was analysed and used for comparing with the simulation results.

Carbon dioxide (CO2) is considered as a main indicator of indoor air quality especially in cases of multiple occupancy (Karthikeyan & Samuel, 2008). The CO2 level was measured using a Telaire® 7001 CO2 sensor with a measurement range of 10,000 ppm (accuracy of ± 50 ppm). Temperature and relative humidity was measured using Onset HOBO U12 sensors. HOBO U12 has a temperature measurement range between -20° to 70°C (accuracy of ± 0.35°C from 0° to 50°C) and relative humidity measurement range between 5% - 95% (accuracy of maximum 3.5%). The measurements were carried out in the room at different locations. Due to a limitation in the number of sensors, the temperature, relative humidity and CO2 levels could only be measured at two locations per room simultaneously.

The room considered for this application study is located in the interior of the school at the basement level. The measurements were conducted between the months of May and June. The measurement locations within the room were varied in three measurement rounds for the complete measurement period. A floor plan of the room along with the sensor positions installed in the room are shown in Figure 8-1. Three ‘rounds’ of measurements were conducted. The sensor positions shown in Figure 8-1 were retained for a measurement period of 14 days (3rd round). The sensor position for all three measuring rounds are shown in Figure 8-2.

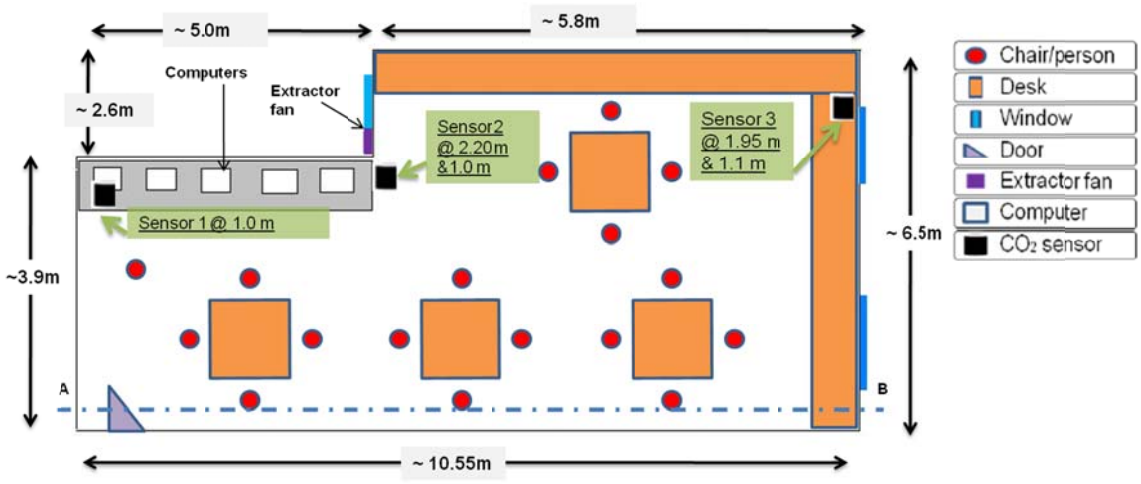

Figure 8-1: Floor plan showing sensor locations

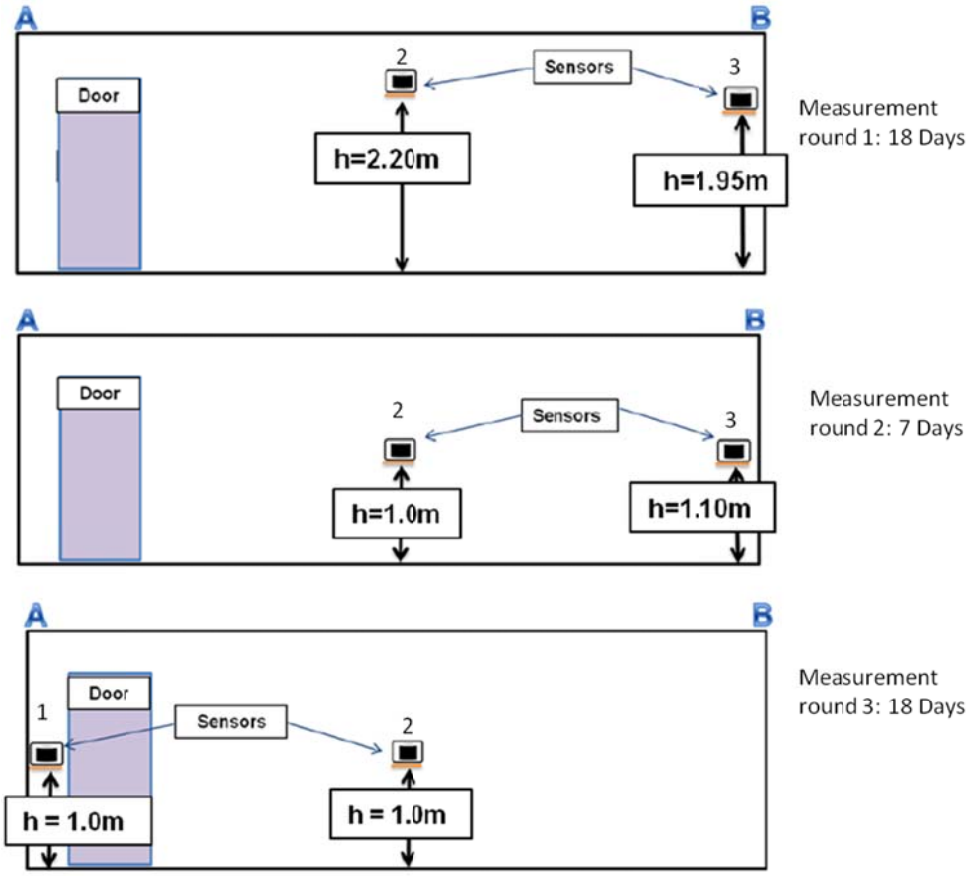

Figure 8-2: Cross sectional view showing the vertical positioning of the sensors

The only door in the room remain closed for the duration of a lecture. The room is fitted with a supply fan and an adjacent window as shown in Figure 8-3. The supply fan is frequently operated during summer and periods of long occupancy whereas the window located adjacent to the fan is only occasionally opened. The windows at the rear of the

room are closed permanently. As the room is located in the interior of the building at the ground level, the lights installed at the ceiling remain on for the duration of the lecture and breaks. The room is mainly used by 15 - 16 students and 1 teacher.

Figure 8-3: View of the classroom showing the supply fan and the adjacent partially open window

The estimated air change rates for the room is 3 ACH. The background CO2 level is acquired by averaging the measured CO2 values (measured between midnight to 5 am) given by the CO2 sensor located near to the fan/window. The background CO2 concentration in the absence of any occupants at night time remained at around 430 ppm (± 50 ppm) for the complete measurement period. The measurement results for a typical day recorded by sensor 1 in the measurement round 3 are shown in Figure 8-4.

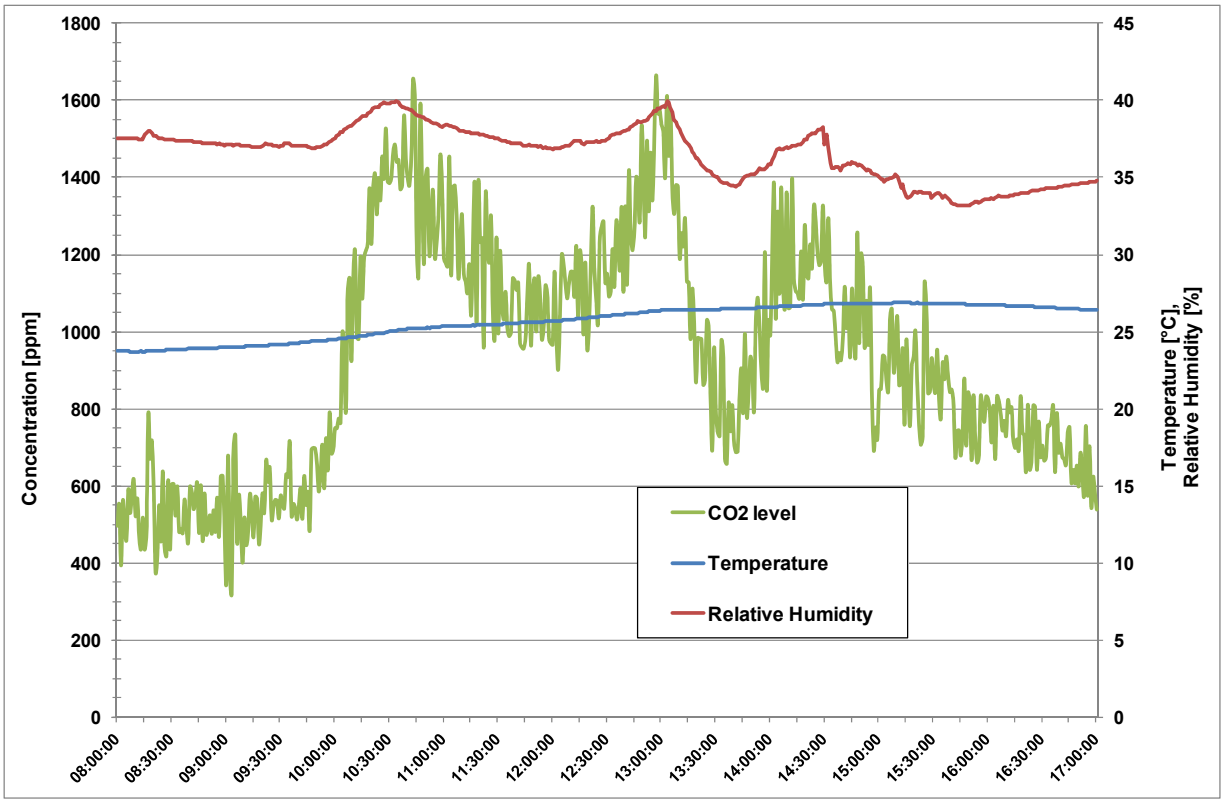

Figure 8-4: CO2 concentration, RH and temperature in classroom for a typical day

The results are further analysed to represent a typical lecture time in the afternoon between 13:45 and 14:40. The average values of the temperature, relative humidity and CO2 concentration are presented in Table 8-1.

Table 8-1: Averaged values of temperature, RH and CO2 level at two sensor locations

Measured variable	Sensor location 1 (class front)	Sensor location 2 (near fan)
Temperature [°C]	26.6	26
Relative humidity [%]	36.5	37.4
CO2 concentration [ppm]	1094.2	1038.7

The recorded outdoor temperature on the typical day with the room characteristics mentioned above was 21°C with a relative outdoor humidity of 50%. The local temperature and relative humidity variation recorded at the sensor locations remained within ± 0.2°C and ± 2% respectively whereas the CO2 concentration varied by almost

± 400 ppm for the lecture duration. During the morning lectures, CO2 values of slightly more than 1600 ppm were recorded.

8.3 Simulation Methodology

Besides the complexity of geometrical details/orientation of a real indoor space, a number of physical variables affect the thermal comfort and IAQ. Not all of these variables can be recorded as a function of space and time for the complete measurement period. For the experimental work mentioned above these key physical variables which influence the comparison of results can be categorised as either "air flow" or "heat sources" as explained below.

i. Air flow: the air flow coming in and going out of the room is not measured. Different flow paths exist in the room e.g. leakages via building fabric, instant opening and closing of door/window as well as possible variation in fan operating condition.

ii. Heat Sources: the heat load of the stationary heat sources such as lights, CPUs, computer screens, and other electronic devices in operation were not measured. The movement/seating position of the occupants (transient heat sources) was not recorded for the complete period of the lecture. The surface radiation properties of the surrounding surfaces as well as the surface temperatures could not be measured during the measurement phase.

The aim of this application work is to show that with limited measurements, a good engineering judgment of the room conditions along with the use of a validated model, one can effectively underpin the major issues related to thermal comfort and IAQ. For the application study, a simulation was run with 16 students and 1 teacher. The simulations were performed in a steady state mode thereby not accounting for change in position of the occupants. The seating arrangement is shown in Figure 8-5.

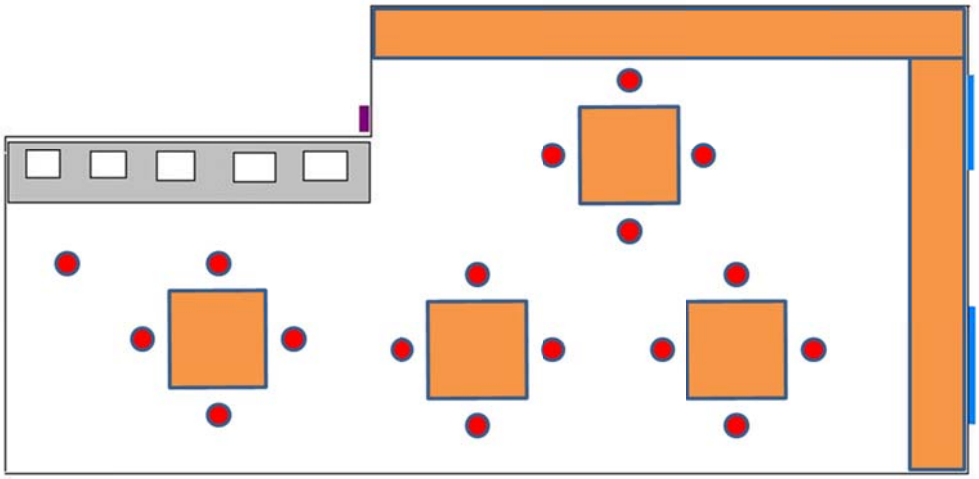

Figure 8-5: Diagrammatic representation of the seating arrangements

Multiple occupancy in the classroom was modelled using the detailed and simplified breathing thermal manikins. The sedentary teacher was modelled as a detailed manikin whereas the students were modelled as simplified breathing manikins (see chapter 7 for the differences between detailed and simple manikins) seated at tables.

The current application study compares the measured results in a classroom with actual breathing and seated people (people may have moved occasionally during the periods) with sedentary breathing thermal manikins. The comparison is made for the measured values of air temperature, relative humidity and CO2 concentration at different positions. No measurement is made for the above mentioned variables in the breathing zone of the real occupants.

The aim of this application study is not to obtain results that exactly match the measured values, rather it is aimed to see the extent to which a validated model can be applied to a real case scenario for which the exact boundary conditions are often unknown. The unknown boundary conditions for the current study are estimated by engineering judgment and simulation experience gained during the course of this PhD work.

8.4 Geometrical Model and Meshing

The complete model was generated using the CAD tool Rhinoceros 4.0 and exported to ANSYS ICEM CFD. Initially the model was created without occupants. The modelled geometry included the room with major internal heat loads i.e. lights, CPUs and

computer screens. Only the major geometrical details that affect flow restrictions were modelled. These restrictions were a) an I-beam projecting down from the roof in the room b) computer screens and CPUs c) central and side tables.

The room without the occupants was meshed with the location of the occupants indicated in the simulation model by empty box structures as shown in Figure 8-6.

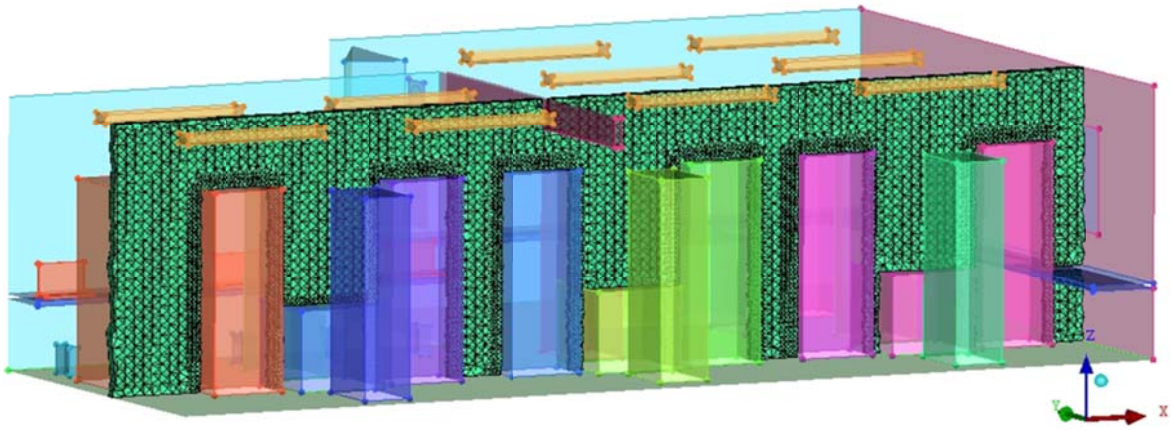

Figure 8-6: Meshed domain without the occupants

The simplified and detailed manikins were meshed separately inside boxes as shown in Figure 8-7.

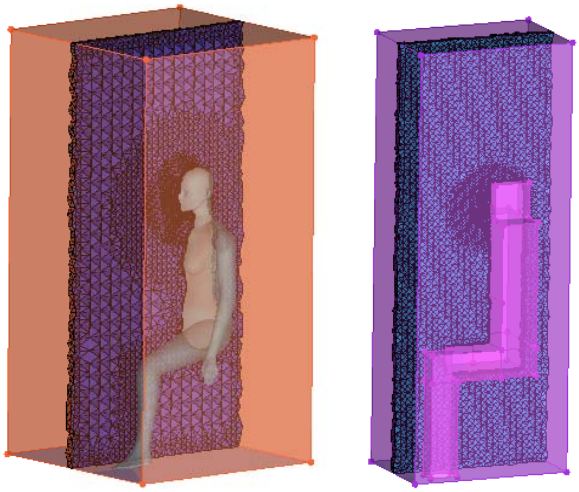

Figure 8-7: Meshed geometries of simple and detailed manikins inside box domains

The size of the boxes was reduced from the size used in previous chapters due to the space limitation inside the modelled classroom. The complete classroom (without occupants) was meshed using 1.7 M tetrahedral cells with 4 prism layers on the wall

type objects (heat sources, floor, roof, tables etc.). No prism layers were generated on the fan inlet. For the open window, 3 prism layers were generated normal to the surface in order to capture pressure drop effects, especially due to application of loss coefficients/pressure jumps etc.

Each box containing a simplified manikin was meshed using about 900 k cells whereas the zone containing the detailed manikin was meshed using 1.2 M cells. The multiple occupancy in the classroom was modelled by placing 15 (or 16 depending upon the simulation variation) simple manikins representing sedentary students as well as 1 detailed manikin representing a sedentary teacher. The simple and detailed manikins were imported directly as meshes and placed at different locations in the room. The composite meshing resulted in a mesh size of about 13 M cells. A 3 D geometrical model of the investigated classroom is shown in Figure 8-8.

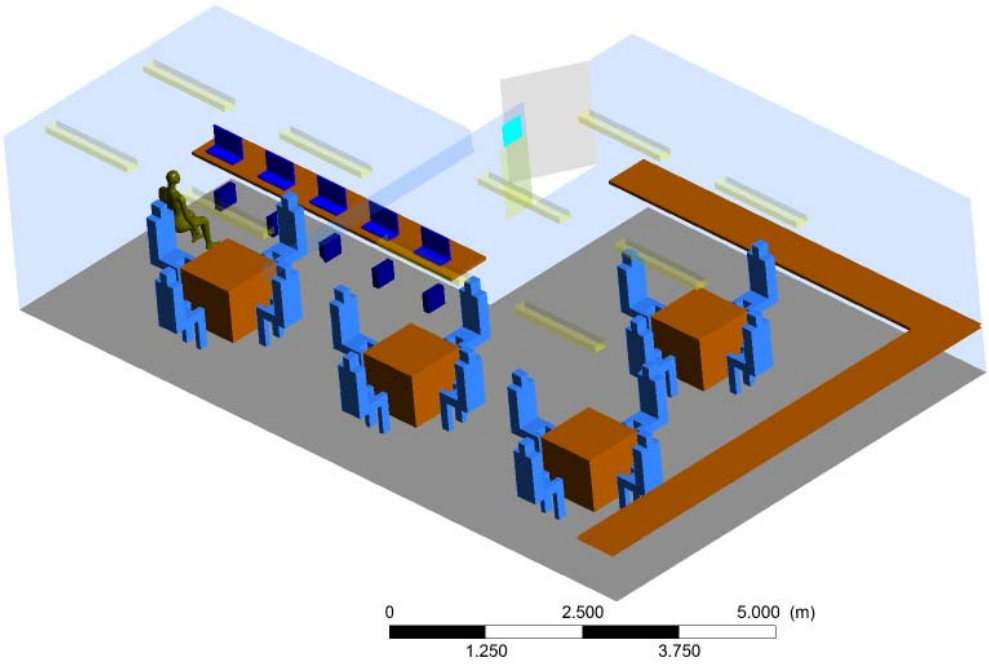

Figure 8-8: Geometrical model of the room with 17 seated occupants

8.5 Assumptions & Boundary Conditions

Within the application model, the following assumptions were made:

- The infiltration via the door, leakages through the window and building constructional joints/cracks are not included.

- The fan was modelled to have an effective opening area of 0.1156 m^2 supplying air at 1 m/s thereby causing an air change rate of about 2.8 ACH. The radial flow component of velocity imparted to flow by the supply fan was not modelled.
- As the influence of occupancy and short comings of present ventilation mode is focused for the complete room, only the net breathing process contributing to the exhalation and re-inhalation of CO2 is simulated in steady state.
- The amount of background concentration is estimated on the basis of sensor measurements during the night. The sensor chosen to represent this background concentration is the one located in close proximity to the fan/window opening. This background concentration of CO2 used for the simulations was 430 ppm.
- The effects due to motion of the occupants were not taken into account.
- In the absence of exact building physics data of the room and considering the fact that a major portion of the classroom is located in the interior of the building and the averaged measured room air temperature for the period of occupancy is 25°C (±1°C), the walls are considered to be at the same temperature as the average room air temperature of the two sensors i.e. 25°C.
- The amount of the modelled window opening was based on the observation/photographs and may differ slightly from reality. A pressure loss coefficient of 0.3 was employed for the slightly open window.
- The position of the sensors is correctly recorded for the vertical co-ordinates of the room but the information about their adjacency from the walls/objects is not mentioned. In order to compensate for this missing information, a sensor cloud consisting of a set of points was used in simulations as shown in Figure 8-9 (marked with coloured cross hairs). In addition to the point locations, the variables are plotted on a vertical line to show their vertical gradient in space.

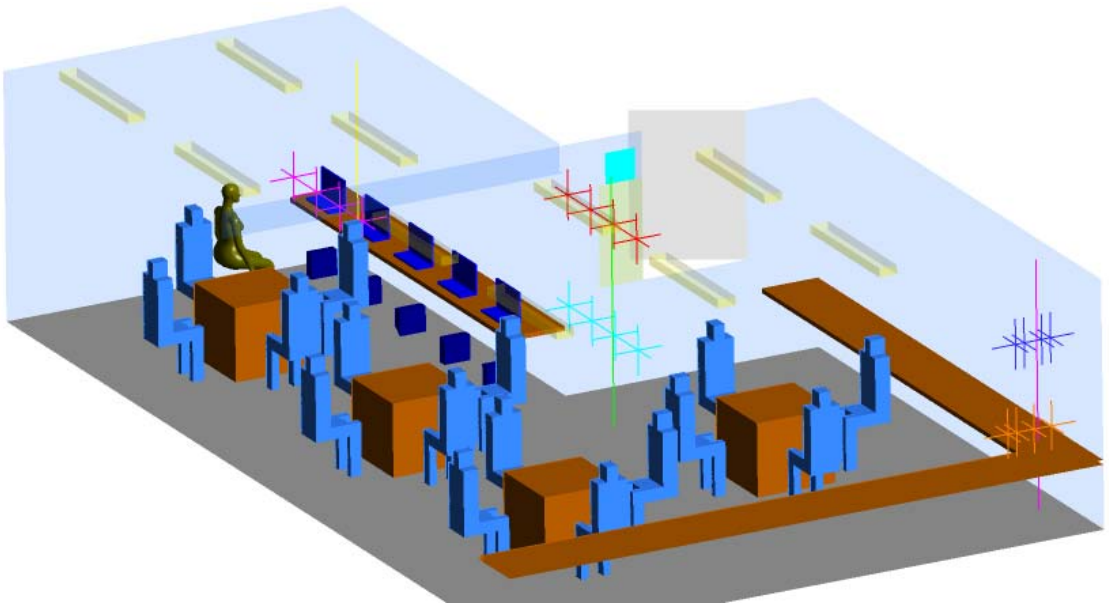

Figure 8-9: Measurement points used in simulations

In light of the literature review (see chapter 2), the thermal manikins were given a constant surface temperature of 32.8°C. The exhaled breath was modelled to be at an exhale temperature of 35°C with 100% relative humidity and 4.5% (volumetric) CO2. The exhaled air corresponds to a sedentary person breathing at a rate of 12 breaths per minute. Considering a tidal volume of 500 ml, this breathing rate results in a volume flow rate of 6 L/min. The volume flow was applied as a velocity boundary condition at the nostrils of the manikins.

8.6 Results

The results of this study are presented as iso-volumes of CO2 concentration in the room along with temperature, relative humidity, CO2 concentration contours and velocity streamlines at different locations. The simulation results of the variables are plotted on a vertical line at sensor locations whereas the experimentally measured values are added to the plots as point values (averaged values).

The results in Figure 8-10 and Figure 8-11 show iso-volume of CO2 concentration levels above 1500 ppm and 1000 ppm respectively. The results show that the concentrations above 1500 ppm are localized in the near breathing zone of the sedentary occupants whereas the concentration levels above 1000 ppm are evenly filled in the room.

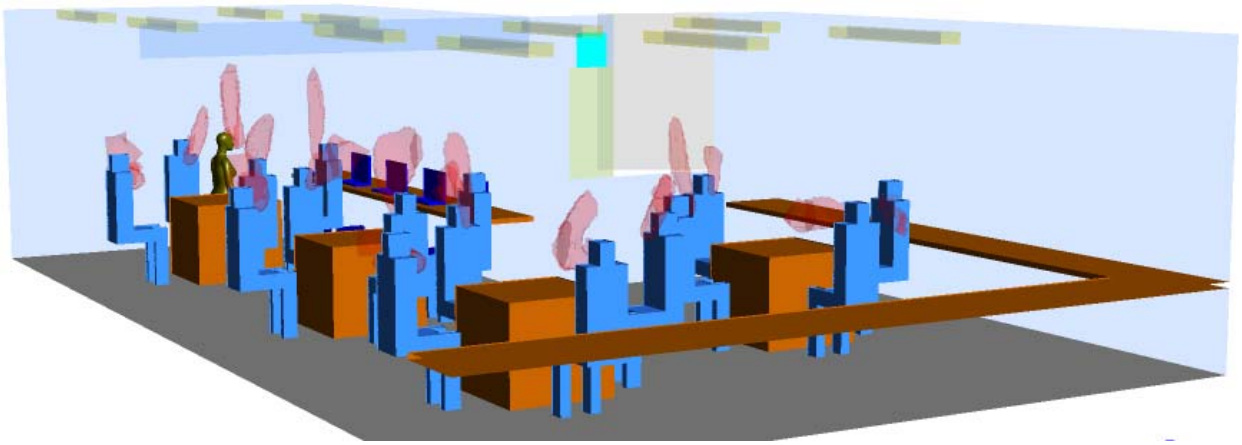

Figure 8-10: Iso-volumes CO2 concentration level at and above 1500 ppm

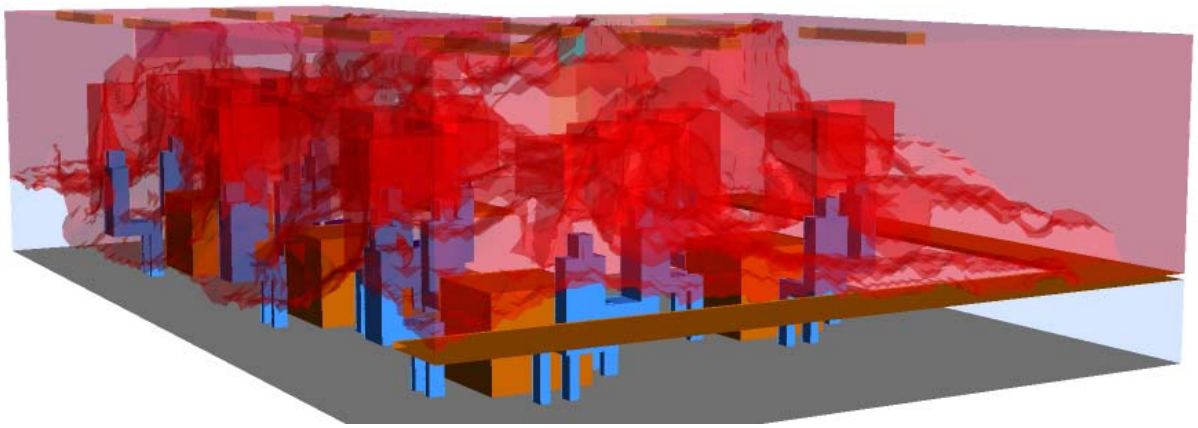

Figure 8-11: Iso-volumes CO2 concentration level at and above 1000 ppm

The CO2 contour plot at head height is shown in Figure 8-12. This contour plane shows that at head height the CO2 tends to accumulate more in the corner opposite the door indicating a lower mixing and air flow zone. The air jet entering the room through the fan disperses the CO2 exhaled by the thermal manikins that are positioned in line with the air jet, thereby not allowing the CO2 to completely remain inside the thermal plume. This fact decreases the local concentration of CO2 in zone immediately opposite the fan and open window and increases the local concentration in the zone in front of the closed door of the classroom.

The thermal plumes generated by the sedentary occupants in the regions away from the fan retained their form due to strong thermal forces. The strength and form of these plumes vary in space due to asymmetrical thermal and velocity flow fields.

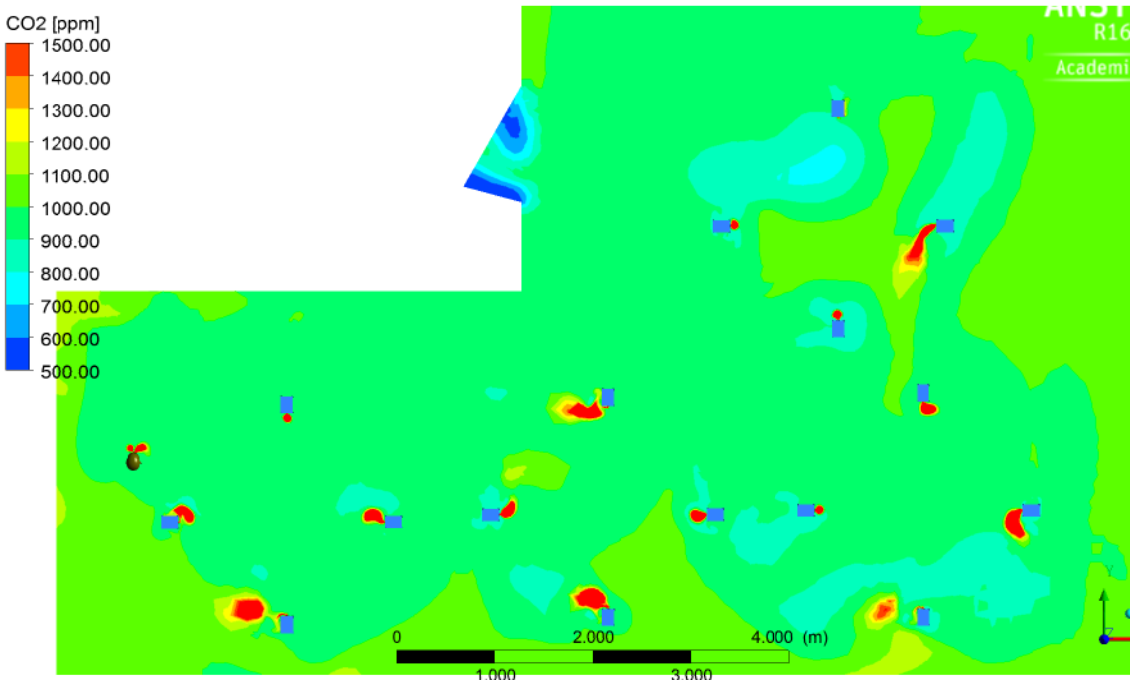

Figure 8-12: CO2 concentration level at head level of sedentary manikins

The temperature stratification and the form of the thermal plumes generated by the heat load of the sedentary manikins are plotted on a vertical plane in Figure 8-13.

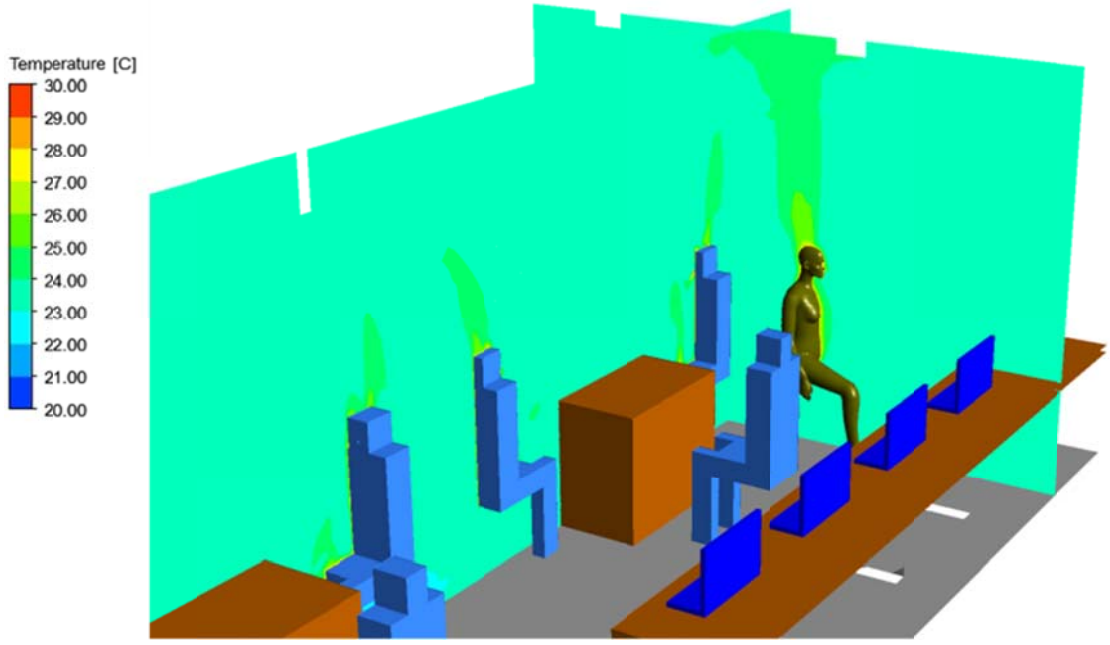

Figure 8-13: Temperature stratification on planes near the door of the classroom

The quantitative comparison between the simulation results and the field measurements is presented in Figure 8-14 to Figure 8-16. The measurement value for sensor 3 was not available for the simulated conditions.

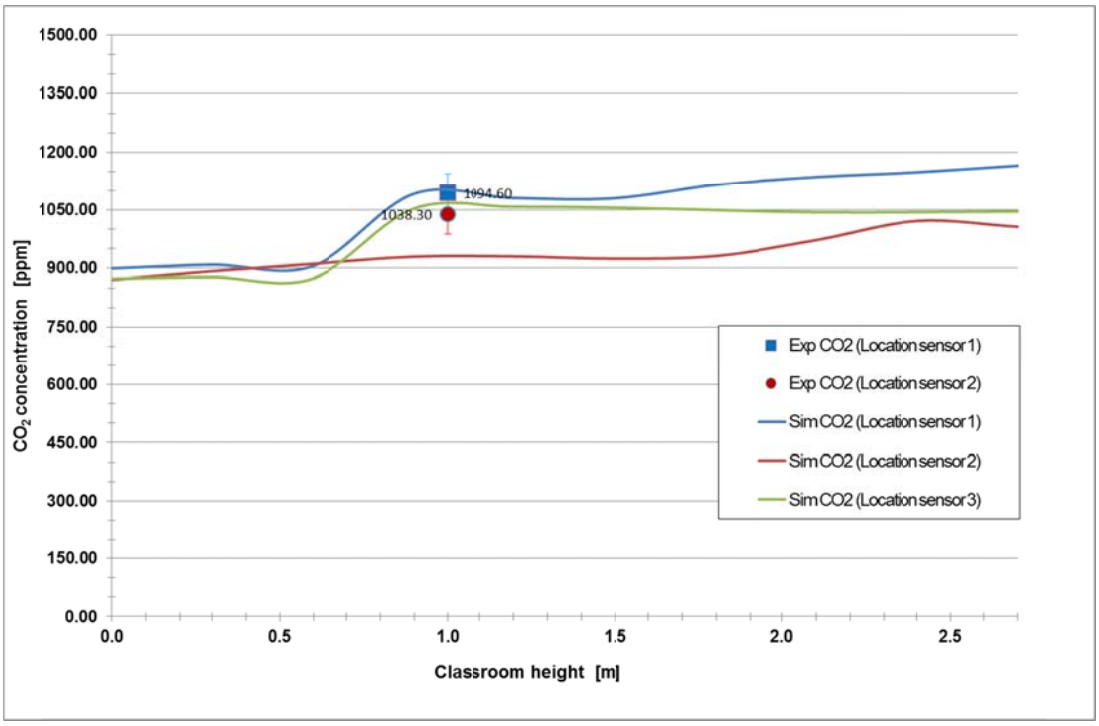

Figure 8-14: Results of simulation showing CO2 concentration in the classroom. (Simulation results = Lines and measured values = points). Error bars refer to the measurement error of ± 50 ppm.

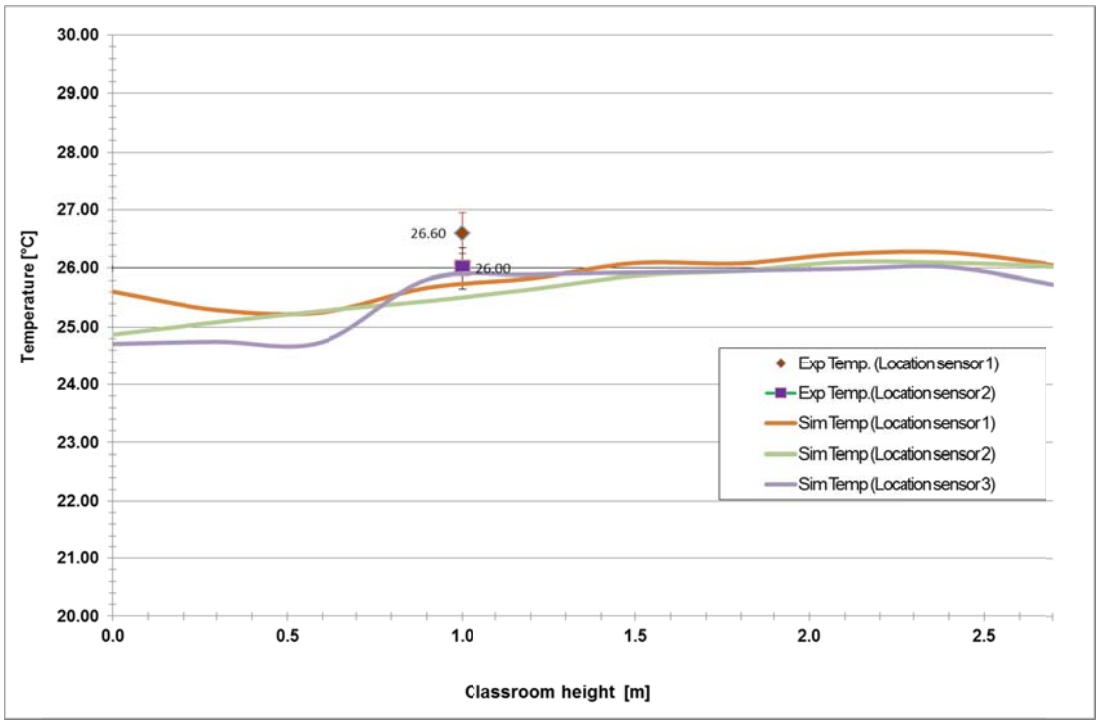

Figure 8-15: Results of simulation showing temperature variation in the classroom. (Simulation results = Lines and measured values = points). Error bars refer to the measurement error of ± 0.35°C.

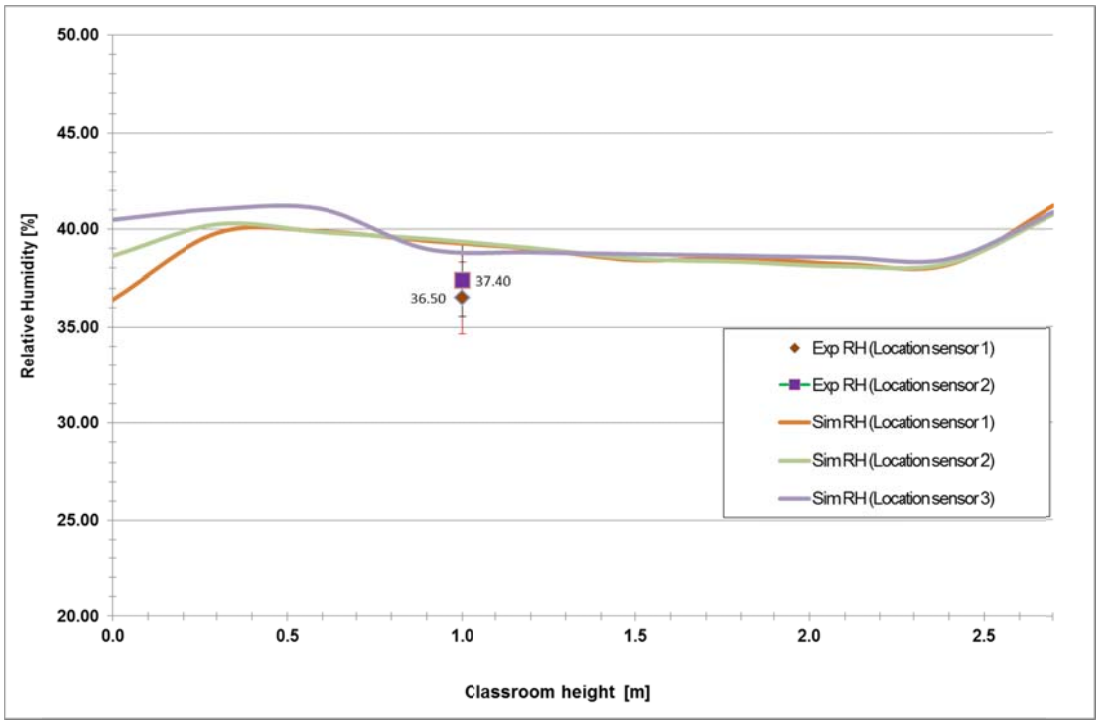

Figure 8-16: Results of simulation showing relative humidity variation in the classroom. (Simulation results = Lines and measured values = points). Error bars refer to the measurement error of ± 5% RH.

The quantitative results show a very good agreement with the measured quantities. The simulations show less than 2% deviation (8 ppm) for the concentration level in the zone in front of the door (sensor 1) and about 10% (100 ppm) for the concentration level near to the fan. The simulated temperature and relative humidity also compare well with the measured values (within 5%). The relatively higher difference in the measured and simulated CO2 concentrations near to sensors is due to the strong local transient conditions that occur near the air inlets and cannot be simulated using steady state conditions and in the absence of detailed boundary conditions (turbulence intensity, velocity components etc.).

Besides measured variables (temperature, CO2 concentration and relative humidity level), CFD simulations provide valuable information about heat transfer coefficients. The heat transfer coefficient plays a vital role in estimating the local thermal comfort of the occupants as it incorporates the effect of local flow velocities. These coefficients are widely published in literature for different indoor climates ranging between 2.5 W/m^2K to over 10 W/m^2K as surface averaged values for sedentary occupants and/or thermal manikins (see chapter 2 of this PhD work).

The validated thermal manikin models used in this study readily provide the information about these coefficients. The convective heat transfer coefficients for the sedentary manikins in the classroom are plotted on the thermal manikins in Figure 8-17. These heat transfer coefficients provide an overview of the variation in thermal comfort that can exist in the room depending upon the mode of ventilation and seating arrangement.

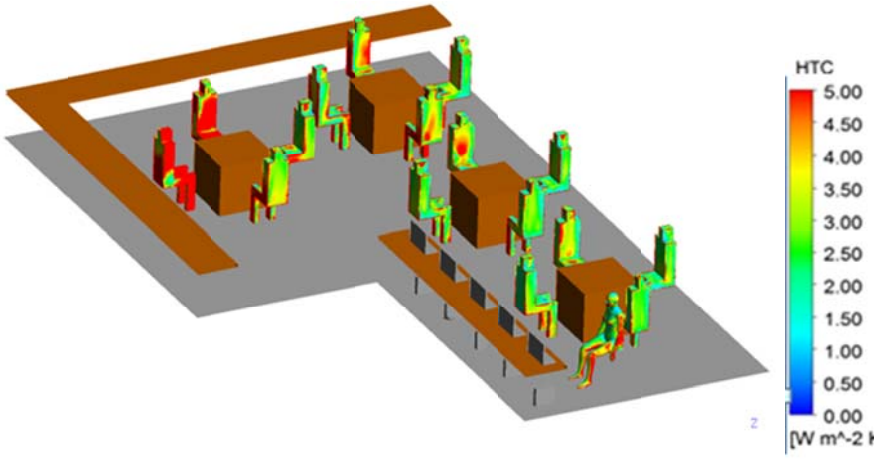

Figure 8-17: Convective heat transfer coefficients for seating arrangement 1 (left) and seating arrangement 2 (right)

The results show that occupants seated in the zone opposite the fan and lying in air flow trajectory experience higher local heat loss. In summer conditions such higher heat loss coefficient results in an improved local IAQ and thermal comfort condition of these occupants when compared to the rest of the occupants in the classroom. In winter however, activating the fan to improve IAQ of the complete classroom, would decrease the thermal comfort perception of these occupants.

8.7 Summary

The aim of this application study was to show the performance of a validated model for modelling IAQ and thermal comfort. By appropriately addressing the boundary conditions of the surroundings, issues related to HVAC design, IAQ and thermal comfort can be concurrently addressed. Applying multiple instances of a simplified manikin and one (or more) instances of detailed manikins not only enable the visualization and quantification of the IAQ in the room as a whole but can also give detailed information related to potential spread of contaminants and help localize zones of higher residence time of air as shown in this application example.

The basis of this application study is formed by the results provided by the measurements in a classroom (Hedger, 2011). The primary focus of the measurements was to investigate and address the IAQ issues of the classrooms. This application study compared the measured values with the simulation results mainly to show the potential of a validated CFD model to closely replicate the reality. Only temperature, relative humidity and CO2 concentrations values at certain locations in classroom were available for comparing against CFD simulations.

The measurement results showed that the average CO2 concentration in the classroom for an occupancy level of 17 people remains above 1000 ppm in most of the room space for the measured duration of time. Simulations replicated this trend of CO2 concentration above 1000 ppm for occupancy of 17 people with very little deviation.

Interpreting the measured results together with additional CFD results of heat transfer coefficients show that although the IAQ is much better in the zone opposite the fan, the thermal comfort conditions may not be optimal due to high local heat transfer coefficients. Reducing the ventilation rate would decrease further the air change rates causing a further decrease in IAQ in the region in front of the classroom door. The application study results show that there are regions in the room where the turbulence levels are low and CO2 is not fully mixed. Such information can be very helpful in the early phase of the building design in order to properly plan the ventilation system.

9 Conclusions and Modelling Guidelines

This chapter concludes the main findings of the complete verification, validation and application process of using thermal manikins in indoor climates using CFD. The following sections are intended to form a set of guidelines that can be followed to achieve reliable results when studying IAQ and thermal comfort in indoor climates. The conclusions drawn from this research serve to analyse CFD results in a critical fashion and are intended to avoid common mistakes and errors while setting up, running and analysing results for weakly buoyant flows in indoor climates.

9.1 Modelling Guidelines

9.1.1 Modelling Geometry

The first step while conducting a CFD study is to create the geometry for which the physics scenario needs to be defined. Different software are available on the market to model 2- and 3D geometries. The choice of these software is very often dictated by the price of the software. The level of detail a software offers has a direct correlation with the amount of time required to effectively and appropriately use the software.

For the current PhD work, the detailed human bodies employed were generated using the software Poser (Poser V6, 2013). Poser is a specific software for modelling human geometries with the possibility of generating individual body features and postures. A number of 3-D output formats are available, that can be directly used in the meshing software ANSYS ICEM CFD (e.g. .stl, .dwg, .stp, .sat) used extensively during this PhD work. Another software that was used during the course of this PhD work is Rhinoceros. Rhinoceros is a NURBS software that is mainly devised for creating 2- and 3-D surfaces.

This work has emphasized the fact that it is important to simplify the geometry involved in the model as much as possible without making a compromise on the loss of important information. For example when dealing with detailed manikins for investigating IAQ or local view factors, certain details such as space between fingers, length of nails, near eye and ear details etc. should be avoided by ‘wrapping up’ the geometry. This is done by joining such detailed surfaces together. It is recommended to optimize the geometry in a surface preparation tool such as Rhinoceros prior to importing the model into mesh

generation software. Although many mesh generation software codes (including ANSYS ICEM CFD used in this work) provide geometry clean-up options, they are not specialized for geometry clean-up and hence should be avoided for this purpose. Where possible, the complete domain should be modelled within a geometry modelling software and be exported to a meshing tool using parasolid formats (.x_t or .sat). If only some surface parts need to be imported into a meshing software, use of .stl gives a good option of exporting the model to a mesh generation software. Use of IGES and STEPS formats should be avoided (or optimized using export functions) where possible due to the level of unnecessary subdivision of the models and presence of lines and points.

9.1.2 Mesh Generation

Most of the time taken during this research work was spent on mesh generation and carrying out mesh independency studies. The turbulence models are found to be very sensitive to near wall mesh gradients. The application and limitation of turbulence models is very often dictated by the dimensionless distance of the first node from the wall surface namely the y+ value. The simulations conducted in this work with the focus on heat transfer mechanisms, showed that with an increase in mesh size and a decrease in y+ value, there is a general tendency of convergence and improvement in the simulation results. It is however important to note that even though the y+ value remains constant (same prism layer size), there is a large relative change in heat transfer coefficient values showing the impact and importance of local mesh refinement.

The physical variables dictating the flow in a natural convection dominated environment such as temperature, pressure, velocity etc. vary significantly in the surface normal region compared to the surface tangential region. As the surface normal flow or cross stream flow varies rapidly, a regular shaped mesh representation is necessary to capture these strong cross stream effects. Regular shaped hexahedral elements with high aspect ratios between element edge length (1=perfectly regular) are recommended to capture these flow gradients. In tetrahedral meshes, the elements are mostly triangular and high aspect ratios cannot be achieved for most of the cases (remaining less than 0.5 in most regions). Ideal would be to use a complete hexahedral mesh for simulations. This however is a very cumbersome (if not practically impossible) task for

complex real world geometries and hence a compromise is achieved using a mesh with a mix of triangular and hexahedral mesh cells. The mesh sensitivity study for vertical plate confirmed the fact that compared to hexahedral cells, almost 3-5 times more tetrahedral cells are required to get the same results with similar convergence level. The study also confirmed the importance of local mesh refinement. It is was noted that the run time to achieve a converged solution decreased with a mesh having prism layers perpendicular to the wall. These findings suggest that tetrahedral type mesh cells require more computational load to minimize the discretization errors, especially in regions of high gradients compared to regular (or near to regular) shaped prism layer elements (hexahedral).

In this work, verification and validation was carried out to develop a meshing methodology that can be applied to simulate occupants in natural convection dominated flows. In this methodology, the zone surrounding the occupant that needs to be investigated for the presence of human occupancy is modelled and meshed as shown in Figure 9-1. The hollow rectangular cavities (boxes) that are not meshed represent the location where the occupants need to be placed. These cavities are filled with previously generated meshes of computational manikins enclosed in a hypothetical enclosure of the same size. The enclosures that are fitted into these cavities are already validated for heat and mass transfer related phenomena under different laboratory controlled circumstances. Figure 9-2 shows a surrounding with an imported mesh enclosure containing a simplified validated manikin. It can be seen that just by importing the mesh, the vertices of the mesh are not properly aligned (do not lie on the same nodes). This non-alignment can lead to significant errors in the simulation results at the interface of the two meshes.

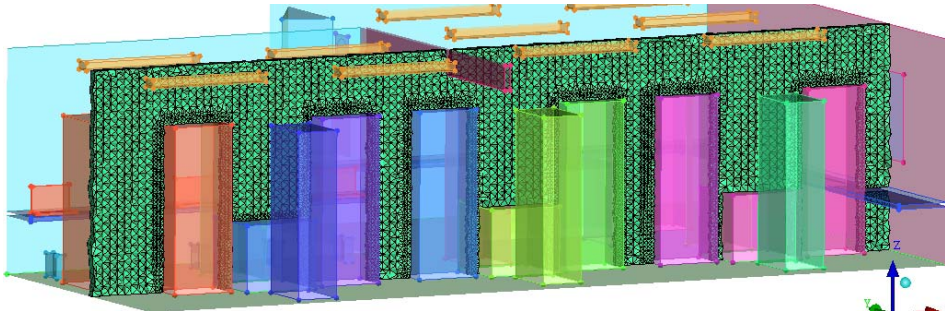

Figure 9-1: Meshed model surrounding without a mesh enclosure

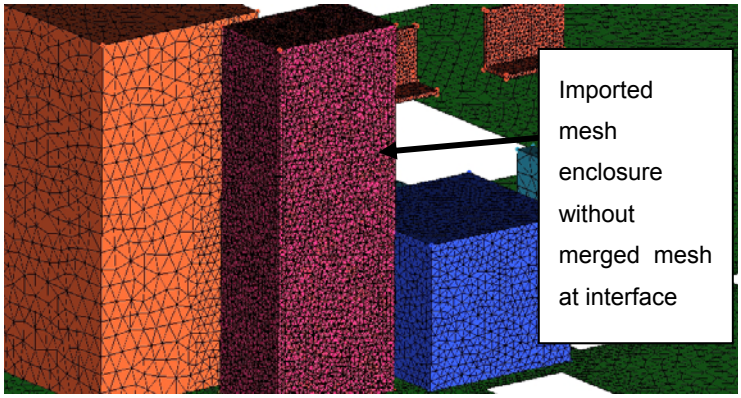

Figure 9-2: Meshed model with a mesh enclosure and surrounding without merged meshes

In order to avoid this mismatching of nodes at the interface of the two meshes, the two meshes should be appropriately merged. It is important to handle the imported (validated) mesh enclosure as a "frozen zone". A frozen zone is one where the mesh configuration takes precedence while the merging operation is performed by the mesh generator. The mesh vertices and elements of the surroundings at the interface level are then adjusted to generate the mesh interface that is conformed at the vertices to transfer the data at the interface without numerical issues. The resulting mesh interface is shown in Figure 9-3.

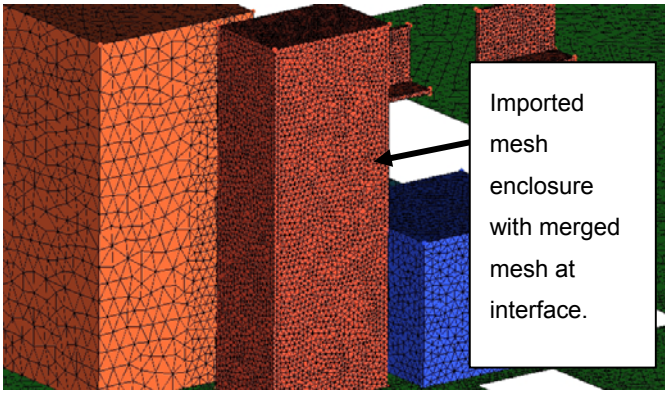

Figure 9-3: Meshed model with a mesh enclosure and surrounding with merged meshes

The result of a successful mesh merging process results in the generation of two separate meshed domains i.e. a surrounding domain and an enclosed domain as shown in Figure 9-4.

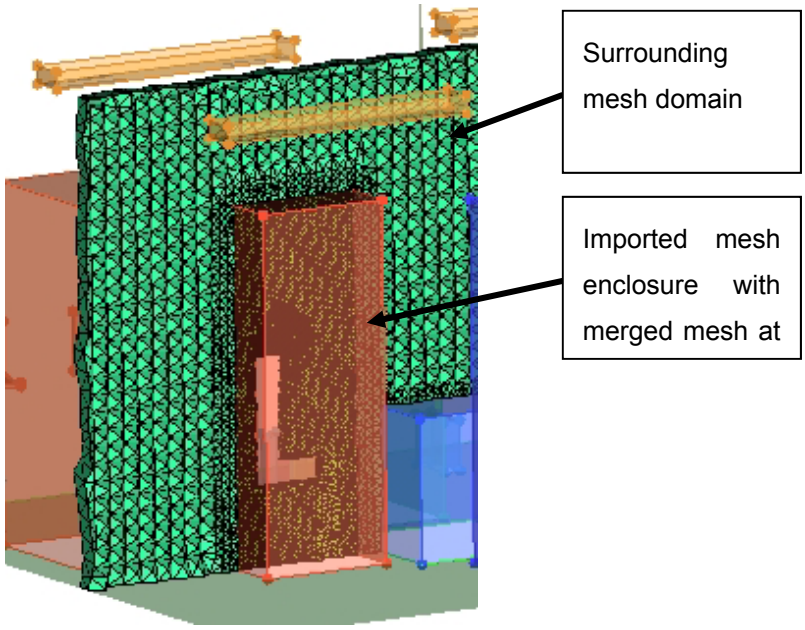

Figure 9-4: Cut plane showing meshed domains after mesh merging process.

Employing this methodology for multiple cases obviates the need for regenerating the complete mesh of the domain. Only local smoothing at mesh level will suffice to achieve an optimal mesh for simulation runs. In order to gain confidence about the flow in the surrounding area and compare it with the effect of the presence of the human occupants, the box cavities can be filled with meshes without the manikin, for a preliminary simulation. In case of presence of openings with sudden pressure jumps and loss coefficients, extrusion layers (prism layers) should be generated at the opening surfaces (normal to opening surface).

9.1.3 Modelling Radiation

The use of radiation models was addressed for different radiation types (directional and diffuse radiation) and for different postures. For indoor climates, the effect of radiation can be adequately modelled using the grey diffused assumption with surface to surface radiation modelling with the air being considered as a ‘thin medium’ which does not participate in the radiation.

For conditions involving indoor climates charged heavily with particles having radiation properties e.g. scattering, emissivity, air needs to be modelled as a participating media. Examples of indoor climate requiring air to be treated as participating media are smoking rooms or spaces involved in case of a fire emergency. For directional radiation

e.g. solar radiation into the room, spot lights etc. the use of the "Monte Carlo" radiation model is inevitable. The radiation modelling together with convective heat transfer modelling involves a considerable amount of time due to the complexities of real life scenarios. It is recommended to freeze the flow solver and calculate the radiation heat transfer with given boundary condition where possible (refer to radiation modelling section).

9.1.4 Modelling Convection

In the work reported here, the Boussinesq approximation was employed for simple verification and validation cases as well as for cases involving a single component gas medium. Modelling IAQ requires modelling of air with water vapour and CO2 as multi-component gases, the application of the Boussinesq approximation is not valid due to gas dependent density differences. While modelling convection dominated flows, it is important to resolve the resulting variable gradients normal to the wall surface. The production and dissipation of buoyancy terms need to be included in momentum equations. This demands additional fine resolution near solid surfaces in cases of natural buoyancy flow. For the work reported here, activating the calculation of production and dissipation of buoyancy helps resolve the shear dominated regions but led to increased transient oscillations during the simulations. These oscillations were controlled by running the simulation in transient mode with constant boundary conditions.

In order to account for flow phenomena in the breathing zone, the exact geometry description is necessary. Failing to do so would under- or overestimate important aspects such as re-inhalation of CO2 and other pollutants. While simulating the breathing zone, the inclusion of a pause between the inhalation and exhalation cycle is found to have a significant effect on the ratio between entrained and re-inhaled air. A one second pause between the inhalation and exhalation can reduce the amount of re-inhaled CO2 to less than 1%. Past research work mainly ignored this pause and reported the amount of re-inhaled CO2 to be well above 10% (Gao & Niu, 2006) (Gao, et al., 2008). The application study conducted during the course of this PhD work showed that the geometrical detail of the manikin has little or no influence on the global distribution of CO2 (and hence on the IAQ with CO2 considered as an indicator of IAQ).

For sedentary and normal breathing manikins in flows dominated by natural convection, the exhaled CO2 and pollutants become entrained inside the thermal plume itself. This statement however does not hold true for rooms and interpersonal contamination transport in case of strong forced flows or processes such as coughing and sneezing.

9.1.5 Modelling Turbulence

Mainly two turbulence models were investigated in this work: the k-ε model and the Shear Stress Transport (SST) model. The results have shown that an improvement in two equation models, namely the SST model, predicts the near wall region much better than standard eddy viscosity models. In order to make full use of the SST turbulence model and use its capability to resolve the flow separation and adverse gradient zones, the y+ value should be near to 1. In the work reported here, the SST model has shown to have very good results even at y+ values in the range of 1 - 3.

9.2 Conclusions

The major conclusions of the present work can be summarized as follows:

1. Numerical simulations of radiative heat transfer using detailed human geometrical models have shown that the geometrical posture has a significant effect on effective radiation area. A globally accepted value of 0.725 of effective radiation factor for standing objects (Fanger, 1972) does not account for this variation. During this work, study of three different standing postures have been shown to have higher values of effective radiation factors (in range of 7 - 13%).
2. The simulation results have shown that simulating a pause between inhalation and exhalation can decrease the re-inhaled CO2 from the reported 10 - 19% to less than 1%.
3. This work has shown that simplified seated manikins are appropriate to investigate the IAQ of complete indoor spaces but can cause an underestimation in the amount of re-inhaled CO2 and pollutants by about 37% when compared with detailed seated manikins.

9.3 Recommendations

Based on the work done as part of the present PhD, the following generic guidelines and recommendations can be made:

1. Simplify the geometry prior to exporting into a meshing tool. This involves joining and refining the model at joints and edges and deleting any unnecessary point and line details.
2. Ensure a ‘water tight’ surface within a NURBS modelling tool.
3. Convert meshes in the model to a NURB surface. Very often large meshes are not converted to NURBS by standard version (32 bit) of software. The use of 64 bit versions and relevant plug-ins however allow these conversions.
4. Generation of prism layers at boundary surfaces is required for buoyancy driven flows in order to capture the strong flow and thermal gradients. An auto-reduction in prism layer generation to follow the surface contour helps in correct generation and avoidance of layers with zero cell thickness.
5. Local mesh refinement, particularly in areas of special interest (e.g. the nostril region) avoid the occurrence of large mesh gradients which can cause numerical instabilities such as oscillating residuals, divergence etc.
6. Mesh merging is a helpful way to increase local control on meshing along with saving time required for meshing. It is important that the validated enclosure should be defined as the "frozen zone" (see section 9.1.2 for explanation).
7. In the case of openings with large pressure changes, extrusion layers (prism layers) should be generated in the direction normal to the plane of the opening.
8. The Boussinesq approximation for modelling of buoyancy is sufficient for simple cases with single component gases. It should be employed for indoor conditions where the maximum temperature difference is below 30 K.
9. Use buoyancy production and dissipation term in momentum equations of the turbulence models while calculating the near wall turbulence.
10. Despite fine mesh resolution, use of buoyancy production and dissipation terms can cause oscillatory flow behaviour (non-convergence). Such problems can be resolved by running a transient simulation with constant boundary conditions.
11. Use the SST turbulence model as it can resolve simultaneously the low Reynolds number flow near the wall region using k-ω type turbulence modelling approach and a

k-ε type turbulence modelling approach in regions dominated with high Reynolds number flows. The SST model performs better at low y+ values. It was difficult to achieve meshes with y+ below 1 for real world scenarios due to geometrical complexity.

12. Second or high resolution discretization scheme should be used to discretize the partial differential equations in order to avoid numerical diffusion which is pronounced in case of non-regular meshes.
13. The simulations with low scalar quantities in the simulation domain require a profound engineering judgment in terms of initial boundary condition modelling. In pursuit of achieving a physically and mathematically converged numerical solution, an appropriate engineering judgment has shown to have saved simulation run time by order of magnitudes (see chapter 7 for details).

9.4 Summary

Application of CFD for solving buoyancy driven flow due to occupants is a challenge for the engineers and designers of indoor environments. As well as engineering judgment, thorough validation and application examples are necessary to gain more confidence in the use of CFD for detailed full scale real life scenarios.

The main contribution of this research work is the provision of a validated seated computational human thermal manikin. Following the modelling guidelines mentioned above, this thoroughly validated manikin can be directly imported into any indoor surrounding to simultaneously investigate the effects of heat transfer pertaining to the estimation of human thermal comfort, estimate the indoor quality and evaluate the effects of respiration in the micro and macro surroundings of a seated thermal manikin.

Using a structured approach and validated models, this PhD work could prove its novelty in the form of the key findings mentioned in section 9.2. Besides the concrete outcomes mentioned above, a set of generic guidelines for modelling factors affecting human thermal comfort and IAQ are given in section 9.3. Although CO2 and its dispersal is modelled as a multi-component mixture, the current work can not address the dispersal of pollutants with aerodynamic particle sizes larger than 2.5 - 3 μm. The complete work is based on the assumption that the particle sizes are small enough to remain airborne.

10 References

ANSI/ASHRAE, 2003. Ventilation for Acceptable Air Quality. *Standard 62-2001*.

ANSI/ASHRAE, 2004. Standard 55-2004. *American Society of Heating Refrigeration and Air Conditioning Engineers Inc*.

Ansys, Inc., 2016. *www.Ansys.com.* [Online]
[Accessed 1 Feburary 2009].

Asmussen, E. & Nielsen, M., 1989. Laerebog i menneskets fysiologi. *Akademisk Forlag.*

Auliciems, 1990. Air conditioning in Australia III thermobile controls. *Architectural Science Reveiw,* Band 33, pp. 43-48.

Awbi, H. B., 2003. *Ventilation in Buildings.* London and Newyork: Taylor & Francis.

Azer, N. Z. & Hsu, S., 1977. The prediction of thermal sensation from a simple model of human physiological regulatory response. *ASHRAE Trans 83 (1)*, pp. 88-102.

Barankova, P., Naydenov, K. G., Melikov, A. K. & Sundell, J., 2004. *Distribution of carbon dioxide produced by people in a room: Part 1 - Laboratory study.* Coimbra, RoomVent.

Barrett, K. E., Barman, S. M., Boitano, S. & Brooks, H., 2012. *Ganong's Review of Medical Physiology.* 24th Edition Hrsg. New York: McGraw-Hill Education.

Baughman, A. V., Gadgil, A. J. & Nazaroff, W. W., 1994. Mixing of a Point source pollutant by natural convection flow within a room. *Indoor Air ,* pp. 4 114-112.

Benedict, F. G., Miles, W. R. & Johnson, A., 1919. The Temperature of the Human Skin. *Proceedings of the National Academy of Sciences of the United States of America,* 5(6), pp. 218-222.

Bjørn, E., 2001. *Mechanical and anthropometric considerations for physical and.* Switzerland, EMPA.

Bjørn, E. & Nielsen, P. V., 1988. CFD Simulations of contamination transport between two breathing person. *Indoor Envrionmental Engineering,* R9809(96).

Borges, C. P. et al., 2002. *Analysis of thermal plumes generated by a seated person, a thermal manikin and a dummy.* Copenhagen, Roomvent 2002 vol 1 253-256.

Boussinesq, J., 1903. Therie Analytique de la Chaleur. *Gauthier-Villars,* Band 2.

Brohus, H., 1997. *CFD Simulation of Personal Exposure to Contaminant sources in Ventilated Rooms,* s.l.: Aalborg University Denmark.

Burchill, Shirley;, 2011. *http://www.saburchill.com/chapters/chap0019.html.* [Online] [Accessed April 2001].

Cannistraro, G., Franzitta, G., Giaconia, C. & Rizzo, G., 1992. Algorithms for the calculation of the view factors between human body and rectangular surfaces in parallelepiped environments. *Energy and Buildings,* Band 19, pp. 51-60.

Castro, M., 1998. Control of breathing. In: R. M. Berne, M. N. Levy, B. M. M. Koeppen & B. A. P. Stanton, Hrsg. *Physiology.* St. Louis: Mosby Inc.

CD-adapco, 2002. *www.cd-adapco.com.* [Online]
[Zugriff am 2010].

CD-adapco, 2016. *Spotlight on Turbulence,* Nuernberg: CD-Adapco.

CFX, A., 2010. *ANSYS CFX Solver Guide Manual.* South Pointe: ANSYS Inc..

Chmielewski, M. & Gieras, M., 2013. Three-zonal Wall Function for k-e Turbulence Models. *Computational Methods in Science and Technology,* 19(2), pp. 107-114.

Churchill, S. W. & Chu, H. S., 1975. Correlating equations for laminar and turbulent free convection from a vertical plate. *International Journal of Heat and Mass Transfer,* 18(1), pp. 1323-1329.

CIBSE Guide A, 2006. *Environmental design.* 7th Hrsg. London: CIBSE.

Clark, R. P. & Toy, N., 1975. Natural convection around the human head. *Journal of Physiology,* Band 244(2), pp. 283-293.

Clausen, G. et al., 1993. A comparative study of discomfort caused by indoor air pollution, thermal load and noise. *Indoor Air,* pp. 255-262.

Cook, M. J., 1998. *An Evaluation of Computational Fluid Dynamics for Modelling Buoyancy Driven Displacement Ventilation.* Leicester: De Montfort University.

Corbett, E. L. et al., 2003. The growing burden of tuberculosis: global trends and interactions with the HIV epidemic. *Arch Intern Med,* Band 163, pp. 1009-1021.

CR 1752 CEN, 1988. *Ventilation for Buildings: Design Criteria for the Indoor Environment,* Brussels: European Committee for Standardization.

Cropper, P. C. et al., 2008. *Exchange of simulation data between CFD programmes and a multi-segmented human thermal comfort model.* London, Cumberland Lodge Windsor.

de Dear, R. J., Edward, A., Zhang, H. & Masayuki, O., 2001. Convective and radiative heat transfer coefficients for individual human body segments. *Intl. Journal of Biometerology,* Band 40, pp. 141-156.

Donghyun, R. & Novoselac, A., 2008. Transient Simulation of Airflow and Pollutant Dispersion under Mixing Flow and Buoyancy driven Flow Regimes in Residential Buildings. *ASHRAE Trans,* 114(2), pp. 130-142.

Douglas, C. G. & Haldane, J. S., 1909. The regulation of normal breathing. *Journal of Physiology ,* Band 38, p. 420–440.

DuBois, D. & Du Bois, E., 1989. A formula to estimate the approximate surface area if height and weight be known.1916.. *Nutrition,* 5(5).

Dunkle, R. V., 1963. Configuration factors for radiant heat transfer calculations involving people. *Journal of Heat Transfer,* Band 83, pp. 71-76.

Dye, C. et al., 1999. Global Burden of Tuberculosis, Estimated Incidence, Prevalence, and Mortality by Country. *JAMA,* Band 282, pp. 677-686.

Egan, M. D., 1975. *Concepts in Thermal Comfort.* Dunfermline, UK: Prentice Hall.

Etheridge, D. W. & Sandberg, M., 1996. *Building Ventilation: Theory and Measurement.* s.l.:John Wiley and Sons Inc.

Fanger, P. O., 1972. *Thermal Comfort.* New York: McGraw Hill Book Company.

Fanger, P. O., 1988. *A comfort equation for indoor air quality and ventilation.* Stolkholm, State of the Art Reviews, pp. 39-51.

Fanger, P. O., 1988. Air pollution sources in offices and assemble halls, quantified by the olf unit. *Energy and Buildings 12,* pp. 7-19.

Fang, I., Clausen, G. & Fanger, P. O., 2000. Temperature and humidity; important factors for perception of air quality and for ventilation requirements. *ASHRAE Trans. 106*, pp. 503-510.

Fiala, D., 1998. *Dynamic Simulation of Human Heat Transfer and Thermal Comfort,* Leicester: De Montfort University.

Fiala, D. & Lomas, K. J., 1999. A computer model of human thermoregulation for a wide range of envionmental conditions: the passive system. *American Physiological Society.*

Gagge, A. P., 1973. Rational temperautre indices of man's thermal envionment and their use with a two node model of his temperature regulation. *Fed. Proc vol 32,* pp. 1572-2582.

Gagge, A. P., Fobelets, A. P. & Berglund, L. G., 1986. A standard predictive index of human response to the thermal environment. *ASHRAE Transaction 92 (2)*, pp. 709-731.

Gagge, A. P., Stolwijk, A. J. & Nishi, Y., 1971. An effective temperature scale based on a simple model of human physiological regulatory response. *ASHRAE Trans,* Band 77, pp. 247-262.

Gao, N. & Niu, J., 2006. Transient CFD simulation of the respiration process and inter-person exposure assessment. *Building and Environment,* pp. 1214-1222.

Gao, N., Niu, J. & Morawska, L., 2008. Distribution of Respiratory Droplets in Enclosed Environments under Different Air Distributin Methods. *Building and Simualation,* Band 1, pp. 326-335.

Griffiths, M. & Eftekhari, M., 2008. Control of CO2 in a naturally ventilated classroom. *Energy and Buildings,* 4(40), pp. 556-560.

Gupta, J., Lin, C. & Chen, Q., 2010. Characterizing exhaled airflow from breathing and talking. *Indoor Air,* Band 20, pp. 31-39.

Guyton, A., 1984. *Physiology of the human body.* 6th Hrsg. Philadelphia: Suanders College Publ.

Harger, R. N., Forney, R. B. & Barnes, H. B., 1950. Estimation of Level of Blood Alcohol from Analysis of Breath. *Journal of Laboratory and Clinical Medicine,* Band 36, pp. 306-318.

Hart, D. P., 1998. *The Elimination of Correlation Errors in PIV Processing.* Lisbon, 9th Intl. Symposium on Applicaiton of Laser Techniques to Fluid Mechanics.

Hathway, E. A. et al., 2013. The Role of Nursing Activities on the Bioaerosol Production in Hospital Wards. *Indoor and Built Environment,* 22(2), pp. 410-421.

Hayashi, T., Yoshiaki, I., Shinsuke, K. & Murakami, S., 2002. CFD analysis on characteristics of contaminated indoor air ventilation and its appliation in evalatin of the effect of contaminant inhalation by a human occupant. *Building and Environment,* Band 37, pp. 219-230.

Hedger, J., 2011. *Understanding CO2 Dispersion and Distribution in School Classrooms,* Loughborough: Department of Civil and Building Engineering, Loughborough University.

Homma, H. & Yakiyama, M., 1988. Examination of free convection around occupant's body caused by its metabolic heat. *ASHRAE Transactions,* Band 94(1), pp. 104-124.

Homma, H. & Yakiyama, M., 1991. Examination of free convection around occupant's body caused by its metabolic heat. *ASHRAE Trans 94 part 1 (3118)*, pp. 104-124.

Höppe, P., 1981. Temperature of expired air under varying climatic conditions. *Int. J. Biometeorol.,25,* pp. 127-132.

Höppe, P. R., 1993. *Heat balance modelling.* Basel, Birkhäuser Verlag, pp. 741-746.

Houghoton, F. C. & Yaglou, C. P., 1923. Determination of the comort zone: ASHVE Research Report No. 673. *ASHVE Trans.* , pp. 29, 361.

Huizenga, C. & Hui, Z., 2001. A model of human physiology and comfort for assessing complex thermal environments. *Building and Environment,* 36(6), pp. 691-699.

Humphrey, M. & Nicol, J., 1998. Understanding the Adaptive Approach to Thermal Comfort. *ASHRAE Trans*.

Incropera, F. P., 2006. *Fundamentals of Heat and Mass Transfer.* 6th Hrsg. New York: John Wiley & Sons.

Institut für Rationelle Psychologie, 2007. *KÖRPERMASSE BUNDESLÄNDER & STÄDTE,* Stuttgart: Institut für Rationelle Psychologie.

Institute für Arbeitssicherheit, 1995. *BIA- Report 2/1995: Innenraumluftqualität.* Sankt Augustin: Berufsgenossenschaftl. Institut für Arbeitssicherheit.

Jianjian, W. et al., 2016. Low re-inhalation of the exhaled flow during normal nasal breathing in a pediatric airway replica. *Building and Environment,* Band 97, pp. 40-47.

Karthikeyan, C. P. & Samuel, A., 2008. CO2 dispersion studies in an operation theatre under transient conditions. *Energy and Buildings,* Band 40(3), pp. 231-239.

Kato, S., Murakami, S. & Yoshie, R., 1993. Experimental and numerical study on natural convection with strong desnity variation along a heated vertical plate. *Proc. of 9th Symposium on Turbulent Shear Flows,* pp. 12.5.1-12.5.6.

Kitchin, C. R., 1987. *Stars, Nebulae and the Interstellar Medium: Observational Physics and Astrophysics.* Philadelphia: CRC Press.

Kofoed, P. & Nielsen, P. V., 1990. Thermal plumes in ventilated rooms. *RoomVent.*

Kubaha, K., 2005. *Asymmetric Radiant Fields and Human Comfort,* Leicester: Institute of Energy and Sustainable Development, DeMontfort University, UK..

Lavergea, J., Spilak, M. & Novoselac, A., 2014. Experimental assessment of the inhalation zone of standing, sitting and sleeping persons. *Building and Environment,* Band 82, pp. 258-266.

Laverge, J., Novoselac, A., Corsi, R. & Janssens, A., 2013. Experimental assessment of exposure to gaseous pollutants from mattresses and pillows while asleep. *Building Environment,* Band 59, pp. 203-210.

LaVision, 2011. *www.lavision.de,* Goettingen: LaVision.

Lia, X., Inthavong, K., Ge, Q. & Tu, J., 2013. Numerical investigation of particle transport and inhalation using standing thermal manikins. *Building and Environment,* Band 60, pp. 116-125.

Mahyuddin, N., Awbi, H. B. & Essah, E. A., 2015. Computational fluid dynamics modelling of the air movement in an environmental test chamber with a respiring manikin. *Journal of Building Performance Simulation,* Band 8, pp. 359-374.

Mayer, E., 1983. *Entwicklung eines Messgeräts zu getrennten und integrative Erfassung der physikalischen Raumklimakomponenten,* Stuttgart: Diss Tech. Univ. München.

Mayer, E., 1993. Objective criteria for thermal comfort. *Building and Environment ,* pp. 28(4) 399-403.

McNaught, A. D. & Wilkinson, A., 1997. *Compendium of Chemical Terminology.* 2nd Hrsg. Oxford: Wiley.

Meckler, M., 1996. Improving Indoor Air Quality Through Design, Operation and Maintenance. *The Fairmount Press Inc..*

Melikov, A., Cermak, R. & Mayer, M., 2002. Personalized ventilation: Evaluation of different air terminal devices. *Energy and Buildings,* 34(8), pp. 829-836.

Melikov, A. K., 2004. Breathing thermal manikins for indoor enviornment assessment: important characteristics and requirements. *European Journal of Applied Physiology,* Band 92, pp. 710-713.

Melikov, A. & Kaczmarczyk, J., 2007. Measurement and prediction of indoor air quality using a breathing thermal manikin. *Indoor air,* Band 17, pp. 50-59.

Melikov, A. K., Kaczmarczyk, J. & Cygan, L., 2000. *Indoor air quality assessment by a breathing thermal manikin.* Coimbra, RoomVent.

Melikov, A. & Zou, H., 1999. Comparison of methods for determining equivalent temperature under well designed conditions. *Proceedings of the sixth intl. conference Florence ATA.*

Mendell, M. J. & Heath, G. A., 2005. Do indoor pollutants and thermal conditions in schools influence student performance ? A critical review of literature. *Indoor Air,* 1(15), pp. 27-52.

Menter, F. R., 1994. Two-equation eddy-viscosity turbulence models for engineering applications. *American Institute of Aeronautics and Astronautics,* 32(8), pp. 1598-1605.

Milton, D. K., Glencross, P. M. & Walters, M. D., 1999. Risk of sick leave associated with outdoor air supply rate, humidification and occupant complaints. *Indoor Air, Vol 10,* pp. 212-221.

Mobiok, A. & Weber, R., 2000. *Radiation in Enclosures.* Berlin: Scientific Computations, Springer-Verlag.

Mora, L. & Gadgil, A. J., 2002. *Theoratical study of pollutant mixing in rooms induced by occupancy, Interaction of room air movement and occupants.* Copenhagen, LBNL.

Morton, B. R., Taylor, G. I. & Turner, J. S., 1956. Turbulent Gravitational Convection for Maintained and Instantaneous Sources. *Proc. Royal Soc. London,* Band 234, pp. 1-23.

Murakami, S., Kato, S. & Zeng, J., 2000. Combined simulation of air flow, radiation and moisture transport for theat release from a human body. *Building and Environment,* Band 35, pp. 489-500.

Nazaroff, W. W. & Cass, G. R., 2002. Mathematical modelling of indoor aerosol dynamics.. *Environmental Science Technology 36,* pp. 200-7.

Nielsen, P. V. et al., 2003. *Benchmark Tests for a Computer Simulated Person,* Aalborg: Aalborg University.

Nishi, Y. & Gagge, A. P., 1972. Direct evaluation of convective heat transfer coefficient by napthalene sublimation. *Journal of Applied Physiology,* 29(6).

Olmedo, I., Ruiz de Adanan, R. M. & Nielsen, P. V., 2012. *Validation of a human exhalation flow simulatin in a room with vertical ventilation.* Paris, 10th Intl. Conference on Industrial Ventilation.

Özcan, O., Meyer, K. E. & Melikov, A., 2005. A Visual Description of the Convective Flow Field around the Head of a Human. *Journal of Visualization,* Band 8, pp. 23-31.

P T Teknik, 2016. Espergærde, Denmark: s.n.

Pettenkofer, M. v., 1858. *Über den Luftwechsel in Wohngebäuden.* München: Literarisch-Artistische Anstalt der J.G. Cotta'schen Buchhandlung.

Poser V6, 2013. *Poser, The Premier 3D Design Tool, User Guide,* CA: Curuous Labs Inc. Santa Cruz.

Raber, B. F. & Hutchinson, F. W., 1944. Optimum surface distribtion in panel heating and cooling systems. *ASHVE Trans,* Band 48, pp. 231-265.

Rapp, G. M., 1973. Convective heat transfer and convective coefficients of nude man, cylinders and spheres at low air velocities. *ASHRAE Trans,* Band 79 (1).

Rapp, G. M., 1976. Convective heat transfer and convective coefficients of nude man, cylinder and spheres at low air velocities. *ASHRAE Trans.,* Band 2264.

Recknagel & Sprenger, 2007. *Taschenbuch für Heizung + Klima Technik.* 73 Hrsg. Munich: Olderbourg Industrieverlag.

Rhinoceros, 2010. *Robert McNeel & Associates.* Barcelona: McNeel Europe.

Roberts, K. et al., 2006. Bioaerosol Production on a Respiratory Ward. *Indoor and Built Environment,* Band 15, pp. 35-40.

Rohles, F. H. & Nevins, R. G., 1971. The nature of thermal comfort for sedentary man. *ASHRAE Transactions ,* 77(1), pp. 239-246.

Salim, M. S. & Cheah, S. C., 2009. Wall y+ Strategy for Dealing with Wall-bounded Turbulent Flows. *Intl. Mulit Conference of Engineers and Computer Scientists,* Band II.

Schonecht, G. & Stock, B., 1995. *The Technical Concept for Evidential Breath Testing in Germany.* Adelaide, ICADTS T-95.

Shair, F. H. & Heitner, K. L., 1974. Theoratical model for relating indoor pollutant concentrations to those outside. *Environmental Science Technology 8(5),* pp. 444-51.

Shaw, C. T., 1992. *Using Computational Fluid Dynamics.* s.l.:Prentice Hall.

Sideroff, C. N. & Dang, T. Q., 2005. *Validation of CFD for the flow around computer simulated person in a mixing ventilated room.* Beijing, International Conference on Indoor Air Quality and Climate.

Siegel, R. & Howell, J. R., 1992. *Thermal Radiation Heat Transfer.* 3rd Hrsg. s.l.:Hemisphere Publishing.

Sørensen, D. N. & Vøigt, L. K., 2003. Modelling flow and heat transfer around a seated human body by computational fluid dynamics. *Building and Environment,* Band 38, pp. 753-762.

Spitzer, I. M., Marrb, D. R. & Glausera, M. N., 2010. Impact of manikin motion on partical transport in the breathing zone. *Journal of Aerosol Science,* 41(4), pp. 373-383.

Steiger, S., Hellwig, R. T. & Junker, E., 2008. Distribution of carbon dioxide in a naturall ventilated room with high internal heat load. *Proc. 8th Symposium on building physics in the nordic countries,* Band 1, p. 377.

Stolwijk, J. A., 1971. *A mathematical model of physiological temperature regulation in man,* Washington DC: NASA CR-1855.

Straub, N. C., 1998. The Respiratory System. In: R. M. Berne, M. N. Levy, B. M. M. Koeppen & B. A. P. Stanton, Hrsg. *The Respiratory System.* St. Louis: Mosby.

Switzer, P. & Wayne, O., 1992. Derivatin of an indoor air averaging time model from the mass balance equation of the case of independent source inputs and fixed air exchange rates. *Jounal of Exposure Analysis and Environmental Epidemiology 2(S2),* pp. 113-55.

Tanabe, S. et al., 1994. Evaluating thermal environments by using a thermal manikin with controlled skin surface temperature. *ASHRAE Trans.,* 100(1), pp. 39-48.

Tanabe, S. et al., 2002. Evaluation of thermal comfort uisng combined multi-node thermoregulation (65 MN) and radiation models and computational fluid dynamics (CFD). *Energy and Buildings,* 34(6), pp. 637-646.

Tanabe, S., Nakano, J. & Koboyashi, K., 2001. Development of 65-Node thermoregulation model for evaluation of thermal environment. *Jounal of Achritectural Planning and Environmental Engineering (AIJ),* pp. 541 205-215.

Topp, C., 2002. *Influence of geometry of a computer simulated person on contaminant distributin and personal exposure.* Copenhagen, Roomvent, 8th Int. Conference on Air Distribution in Rooms.

Valerie, S. C. & Sanders, T., 2010. *Essentials of Anatomy and Physilogy.* 6 Hrsg. New York: F.A. Davis Company.

Versteeg, H. K. & Malalasekera, W., 2007. *An introduction to computational fluid dynamics: The Finite Volume Method.* 2nd Hrsg. London: Person Education Limited.

Viboud, C. et al., 2004. Influenza Epidemics in the United States, France, and Australia, 1972–1997. *Emerging Infectious Diseases,* Band 10, pp. 32-39.

Wargocki, P., Wyonn, D. P. & Fanger, P. O., 2000. *Pollution source control and ventilation improve health comfort and productivity.* Bremen, s.n., pp. Band 4, pp 47-54.

Westerweel, J., 1997. Fundamentals of digital particle image velocimetry. *Meas. Sci. Technol. ,* Band 8, pp. 1379-1392.

Wilcox, D. C., 1986. *Multiscale model for turblent flows,* Reno NV: American Institute of Aeronautics and Astronautics.

Wilcox, D. C., 1998. *Turbulence Modeling for CFD,* California: DCW Industries, Inc. La Canada.

Wissler, E. H., 1964. A mathematical model of the human thermal system. *Bulletin of mathematical biophysics,* pp. vol 26 147-166.

Xiaoxiong, Y., 1995. *Wall Functions for Numerical Simulation of Natural Convection along Vertical Surfaces,* Zürich: Swiss Federal Institute of Technology.

Yaglou, C. P., Riley, B. C. & Coggins, D. J., 1936. Ventilation requirements. *Trans. ASHVE, 42*, pp. 133-62.

Yang, T. et al., 2007. *A new simulation system to predict human environment thermal interaction in naturally ventilated buildings.* Beijing, Building Simulation.

Ye, X. J. et al., 2006. Field study of a thermal environment and adaptive model in Shanghai. *Indoor Air,* Band 16 , pp. 320-326.

Yi, Z., Novieto, D. & Yingchun, J., 2007. *Human environmental heat transfer simulation with CFD - The advances and challenges.* Glasgow, 11th IBPSA Conference.

Zhang, H., 2003. *Human thermal sensation and comfort in transient and non-uniform thermal environment,* California: University of California at Berkeley.

Zhao, B., Zhang, Z. & Li, X., 2005. Numerical study of the transport of droplets or particles generated by respiratory systems indoors. *Building and Environment,* Band 40, pp. 1032-1039.

Zhu, S., Yang, J.-H. & Kato, S., 2006. Investigation into Airborne Transport Characteristics of Airflow Due to Coughing in a Stagnant Indoor Environment. *ASHRAE Transaction,* 112(1), p. 123.

Zukowska, D., Melikov, A. K. & Popiolek, Z. J., 2007. Thermal plume above a simulated sitting person with different complexity of body geometry. *RoomVent.*

Zukowska, D., Melikov, A. K. & Popiolek, Z. J., 2012. Impact of personal factors and furniture arrangement on the thermal plume above sitting occupant. *Building and Environment,* Band 49, pp. 104-116.

APPENDIX A

A.1. Convergence history of medium grid mesh with SST Turbulence model

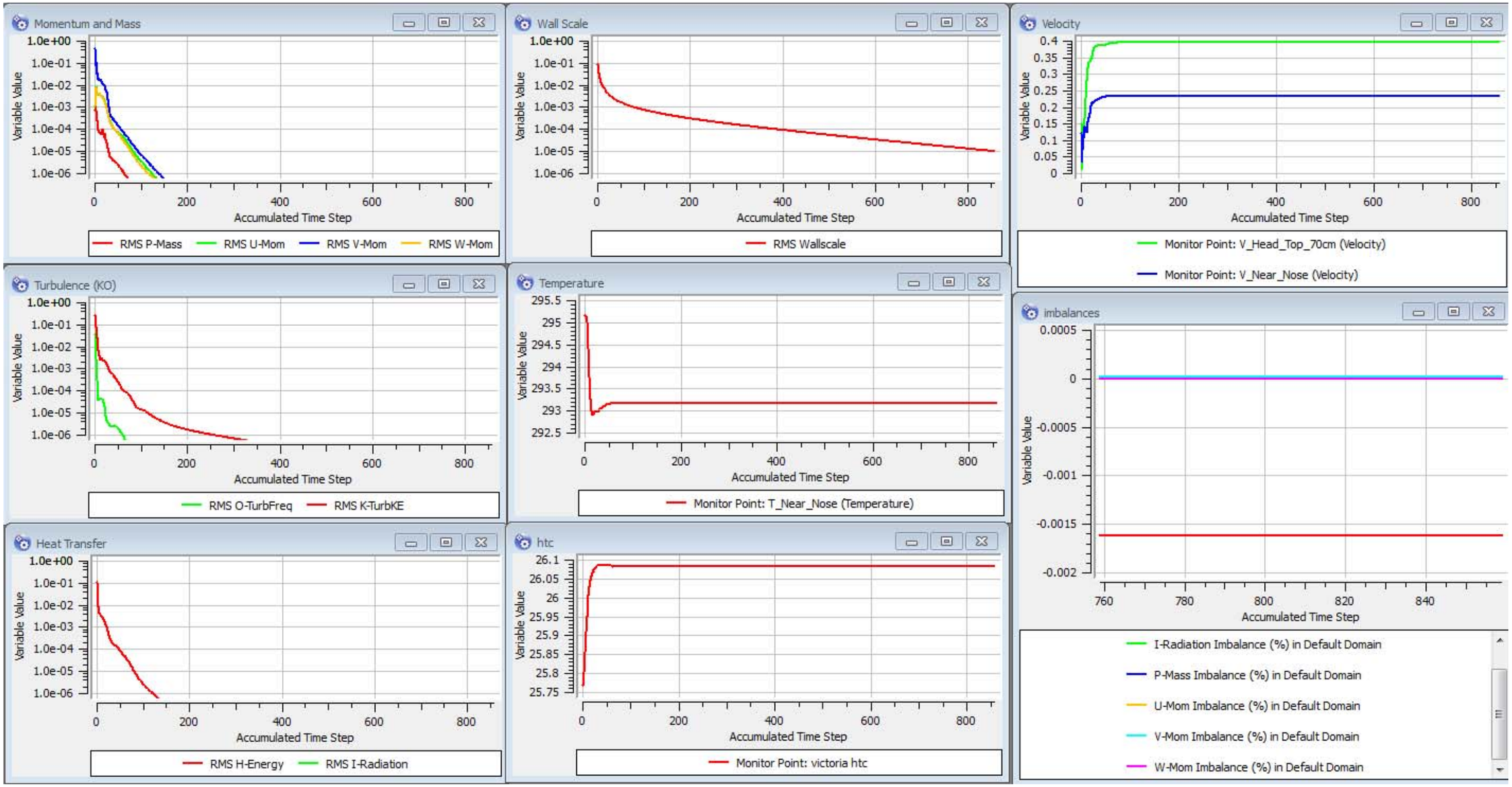

A.2. Results of zero equation eddy viscosity turbulence model

Zero Equation Eddy Viscosity Turbulence Model						
Mesh	**Flow Field**		**Temperature Field**		**Convective Heat Transfer Coefficients**	
Coarse	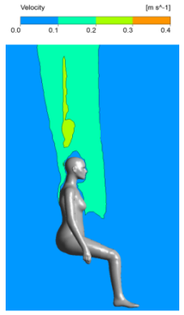	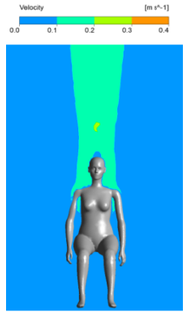	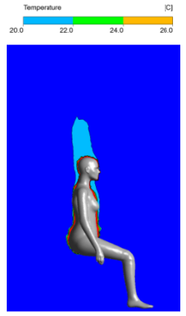	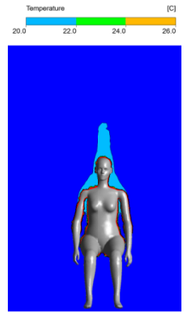	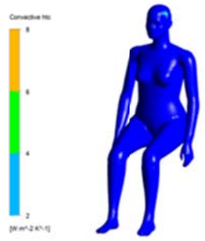	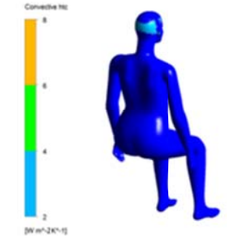
Medium	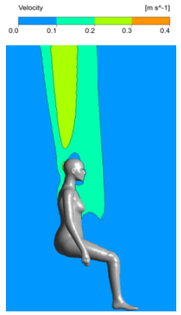	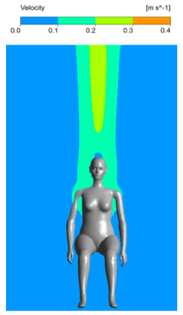	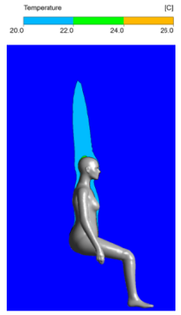	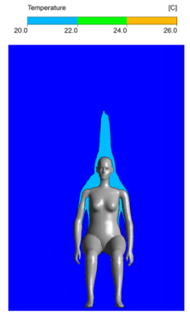	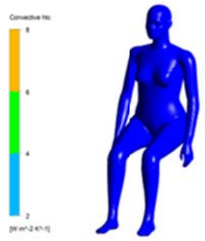	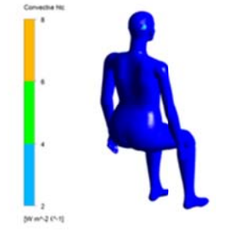
Fine	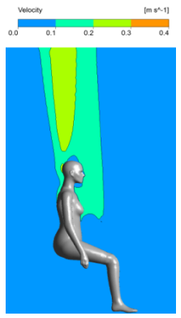		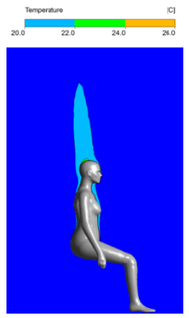	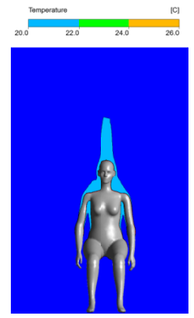	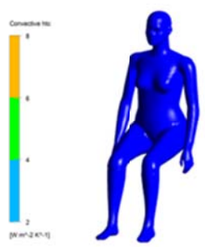	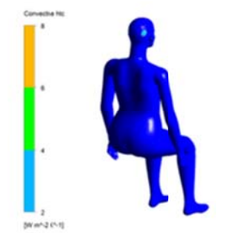

A.3. Results of k-ε eddy viscosity turbulence model

k-ε Turbulence Model						
Mesh	**Flow Field**		**Temperature Field**		**Convective Heat Transfer Coefficients**	
Coarse	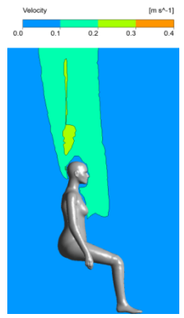		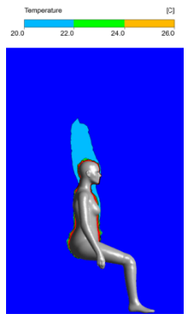	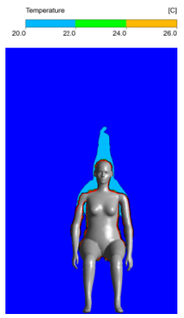	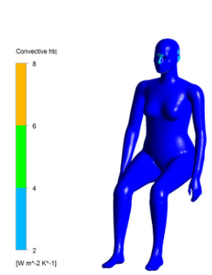	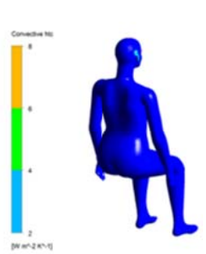
Medium	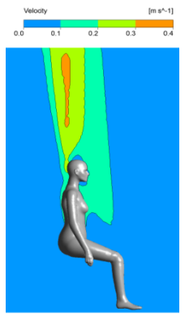	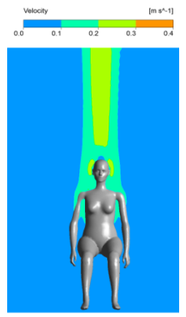	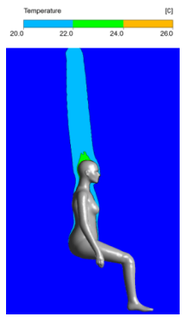	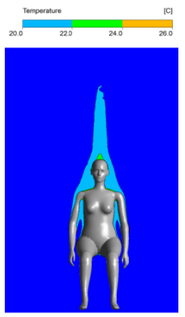	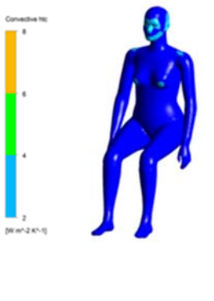	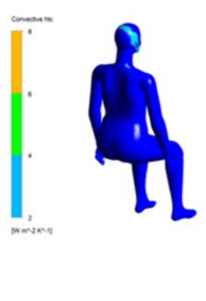
Fine	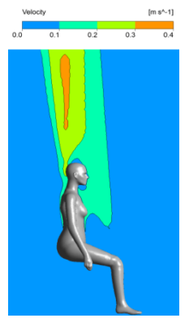	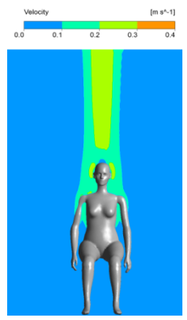	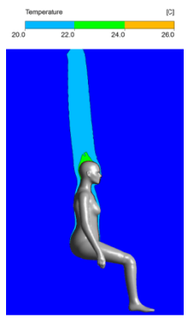	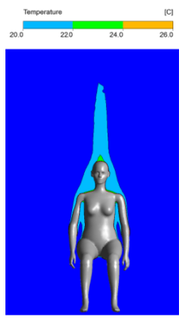	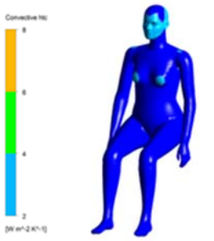	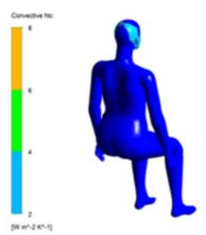

A.4. Results of RNG k-ε eddy viscosity turbulence model

RNG k-ε Turbulence Model						
Mesh	**Flow Field**		**Temperature Field**		**Convective Heat Transfer Coefficients**	
Coarse	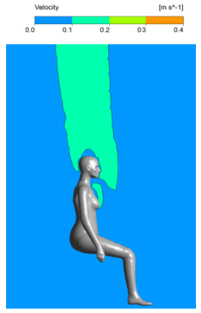	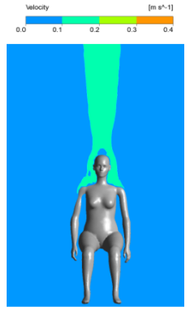	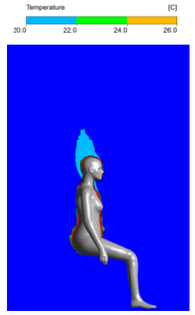	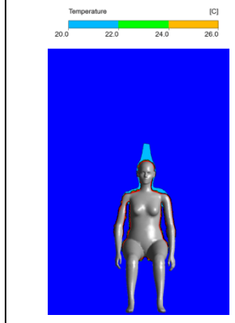	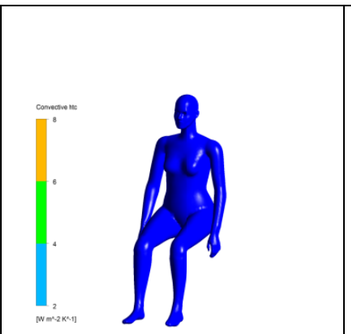	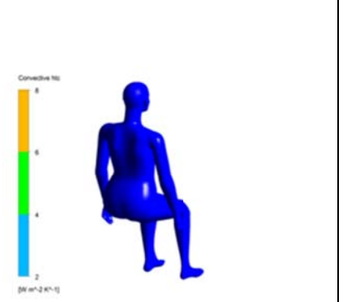
Medium	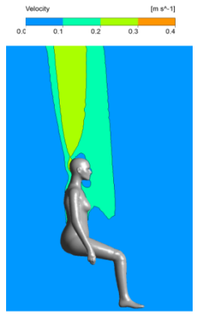	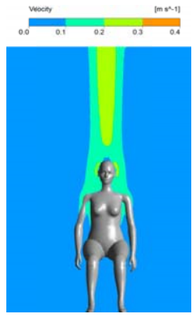	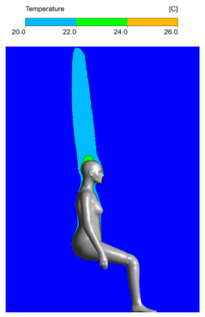	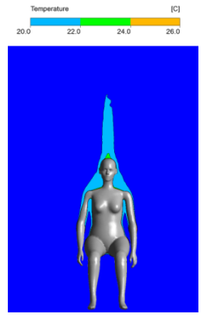	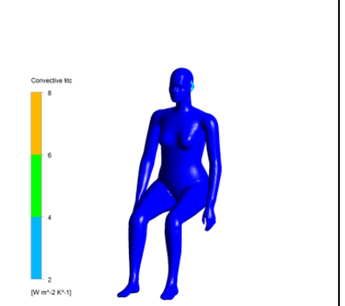	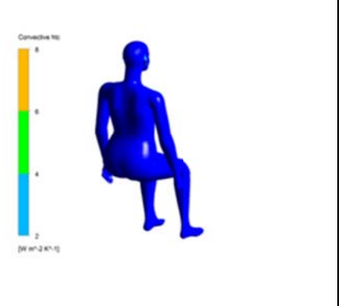
Fine	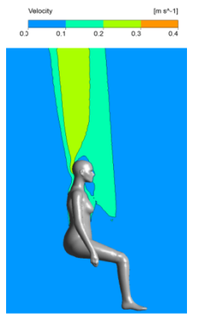	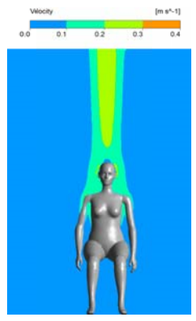	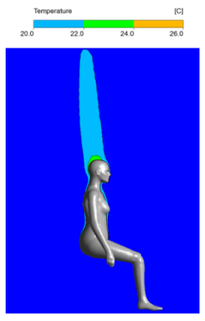	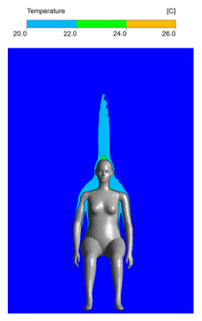	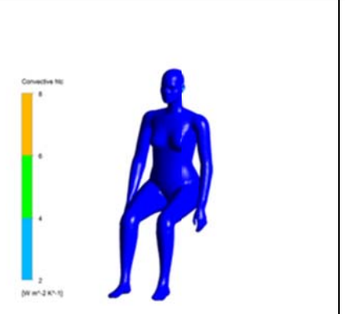	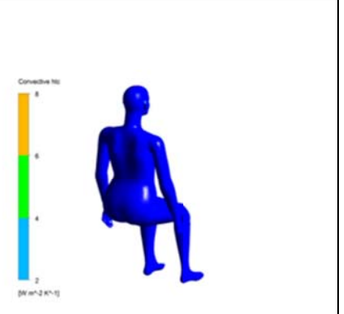

APPENDIX B

B1. Quantitative analysis of temperature, velocity, concentration level, CO2 level and relative humidity at 15 cm above (a) simple manikin and (b) detailed manikin in exhalation mode

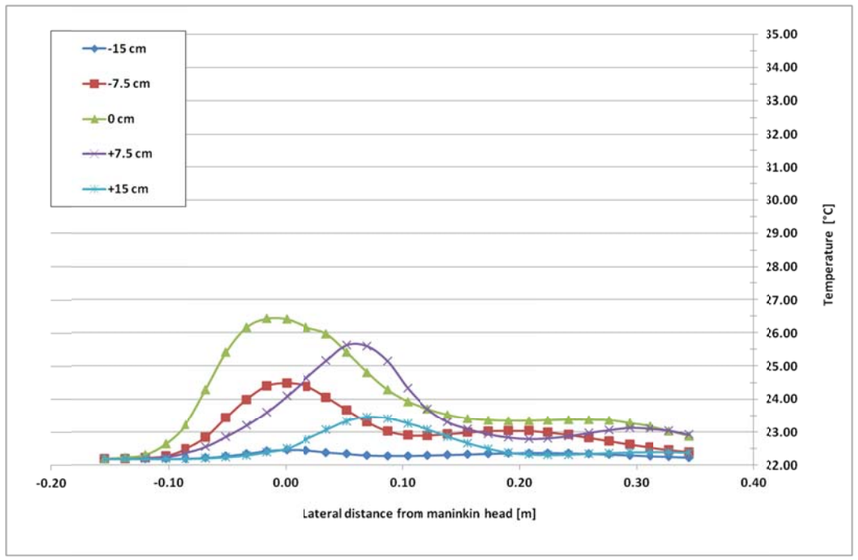

Temperature variation at 15 cm above simple manikin

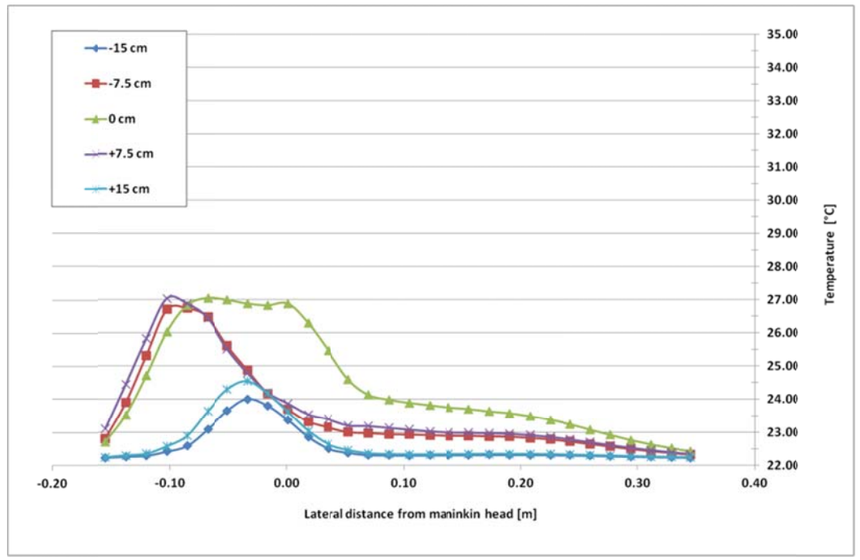

Temperature variation at 15 cm above detailed manikin

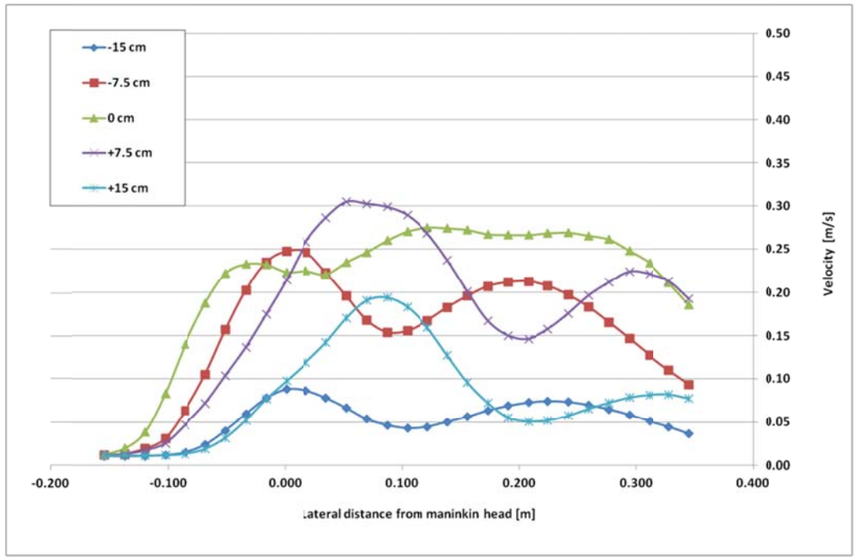

Velocity variation at 15 cm above simple manikin

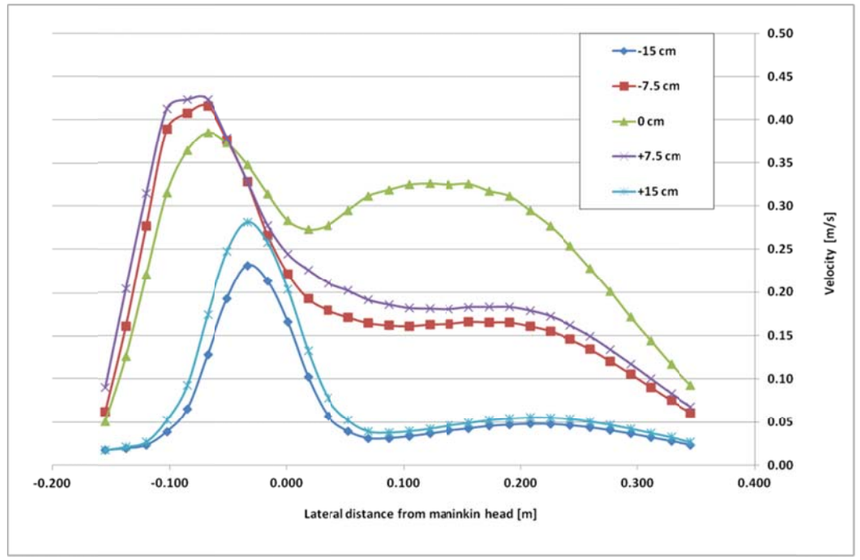

Velocity variation at 15 cm above detailed manikin

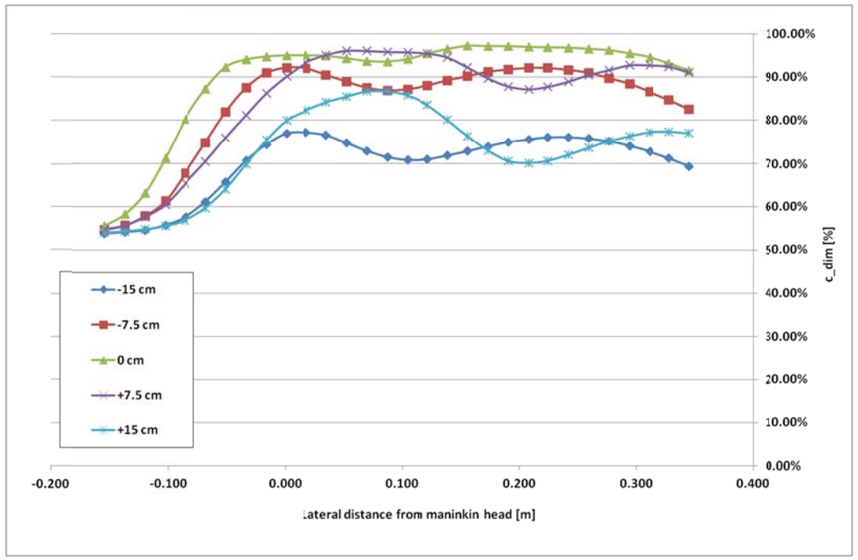

Pollutant variation at 15 cm above simple manikin

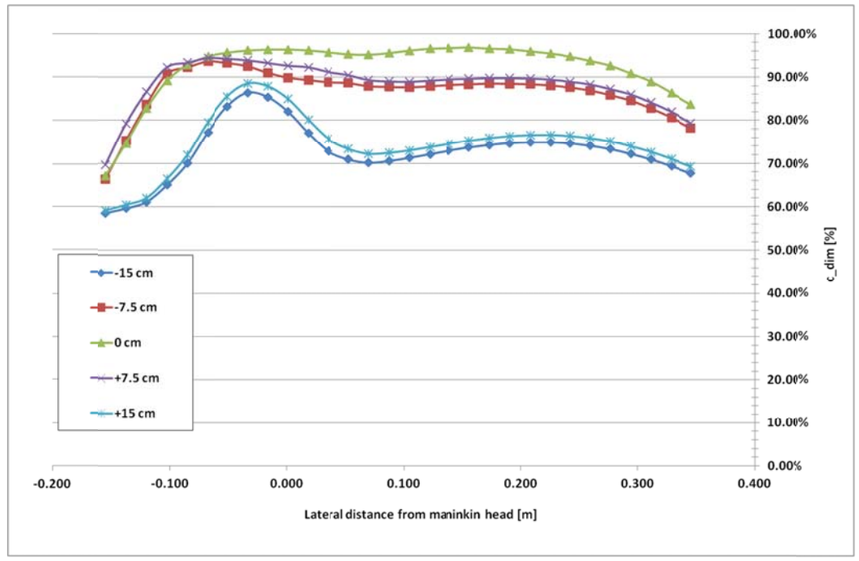

Pollutant variation at 15 cm above detailed manikin

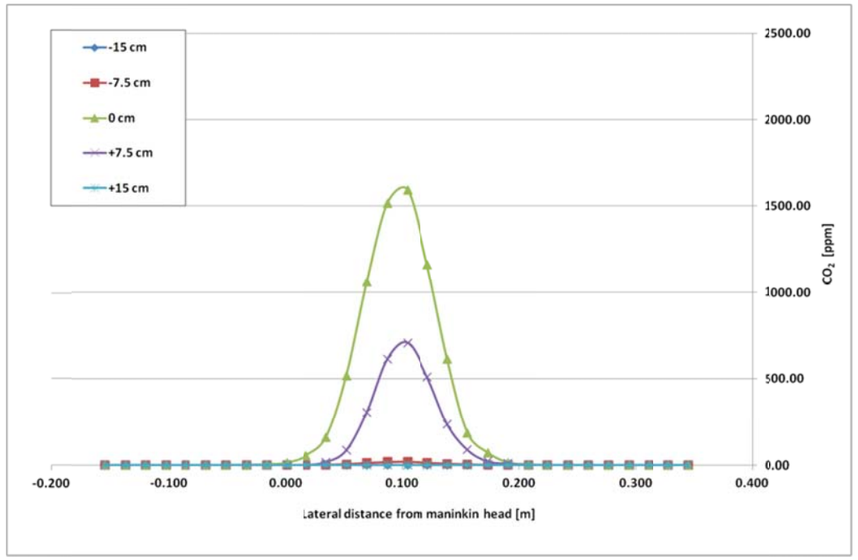

CO2 variation at 15 cm above simple manikin

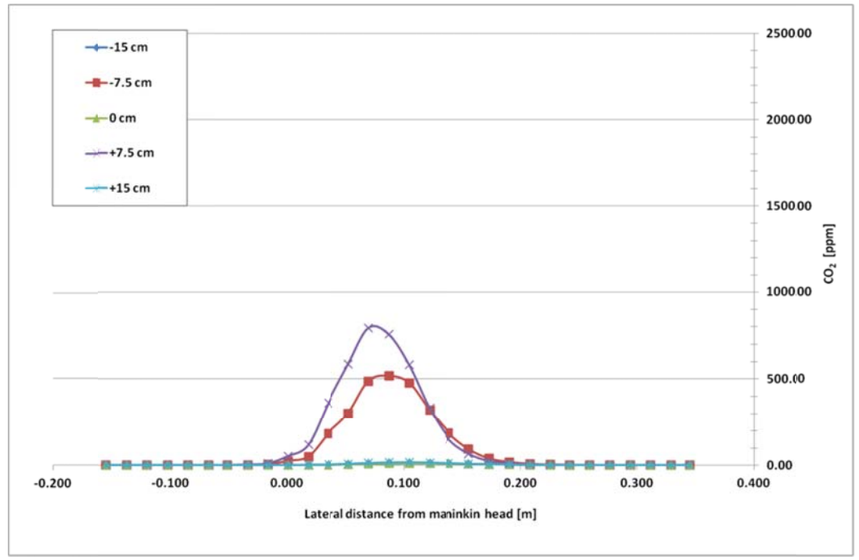

CO2 variation at 15 cm above detailed manikin

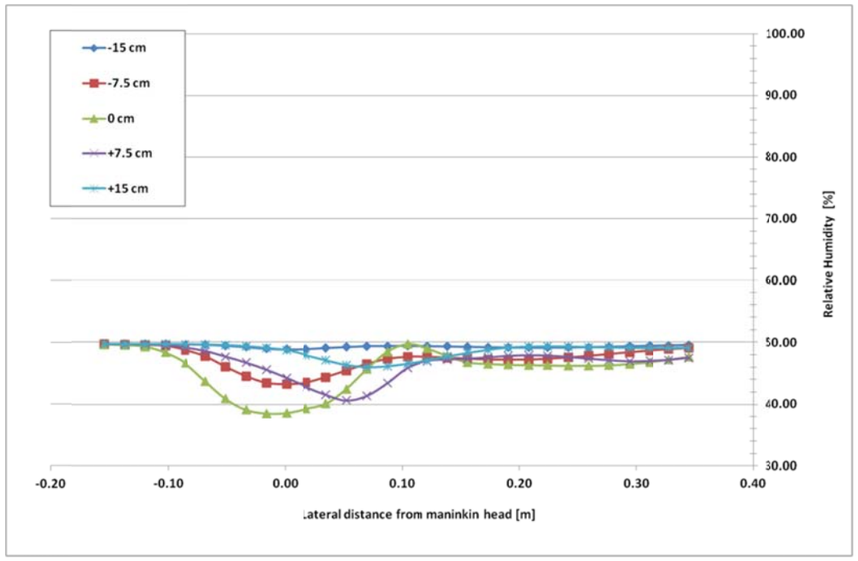

Relative Humidity variation at 15 cm above simple manikin

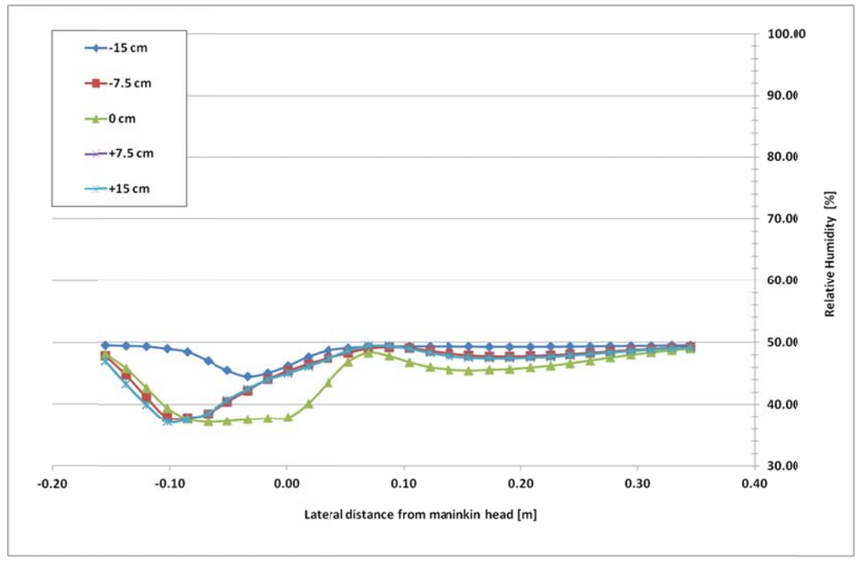

Relative Humidity variation at 15 cm above detailed manikin

B2. Quantitative analysis of temperature, velocity, concentration level, CO2 level and relative humidity at 30 cm above (a) simple manikin and (b) detailed manikin in exhalation mode

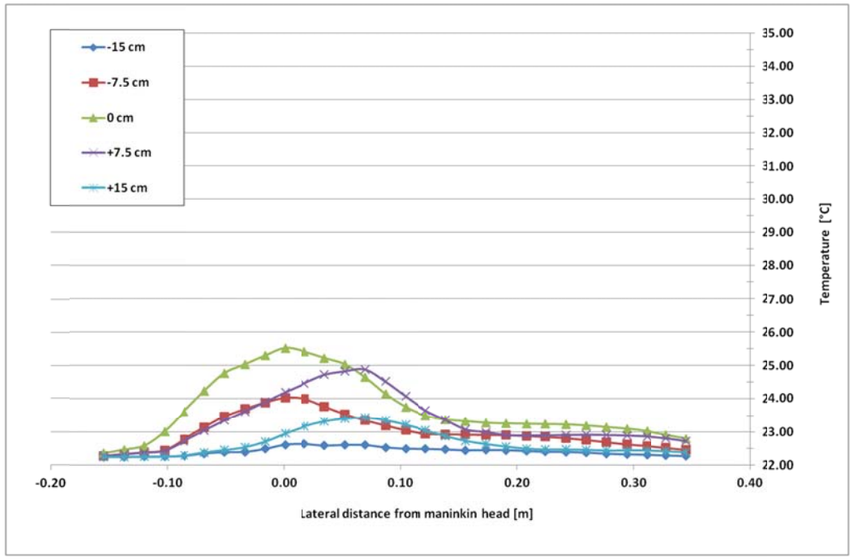

Temperature variation at 30 cm above simple manikin

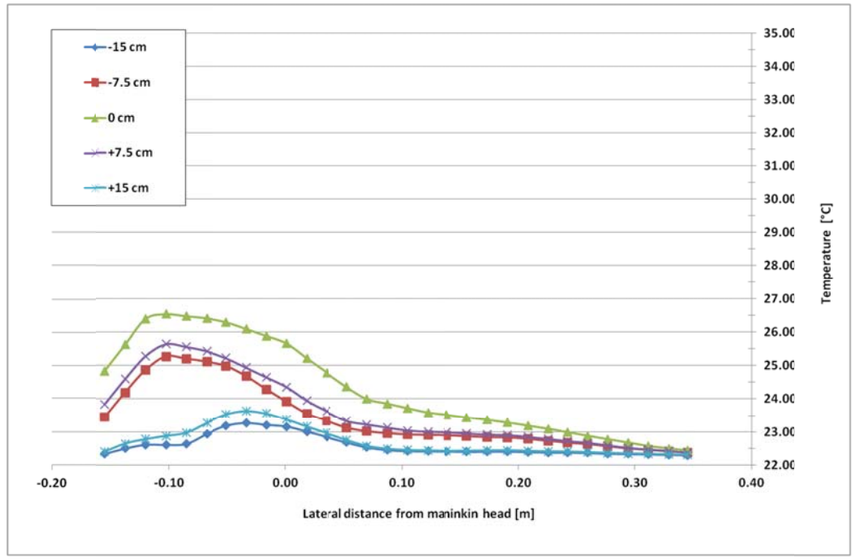

Temperature variation at 30 cm above detailed manikin

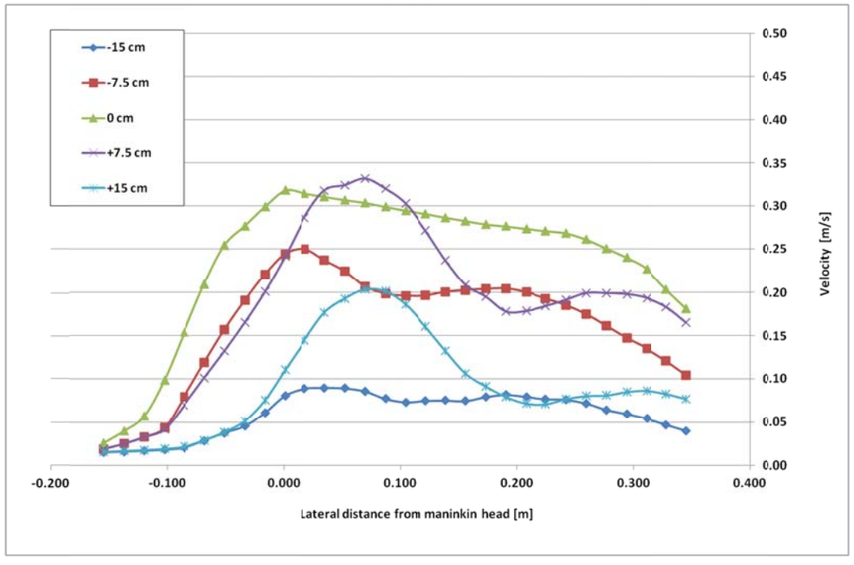

Velocity variation at 30 cm above simple manikin

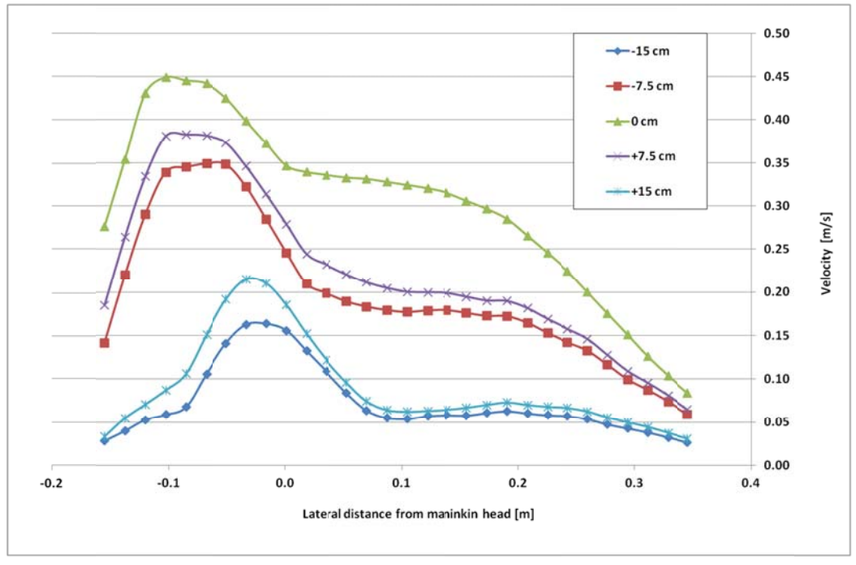

Velocity variation at 30 cm above detailed manikin

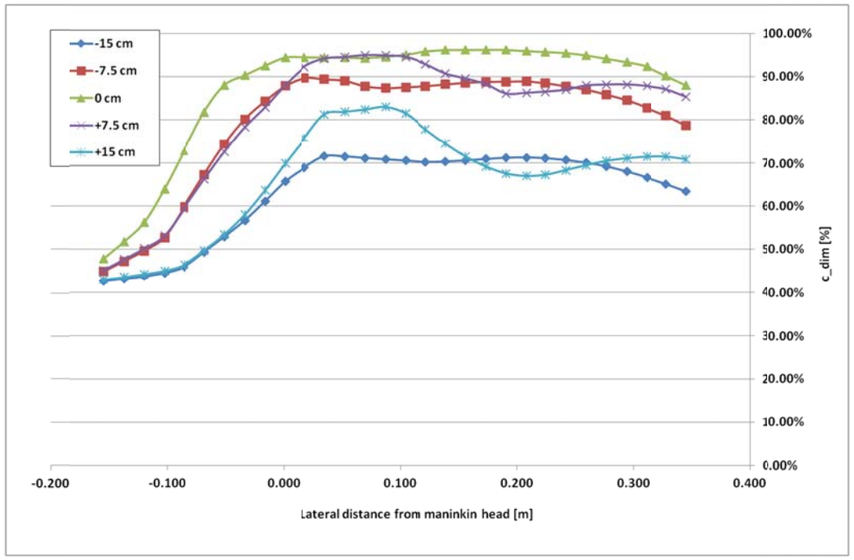

Pollutant variation at 30 cm above simple manikin

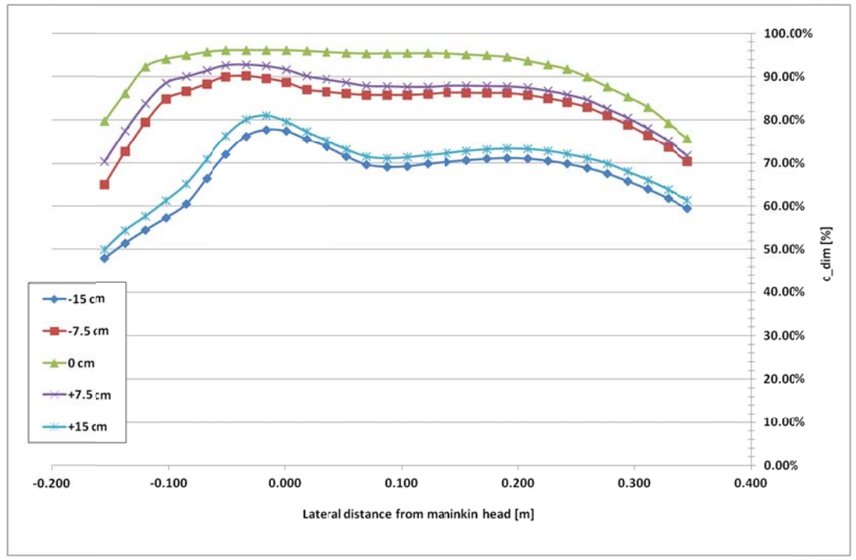

Pollutant variation at 30 cm above detailed manikin

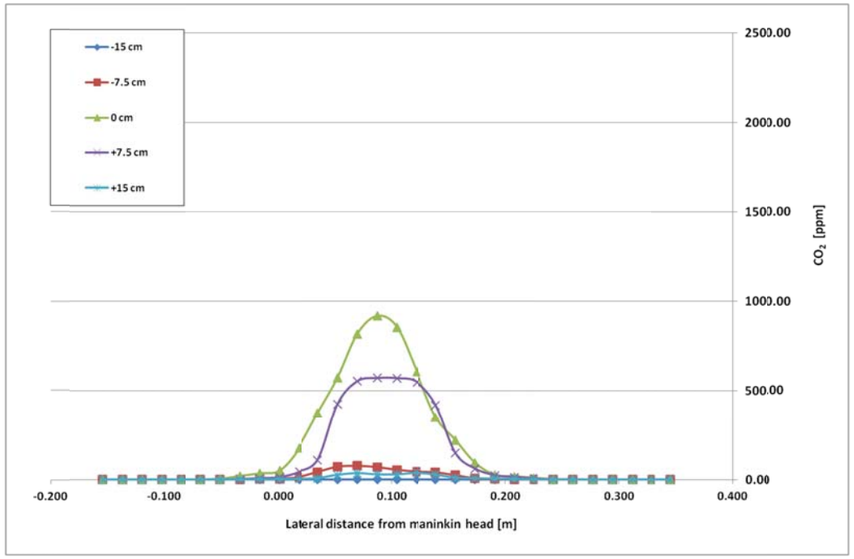

CO2 variation at 30 cm above simple manikin

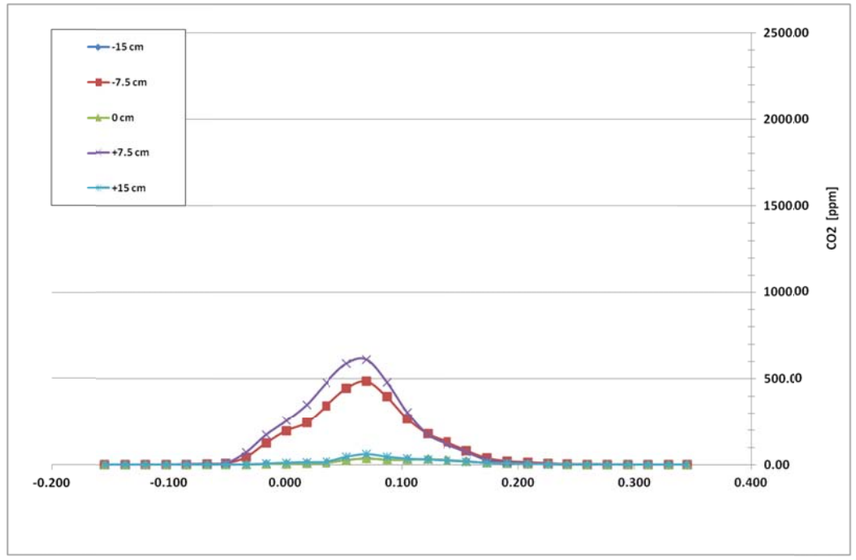

CO2 variation at 30 cm above detailed manikin

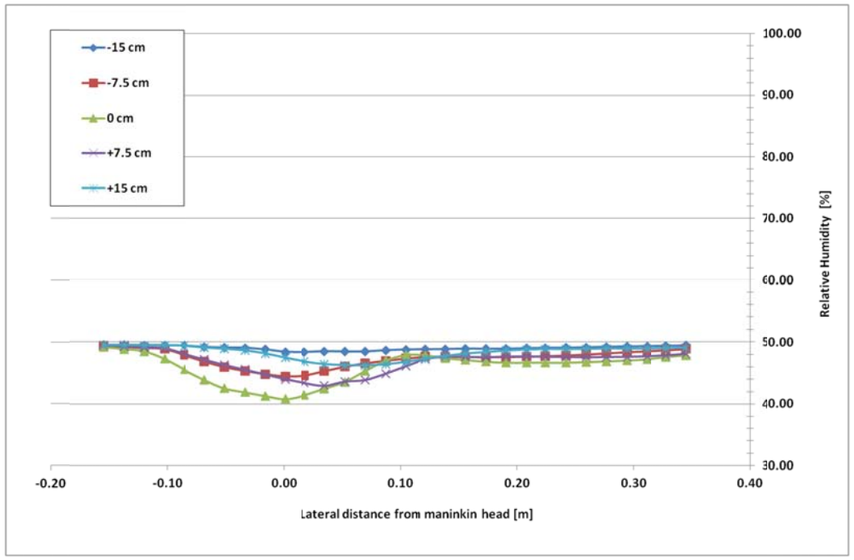

Relative Humidity variation at 30 cm above simple manikin

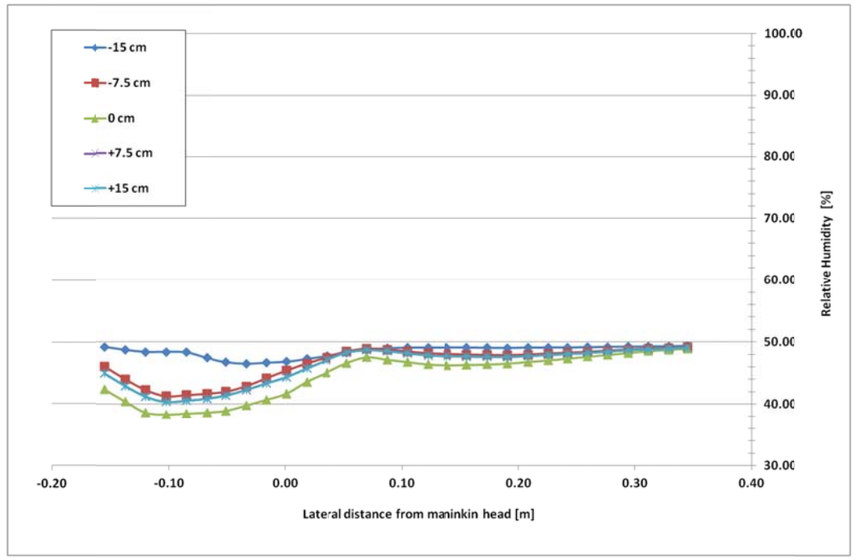

Relative Humidity variation at 30 cm above detailed manikin

X

B3. Quantitative analysis of temperature, velocity, concentration level, CO2 level and relative humidity at 70 cm above (a) simple manikin and (b) detailed manikin in exhalation mode

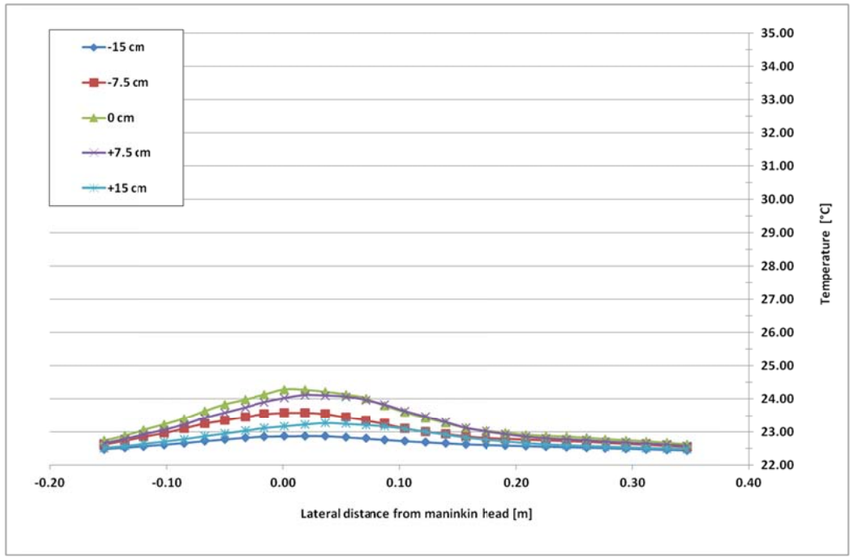

Temperature variation at 70 cm above simple manikin

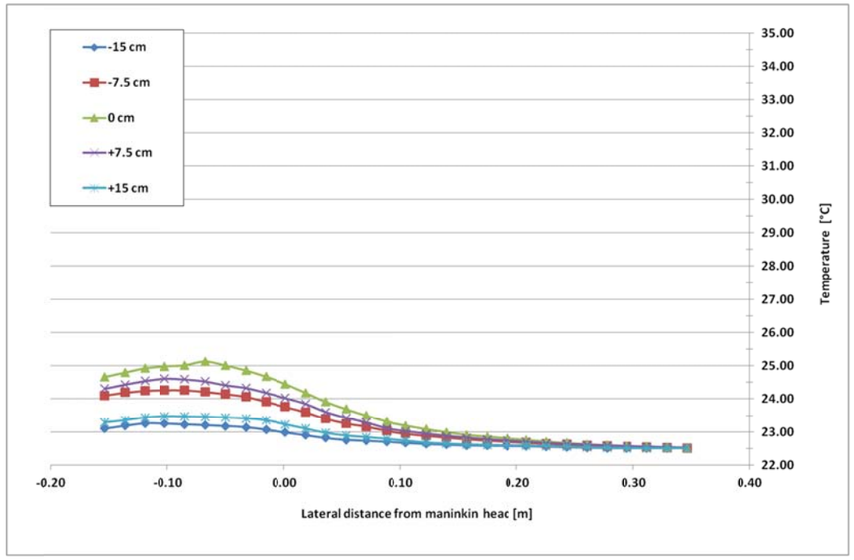

Temperature variation at 70 cm above detailed manikin

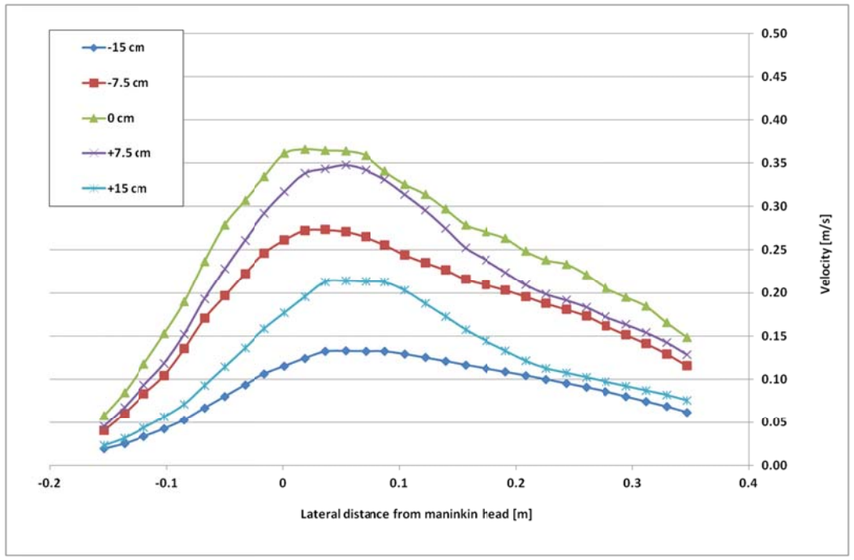

Velocity variation at 70 cm above simple manikin

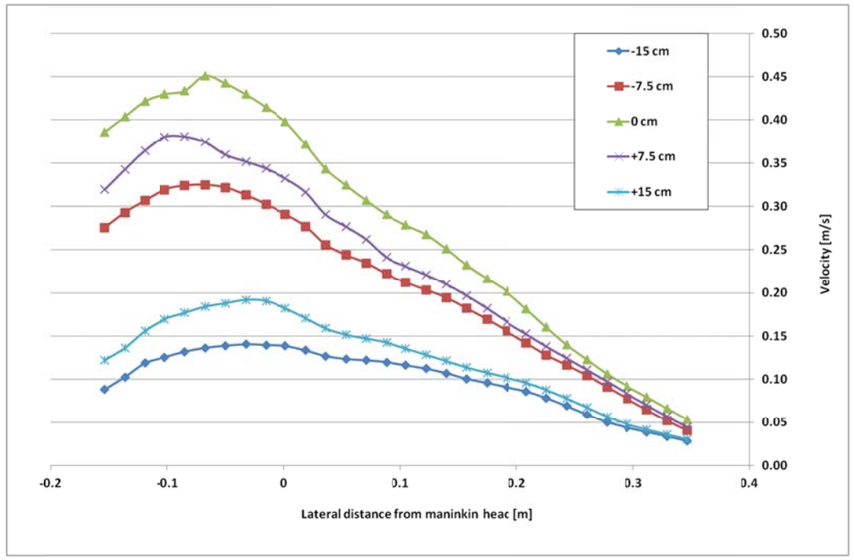

Velocity variation at 70 cm above detailed manikin

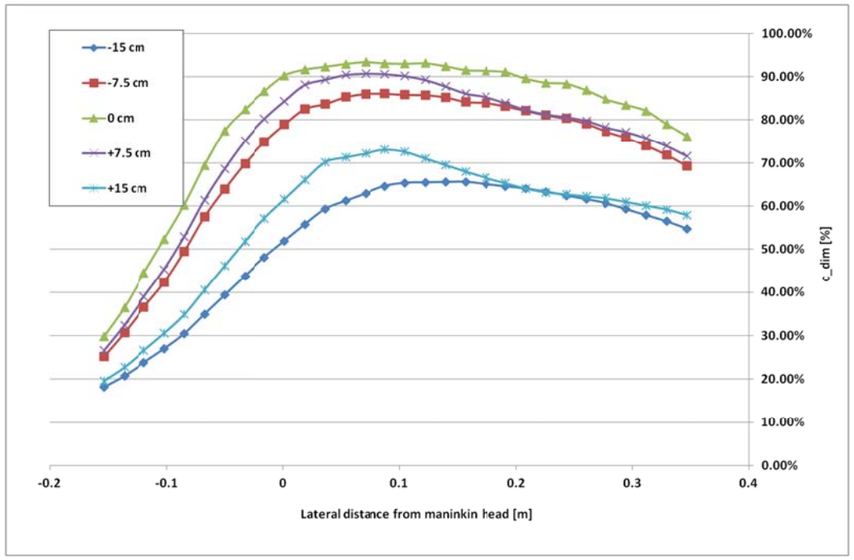

Pollutant variation at 70 cm above simple manikin

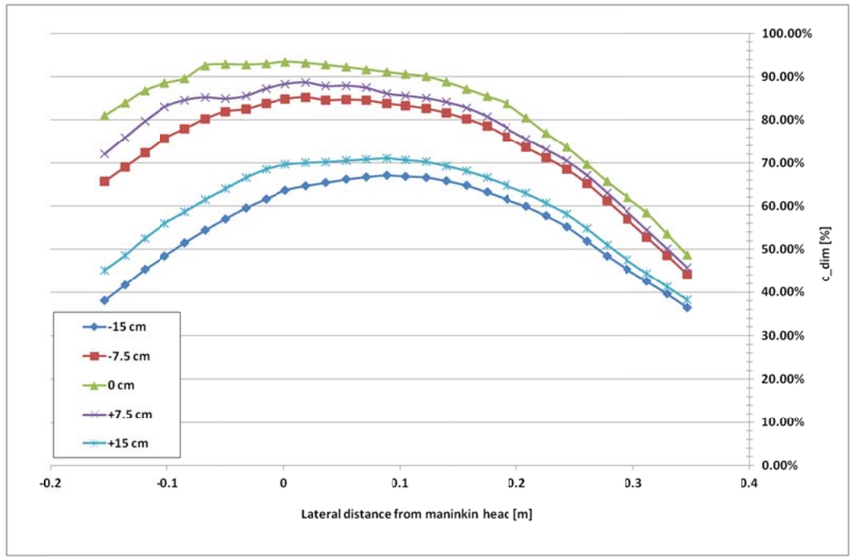

Pollutant variation at 70 cm above detailed manikin

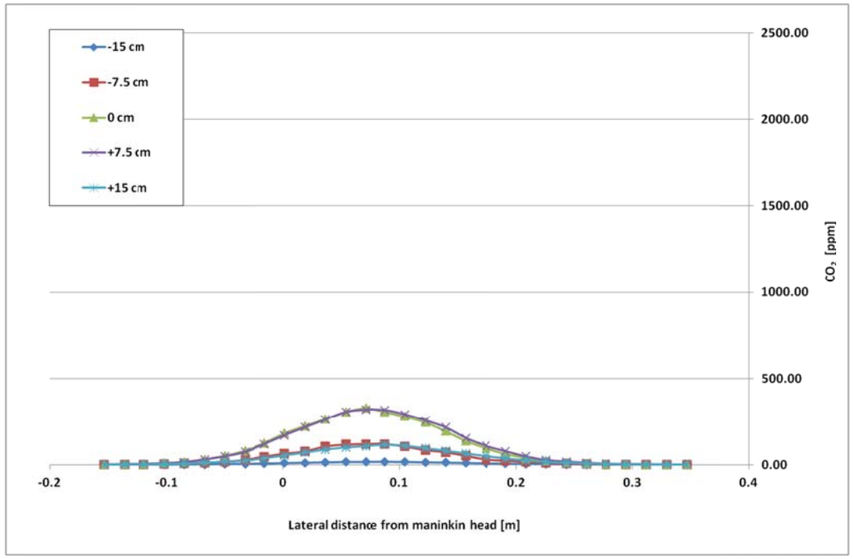

CO2 variation at 70 cm above simple manikin

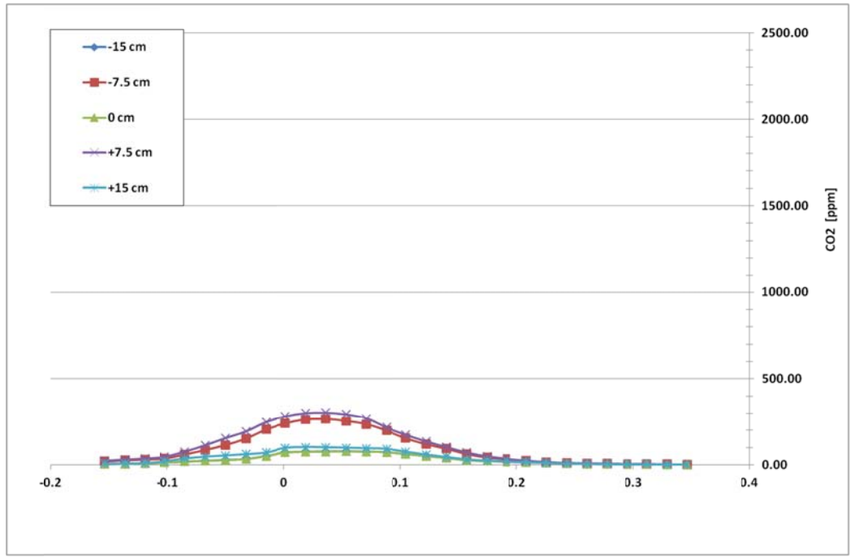

CO2 variation at 70 cm above detailed manikin

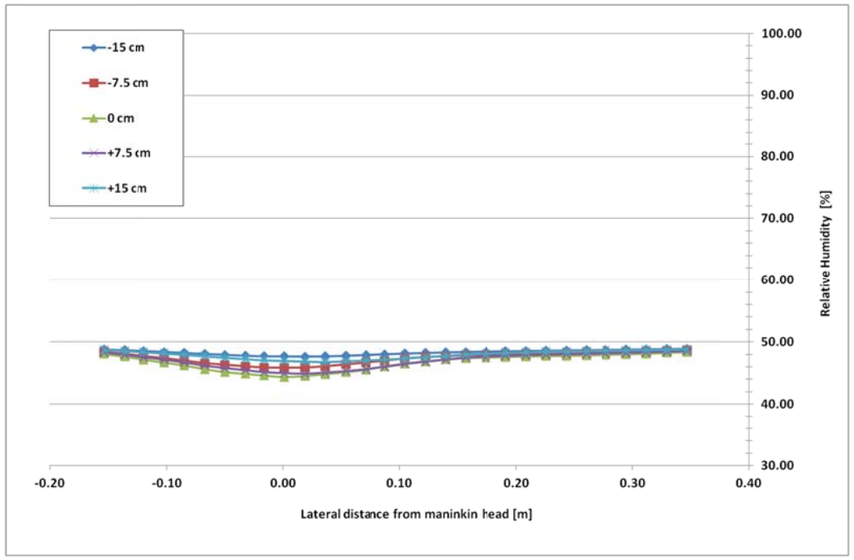

Relative Humidity variation at 70 cm above simple manikin

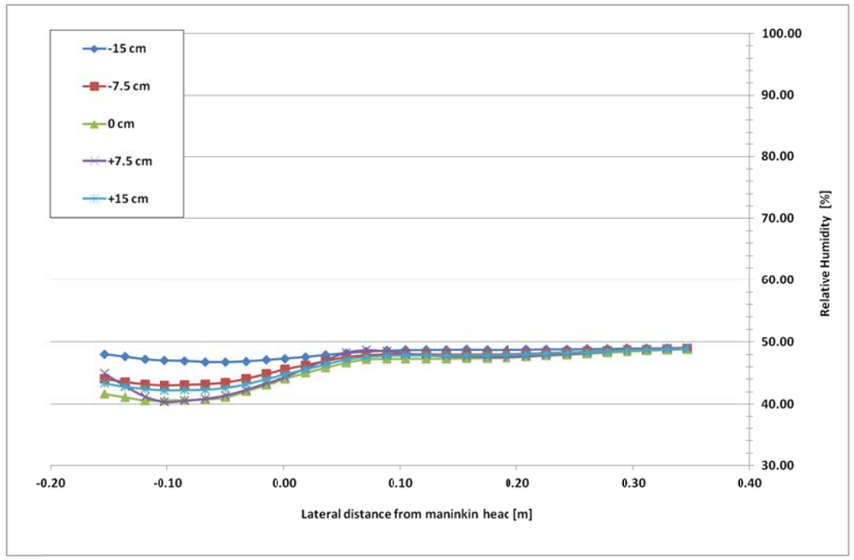

Relative Humidity variation at 70 cm above detailed manikin

B4. Quantitative analysis of temperature, velocity, concentration level and relative humidity at 15 cm above (a) simple manikin and (b) detailed manikin in inhalation mode

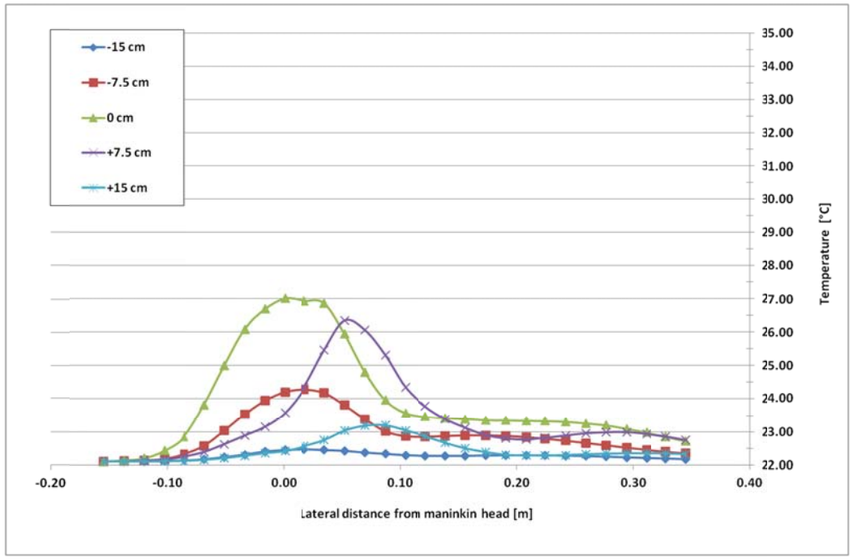

Temperature variation at 15 cm above simple manikin

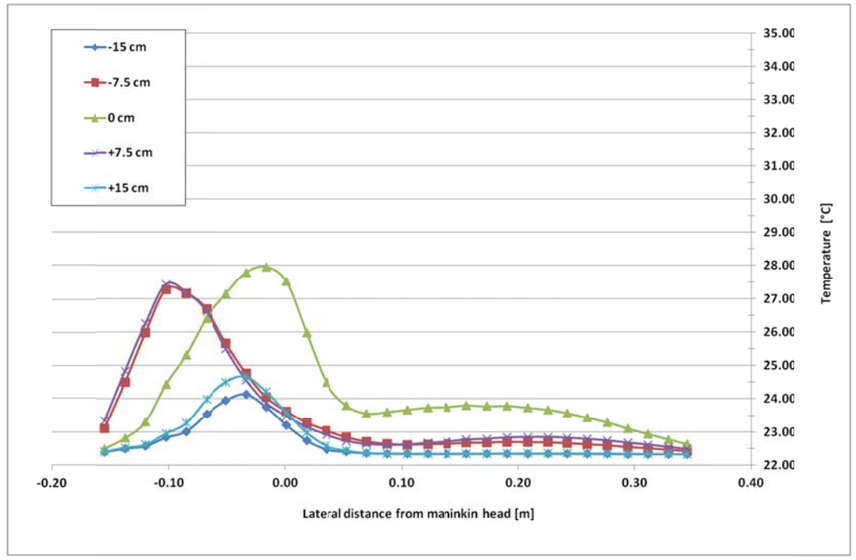

Temperature variation at 15 cm above detailed manikin

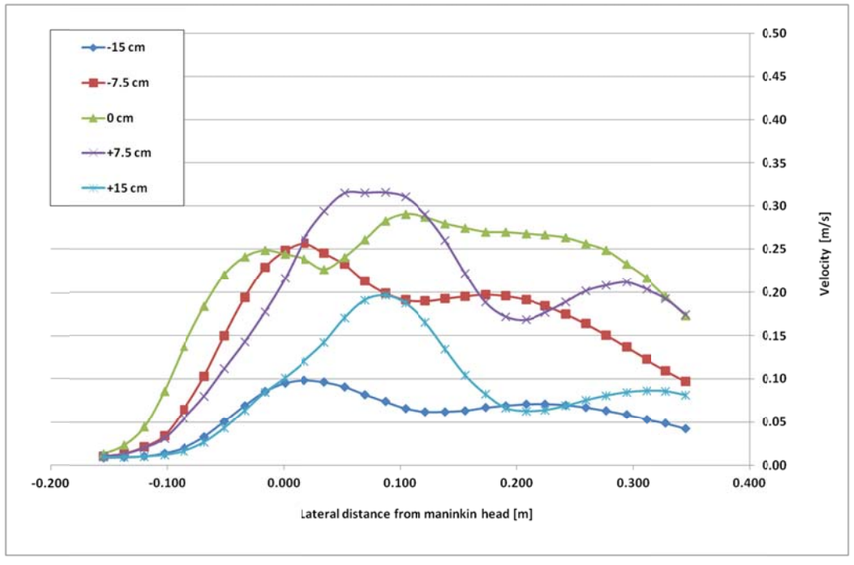

Velocity variation at 15 cm above simple manikin

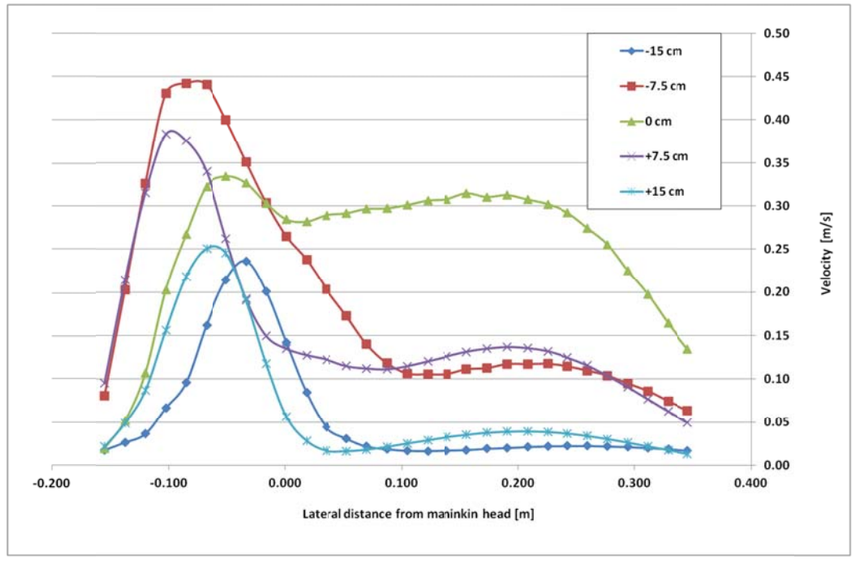

Velocity variation at 15 cm above detailed manikin

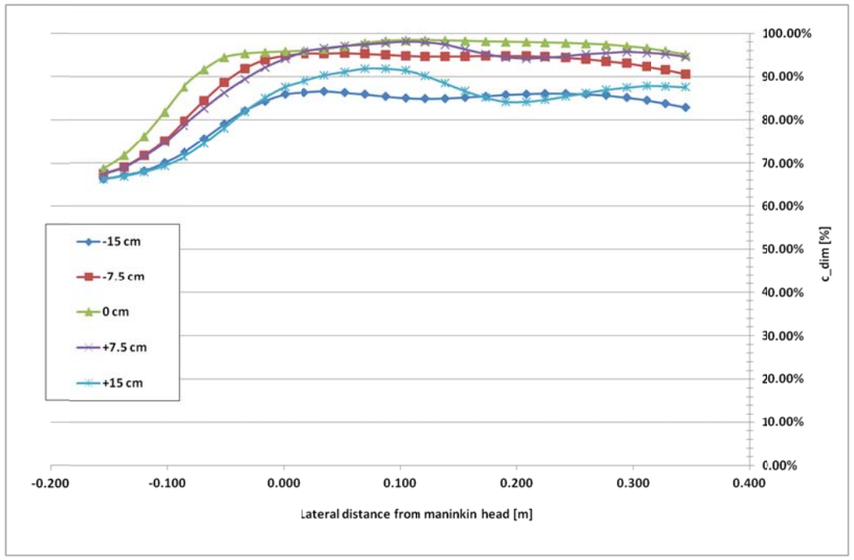

Pollutant variation at 15 cm above simple manikin

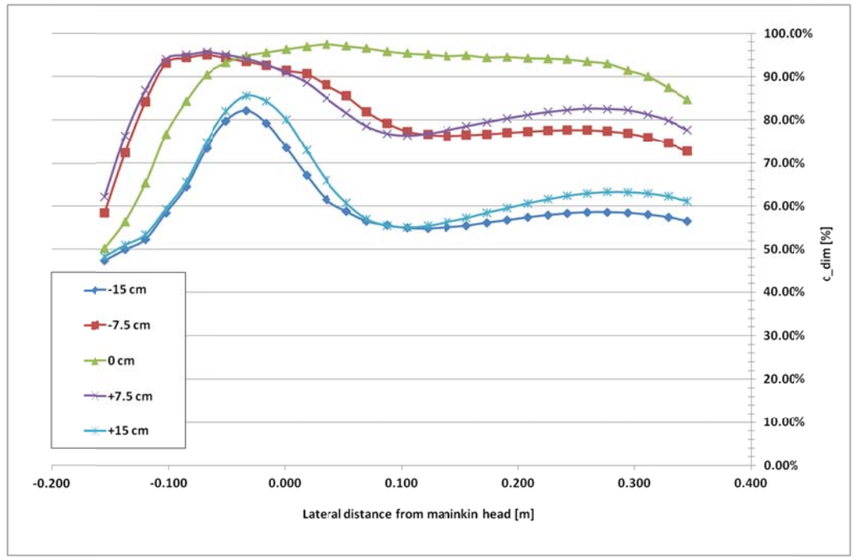

Pollutant variation at 15 cm above detailed manikin

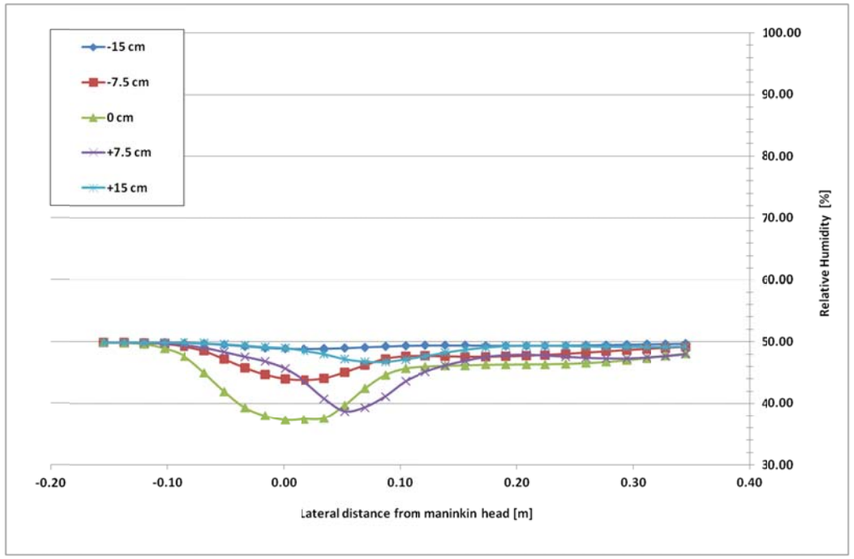

Relative Humidity variation at 15 cm above simple manikin

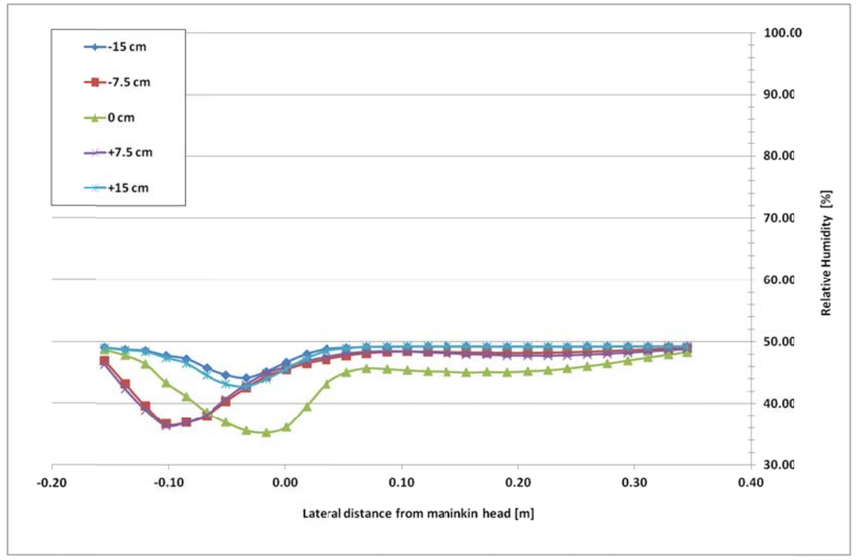

Relative Humidity variation at 15 cm above detailed manikin

B5. Quantitative analysis of temperature, velocity, concentration level and relative humidity at 30 cm above (a) simple manikin and (b) detailed manikin in inhalation mode

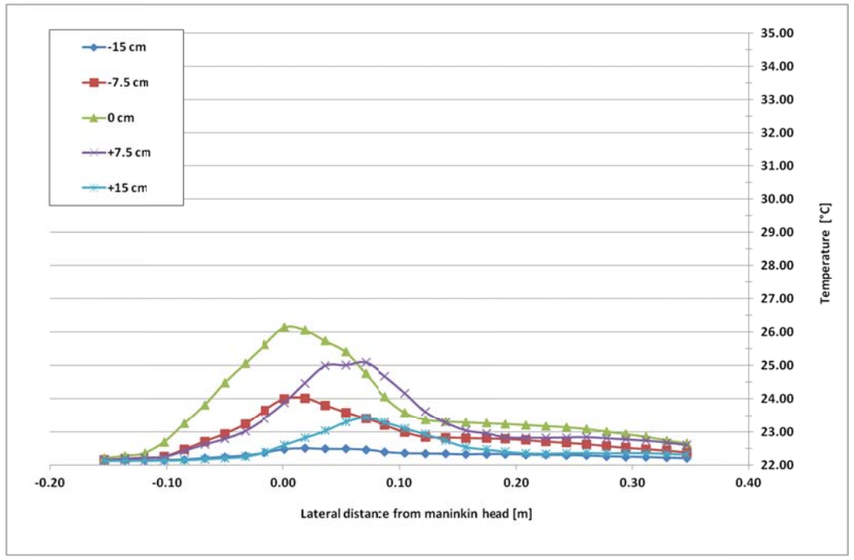

Temperature variation at 30 cm above simple manikin

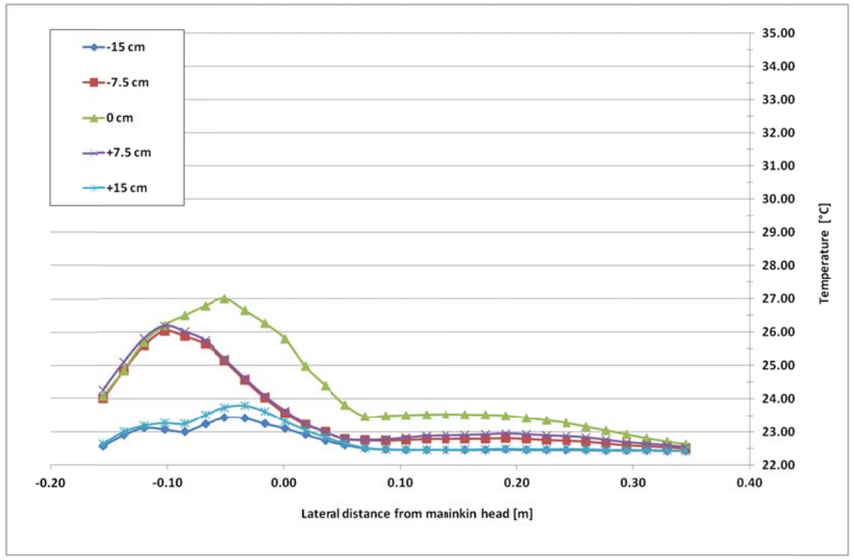

Temperature variation at 30 cm above detailed manikin

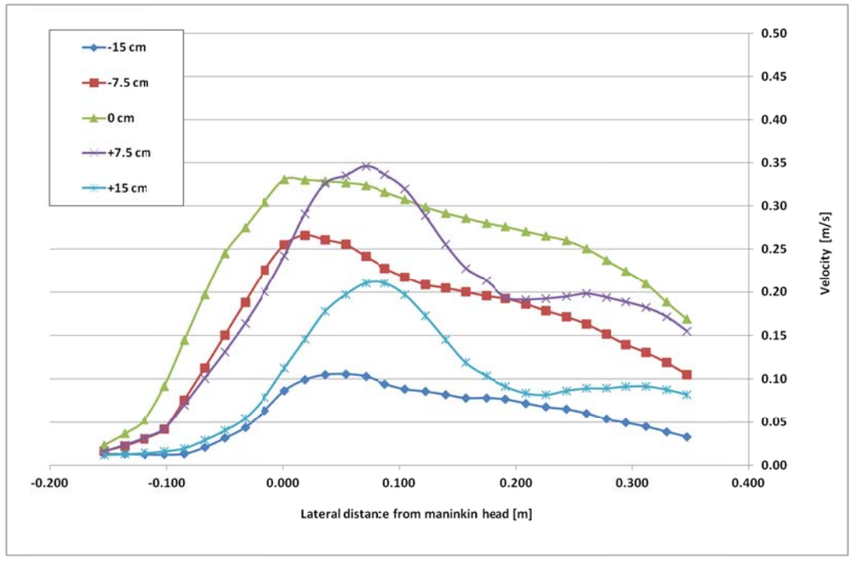

Velocity variation at 30 cm above simple manikin

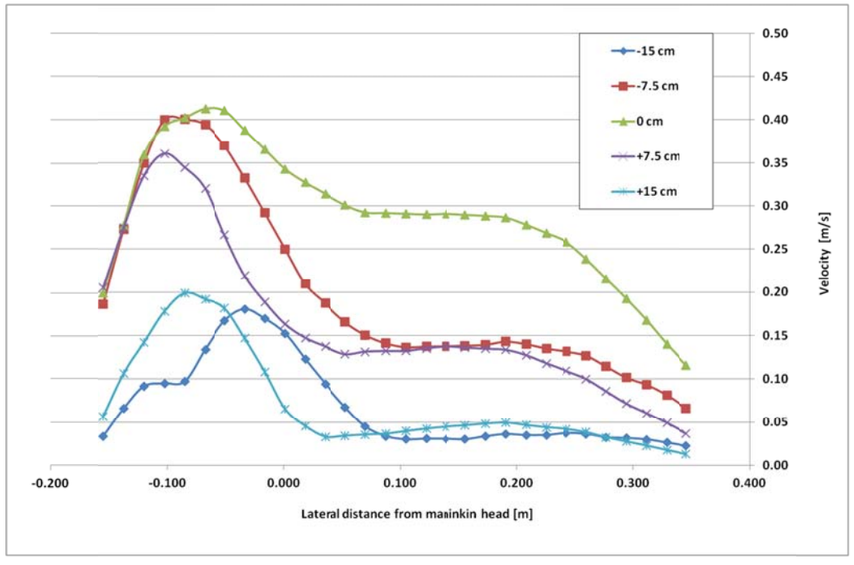

Velocity variation at 30 cm above detailed manikin

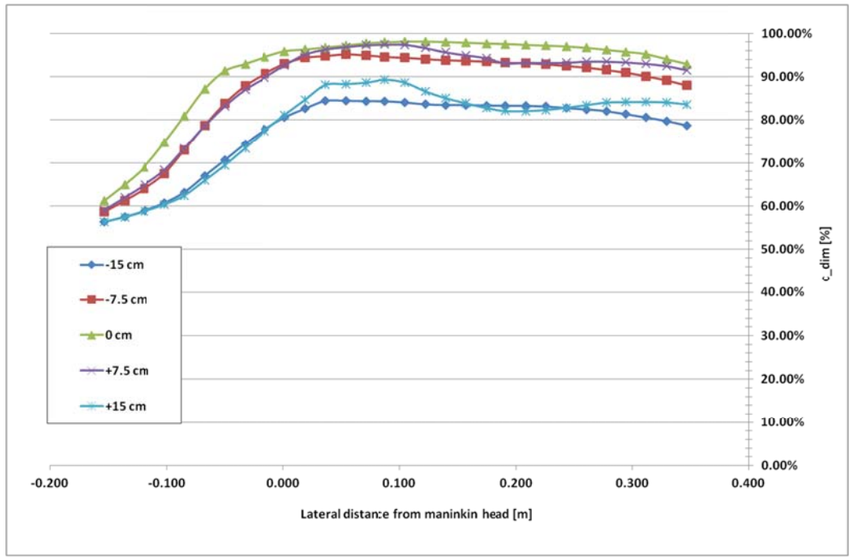

Pollutant variation at 30 cm above simple manikin

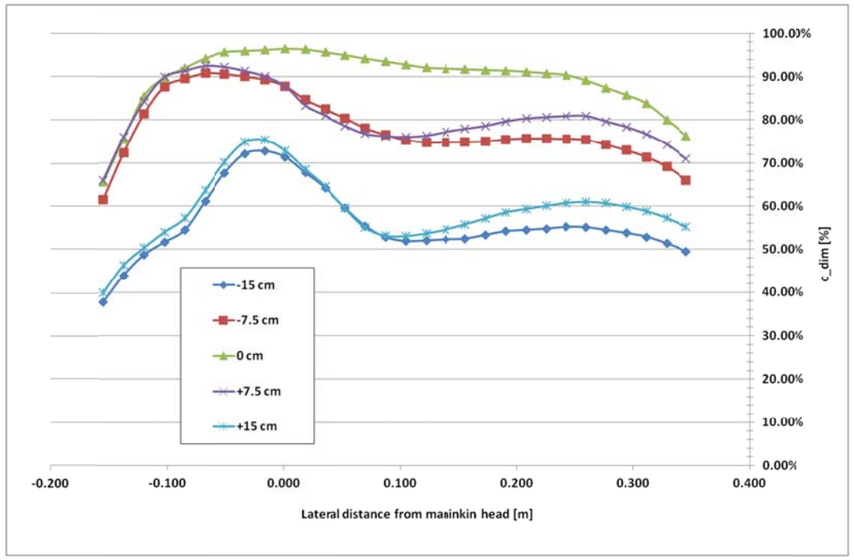

Pollutant variation at 30 cm above detailed manikin

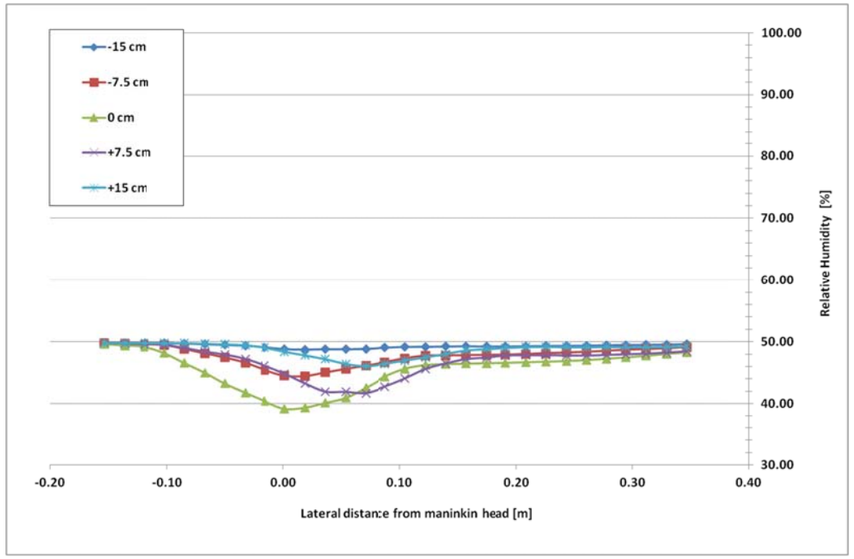

Relative Humidity variation at 30 cm above simple manikin

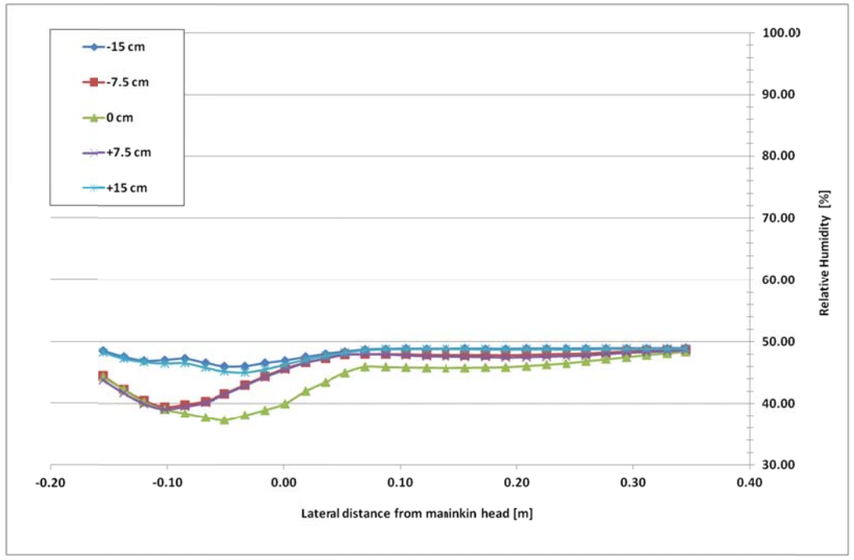

Relative Humidity variation at 30 cm above detailed manikin

B6. Quantitative analysis of temperature, velocity, concentration level and relative humidity at 70 cm above (a) simple manikin and (b) detailed manikin in inhalation mode

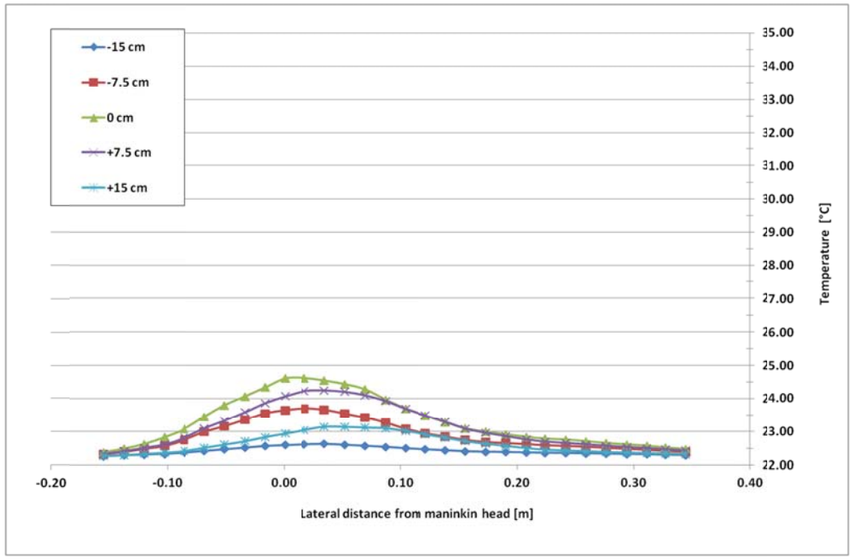

Temperature variation at 70 cm above simple manikin

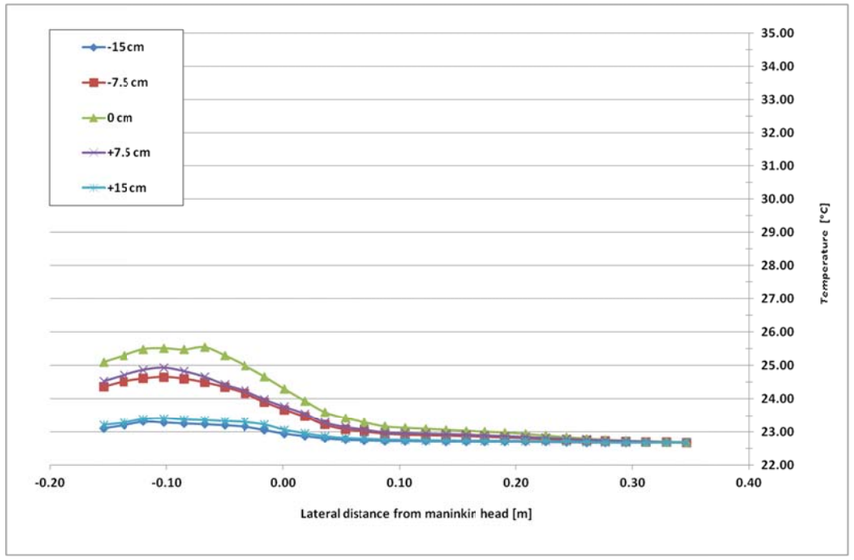

Temperature variation at 70 cm above detailed manikin

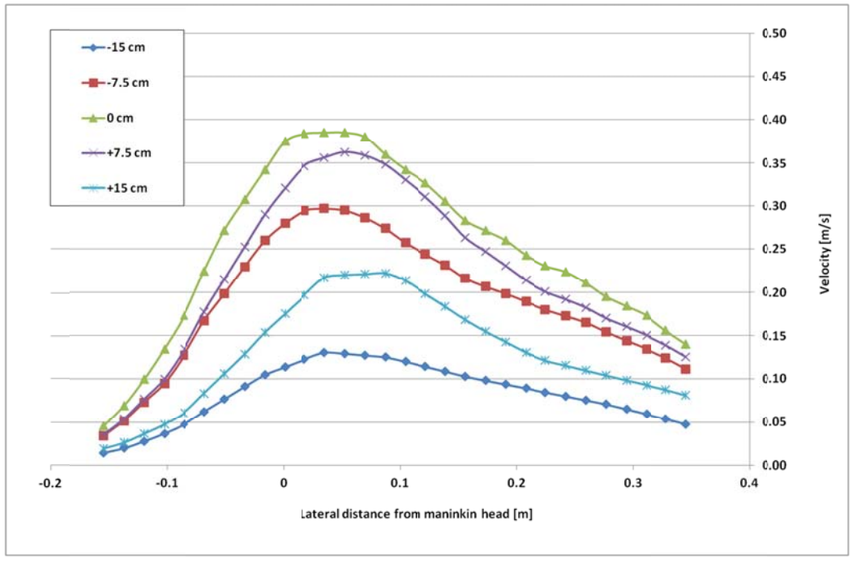

Velocity variation at 70 cm above simple manikin

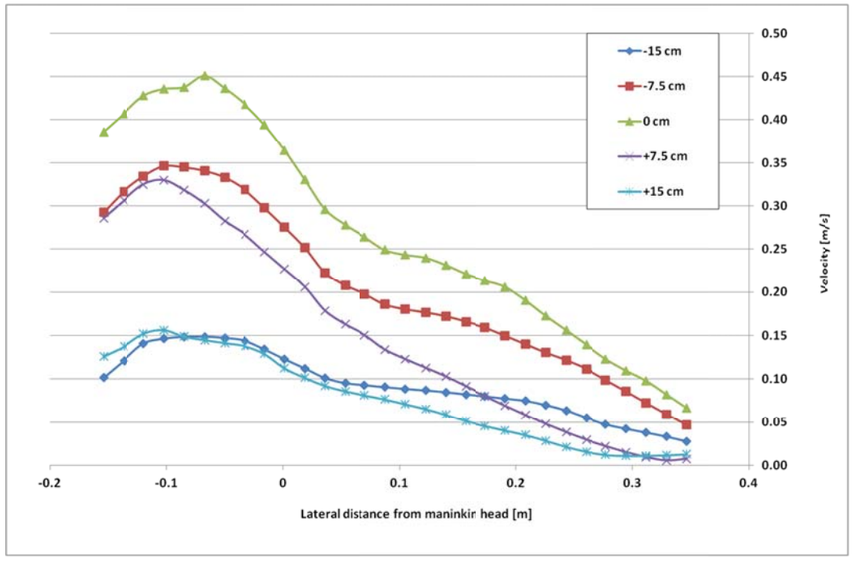

Velocity variation at 70 cm above detailed manikin

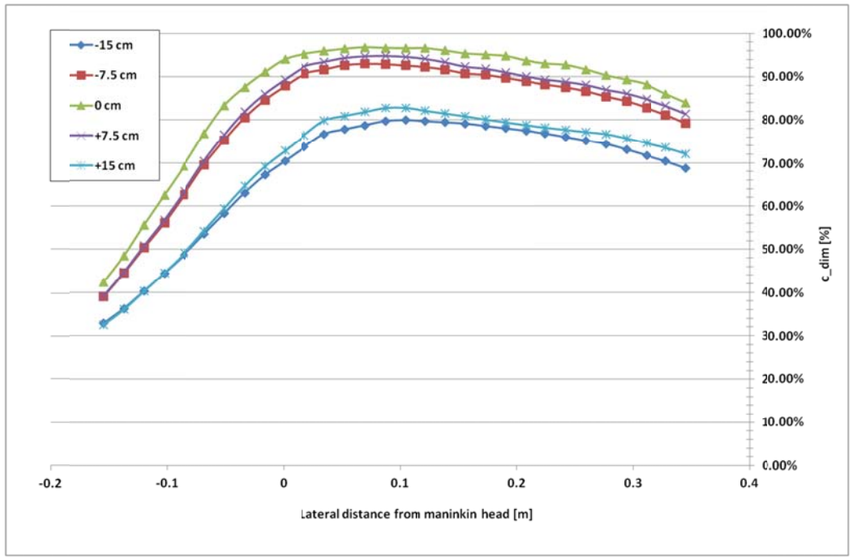

Pollutant variation at 70 cm above simple manikin

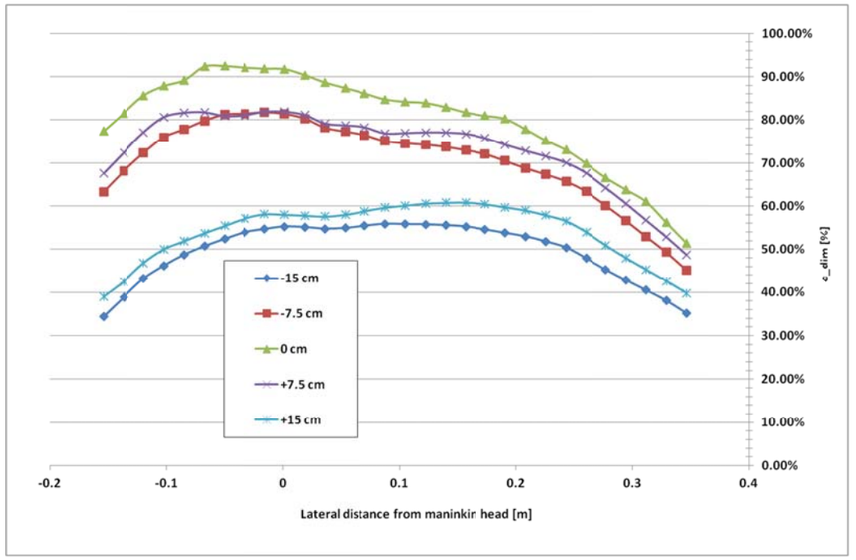

Pollutant variation at 70 cm above detailed manikin

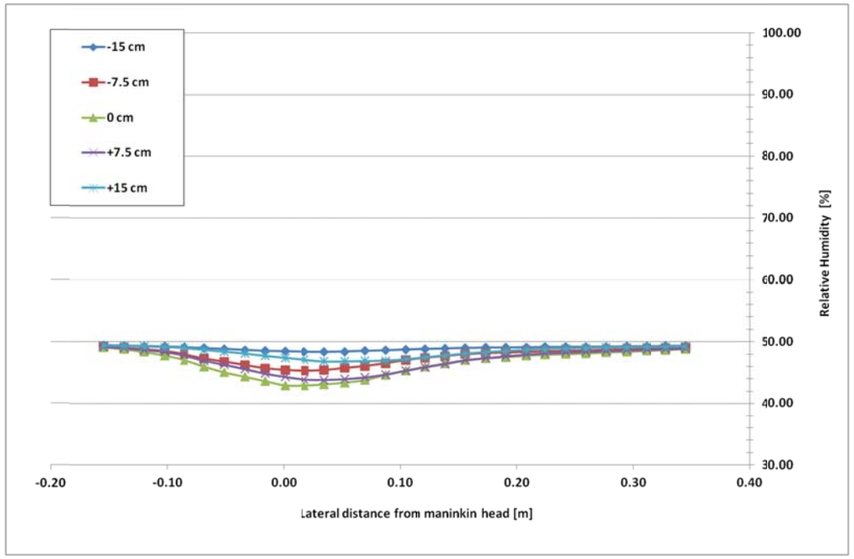

Relative Humidity variation at 70 cm above simple manikin

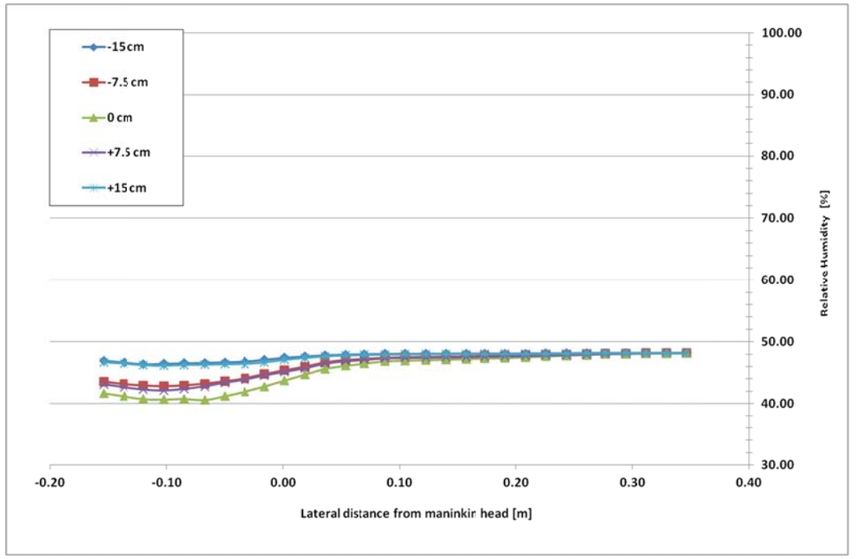

Relative Humidity variation at 70 cm above detailed manikin